

**Study of top-quark pair
cross-section measurement in the
dilepton channel with the ATLAS
detector at the LHC**

Dissertation

zur

Erlangung des Doktorgrades (Dr. rer. nat.)

der

Mathematisch-Naturwissenschaftlichen Fakultät

der

Rheinischen Friedrich-Wilhelms-Universität Bonn

vorgelegt von

Duc Bao Ta

aus

Haiphong

Bonn, Oktober 2010

Angefertigt mit Genehmigung der
Mathematisch-Naturwissenschaftlichen Fakultät
der Rheinischen Friedrich-Wilhelms-Universität
Bonn

1. Referent: Prof. Dr. Norbert Wermes
2. Referent: Prof. Dr. Ian Brock

Tag der Promotion: 28. Oktober 2010
Erscheinungsjahr: 2011

Abstract

The top quark is the heaviest of the known fundamental particles in the *Standard Model* (SM) with a mass of 173.3 ± 1.1 GeV. It is the sixth quark in the SM and the weak isospin partner of the bottom quark. Properties such as the mass and the cross section have been measured since its discovery in 1995 with great precision at the proton-antiproton Fermilab Tevatron Collider, Chicago at a centre-of-mass energy of 1.8 GeV and 1.96 GeV. With the start of the proton-proton CERN *Large Hadron Collider* (LHC), Geneva, a new record in the centre-of-mass energy was achieved. The LHC opens a new energy frontier and probes the SM at energies of the electro-weak symmetry-breaking scale and beyond. The measurement of the top-quark pair cross-section at this new energy is an important step, since it will either re-establish the SM at these energies by confirming the theoretical calculations or it can point to new phenomena that help to understand the so far not explained experimental findings in particle physics and cosmology.

This thesis presents a study of the production cross-section measurement of top-quark pair in the dilepton channel at the LHC with the ATLAS experiment at a centre-of-mass energy of $\sqrt{s} = 10$ TeV and for a data amount of $\mathcal{L}_{\text{int.}} = 200$ pb⁻¹. This study investigates the performance of the cross-section measurement with a cut-and-count analysis on Monte Carlo simulated samples. Important background processes are taken into account such as leptonically decaying *Z*-boson and single top-quark events. Data-driven background methods for *Z*-boson and fake event rates are discussed. A full list of systematic uncertainties is investigated and finally combined with the statistical uncertainties in a likelihood to extract the combined uncertainty. A “top mass”-like variable is presented that can help to distinguish dileptonic top-quark pair decays from similar signatures in new physics models. The combined sensitivity of the analysis in all dilepton decay-channels is a relative uncertainty on the cross-section measurement of:

$$\frac{\Delta\sigma_{\text{combined}}}{\sigma_{\text{combined}}} [\%] = {}^{+3.1}_{-3.1}(\text{stat}) {}^{+9.6}_{-8.7}(\text{syst}) {}^{+26.2}_{-17.4}(\text{lumi})$$

Finally the study is compared to the same analyses performed at different centre-of-mass energies of 14 GeV and 7 GeV and two dilepton $t\bar{t}$ -pair event candidates in 280 pb⁻¹ of first ATLAS data are presented.

Contents

1	Introduction	1
2	Theoretical Aspects	7
2.1	The Standard Model	7
2.2	The Physics of Top Quark in the Standard Model	10
2.2.1	Top-Antitop-Quark Pair Production Cross-Section and Decay	11
2.2.2	Other Top-Quark Properties	18
2.3	Top Quark and New Physics	29
2.3.1	Model-Independent Characterisation	30
2.3.2	Indirect and Direct Evidence of New Particles	31
2.3.3	Top-Quark Decay into New Particles	33
3	Experimental Environment	35
3.1	The Large Hadron Collider	35
3.2	The ATLAS Detector	38
3.2.1	Physics Requirements	39
3.2.2	Inner Tracking Detectors	41
3.2.3	Calorimeters	45
3.2.4	The Muon System	51
3.2.5	The Trigger System	55
4	Monte Carlo Simulation and Samples	57
4.1	Monte Carlo Generators	58
4.2	Monte Carlo Simulation	62
4.3	Experimental Signature and Background Events	63
4.4	Samples	66
5	Object Identification, Reconstruction and Selection	69
5.1	Electrons	69
5.2	Muons	73
5.3	Jets	77

5.4	Missing Transverse Energy	82
5.5	Trigger Algorithms	85
5.6	Luminosity Determination	88
5.7	Object Selection for the analysis at $\sqrt{s}=10$ TeV	90
5.7.1	Trigger	91
5.7.2	Electrons	92
5.7.3	Jets	92
5.7.4	Muons	93
5.7.5	missing transverse energy	95
6	Cut-and-count Analysis at $\sqrt{s}=10$ TeV	97
6.1	Event Selection	97
6.2	Expected Number of Events from MC	100
6.3	Data-Driven Methods	104
6.3.1	Estimation of $Z \rightarrow \ell^+\ell^-$ /Drell-Yan Events from Side Bands	105
6.3.2	Fake Rate Estimation using the Matrix Method	107
6.3.3	Background Normalisation in Control Regions	110
7	Systematic Uncertainties for the Analysis	113
7.1	Luminosity	113
7.2	Trigger and Lepton Identification Efficiencies	113
7.3	Missing Transverse Energy	114
7.4	Lepton Energy Scale	115
7.5	Jet Energy Scale	116
7.6	PDF Uncertainties	116
7.7	Initial and Final State Radiation	120
7.8	Monte-Carlo-Model	121
7.9	Theoretical Cross Section	122
7.10	Drell-Yan Background Estimation	123
7.11	Jets Misidentified as Leptons	123
7.12	Summary of Statistical and Systematic Uncertainties	123
7.13	Pile-up Effects	123
8	Expected Precision for the Analysis	127
8.1	Combination of Uncertainties	127
8.2	Cross-Check of Dilepton Events with the Stransverse Mass	133

9	Analyses at Different Centre-of-Mass Energies	143
9.1	Cross Section Analysis at $\sqrt{s}=14$ TeV	143
9.1.1	Differences Between the Analysis	144
9.1.2	Event Yields for the Event Selection	145
9.1.3	Systematic Uncertainties for the Analysis	145
9.1.4	Expected Sensitivity for the Analysis at $\sqrt{s}=14$ TeV	146
9.2	Cross Section Analysis at $\sqrt{s}=7$ TeV	147
9.2.1	Differences Between the Analysis	148
9.2.2	Event Yields for the Event Selection	152
9.2.3	Systematic Uncertainties for the Analysis	153
9.2.4	Expected Sensitivity of the Analysis at $\sqrt{s}=7$ TeV	156
10	Conclusion and Outlook	159
A	List of Samples Used for the Study at $\sqrt{s}=10$ TeV	163
B	Coordinate System	169
Bibliography		171
Curriculum Vitae		193

1. Introduction

The 10th September 2008 marked a historical date for particle physics. It was the start of the LHC, the CERN¹ *Large Hadron Collider*, after almost 15 years of the construction of the accelerator and its detectors. The LHC collides protons at the highest centre-of-mass energy to date and supersedes at its design energy the previous record holder, the Tevatron Collider at Fermilab, Chicago, by over a factor of 7. More important the collision rate is also increased by a roughly a factor of 10–100.

The LHC and the ATLAS detector

LHC was constructed in the 27 km circumference tunnel that was formerly used for the *Large Electron Positron collider* (LEP) and which lies about 100 m underground. At nominal operation two proton beams circulating in opposite directions will be accelerated to a beam energy of 7 TeV each. Every 25 ns the proton bunches will be collided at the centres of four detectors. On average 5–25 proton-proton interactions are expected per bunch collision. Also heavy-ion collisions are foreseen with a centre-of-mass energy of 5.5 TeV per nucleon at an instantaneous luminosity of $\mathcal{L}_{\text{inst.}}=10^{27} \text{ cm}^{-2}\text{s}^{-1}$.

At one of the collision points the ATLAS² detector is located. It is a multi-purpose detector and follows a multi-layered design. The largest volume is taken by its eight-fold magnet toroid structure surrounded by the muon chambers. The toroids deliver an air-magnetic field of up to 4 T, which bends charged muons, so that from the curvature the momentum and charge of the muons can be measured. The layers of calorimeter stop electromagnetic and hadronic interacting particle, so that from the energy deposition, shape and amount the nature of the particle can be inferred. Finally, the innermost tracking detectors record the flight track of charged particles in a 2 T solenoid magnetic field. From the combined measurement of the inner track, the energy deposition in the calorimeters and the tracks in the muon chambers the collision fragments from the proton-proton interactions in the centre of the detector can be identified.

¹Conseil Européen pour la Recherche Nucléaire

²A Toroidal LHC ApparatuS

Physics goals of the LHC: The Standard Model and new physics

The purpose of the LHC and its detectors is to find new phenomena that help to understand the particle physics and cosmological experimental findings that our current model cannot explain. The hitherto very successful model is the so-called *Standard Model* (SM) of elementary particles and interactions. Many of its predictions have been confirmed by precision measurements. Also the results from a global fit of the SM parameters to experimental results show a good consistency of the model. One missing piece in the model is the particle that is responsible for the electro-weak symmetry-breaking and hence the masses of the elementary particles, the Higgs boson. From the LEP and the Fermilab Tevatron Collider experiments a lower and an upper limit is set on the Higgs-boson mass. If it exists, the LHC will find it.

The SM is viewed only as an effective theory and it has known limits. It does not explain the origin of the Higgs boson nor the masses elementary particles should have a priori. Also neutrino masses are not included in the Higgs mechanism. It does not explain why the electro-weak symmetry is broken, it only states that it is broken. The hierarchy problem in the SM refers to the fact that the fundamental parameter in the SM, the Planck mass $\sim 10^{19}$ GeV, is so much larger than the Higgs-boson mass. Only fine-tuned cancellations of large quantum loop corrections can result in a small value of the Higgs-boson mass. It does not seem natural for a theory to have such delicate parameters governing our common physics scale.

Also the latest cosmological findings about the matter and energy contents of the universe such as the dark matter and dark energy are not part of the SM. It also lacks an effective explanation of the matter-antimatter asymmetry that we observe in the universe. This asymmetry seems to arise from the *Charge Parity symmetry* (CP) violation of the weak interaction, but the current value of the CP violation in the SM cannot explain the matter dominance in our universe. In many new physics models a larger CP violation or a CP violating Higgs-boson coupling is introduced to accommodate this fact. An explanation is missing in the SM for the inflation right after the Big Bang, which is responsible for the large scale structure of today's universe. Also it does not include the gravitational force at all.

The SM is seen as an effective model at the low energy end. At the highest energies or initially at the beginning of the universe, at the Planck scale, all forces were unified in the *Grand Unified Theory* (GUT) theory. Only with smaller interaction energies or after the expansion and cooling of the universe, the forces separated and a rich set of particles was available. A very popular model of particles and interactions for this scenario is the *Supersymmetry Model* (SUSY), which treats fermions and bosons alike. It solves the fine-tuning problem, since the loop contributions of the new particles cancel the loop contributions that are present in the SM and hence no fine-tuning is needed. Since such a symmetry is not observed at low energies, this symmetry must be broken. This leads to the electro-weak symmetry in which the

mediators of the electromagnetic and the weak force are unified and massless. This is also not observed at low energies, since the weak force mediators, the Z -boson and W -boson are massive and hence this symmetry is again broken, which finally leads to the state of the particles and forces that we can observe today.

The LHC cannot reach the final Planck scale, but it will go beyond the scale of the electro-weak symmetry-breaking. It will give a first hint or find the next effective model that lies beyond the energy scale that is reachable with today's accelerators. Since the Higgs boson has not been discovered yet, there is still some room left by the global fit for other models that try to introduce new mechanisms of electro-weak symmetry-breaking. Some models e.g. introduce a two-Higgs doublet that can have different couplings to bosons and fermions. Finally, there are models that try to incorporate a quantum field theory of gravitation with e.g. extra dimensions.

The role of the top quark in the Standard Model and in new physics models

At this edge towards new physics lies the top quark with its huge mass compared to other quarks. It is even roughly 40 times heavier than its weak-isospin partner, the bottom quark.

The top quark was predicted long before it has been discovered in 1995. There are theoretical arguments for the arrangement of the particles in the SM in families. In 1975 the tau lepton, as the first member of a new, third family, was discovered, followed by the bottom quark in 1977 and the tau neutrino³.

Apart from theoretical reasons, indirect experimental evidence also pointed to the top quark before its discovery. Experiments at the CESR⁴, DORIS⁵II and LEP accelerators, which investigated the bottom quark, indicated that it is a member of a doublet. In measurements of the ratio of the Z -boson decay width to bottom pairs and to all hadronic final states also a prediction of the top-quark mass was made and pointed to m_t around 175 GeV. The top quark was finally found at the Fermilab Tevatron collider with a centre-of-mass energy in the first run of 1.8 TeV that was sufficient enough to produce this massive particle.

The top quark is the heaviest of the known fundamental particles in the SM with a mass of around 173 GeV, the uncertainty on the measurement is smaller than 1%. This is the most precise quark-mass measurement. Also other properties, such as the charge, colour and spin have been measured. The measurements at the Fermilab Tevatron Collider indicate that the top quark is really the isospin partner of the bottom quark and that it completes the SM quark-sector.

Due to its huge mass, it can decay fast into other particles, so there is no time to form a $t\bar{t}$ bound state or top-quark hadrons. The top quark decays as an almost

³There was already indirect evidence for the existence of the tau neutrino earlier than its direct observation. This was only made in 2000 at the DONUT experiment.

⁴Cornell Electron-Positron Storage Ring

⁵Doppel-Ring-Speicher accelerator

free quark and properties that are usually diluted by hadronisation effects such as the spin are preserved and passed onto the decay particles. The top quark decays into a signature that requires most of the detector components. There are leptons, jets and missing transverse energy.

The top-quark pair production at hadron colliders is either by quark-quark annihilation or gluon fusion. The latter process is dominant at the LHC. With the high centre-of-mass energy of $\sqrt{s} = 14$ TeV available, the production cross-section is sizeable. It is 8 orders of magnitude lower than the total cross section, but e.g. still 1-2 orders higher than the Higgs-boson production. The LHC is hence also dubbed as a “top quark factory” as a reference to the former LEP collider, which was a Z -boson factory. A ballpark number is that at nominal operational parameters one top quark per second is produced.

With the known properties from the experimental observations and the large cross section, the top quark is a good standard candle. This means at the detector side that with the rich decay signature one can try to calibrate the detector and object reconstruction algorithms. For example a top-quark pair can be easily selected with a good purity. While the counting of such events leads to a cross-section measurement, the selected events can be used to measure the efficiency and purity of an useful tool, the so-called b -tagging. Both top quarks decay into bottom quarks that hadronise to B -hadrons. These hadrons decay after travelling a few mm in the detector. If a top-quark pair event was selected, both particle jets from the hadron decay can be tagged. From the number of events in which both or only one of the jets was tagged, the tagging efficiency can be calculated. This helps to understand the efficiency and purity when tagging b -quark jets from other processes such as the decay of a Higgs bosons to two bottom quarks.

On the theoretical side, the physics of the top quark is embedded in the SM physics. The theoretical prediction of its properties involves some of the parameters in the model, such as the proton structure, since the top quarks are produced from the partons in the proton. The top-quark mass depends also on the cross section and the mass in turn is a parameter in the W -boson mass and the Higgs-boson mass calculation. The dependence is logarithmic, but still, from the good measurement of the top-quark and W -boson masses, limits on the Higgs-boson mass are derived. A small Higgs-boson mass is favoured that lies just in the energy regime of the LHC. Because of its large mass, the top quark is expected to have the largest coupling to the Higgs boson and it might reveal the nature of the electro-weak symmetry-breaking. Heavy particles in new physics models can decay into top-quark pairs. Some physics models even promote the top quark to a special quark. In those models, such as Top-Colour, the top-quark pairs are responsible for symmetry breaking.

Even if the top quark is not involved in new physics effects, it is an important background to new physics searches because of the large cross section and the final state can be similar to Higgs and/or SUSY particle final states. Before a Higgs

or new physics discovery can be claimed the $t\bar{t}$ background needs to be understood as much as possible.

So far no evidence for new physics has been found. The top quark properties measured at the current colliders seem to support the good consistency of the SM. Still, properties such as the cross section need to be remeasured at higher centre-of-mass energies, because the production mode is dominated by gluon fusion which was not the case at the Fermilab Tevatron Collider. Here the opportunity opens up to use the top-quark cross-section measurement as a probe for the consistency of the SM or even for new physics. A consistent value with the prediction would approve the SM further, but there are also hopes that at the collision energies of the LHC new phenomena can be revealed. Either the total cross section is changed by the decay of new particles into top quarks or branching ratios are modified such that SM ratios are changed in favour of new decay particles. A measurement of top-quark pair production in the dilepton channel will very likely contribute to the findings of new physics at the LHC.

Study of top-quark pair cross-section measurement in the dilepton channel with the ATLAS detector at the LHC

This thesis is a study of the cross-section measurement in the dilepton channel at a centre-of-mass energy of $\sqrt{s} = 10$ TeV and for an integrated luminosity of $\mathcal{L} = 200 \text{ pb}^{-1}$. The signature of two leptons has the smallest branching fraction of $\sim 6.3\%$, but the two leptons are very beneficial for the background rejection. A good rejection of uninteresting events can be achieved by requiring that at least one lepton is detected by the first stage detection system, the trigger. Upon identification and reconstruction of the final state particles, the selection of two leptons and a decent amount of missing transverse energy plus two jets gives a unique signature that can easily achieve a signal-to-background ratio of 6:1. Together with the high cross section, statistical uncertainties that were the dominant uncertainty at the Fermilab Tevatron Collider when the top quark was discovered are no longer an issue. Very quickly the top quark can be observed and a first cross section can be made with simple selection cuts.

This thesis describes the physics of the top quark in the SM and the latest results from the Fermilab Tevatron Collider in Chapter 2. Shortly the role of the top quark in new physics models is presented. More details about the LHC and the ATLAS experiment can be found in Chapter 3. Chapter 4 discusses the aspects of *Monte Carlo* (MC) generation and simulation on which this study is based. The identification and reconstruction algorithms of the objects that are used in this study are described in Chapter 5. The object selection cuts that are used for this analysis will also be motivated. The cut-and-count cross-section analysis is explained in Chapter 6 and data-driven methods are presented. Statistical sensitivities are calculated for different luminosities up to the target luminosity. The study of the

systematic uncertainties for the analysis are described in Chapter 7. Finally, the result of the study can be found in Chapter 8 in which the systematic and statistical uncertainties are combined. The same method is used to combine the results from all dilepton subchannels. With the help of a “top mass”-like variable the dilepton top-quark pair signature is cross-checked. A comparison of the analysis at different centre-of-mass energies of $\sqrt{s} = 14$ TeV and $\sqrt{s} = 7$ TeV is done in Chapter 9. Also the statistical sensitivity of this analysis at the different centre-of-mass energies is calculated. This thesis will conclude in Chapter 10 and a first look on two real data dilepton $t\bar{t}$ -pair event candidates in 280 pb^{-1} of first ATLAS data is given.

2. Theoretical Aspects

This chapter briefly describes the *Standard Model* (SM) [1, 2] of elementary particles and its interactions in more detail. Embedded in the framework of the SM is the physics of the top quark that describes the production, decay and the properties of the top quark. Especially the first two aspects are important for this study, since a theoretical expectation for the cross section must be calculated and the decay signature of the top-quark pair must be known in order to select top-quark pair events. There are already measurements of some top quark properties at the two Fermilab Tevatron Collider experiments. Most of the properties do not change with the centre-of-mass energy, but it will be shown that the cross section needs to be newly measured to confirm the theoretical SM calculation. Also the role of the top quark in the discovery of new physics models, such as the *Supersymmetry Model* (SUSY) is touched upon. Several discovery modes also involve a cross-section measurement of $t\bar{t}$ pairs, so that this study can contribute to a discovery. Any deviation from the calculated cross section and *Branching Ratios* (BRs) will point towards new physics.

2.1. The Standard Model

The following review of the SM presented here is largely based on [3] and [4]. The particle spectrum of the SM consists of fermions (spin-half particles) and of bosons (integer spin particles) as summarised in Table 2.1.

The gauge bosons are the mediators of the fundamental forces. In the SM three of the four fundamental interactions are described, the strong, the weak and the electromagnetic interaction. The corresponding force carriers are 8 gluons for the strong interaction, W^\pm -bosons, Z -boson for the weak interaction and the photon (γ) for the electromagnetic interaction. From a theoretical point of view the SM is a quantum field theory based on the local gauge symmetry $SU(3)_C \times SU(2)_L \times U(1)_Y$, which includes the symmetry group of strong interactions ($SU(3)_C$) and the unified group of electro-weak interactions ($SU(2)_L \times U(1)_Y$). The theory of interactions through the strong force is treated in *Quantum Chromodynamics* (QCD). The theory of interactions through the electro-weak force is treated in electro-weak theory. The gauge bosons appear in this theory as the generators of the group. This determines the number of gauge bosons for each interaction. The W/Z -bosons are massive contrary to the massless photons. This indicates that the electro-weak sym-

Table 2.1.: Particle spectrum of the SM. The leptons and quarks are the spin-half fermions and are arranged into three families. The bosons are the interaction mediating particles for the three fundamental forces. The gravitation is not included here.

Family	I	II	III	charge [e]
Fermions				
Leptons	ν_e	ν_μ	ν_τ	0
	e	μ	τ	-1
Quarks	u	c	t	+2/3
	d	s	b	-1/3
Bosons				Interaction
	$g_1 \dots g_8$	gluons		strong
	$W^\pm Z$	bosons		weak
	γ	photon		electromagnetic
	H	Higgs		

metry group is not a symmetry of the vacuum. A spontaneous symmetry-breaking pattern is introduced, the so-called Higgs mechanism [5, 6], that breaks the SM group $SU(3)_C \times SU(2)_L \times U(1)_Y$ into $SU(3)_C \times U(1)_{em}$. This leads to the massive W/Z -bosons and to a scalar field with its associated particle, the Higgs boson. The Higgs boson has not been observed yet, and it is the last remaining particle that would complete the SM theory.

The fermions are the matter particles and can be divided into leptons (electron, e ; muon, μ ; tau, τ and their corresponding neutrinos, ν) and quarks (d , down; u , up; s , strange; c , charm; b , bottom; t , top). They are usually ordered in families and are arranged according to their weak isospin, T , property. Left-handed fermions are doublets ($T = 1/2$) under the $SU(2)_L$ group with two particles assigned to different third components of the weak isospin, T_3 (left-handed charged lepton, $T_3 = -1/2$ and left-handed neutrino, $T_3 = 1/2$). Right-handed neutrinos do not couple to any of the fundamental forces, therefore right-handed fermions $(e, \mu, \tau)_R$ are singlets

($T = 0$). Quarks appear as left-handed doublets and right-handed singlets. All particles also have their corresponding antiparticle.

$$\begin{array}{cc}
 \text{leptons} & \text{quarks} \\
 \left(\begin{array}{c} \nu_e \\ e^- \end{array} \right)_L, e_R^- & \left(\begin{array}{c} u \\ d \end{array} \right)_L, u_R, d_R \\
 \left(\begin{array}{c} \nu_\mu \\ \mu^- \end{array} \right)_L, \mu_R^- & \left(\begin{array}{c} c \\ s \end{array} \right)_L, c_R, s_R \\
 \left(\begin{array}{c} \nu_\tau \\ \tau^- \end{array} \right)_L, \tau_R^- & \left(\begin{array}{c} t \\ b \end{array} \right)_L, t_R, b_R
 \end{array}$$

The existence of hadrons composed of quarks of the same flavour, e.g. Δ^{++} is composed of three u-quarks (uuu), implies a new quantum number or degree of freedom, the strong colour charge. Each quark is present in three colour states and the confinement of quarks (i.e. no free quark can be observed) implies that observable hadrons are colourless (combination of three quarks in different colour state or quark/antiquark pairs in the same colour state). Not all fermions take part in all interactions, only the quarks interact through all three forces. They carry a strong colour charge, a weak hypercharge $Y = 2(Q - T_3)$ and an electric charge. The leptons do not take part in the strong interaction and the neutrinos only take part in the weak interaction. The weak interaction can be described as an interaction with a V-A (vector-axial vector) structure. It allows only for couplings to left-handed fermions. For quarks the mass eigenstates are not the same as the weakly interacting states. The quarks are transformed between the two states by a mixing matrix, the unitary 3×3 *Cabibbo-Kobayashi-Maskawa* (CKM) matrix.

The fermions are massive particles with different masses. The masses are again generated through the spontaneous symmetry-breaking mechanism by the interaction of the fermion with the Higgs field. The order of the families roughly follows a mass ordering of the particles¹. The mass spectrum ends with the heaviest quark, the top quark.

The SM has at least 19 input parameters that need to be determined by experimental measurements. These are the masses of the fermions (9 parameters), electromagnetic and strong coupling (2 parameters), W/Z -boson masses (2 parameters), the Higgs field (2 parameters) and the CKM matrix elements (4 parameters). There is no particular reason for the three generations of the fermions. The latest review of the SM [7] shows that many of its predictions have been confirmed by precision measurements. Also the results from a global fit of the SM parameters with the experimental results show a good consistency of the parameters.

¹The mass ordering is true for the charged leptons and the quarks separately. The neutrinos are massless in the SM. Although measurements have shown that at least some of the neutrinos have masses, the mass ordering is still unknown.

2.2. The Physics of Top Quark in the Standard Model

A more detailed review of physics of the top quark can be found in [8, 9], the following section summarises the most important aspects of top-quark physics.

The top-quark prediction follows two theoretical arguments that, as a consequence of the existence of a third fermion family, demand a sixth quark. Already in 1975 the tau lepton as the first member of a new, third family was discovered [10].

The first theoretical reason is the requirement on the SM to be a renormalisable and anomaly-free gauge theory. On the one hand it can be proven that the SM gauge theory is renormalisable if the sum of the weak hypercharges, Y , of all left-handed fermions is zero. On the other hand anomalies in the SM gauge theory would lead to triangle diagrams with fermions in the loop. The couplings in such diagrams are related to the number of existing leptons and quarks within a family. The couplings are cancelled out if the theory has the same number of lepton and quark doublets. With the existence of a third lepton family (complemented by the indirect evidence at LEP [11] and direct observation of the tau neutrino [12]) a third quark family must also exist in a renormalisable and anomaly-free theory. In 1977 the bottom quark as the first member of the third quark family was discovered [13]. With this discovery the second theoretical reason for the existence of the top quark applies that is based on the *Glashow-Iliopoulos-Maiani* (GIM) mechanism [14]. An isospin partner of the bottom quark must exist to suppress not observed flavour-changing neutral currents.

Indirect experimental evidence was also available before the top-quark discovery. Experiments at the CESR², DORIS³ II and LEP accelerators [15, 16, 17, 18, 19, 20, 21] with the bottom quark indicated that it is a member of a weak isospin doublet. Also in measurements of the ratio of the Z -boson decay width to bottom pairs and to all hadronic final states a prediction of the top-quark mass was made and pointed to m_t around 175 GeV. The top quark was found at the Fermilab Tevatron collider [22, 23] with a centre-of-mass energy in the first run of 1.8 TeV [24, 25].

Due to its huge mass the decay time is small, so that no $t\bar{t}$ bound states and no top-quark hadrons can form, which usually dilute the properties of a free quark (e.g. spin information). The physics of the top quark is closely related to its properties that are described in the following subsections. The rich physics program with the top quark can be used as a probe for the consistency of the SM as well as a probe for new physics.

²Cornell Electron-Positron Storage Ring

³Doppel-Ring-Speicher accelerator

2.2.1. Top-Antitop-Quark Pair Production Cross-Section and Decay

The top quark is currently only produced at the Fermilab Tevatron Collider, which is a proton-antiproton accelerator with a centre-of-mass energy of 1.96 TeV (increased in run II). At the LHC, which is a proton-proton collider⁴, the top quark is also produced in hadronic collisions. The top quark can be produced as single top-quarks via the weak interaction or as top-quark pairs via the strong interaction. The cross section for the latter one is dominant at both colliders and subject of this thesis.

The top quark cannot be detected directly due to its short lifetime, but it can be inferred through its decay products.

Theoretical treatment of top-quark pair production

The production cross-section of top-antitop-quark pairs can be calculated in the QCD theory. The basic production mechanism is the interaction of two partons, i and j , from the colliding protons via the strong interaction. At leading order the top-quark pairs are either produced via quark antiquark annihilation or gluon-gluon fusion. The corresponding Feynman diagrams for the top-quark pair production are shown in Figure 2.1.

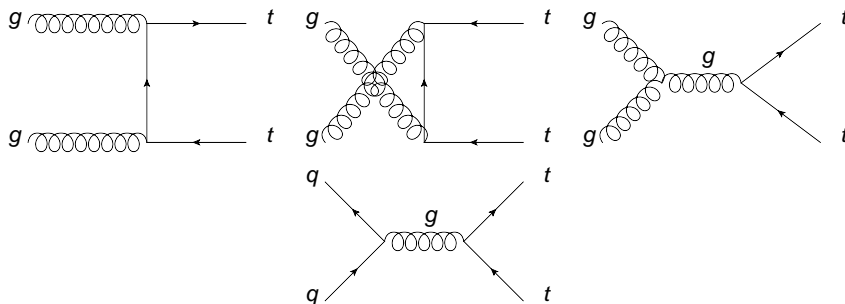


Figure 2.1.: Leading-order Feynman diagrams for $t\bar{t}$ -pair production with the gluon fusion processes in the top row and the quark-antiquark-annihilation process in the bottom row.

The cross-section calculation for hadronic collisions is usually factorised into two parts by the factorisation theorem [26] at the factorisation scale: The hard scattering (or short distance) part is $\sigma^{ij \rightarrow t\bar{t}}$ that describes the dynamics of the partons producing a $t\bar{t}$ -pair. The calculation is performed with the underlying theory of the dynamics, here QCD. It can be expressed in an expansion series of the coupling constant, so that the calculation can be simplified to different orders of the expansion i.e. different orders of the perturbative calculation, the so-called *Leading-Order* (LO), *Next-to-Leading-Order* (NLO), etc. calculations. The other part of

⁴see later in Section 3.1

the cross-section calculation is the long distance part that deals with the initial kinematics of the incoming partons. The *Parton Distribution Functions* (PDFs) $f_i^a(x_i, \mu^2)$ and $f_j^b(x_j, \mu^2)$ describe the momentum distribution of the partons in the proton, given as the fraction x_i, x_j of the total proton momentum. The PDFs cannot be calculated in perturbative QCD and must be extracted from global QCD fits to deep inelastic scattering data [27, 28, 29, 30]. Figure 2.2 shows the PDFs extracted with the current QCD fit by the CTEQ⁵ collaboration.

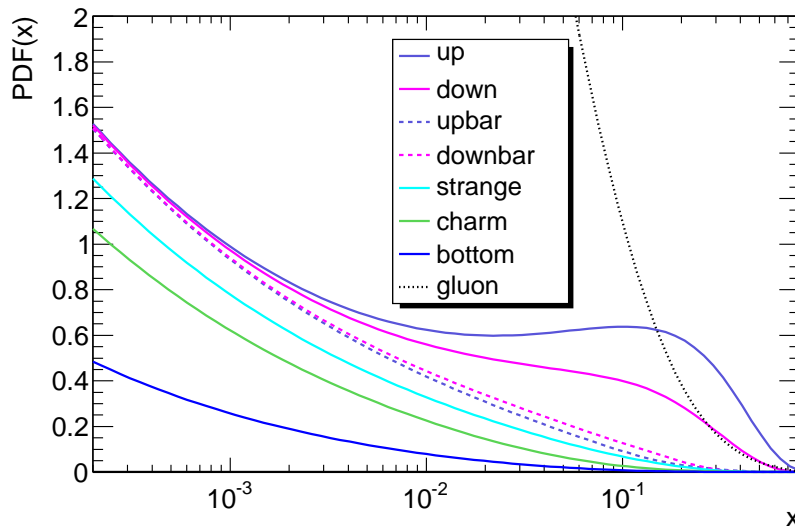


Figure 2.2.: Parton distribution functions CTEQ6.5 from the CTEQ collaboration [27] as an example. The dotted lines represent the PDF of the antiquarks, here only the anti-up and anti-down quark are shown. The gluon PDF is not scaled here and increases quickly as the momentum fraction $x \rightarrow 0$.

The factorisation scale, μ_F , is an unphysical scale and any calculation of physical observables should not depend on it when calculated in all orders of perturbation. Usually higher order calculations are found to be more stable against the choice of factorisation scale. Another scale that has to be introduced to obtain physically reasonable observables is the renormalisation scale, μ_R . When including virtual loop diagrams in the calculation, ultra-violet divergences occur that can be removed by a renormalisation procedure, which introduces μ_R^2 . For this calculation both scales μ_F and μ_R are chosen to be equal $\mu_F = \mu_R = \mu$ and are set typically to the scale of the problem, here $\mu = m_t$. Finally, the cross section depends on two further parameters, the effective centre-of-mass energy, $\sqrt{\hat{s}} = \sqrt{x_i \cdot x_j \cdot \bar{s}}$, and the top-quark mass, m_t .

⁵Coordinated Theoretical-Experimental project on QCD

The full formula for the cross section for $t\bar{t}$ pairs at hadron colliders has the following form:

$$\sigma^{ab\rightarrow t\bar{t}+X}(s, m_t) = \sum_{i,j=q,\bar{q},g} \int dx_i dx_j f_i^a(x_i, \mu^2) f_j^b(x_j, \mu^2) \sigma^{ij\rightarrow t\bar{t}}(\hat{s}, m_t^2, \alpha_s(\mu^2), \mu^2). \quad (2.1)$$

The results of the cross-section calculations are as follows: from the centre-of-mass energy of the experiment e.g. LHC with nominal $\sqrt{s} = 14$ TeV one can calculate that a minimum momentum fraction of $x = 2m_t/\sqrt{s} \approx 0.025$ is needed for the two partons to produce a top-quark pair. This is the range in the PDF distributions in Figure 2.2 that is dominated by gluons and thus the production modes, as depicted in Figure 2.1, are dominated by gluon-gluon fusion ($\sim 90\%$, $\sim 10\%$ quark-quark-annihilation).

The total cross section has been calculated up to NLO+NLL⁶ [31] and approximate NNLO⁷ [32]. NLL accuracy has been achieved by including soft-gluon corrections by resummation of large Sudakov logarithms. From the extension of the NLL calculation to NNLL⁸ accuracy an approximate NNLO result was derived. The theoretical calculations include uncertainties from scale variations⁹ between $m_t/2 < \mu < 2m_t$ and from PDF uncertainties with the CTEQ and MRST¹⁰ PDF sets. The following cross sections are calculated for the LHC nominal centre-of-mass energy $\sqrt{s} = 14$ TeV, reference top-quark mass $m_t = 172.5$ GeV and latest CTEQ6.6 PDFs:

$$\sigma_{t\bar{t}}^{\text{NLO+NLL}} = 875_{-9.3\%}^{+9.0\%} (\text{scales})_{-3.3\%}^{+3.1\%} (\text{PDF}) \text{ pb}, \quad (2.2)$$

$$\sigma_{t\bar{t}}^{\text{approx. NNLO}} = 883_{-4.2\%}^{+1.0\%} (\text{scales})_{-3.1\%}^{+3.3\%} (\text{PDF}) \text{ pb}. \quad (2.3)$$

The calculation is dominated by scale uncertainties, the approximate NNLO calculation yields smaller scale uncertainties. The PDF uncertainties are in both cases smaller for the MRST2006 PDF set ($\sim 1 - 2\%$).

The dependence on the centre-of-mass energy was parametrised in [33] with an accuracy of 0.05% as

$$\sigma^{\text{approx. NNLO}}(\sqrt{s}, \mu) = a + bx + cx^2 + dx \log(x') + ex \log^2(x') + fx^2 \log(x') + gx^2 \log^2(x'), \quad (2.4)$$

⁶Next-to-Leading-Logarithm – In the calculation of the cross section logarithms appear in collinear emission diagrams (of massless particles). The integration over these logarithms can also be done in an expansion series.

⁷Next-to-Next-to-Leading-Order

⁸Next-to-Next-to-Leading-Logarithm

⁹ μ_R and μ_F were varied independently.

¹⁰Martin-Roberts-Stirling-Thorne

2. Theoretical Aspects

with $x = \sqrt{s}/\text{GeV}$ and $x' = \sqrt{s}/14 \text{ TeV}$. The parameters $a-g$ depend on the scale μ . In Figure 2.3 the cross section for different centre-of-mass energies is shown in comparison with calculations at NLO for pp collisions and at NLO for $p\bar{p}$ collisions (both calculations from [34]). The dependence of the cross section on the top-quark mass is shown in Figure 2.4 [32], which is $\Delta\sigma/\sigma \sim -5 \times \Delta m_t/m_t$ for $\sqrt{s} = 14 \text{ TeV}$.

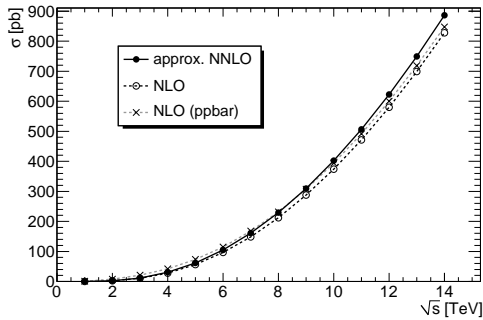


Figure 2.3.: Cross section dependence on the centre-of-mass energy at approx. NNLO [33] (solid line), in comparison with calculations at NLO (dashed line, open circles) and calculations in NLO for $p\bar{p}$ collisions (dashed line, crosses, both calculations are from [34]).

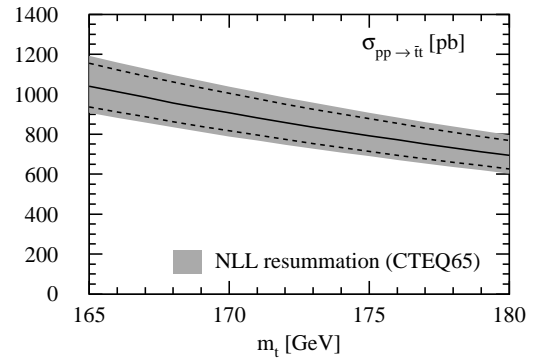


Figure 2.4.: Cross section dependence on the top-quark mass [32] at $\sqrt{s} = 14 \text{ TeV}$. The grey band reflects the PDF uncertainties on the cross-section calculation and the dashed lines reflect the scale uncertainties.

Weak [35, 36] and electromagnetic [37] corrections of the order $O(\alpha_s^2\alpha)$ are smaller than the uncertainty of the QCD calculation (at LHC -1% and 0.5% , respectively).

The comparison of the cross section at approximate NNLO and LHC centre-of-mass energy $\sqrt{s} = 10 \text{ TeV}$ that is assumed throughout this thesis yields:

$$\sigma_{t\bar{t}}^{\text{approx. NNLO}}(\sqrt{s} = 10 \text{ TeV}) = 402_{-4.3\%}^{+3.7\%} (\text{scales})_{-4.5\%}^{+4.6\%} (\text{PDF}) \text{ pb}. \quad (2.5)$$

For a centre-of-mass energy of $\sqrt{s} = 7 \text{ TeV}$ the cross section is:

$$\sigma_{t\bar{t}}^{\text{approx. NNLO}}(\sqrt{s} = 7 \text{ TeV}) = 161 \pm 6\% (\text{scales, PDF}). \quad (2.6)$$

For the centre-of-mass energy relevant for the Fermilab Tevatron Collider of $\sqrt{s} = 2 \text{ TeV}$ the calculation yields:

$$\sigma_{p\bar{p} \rightarrow t\bar{t}}^{\text{approx. NNLO}}(\sqrt{s} = 2 \text{ TeV}) = 7.45_{-0.9\%}^{+3.6\%} (\text{scales})_{-5.6\%}^{+5.7\%} (\text{PDF}) \text{ pb}. \quad (2.7)$$

Figure 2.5 shows the top-quark pair-production cross-section compared to other expected processes at the Fermilab Tevatron Collider and at the LHC. Although

the cross section is 8 orders of magnitudes lower than the total cross section, it is still 1–2 orders of magnitude larger than the Higgs-boson cross-section and only about 2 orders of magnitude smaller than the Z -boson cross-section. Also the ratio of the Z -boson cross-section to the $t\bar{t}$ cross-section is more in favour of top-quark pairs at the LHC compared to the pair production at the Fermilab Tevatron Collider.

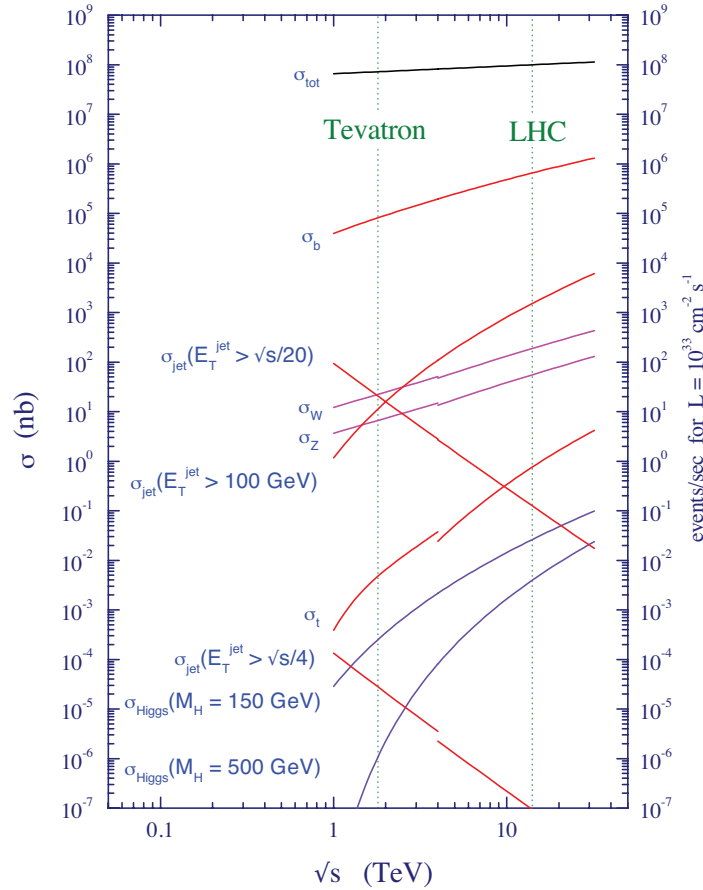


Figure 2.5.: Cross sections for various processes at the Fermilab Tevatron Collider and at the LHC [38]. Shown here are the total cross section, the cross section for b -quark, jet, heavy gauge boson, top-quark and Higgs-boson (at two different masses) production. The lines are not continuous, since on the left side the cross section for $p\bar{p}$ collisions, whereas the right side for pp collisions is shown.

Gluon production versus quark production

At the Fermilab Tevatron Collider the $q\bar{q}$ annihilation dominates with 85% whereas at the LHC top-quark pairs are produced via the gg -fusion in 90% of the cases [33]. The theoretical cross-section uncertainties due to the PDFs are mainly due to the

uncertainty of the quark PDFs in the first case and due to the gluon PDFs in the latter case. The uncertainty on the total cross section due to the PDFs is dominated by the gluon luminosity uncertainty at the LHC and the cross section will be sensitive to this.

Top-quark decay

The top quark decays in the SM almost exclusively into a bottom quark and a W -boson. The decays into strange or down quarks are suppressed and are neglected for the following discussion, since the CKM matrix element $|V_{tb}| \sim 1$. The top-quark decay rate calculated at lowest order [39] is:

$$\Gamma_t = \frac{G_F m_t^3}{8\pi\sqrt{2}} |V_{tb}|^2 \left(1 - \frac{m_W^2}{m_t^2}\right)^2 \left(1 + 2\frac{m_W^2}{m_t^2}\right), \quad (2.8)$$

with first order QCD corrections from [40, 41] that correct the width by -10% , this yields at $m_t = 172.6$ GeV a width of $\Gamma_t = 1.34$ GeV. Electro-weak corrections from [42, 43] and the finite width of the W -boson [44] give a correction of $\delta_{\text{EM}} \sim 1.7\%$ and $\delta_\Gamma \sim -1.5\%$. The lifetime is $\tau_t = 1/\Gamma_t \sim 5 \cdot 10^{-25}$ s, which is smaller than the typical hadronisation time $\tau_{\text{hadr}} \sim 1 \text{ fm}/c \sim 3 \cdot 10^{-24}$ s. Hence neither top-quark hadrons can form nor do bound $t\bar{t}$ states exist before the top quark decays and therefore it can be treated as an almost free quark.

The top-quark decay is characterised by the decay of the W -bosons. For a $t\bar{t}$ pair the decay can be divided into three classes: dilepton, single-leptonic and all hadronic decay modes. Figure 2.6 is a rough graphical representation of the branching ratios such that the smallest branching fraction with the same leptons represents roughly 1/81 of the total branching fraction. This corresponds to a branching fraction of 1/9 for the dilepton case, 4/9 for the semi-leptonic case and 4/9 for the all-hadronic case. Assumed in this rough calculation is that the lepton and light quark (i.e. all except top and bottom quark) masses are all zero. The following table shows the branching ratios (given in parenthesis and with proper lepton/quark masses), here the l denotes e , μ or τ :

all hadronic	$t\bar{t} \rightarrow W^+ b$	$W^- \bar{b} \rightarrow q \bar{q}' b$	$q'' \bar{q}''' \bar{b}$	(46.2%)
semi-leptonic	$t\bar{t} \rightarrow W^+ b$	$W^- \bar{b} \rightarrow q \bar{q}' b$	$l \bar{\nu}_l \bar{b}$ or $\bar{l} \nu_l b$	(43.5%)
dileptonic	$t\bar{t} \rightarrow W^+ b$	$W^- \bar{b} \rightarrow \bar{l} \nu_l b$	$l' \bar{\nu}_{l'} \bar{b}$	(10.3%)

Experimentally the leptonic decay channels often are defined via directly observable leptons, i.e. electron and muon. Final states containing tau leptons are only counted as leptonic if the subsequent decay of the tau lepton is also of leptonic (i.e. electrons and muons) nature. This results in different branching ratios, e.g. 6.3% for the experimental dilepton channel.

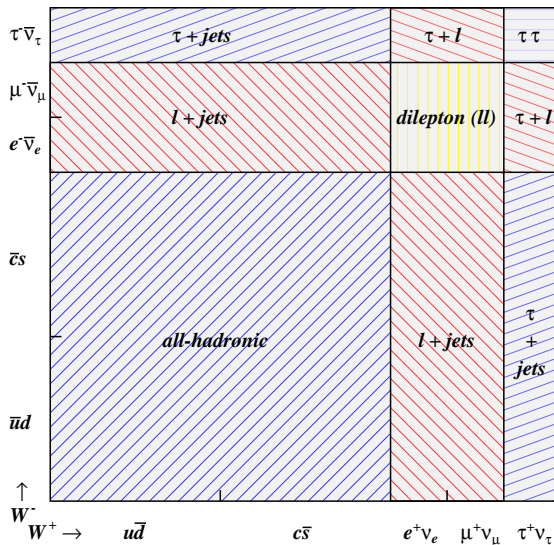


Figure 2.6.: Rough graphical representation of the top-quark decay modes [45].

The smallest branching fraction with same leptons represents roughly $1/81^{\text{th}}$ of the total area, whereas a quark-antiquark pair (with their corresponding antiquark-quark pair) corresponds to roughly $1/9^{\text{th}}$ of the total area, since each quark comes in three colours.

Experimental status

The top-quark pair production cross-section was measured by both experiments CDF¹¹ [46, 47] and D0¹² [48, 49] at the Fermilab Tevatron Collider in the various decay channels.

The measurements in the all hadronic channel is the most difficult since it does not contain any leptons that are needed for simple triggering of such events. It suffers from large contributions of QCD multi-jet background and it has the highest number of possible combinations of assigning a reconstructed jet to the hadronic W -boson decay products and bottom-quark jets, the so-called combinatorial background. CDF used a data sample of 2.9 fb^{-1} with a neural network analysis and b -tagging [50] to select the events. The cross section was determined at the same time with the top-quark mass measurement in this channel by counting the number of events in the top-quark peak distribution. The latest measurement by D0 also used a neural network analysis together with b -tagging for the extraction of the signal content from a data sample of integrated luminosity $\mathcal{L}_{\text{int.}} = 405 \text{ pb}^{-1}$ [51].

The semi-leptonic channel is often referred to as the golden channel, since it has the benefit of a large branching fraction (compared to the dilepton channel) and one

¹¹Collider Detector at the Fermilab Tevatron Collider

¹²D0 experiment located at the interaction point “D0” at the Fermilab Tevatron Collider

lepton that can be used to trigger semi-leptonic events. Most of the information about the top quark was obtained using the selection of the semi-leptonic decay channel. Recent measurements by CDF used a secondary vertex tagger [52] or even a neural network [53]. The analyses were performed on 4.3 fb^{-1} and 4.6 fb^{-1} of data, respectively. In both analyses the systematic uncertainty of the measurements was reduced further by measuring the ratio between the $t\bar{t}$ and Z -boson production cross-sections. A kinematic likelihood analysis of D0 can be found in [54] with 425 pb^{-1} and in [55] with 900 pb^{-1} . The analyses were performed in the single-electron and single-muon channel and in a combination of both lepton channels. Adding b -tagging gives an additional measurement that was combined with the previous measurement.

The first measurements in the dilepton channel by CDF were performed with a selection of a lepton and an isolated track instead of a second lepton. The amount of data was 197 pb^{-1} [56] and it was refined with 1.1 fb^{-1} [57]. The latest measurement with 4.5 fb^{-1} of data was performed with a cut analysis with and without b -tagging [58]. At D0 the lepton+track analysis [59] required b -tagging, used 400 pb^{-1} of data and combined all sub-channels. With a larger dataset of 1 fb^{-1} not only the $t\bar{t}$ cross section, but also the branching ratio of $t\bar{t} \rightarrow l\tau b\bar{b}$ was measured [60]. The inclusion of tau leptonic channels was done with a tau-identification algorithm that is based on a neural network.

The two experiments CDF and D0 combined their most significant results. The CDF combination [61] contains analyses on 4.6 fb^{-1} of data in all channels. The D0 combination [62] consists of the semi-leptonic, dileptonic and lepton+tau analyses for 1 fb^{-1} of run-II data with an assumed top-quark mass of 170 GeV .

Table 2.2 and Table 2.3 summarise the current top-quark cross section measurements at the Fermilab Tevatron Collider. The results of the two experiments agree with each other within the uncertainties.

The ratio of the qq and gg production-modes have also been measured at both Fermilab Tevatron Collider experiments. The different spin states of the initial partons ($J(q\bar{q})=1$, $J(gg)=0$) lead to an angular correlation of the charged leptons in the dilepton channel [64]. Also initial states with gluons lead to more observable jets from initial radiation. The analyses at CDF [65] used the first method and compared the azimuthal angle between the leptons in the dilepton channel. The comparison with the distribution for pure production mechanisms result in a gg fraction 0.53 ± 0.37 . The result is still statistics limited. The second method was applied to the semi-leptonic channel [66]. The number of soft tracks in a p_T region between $0.9 \text{ GeV} < p_T < 2.9 \text{ GeV}$ and $|\eta| \leq 1.1$ was found to be a good measure of initial state radiation. The result for the gg fraction is $0.07 \pm 0.14 \text{ (stat)} \pm 0.07 \text{ (syst)}$.

2.2.2. Other Top-Quark Properties

In the following subsection further interesting top-quark properties are presented and the current experimental status or perspective at the LHC are presented.

Table 2.2.: Current top-quark cross-section measurements by the CDF experiment that are used for the result combination (except for the lepton+track analysis and the latest analyses with 5.1 fb^{-1}).

Channel	Sample	Cross section	Ref.
All hadronic	2.9 fb^{-1}	$7.2 \pm 0.5 \text{ (stat)} \pm 1.1 \text{ (syst)} \pm 0.4 \text{ (lumi) pb}$	[50]
Semi-leptonic			
sec. vertex and $\sigma_{t\bar{t}}$ to σ_Z	4.3 fb^{-1}	$7.14 \pm 0.35 \text{ (stat)} \pm 0.58 \text{ (syst)} \pm 0.14 \text{ (theo) pb}$	[52]
neural netw. and $\sigma_{t\bar{t}}$ to σ_Z	4.6 fb^{-1}	$7.6 \pm 0.37 \text{ (stat)} \pm 0.35 \text{ (syst)} \pm 0.15 \text{ (theo) pb}$	[53]
Dilepton			
lep+track*	1.1 fb^{-1}	$9.6 \pm 1.2 \text{ (stat)} \pm {}_{-0.5}^{0.6} \text{ (syst)} \pm 0.6 \text{ (lumi) pb}$	[57]
0- <i>b</i> -tag	4.5 fb^{-1}	$6.56 \pm 0.65 \text{ (stat)} \pm 0.41 \text{ (syst)} \pm 0.38 \text{ (lumi) pb}$	[58]
1- <i>b</i> -tag	4.5 fb^{-1}	$7.27 \pm 0.71 \text{ (stat)} \pm 0.46 \text{ (syst)} \pm 0.42 \text{ (lumi) pb}$	[58]
<i>b</i> -tag*	5.1 fb^{-1}	$7.25 \pm 0.66 \text{ (stat)} \pm 0.47 \text{ (syst)} \pm 0.44 \text{ (lumi) pb}$	[63]
pretag*	5.1 fb^{-1}	$7.40 \pm 0.58 \text{ (stat)} \pm 0.63 \text{ (syst)} \pm 0.45 \text{ (lumi) pb}$	[63]
Combination	4.6 fb^{-1}	$7.5 \pm 0.31 \text{ (stat)} \pm 0.34 \text{ (syst)} \pm 0.15 \text{ (theo) pb}$	[61]

*Not used for the combination.

Measuring the properties of the top quark does and will confirm that the particle found at the Fermilab Tevatron Collider is actually the isospin partner of the bottom quark and that the physics of the top quark is consistent in the SM.

Top-quark mass

An important result from the two Tevatron Fermilab Collider experiments was the precise measurement of the top-quark mass. The relation between the top-quark mass and the pair-production cross section was already mentioned in the previous section. Here now a link between the top mass and the *W*-boson and Higgs-boson mass is established.

Table 2.3.: Current top-quark cross section measurements by the D0 experiment that are used for the result combination (except for the result from the all-hadronic channel).

Channel	Sample	Cross section	Ref.
All hadronic*	405 pb ⁻¹	4.5 ^{+2.0} _{-1.5} (stat) ^{+1.4} _{-1.1} (syst) ± 0.3 (lumi) pb	[51]
Semi-leptonic	425 pb ⁻¹	6.4 ^{+1.3} _{-1.2} (stat) ± 0.7 (syst) ± 0.4 (lumi) pb	[54]
0- <i>b</i> -tag	900 pb ⁻¹	6.62 ± 0.78 (stat) ± 0.36 (syst) ± 0.40 (lumi) pb	[55]
1- <i>b</i> -tag	900 pb ⁻¹	8.05 ± 0.54 (stat) ± 0.7 (syst) ± 0.49 (lumi) pb	[55]
0/1- <i>b</i> -tag	900 pb ⁻¹	7.42 ± 0.53 (stat) ± 0.46 (syst) ± 0.45 (lumi) pb	[55]
Dilepton	1 fb ⁻¹	7.5 ± 1.0 (stat) ± ^{+0.7} _{-0.6} (syst) ± ^{+0.6} _{-0.5} (lumi) pb	[60]
lep+track	400 pb ⁻¹	7.4 ± 1.4 (stat) ± 0.9 (syst) ± 0.5 (lumi) pb	[59]
Combination	1 fb ⁻¹	8.18 ^{+0.98} _{-0.87} pb	[62]

*Not used for the combination.

The top-quark mass¹³ appears in the SM as a parameter for many electro-weak virtual loop corrections. Precision measurements on electro-weak parameters enabled in the past a prediction of the top-quark mass.

The *W*-boson mass, M_W , calculation depends on the top-quark mass m_t and the Higgs-boson mass, m_H , (with the Weinberg angle, θ_W , and the Fermi constant, G_F) as follows:

$$M_W^2 = \frac{\pi\alpha/\sqrt{2}G_F}{\sin^2\theta_W \cdot (1 - \Delta r)}. \quad (2.9)$$

The correction, $(\Delta r)_{\text{top}}$, due to the top-quark mass is quadratic:

$$(\Delta r)_{\text{top}} \simeq -\frac{3G_F}{8\sqrt{2}\pi^2 \tan^2\theta_W} m_t^2, \quad (2.10)$$

¹³From a theoretical point of view quarks do not have a (pole or on-shell) mass, since they do not exist as free particles. Motivated by the fact that the top quark exists as an almost free quark, one can define a pole mass in a perturbative fashion. Still, the perturbative calculation of the pole mass has an ambiguity of a few hundred MeV. As such measurement precision is not reached with the current colliders, the top-quark mass measurements can be interpreted as the pole mass. A non-perturbative definition of the top-quark mass is the so-called $\overline{\text{MS}}$ mass. A calculation from [8] shows that the $\overline{\text{MS}}$ mass is around 10 GeV lower than the pole mass.

and the correction due to the Higgs-boson mass $(\Delta r)_{\text{Higgs}}$ is only logarithmic (M_Z denotes the Z -boson mass):

$$(\Delta r)_{\text{Higgs}} \simeq \frac{3 G_{\text{F}} M_W^2}{8\sqrt{2}\pi^2} \left(\ln \frac{m_H^2}{M_Z^2} - \frac{5}{6} \right). \quad (2.11)$$

This strong correlation between the W -boson mass and the top-quark mass in formula (2.10) (together with other electro-weak parameters) and the updated measurements for R_{bb} was used for the latest indirect measurement of the top-quark mass at LEP [67]:

$$m_t = 178.9_{-8.6}^{+11.7} \text{ GeV}. \quad (2.12)$$

The latest direct top-quark mass measurements were performed at the Fermilab Tevatron Collider in all three sub-channels of the top-quark pair decay. The most precise measurements were obtained in the semi-leptonic channel. Figure 2.9 shows the most important contributions to the world average combination with the analyses from CDF and D0. This is the most precisely measured quark mass up to date:

$$m_t = 173.3 \pm 1.1 \text{ GeV}, \quad (2.13)$$

both values are in good agreement, which shows the consistency of the SM calculations.

Finally, from these values and the measured W -boson mass a limit on the Higgs-boson mass from the correction in formula (2.11) can be derived [68]. This is shown in Figure 2.10, where the two contour lines correspond to the 68% confidence limits for indirect measurements (dotted line) and including direct measurements (solid line). The overlap of the contours with the lines of constant Higgs-boson mass shows that light Higgs-boson masses are favoured.

Now cross section analyses can serve two purposes, first it can add an additional mass measurement and hence support the limits on the Higgs-boson mass. An analysis, like e.g. [60], exploited the SM relation between the cross section and the top-quark mass of $\Delta\sigma/\sigma \sim -5\Delta m_t/m_t$ and the result can be seen in Figure 2.7. The second purpose is a SM consistency check between the cross-section measurement and the best top-quark mass measurement. This was performed by CDF [61] and the result can be seen in Figure 2.8.

Single Top-Quark Production Cross-Section

A single top-quark can be produced at hadron colliders in three different channels via the weak interaction. The t -channel and s -channel processes involve a virtual W -boson. In the t -channel process the W -boson is exchanged between a bottom and another light quark¹⁴. The bottom quark has to be drawn from the partons

¹⁴Light quarks are quarks lighter than the bottom quark.

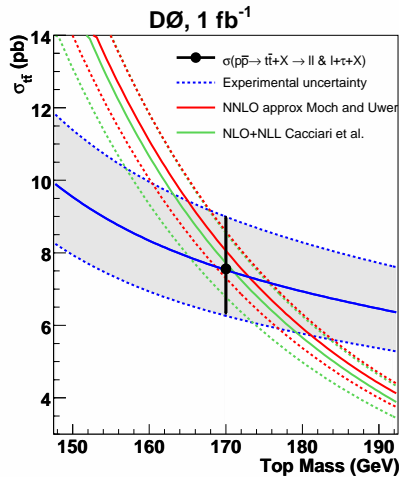


Figure 2.7.: Comparison of the D0 cross section and top-quark mass measurement dependence with theoretical dependence [60].

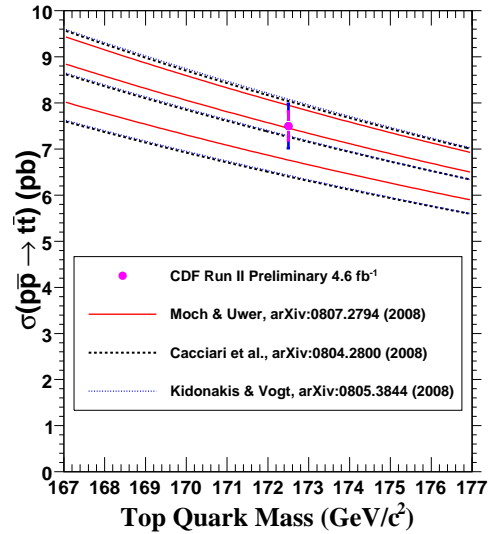


Figure 2.8.: Comparison of the combined CDF top-quark mass measurement and the combined cross-section measurement with the three theoretical predictions [61].

inside the protons or it has to be produced from gluons inside the proton first. In the s -channel process two light quarks produce a W -boson, which decays into a top and a bottom quark. At hadron colliders the light quarks are mostly up and down quarks. A real W -boson is involved in the Wt -channel process (associated top-quark and W -boson production) where a bottom quark and a gluon produce a real W -boson either via fusion or a top-quark exchange. The production cross-section is proportional to the CKM matrix element $|V_{tb}|$. The leading-order diagrams are shown in Figure 2.11.

For the t -channel process the cross section has been calculated to NLO precision [70, 71, 72]. For the $p\bar{p}$ -collisions at the Fermilab Tevatron Collider the rate for single top-quark and single antitop-quark production is equal whereas the production at the LHC is asymmetric. The dependence on the top-quark mass is $\sim -1.6\%/ \text{GeV}$ for the Fermilab Tevatron Collider and $\sim -0.7\%/ \text{GeV}$ for the LHC.

The s -channel production cross-section calculations [73, 74] are also available at NLO. The dependence on m_t leads to an uncertainty of 6% for $\Delta m_t = 2.1 \text{ GeV}$. The PDF uncertainty for the s -channel cross-section is smaller, since it is a $q\bar{q}$ annihilation process. The uncertainty on the PDFs is smaller compared to the t -channel cross-section, which needs gluons to produce the bottom quark and hence

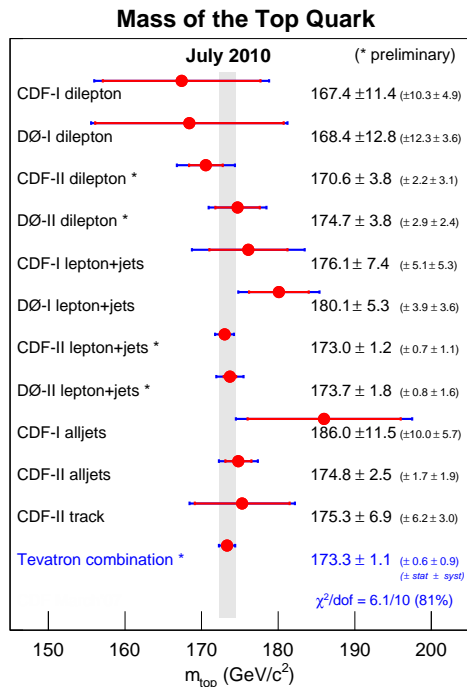


Figure 2.9.: The most significant top-quark mass measurements that were used for the combination of the top-quark mass to a world average value at the Fermilab Tevatron Collider [69].

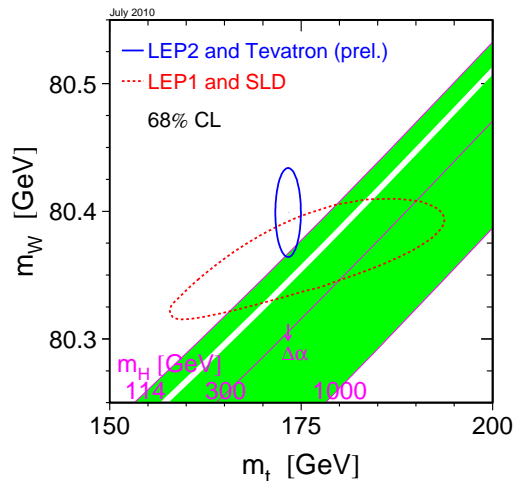


Figure 2.10.: Dependence of the W -boson mass, the top-quark mass and the Higgs-boson mass [69] for indirect measurements (dotted line) and including direct measurements (solid line). The lines in the plot are lines of constant Higgs-boson masses.

depends on the gluon PDF. Still, the dependence of the t -channel process on the gluon PDF leads to a cross section ratio between the gluon initiated t -channel and the s -channel of 1.8 at the Fermilab Tevatron Collider.

The Wt -mode cross-section is negligible at the Fermilab Tevatron Collider. The calculation can be found in [75, 76]. The NLO corrections for the Wt -channel process contain diagrams that correspond to the $t\bar{t}$ production and double counting must be avoided in the calculation.

At the LHC the importance of the different single top-quark channels changes. The ratio of the t -channel cross-section to the $t\bar{t}$ -pair production is about 30% for both colliders. However, the dependence of the t -channel process on the gluon PDF leads to a cross section ratio between the gluon initiated t -channel and the s -channel of 22 at the LHC. Instead of the s -channel, the Wt -mode becomes the second important single top-quark mode at the LHC.

2. Theoretical Aspects

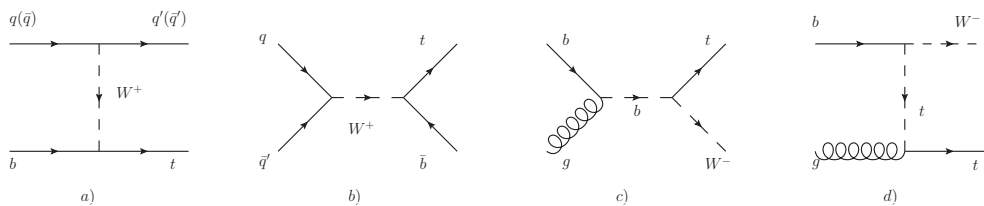


Figure 2.11.: Relevant leading-order Feynman-diagrams for the single top-quark production: (a) t -channel process, (b) s -channel process and (c-d) associated Wt production.

Table 2.4 summarises the single top-quark cross-section calculations for the Fermilab Tevatron Collider and the LHC.

Table 2.4.: Latest single top-quark cross-section calculations at NLO [70, 71, 72, 73, 74, 75, 76] for the Tevatron and the LHC.

Process cross section	collider	\sqrt{s} [TeV]	t -channel [pb]	s -channel [pb]	Wt [pb]
$p\bar{p} \rightarrow t/\bar{t}$	Tevatron	1.96	$1.98^{+0.28}_{-0.22}$	1.02 ± 0.08	0.25 ± 0.03
$pp \rightarrow t$	LHC	14.0	156 ± 8	$7.23^{+0.55}_{-0.47}$	41.1 ± 4.2
$pp \rightarrow \bar{t}$	LHC	14.0	91 ± 5	$4.03^{+0.14}_{-0.16}$	41.1 ± 4.2

Experimental status

Recent analyses at the Fermilab Tevatron Collider with multivariate techniques were able to find evidence [77, 78, 79] and finally observation [80, 81] of single top-quark events. The single top-quark s -channel and t -channel were combined to one single top-quark signal for these searches (combined search). It was also attempted to measure the CKM-matrix element $|V_{tb}|$ at the same time.

Single top-quark events are difficult to distinguish from the data due to the overwhelming background. A cut analysis at the Fermilab Tevatron Collider for example only obtains a signal-to-background ratio of 5 – 6%. Therefore advanced multivariate techniques were employed. The techniques that were used are artificial neural networks, LO matrix elements, boosted decision trees and likelihood ratios. The events for each analysis are correlated at a level of 70% hence a combination using a neural network technique to obtain a super-discriminant increases the sensitivity even further. The significance of the methods were determined in ensemble tests with simulated events, which have higher statistics than the data sample. The combination of the measurements and the significances are summarised in Table 2.5.

Table 2.5.: Cross-section measurements at the Fermilab Tevatron Collider for single top-quarks with expected and observed significances given in standard deviations [80, 81].

Analysis	Cross section [pb]	exp. significance [std. dev.]	obs. significance [std. dev.]
CDF Combined	$2.3^{+0.6}_{-0.5}$	> 5.9	5.0
D0 Combined	3.9 ± 0.9	4.5	5.0
Theory	2.9 ± 0.4		

Top-quark charge, colour and spin

The quantum numbers of the top quark, namely charge, colour and spin, are important properties that identify the top quark as the isospin partner of the bottom quark, so that it completes the third fermion family. In this role the charge of the top quark has to be $Q = +2/3 \cdot e$. The previous analyses of the top-quark cross section and top-quark mass are not sensitive to the top-quark charge. In principle the top quark found at the Fermilab Tevatron Collider could be an exotic heavy quark as described in [82] with a charge of $Q = -4/3 \cdot e$ decaying into $t^* \rightarrow bW^-$. Analyses in the semi-leptonic channel [83, 84] summed up the charges of the top-quark decay products. The W -boson charge was taken from the lepton and the charge of the bottom quark was measured from the weighted sum of charges of the tracks that belonged to the b -quark jet. Crucial for this measurements was the knowledge of the purity of the b -tagging and the correct pairing of the lepton to the b -quark jet. The correct pairing was the pairing with the best kinematic fit result. At CDF the same analysis was also performed in the dilepton channel. Here the pairing was decided with the invariant lepton-bottom quark mass. The results could exclude an exotic top-quark charge of $|Q| = 4/3$ at 95% C.L.

The colour charge of the top quark cannot be measured directly since quarks do not appear as free, single particles, but the colour charge structure of the top quark enters the cross-section calculation. The measurements of the top-quark pair cross-section has not shown any significant deviation from a colour-triplet/antitriplet structure of the top-quark pair.

From the spin of the decay products, the W -boson and the bottom quark and the conservation of angular momentum a half-integer spin mother particle is expected. Again, from the cross section the spin of the top quark can be inferred indirectly. A particle with spin $3/2$ would result in a higher cross section. The differential cross section of the top-quark pair production is also sensitive to the top-quark spin. Further observables that depend on the spin are the top-quark polarisation and the spin correlations between the top quarks of a $t\bar{t}$ pair.

Top-quark polarisation and spin correlations in top-quark pair production

The spin information is kept in the decay products due to the short lifetime of the top quark and it is not diluted by the hadronisation. This makes a measurement of the spin properties feasible.

In the following the spin properties of the top quark in pair production is discussed. The top-quark polarisation is predicted to be orthogonal to the scattering plane. The value is about $\sim 2\%$ in the SM [85, 86]. Parity-violating weak interactions also only result in a small polarisation in the scattering plane.

However, the spin correlation between the two top quarks of the pair production is sizeable from calculations in [87, 64, 88, 89, 90]. The size of the correlation, A , depends on the quantisation axes \vec{a} and \vec{b} , with \vec{S} as the spin of the top quark and $N(\uparrow\downarrow)$ the number of events with certain spin projection of the top quark and antitop quark on the quantisation axis:

$$A = \langle 4(\vec{a} \cdot \vec{S}_t)(\vec{b} \cdot \vec{S}_{\bar{t}}) \rangle = \frac{N(\uparrow\uparrow) + N(\downarrow\downarrow) - N(\uparrow\downarrow) - N(\downarrow\uparrow)}{N(\uparrow\uparrow) + N(\downarrow\downarrow) + N(\uparrow\downarrow) + N(\downarrow\uparrow)}. \quad (2.14)$$

The most promising choices for the quantisation axis at the Fermilab Tevatron Collider are the so-called off-diagonal axis [91] and the beam axis [92, 93], whereas at the LHC the axis described in [94] is most promising¹⁵.

The following observable contains the spin correlation $A = -C/(c_a c_b)$:

$$\frac{1}{\sigma} \frac{d^2\sigma}{d \cos \theta_a d \cos \theta_b} = \frac{1}{4} [1 + B_1 \cos \theta_a + B_2 \cos \theta_b - C \cos \theta_a \cos \theta_b], \quad (2.15)$$

with $\theta_{a,b}$ being the angle between the spin analyser and the quantisation axis (\vec{a}, \vec{b}) in the respective top-quark (antitop-quark) rest frame and the spin analyser power c_a and c_b (e.g. c is $+1$ for l^+). The spin analyser is the decay particle whose differential distribution is used to infer the mother particle's spin properties. The best spin-analyser for the leptonically decaying top quark is the direction of the lepton, for the non-leptonic decaying top quark it is the direction of the least energetic light quark jet. The double differential cross section above is dominated by C , since the values for B_1 and B_2 , the polarisation along the axis \vec{a}, \vec{b} , respectively, are zero in QCD calculations and small ($< 1\%$) in the weak interaction [8]. The observables for the spin require the kinematic reconstruction of the event to obtain the top-quark particle rest frames.

At the Fermilab Tevatron Collider the spin correlation has not been measured so far. At the LHC with the large anticipated amount of $t\bar{t}$ -pairs a measurement should be achievable.

¹⁵The helicity axis is also a good choice.

Top-quark polarisation in singly produced top quarks

With the discovery of singly produced top quarks, the investigation of the spin properties in the single top-quark channels becomes interesting.

The following discussion [8] concerns only the single top-quark t -channel, since it is the single top-quark channel that will have a sizeable cross section at the LHC. The top-quark polarisation, $p_t = \frac{N_{\uparrow} - N_{\downarrow}}{N_{\uparrow} + N_{\downarrow}}$, can be inferred from the distribution of the charged lepton from the W -boson decay. The distribution that depends on the polarisation, p_t , is the differential cross section:

$$\frac{1}{\sigma_t} \frac{d\sigma_t}{d\cos\theta_+} = \frac{1}{2}(1 + p_t c_+ \cos\theta_+), \quad (2.16)$$

with θ_+ as the angle between the lepton and the spectator-jet direction and c_+ the spin analysing power of the lepton. The spectator jet is the jet associated to the down quark. The same formula holds for the \bar{t} production, the symbols have to be replaced correspondingly. As in the case of the spin properties in the top-quark pair production, the whole kinematics has to be reconstructed.

Since single top-quark production was only recently measured at the Fermilab Tevatron Collider there is no measurement of the polarisation yet. It is expected that single top-quark production will be easily observed at the LHC and hence a determination of the polarisation possible.

Width and lifetime

The width of the top quark was already discussed and summarised in equation (2.8). The calculated width is $\Gamma_t(m_t = 172.5 \text{ GeV}) = 1.34 \text{ GeV}$, this corresponds to a lifetime of $\tau_t = 5 \cdot 10^{-25} \text{ s}$.

Experimentally the precision on the top-quark mass measurement is not sufficient to probe the narrow top-quark width. So far limits by CDF were set from reconstructing the top-quark mass values in semi-leptonic events and comparing the distribution with template distributions for different top-quark mass widths [95]. The limit was set at $\Gamma_t < 12.7 \text{ GeV}$ or $\tau_t > 5.2 \cdot 10^{-26} \text{ s}$ at 95% C.L. (for a top-quark mass of 175 GeV).

From the lepton track impact parameter distribution at CDF another limit on the top-quark mass lifetime was derived [96]. Comparisons with template distributions yield a limit at 95% C.L. of $c\tau < 52.5 \mu\text{m} \sim 1.8 \cdot 10^{-15} \text{ s}$.

CKM matrix element V_{tb}

The Cabibbo-Kobayashi-Maskawa matrix element V_{tb} is a free parameter in the SM. The only theoretical constraint comes from the unitarity of the CKM matrix if one makes an assumption about the number of quark/lepton families.

The analysis on the weak decay of hadrons [97] and using the CKM matrix unitarity yields at 95% C.L. that $0.9990 < V_{tb} < 0.9992$. Exploiting the fact that the square of the CKM matrix element V_{tb} is proportional to the decay rate of the top quark into the bottom quark, the measurements of $R_b = \frac{|V_{tb}|^2}{|V_{tb}|^2 + |V_{ts}|^2 + |V_{td}|^2}$ at D0 and CDF both found that R_b is consistent with one [98, 99]. The limit on R_b from the D0 measurement is $R_b > 0.79$ at 95% C.L. This limit is free from the assumption on the number of light quark families.

A direct measurement of V_{tb} is possible with the measurement of the production cross-section of single top-quarks. The discovery of single top-quark production was accompanied with a measurement on the cross section, which was converted into a determination of V_{tb} . The lower limit from this measurement [80, 81] was $|V_{tb}| > 0.78$.

Flavour Changing Neutral Currents

Flavour Changing Neutral Currents (FCNC) are only possible in the SM through loop corrections and these are highly suppressed by the mass squared differences of bottom, strange and down quarks compared to the square of the top-quark mass, the calculation can be found in [100] and the corresponding CKM matrix elements are small.

Searches for FCNC are performed e.g. in the $t \rightarrow Zq$ decay, $t \rightarrow \gamma q$ decay or the single top-quark production without additional jets $u(c) + g \rightarrow t$. The first decay was searched for by selecting $t\bar{t}$ events with leptonically decaying Z -bosons from the first top quark and a hadronically decaying W -boson from the second top quark [101]. The top quarks were reconstructed by adding one additional quark to each boson decay product. A χ^2 distribution was built from the smallest differences of the reconstructed W -boson and top-quark masses to the true values for all combinations. The result did not yield any significant difference from the SM expectation. Limits were set to the branching ratio $B(t \rightarrow Zq) < 3.7\%$ at 95% C.L. Searches will continue in the $t \rightarrow q\gamma$ and $t \rightarrow qZ \rightarrow q\ell^+\ell^-$ channels. The limit on $B(t \rightarrow \gamma q)$ was found to be smaller than 3.2% [102].

Single top-quark production events without additional jets were selected by a lepton from the top-quark decay, *missing transverse energy* (\cancel{E}_T) from the neutrino and exactly one jet identified as a b -quark jet. Both experiments found no significant deviation from the SM expectation and limits were set, e.g. at CDF the limits were $B(t \rightarrow u + g) < 3.9 \cdot 10^{-4}$ and $B(t \rightarrow c + g) < 5.7 \cdot 10^{-3}$ [103, 104]. The D0 result was expressed as contour limits and can be found in [105].

Associated production of $t\bar{t} + [H, Z, \gamma]$

Calculations for the cross section and branching ratios for the associated Higgs-boson production exist and are small (NLO QCD calculation in [106, 107, 108, 109]), so

that the purpose of this measurement is not primarily the discovery of the Higgs boson. The associated production provides a way to determine the top-quark Yukawa coupling $\lambda_t^{\text{SM}} = m_t/v = m_t/(246 \text{ GeV})$. It is more promising to measure the cross-section ratios of the associated production of $t\bar{t}H$ to e.g. WH production since this cancels the unknown Higgs-boson branching fractions. Similarly the measurement of the associated Z -boson and γ production can be used.

The amount of data to measure the couplings with a good precision is high [110, 111], so that a measurement will be targeted to probe new physics.

A search at D0 in the single-lepton channel [112] did not provide any evidence for associated Higgs-boson production so far. Furthermore, a constraint exists for the associated Z -boson production from LEP data [21].

Forward-backward asymmetry

The initial state $|p(p_z)\bar{p}(-p_z)\rangle$ at the Fermilab Tevatron Collider is not invariant under charge conjugation. In QCD a charge asymmetry is generated by the interference term with C-even and C-odd terms for $q\bar{q}$ annihilation, gq and $q\bar{b}$ fusion. The total charge asymmetry is defined as $A_{\text{FB}} = \frac{N_{\text{F}} - N_{\text{B}}}{N_{\text{F}} + N_{\text{B}}}$ with $N_{\text{F,B}}$ the number of events in the forward and backward region, respectively.

Experimentally the charge asymmetry is defined for forward and backward regions in the top-quark pair rest frame. The expected value at NLO is $A_{\text{FB}} = 0.08$ [113]. In the semi-leptonic channel at CDF and D0 a reconstruction and a fit of the kinematics was done with the help of one b -tagged jet and the constraint on the W -boson and top-quark mass to measure the asymmetry. The result for CDF [114, 115] is $A_{\text{FB}} = 0.24 \pm 0.13$ (stat) ± 0.04 (syst), which is an upward deviation of $\sim 2\sigma$. For D0 [116] the result is $A_{\text{FB}} = 0.12 \pm 0.08$ (stat) ± 0.01 (syst), and it is compatible with the predictions in the selected phase space regions.

For the LHC the initial state is invariant under the charge conjugation, thus the asymmetry is expected to be zero.

2.3. Top Quark and New Physics

New physics can show up in the top-quark sector in various ways. New particles can decay into single top-quarks or top-quark pairs and modify the production cross-section or the spin properties and spin correlation. They can also appear in the decay of the top quark and modify the decay rate, branching ratios and the angular distributions of the decay products. New couplings and unusual structure of couplings can have the same effect. The properties which are suppressed in the SM such as the flavour changing neutral currents, can be enhanced due to new physics. In the following first some general approaches are discussed that try to characterise

new physics in a model-independent way. Then some examples of new physics are given and presented in which way they can appear in the top-quark physics sector.

Although no evidence for new physics have been found so far, it can be found in principle by measuring the properties and behaviour of the top quark and any deviation from its SM prediction points towards new physics.

2.3.1. Model-Independent Characterisation

A model-independent way to characterise new physics is to use an effective Lagrangian L_{eff} that contains coupling constants with distinct properties and that are ideally zero in the SM. A parametrisation can be found in [8]:

$$L_{\text{eff}} = -\frac{\mu_m}{2}\bar{t}\sigma_{\mu\nu}G^{\mu\nu}t - i\frac{d_m}{2}\bar{t}\sigma_{\mu\nu}\gamma_5G^{\mu\nu}t. \quad (2.17)$$

It contains a term that describes the anomalous magnetic dipole moment, μ_m , and a term, d_m , that describes the anomalous electric dipole moment. In the SM, μ_m is generated in one-loop corrections and d_m are generated only in two loop corrections. In new physics models these couplings can deviate from the SM value. Models with CP violation larger than in the SM model predict a non-zero value for d_m . Observables for non-zero d_m are e.g. in [117] the high p_T tails in the top-quark p_T distribution or distortions in the invariant mass of the top-quark pairs. For μ_m possible observables according to [118] are CP odd and T odd or energy correlations between the leptons from the $t\bar{t}$ dilepton channel. The total cross section is only little affected by these anomalous couplings.

Similar model-independent effects in associated $t\bar{t}$ production can be quantified by effective couplings. For instance the electric dipole and electro-weak dipole moments that are modified by CP violating Higgs-boson couplings. The same effective Lagrangian ansatz can also be used to determine the effect of flavour changing neutral currents.

Similarly to the effective Lagrangian, the tWb -vertex can be characterised in a model-independent way. The decomposition of the vertex amplitude into form factors as in [119, 120] contains form factors that conserve chirality ($f_{R,L}$) and that flip the chirality ($g_{R,L}$). The form factors are chosen such that their values in the SM at Born level is zero and deviations imply new physics. In normalisable theories the form factor $f_{R,L}$ arises at tree level and $g_{R,L}$ arises in loop corrections. A V+A admixture in the weak vertex causes $f_R \neq 0$. This can be measured from e.g. the neutrino-energy angular distribution [121, 122]. Sizeable effects can also be found in models with alternative electro-weak symmetry-breaking (e.g. in the seesaw model [123]). CP invariant couplings can introduce a difference between the form factors $f_{R,L}$, $g_{R,L}$ of the tWb -vertex and $f'_{R,L}$, $g'_{R,L}$ of the $\bar{t}W\bar{b}$ -vertex¹⁶. W -boson

¹⁶This assumes that the form factors and the CKM matrix element V_{tb} are real.

helicity analyses and the forward-backward asymmetry can give input to the form factors (e.g. [124, 125]) and single top-quark cross section measurements in the s - and t -channel can help to constrain f_L and determine the absolute strength of the tWb -vertex [126].

2.3.2. Indirect and Direct Evidence of New Particles

Indirect evidence for particles of new physics models could be the modification of the cross section due to virtual loop corrections with new particles. In the top-quark sector this is possible if the mass of the particle is a few hundred GeV. So far no significant deviation from the cross section has been found hence the effect in new physics models should be below the measurement sensitivity. The size of the effect e.g. for two-Higgs-doublet models (2HDM¹⁷) [127, 128] is only at the few percent level [129]. An effect of $\sim 5\%$ on the Born level cross section was found in one-loop corrections for the extension of the SM to supersymmetric models [130], such the *Minimal Supersymmetric Standard Model* (MSSM), if the mass of the gluino is close to 230 GeV and the mass difference between the top-squarks are not too big [131]. Also in the single top-quark production the effect on the cross sections due to the virtual exchange of new particles is small (calculations with QCD corrections see [132] and electro-weak corrections in the MSSM see [133, 134]).

More striking evidence for new physics would be a particle that is resonant in the $m_{t\bar{t}}$ -distribution or that appears as a real particle in the single top-quark production vertex. A neutral particle with a mass up to a few TeV and strong couplings to the top quark is predicted in many new physics models. This is the case in models like Top-Colour, Little Higgs (for an overview see [135]) and models with extra-dimensions and Kaluza-Klein excitations [136, 137]. In some models the coupling of new particles to gluons and light quarks is suppressed, thus the decay into top quarks is favoured. The resonance is not only detectable through the $m_{t\bar{t}}$ -distribution, but also a distortion in the top-quark p_T spectrum and changes in the top quark polarisation are possible. The discovery potential depends also on the width of the new particle. For the production and decay of a new particle X_0 that has the same initial and final state ($gg \rightarrow X_0 \rightarrow t\bar{t}$ and $gg \rightarrow t\bar{t}$) the interference between the two processes dilutes the resonance peak the larger the width [8].

Searches at CDF in the semi-leptonic channel [138, 139, 140] with different methods to reconstruct the $t\bar{t}$ kinematics have not found any evidence of heavy particles decaying into top-quark pairs. The result of the analyses can be used to exclude certain mass regions for particles of e.g. Top-Colour models. For such particles, masses up to 720 GeV can be excluded. The same result was found at D0 [141, 142, 143]. The mass limit for heavy particles from Top-Colour models is ~ 820 GeV.

¹⁷Two Higgs Doublet Models

New particles would also appear as resonances in the single top-quark s -channel. In models like in [144, 145, 146] charged bosons W'^{\pm} , charged Higgs boson in technicolour models or top-quark pions in Top-Colour models are proposed to have a strong coupling to top quarks. The production in the s -channel is e.g. $qq' \rightarrow W'^+ \rightarrow t\bar{b}$. The enhancement of the s -channel cross section depends again on the mass and the width of the new particle, since interference effects with a larger width of the new particle will decrease the effect. The t -channel is not so much affected by virtual particle exchange, since the cross section will change proportional to $1/m_X^2$. Measurements at D0 [147] and CDF [148] have not found any evidence of heavy charged bosons in the decay channel $W' \rightarrow l\nu$ and $W' \rightarrow t\bar{b}$. The limits at the Fermilab Tevatron Collider experiments were set to $m_X > 790\text{GeV}$.

New particles can be produced directly in association with top quarks or $t\bar{t}$ -pairs. If the particle in turn couples to top quarks, it can produce $t\bar{t}\bar{t}$ states [149, 150]. In single top-quark channels charged bosons can be produced in association with the single top-quark.

Associated production $t\bar{t} + [H, Z, \gamma]$

The associated production modes $t\bar{t} + [\gamma, Z, H^0]$ are negligible in the SM [106, 107, 108, 109, 110, 111], but new physics can enhance the cross section for such a production. In models with non-SM electro-weak symmetry-breaking such as technicolour or Little Higgs predict modifications up to 10%. A composite top quark would also show an enhancement of the associated production $t\bar{t}\gamma$. The $t\bar{t}H$ associated production on the contrary is suppressed in some MSSM parameter regions where the coupling of the Higgs boson to the bottom quark is enhanced.

Flavour Changing Neutral Currents in new physics

Another effect that is strongly suppressed in the SM [100] are flavour changing neutral currents. In new physics models these production processes can be enhanced and especially in the single top-quark production this can be probed. Among the new production modes are $cg \rightarrow t$, $gg \rightarrow t\bar{c}$ and $cg \rightarrow t + [g, \gamma, Z, H^0]$ or like-sign top-pairs $qq' \rightarrow tt$. These currents can occur in the MSSM when the supersymmetry-breaking terms introduce flavour violation that lead to FCNC production modes. So far the searches [101, 102, 103, 104, 105] have not found any deviations from the SM.

Another possibility are FCNC decay modes, so that there will be additional decay channels other than the three channels characterised by the W -boson decay discussed earlier. Decays $t \rightarrow c, u$ are possible in flavour-violating models even at tree level. Type-III 2HDM models¹⁸ allow FCNC couplings of neutral Higgs bosons to quarks, models with exotic quarks have FCNC coupling of the Z -boson

¹⁸The 2HDM models are classified as type I-III 2HDM¹⁹ models, depending on the allowed couplings of the Higgs-boson doublet.

with quarks or models with new explanation of the electro-weak symmetry-breaking with top quarks having a special role allow naturally for $t \rightarrow c$ transitions [135, 151]. Reference [8] features a list of branching ratios for FCNC in different models. The branching ratios range from $10^{-15} - 10^{-10}$ to $10^{-7} - 10^{-3}$.

2.3.3. Top-Quark Decay into New Particles

The decay of the top quark cannot only have enhanced FCNC decay modes in new physics models, but new particles can also appear in the decay of the top quark. In the following the decay to charged Higgs bosons and to supersymmetric particles are discussed. The lower bound on the mass of a charged Higgs boson is set by the LEP experiments with $m_{H^\pm} > 79.3 \text{ GeV}$ at 95% C.L. [97]. Apart from this limit the mass of the charged Higgs boson in the MSSM is not limited, but is it possible to have $m_{H^\pm} < m_t$. The branching fraction to a charged Higgs boson can be found in [8]. It depends on the mass ratio of the charged Higgs boson to the top-quark mass and the model parameter $\tan \beta$. For $m_{H^\pm} = 140 \text{ GeV}$ the branching fraction can be as large as 10% (1%) for $\tan \beta = 30$ ($\tan \beta = 6$). To discover such a decay, one has to search for the decay products of the charged Higgs boson. Depending on the model parameters the decays $H \rightarrow [\tau\nu_\tau, cs, cb, W^+b\bar{b}]$ are possible. The branching ratio of the final state ($t \rightarrow Hb \rightarrow b + [\tau\nu_\tau, cs, cb]$) can be larger than the SM prediction. Since the total cross section is not affected by this decay mode, a measurement of the branching ratios of the SM decay channels can reveal a decay mode into a charged Higgs boson. From the measurement of the decay rates one can infer the model parameters²⁰ such as m_{H^\pm} and $\tan \beta$. Searches for these new decay modes were performed at D0 and CDF [152, 153, 154]. Limits on m_{H^\pm} and $\tan \beta$ can be found in [153].

The decay to supersymmetric particles depends on the detailed parameters of the supersymmetric models. Here only the kinematic constraints are discussed that can arise from the masses and dynamics of the supersymmetric particles²¹. It is then compared to the SM decay mode signatures, so that the similarities and differences can be seen. The lightest, neutral and stable SUSY particle is denoted as $\tilde{\chi}_1^0$ (neutralino), the second lightest particle, but charged, is denoted as $\tilde{\chi}_1^+$ (chargino). The supersymmetric partners (so-called stops) of the top-quark are denoted as \tilde{t}_1 and \tilde{t}_2 of which \tilde{t}_1 is the lighter particle. The following kinematic situations are possible: if the lightest stop has a mass smaller than the top-quark mass, the top quark can decay into the stop quark and the neutralino. The subsequent decay of the stop can happen via the chargino, if it is light enough. The chargino itself decays

²⁰Additional measurements of the $t\bar{t}$ spin correlation can even further constrain $\tan \beta$.

²¹For the supersymmetric model it is assumed that R parity is conserved, so that supersymmetric particles can only appear in pairs.

either leptonically or hadronically, but always accompanied by a neutralino. The final state would result in

$$t \rightarrow \tilde{t}_1 \tilde{\chi}_1^0 \rightarrow \tilde{\chi}_1^+ b \tilde{\chi}_1^0 \rightarrow b f f' \tilde{\chi}_1^0 \tilde{\chi}_1^0 \quad (2.18)$$

If the mass of the chargino does not allow a real chargino in the decay vertex of the stop, then the stop decays in a three body decay directly into a bottom quark, a W -boson and a neutralino. One could also think of replacing the W -boson by a charged Higgs boson or the R -parity could be preserved by means of scalar leptons (sleptons) instead of the neutralino. The W -boson and the charged Higgs boson can decay hadronically or leptonically, the sleptons will decay leptonically with some neutralinos. Both the charged Higgs boson and the scalar leptons must be lighter enough for this direct decay:

$$t \rightarrow \tilde{t}_1 \tilde{\chi}_1^0 \rightarrow b [[W^+, H^+], \tilde{\chi}_1^0], l^+ \tilde{\nu}_l, \tilde{l}^+ \nu_l \tilde{\chi}_1^0. \quad (2.19)$$

Finally, if also the masses of the chargino, the charged Higgs boson and the sleptons do not allow kinematically the decay of the stop there is a possible four body decay mode. The stop would decay into the bottom quark, neutralino and fermions, which is in some parameter space of MSSM [155] favourable:

$$t \rightarrow \tilde{t}_1 \tilde{\chi}_1^0 \rightarrow b f f' \tilde{\chi}_1^0 \tilde{\chi}_1^0. \quad (2.20)$$

The new decay modes have similar final state signatures to the SM decay modes of the top quark. Almost all decay modes contain a bottom quark, fermions that could be mistaken as the decay products of the W -boson and a number of neutral and not (or only weak) interacting particle that escape the detector. One can distinguish the SM top-quark decay from the top-quark decay via supersymmetric particles either by the large amount of \cancel{E}_T or by the changed angular distribution of the visible decay products. Some of the new decay modes feature an additional lepton that would lead to a tri-lepton state. Even modes with one or two leptons would have different branching ratios from the SM prediction. A measurement of the ratio of BRs can reveal such deviations. Searches for these new decay modes have been performed at CDF [156] and no evidence have been found so far.

3. Experimental Environment

This chapter describes the *Large Hadron Collider* (LHC) that will provide the collision protons and the ATLAS¹ detector that is used to record their collision fragments. The experimental environment sets the basic conditions for the cross-section measurement. The available centre-of-mass energy will be decisive on what physics range can be probed. The expected total rate of collisions, the luminosity, must be known, so that the number of selected events can be related to the cross section, but also the expected statistical precision of the measurement depend on this. However, the more dense and more often the protons collide will have an impact on the number of multiple interactions that will happen at the same time as the interesting interaction.

The detector parameters will decide which decay signatures and decay particles can be probed, which are electrons, muons, jets and total transverse energy. The challenges for the multi-purpose detector is the high collision rate and particle density. State-of-the-art detectors have been developed to cope with this high and dense particle rate as well as the high radiation dose. The performance of each detector component will influence the precision on the measured particles properties, the final efficiency and purity of the event selection and hence the precision on the cross-section measurement.

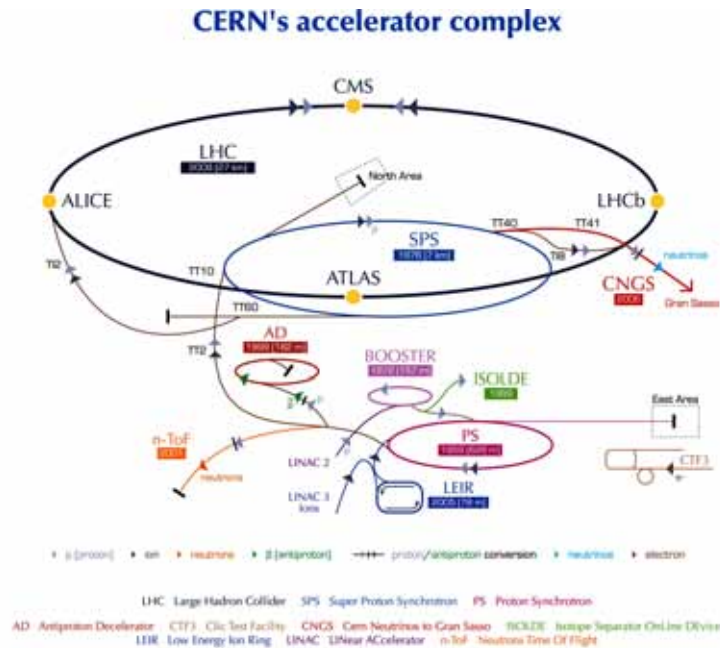
3.1. The Large Hadron Collider

As already briefly described in the introduction, the LHC [157, 158, 159] is a proton-proton collider that collides protons at a centre-of-mass energy of $\sqrt{s} = 14$ TeV. The beam contains 2808 proton bunches with up to $1.1 \cdot 10^{11}$ protons. The bunch-crossing rate will be 40 MHz at an instantaneous luminosity of $\mathcal{L}_{\text{inst.}} = 2 \cdot 10^{33} \text{ cm}^{-2}\text{s}^{-1}$ in the low luminosity phase and $\mathcal{L}_{\text{inst.}} = 10^{34} \text{ cm}^{-2}\text{s}^{-1}$ in the high luminosity phase². On average 5 proton-proton (low luminosity phase) and 25 proton-proton (high luminosity phase) interactions are expected per bunch collision.

The nominal parameters for the collider are summarised in Table 3.1 and Figure 3.1 shows an overview of the accelerator complex.

¹A Toroidal LHC ApparatuS

²The instantaneous luminosity is a measure for the density of incoming particles per area and time. See also Section 5.6.



European Organization for Nuclear Research | Organisation européenne pour la recherche nucléaire

© CERN 2008

Figure 3.1.: The LHC accelerator complex [160].

The protons are accelerated in several steps in the already existing accelerator facilities. The protons originate from a hydrogen source and are accelerated in the *Linear Accelerator* (LINAC) to an energy of 5 MeV. In the synchrotron booster the protons obtain an energy of 1.4 GeV, then they are transferred into the *Proton Synchrotron* (PS) and accelerated to 25 GeV further and finally the energy is increased to 450 GeV in the *Super Proton Synchrotron* (SPS). From the SPS they are injected into the LHC ring where they are eventually accelerated in RF-cavities up to their final energy.

For the acceleration there are eight RF-cavities installed per beam. Each cavity provides an acceleration voltage of 2 MV at an operation frequency of 400 MHz. The bunch spacing in time is 25 ns. The cavities operate at a temperature of 4.5 K.

The two beams are accelerated in opposite directions and have separate magnetic channels in the superconducting dipole magnets. This is achieved by two apertures and an eight-shaped magnetic field. Both beams share the same yoke and cryostat system. In total there are 9593 superconducting magnets of which 1232 are dipole magnets, 500 are quadrupole and 4000 are corrector magnets. The dipole magnets are made of copper-clad niobium-titanium cables. With a total current in the dipoles of 11.7 kA, a peak field of 8.33 T can be reached. The magnets are cooled to a temperature of 1.9 K with super-fluid helium in a vacuum-vessel contained cryostat.

Table 3.1.: Nominal parameters of the Large Hadron Collider [157, 158, 159].

Property	Injection	Collision
Ring circumference [m]	26658.883	
Number of main bends	1232	
Length of main bends [m]	14.3	
Revolution frequency [kHz]	11.245	
RF frequency [MHz]	400.8	
RF voltage [MV]	8	16
Proton energy [GeV]	450	7000
Relativistic γ	479.6	7461
Number of particles per bunch	$1.15 \cdot 10^{11}$	
Number of bunches	2808	
Transverse normalised emittance ϵ_N [$\mu\text{m rad}$]	3.5	3.75
Circulating beam current [A]	0.582	
Stored energy per beam [MJ]	23.3	362
RMS bunch length [cm]	11.24	7.55
RMS beam size at ATLAS/CMS* [μm]	375.2	16.7
RMS energy spread $\delta E/E_0$ [10^{-4}]	3.06	1.129
Inelastic cross section [mb]	60.0	
Total cross section [mb]	100.0	
Events per bunch crossing	-	19
Crossing angle [μrad]	-	285
Beam current lifetime ⁺ [h]	-	18.4
Luminosity lifetime ⁺ [h]	-	14.9
Beam (intensity) lifetime [h]	100	100
Instantaneous power loss per proton [W]	$3.15 \cdot 10^{-16}$	$1.84 \cdot 10^{-11}$
Synchrotron radiation power per ring [W]	$6.15 \cdot 10^{-2}$	$3.6 \cdot 10^3$
Energy loss per turn [eV]	$1.15 \cdot 10^{-1}$	$6.71 \cdot 10^3$

⁺due to beam-beam and rest gas interaction

*at the collision point

The beams travel in a beam pipe, which is held at a pressure of 10^{-13} atm. In the collision areas the beam pipe is made of beryllium.

The beams are brought to collision at four points along the ring at which detectors are positioned. ATLAS [161, 162, 163] and CMS³ [164] are multiple-purpose

³Compact Muon System

detectors that cover a broad range of physics, whereas the ALICE⁴ detector [165] aims at heavy-ion physics and LHC-B⁵ [166] at B -physics.

The LHC was completed in 2008 and started the same year with first beams. Due to problems with the dipole magnets at currents needed for 7 TeV beams, the initial centre-of-mass energy was planned to be $\sqrt{s} = 10$ TeV. However, an incident in September 2008 with a superconductive connection bar between two dipole magnets stopped the further running of the LHC. This connection bar inside the helium vessel had a small resistance that led to an electrical arc and it destroyed the helium enclosure. The sudden escape and expansion of helium into the tunnel to atmospheric pressure led to a mechanical shock wave, which dislocated and damaged 58 of the dipole magnets. This incident led to a further decrease of the centre-of-mass energy to a safer level of $\sqrt{s} = 7$ TeV. After several months of repair, in November 2009 first collisions were achieved with collision energies of up to 2.36 TeV. In early 2010 the machine restarted with beams and collisions for a physics run with a collision energy of $\sqrt{s} = 7$ TeV. The parameters that are planned to be achieved by the end of 2010 are now 10^{11} protons per bunch, with a bunch spacing of 50 ns in 796 bunches, a $\beta^* = 2.5$ at the interaction point (see Section 5.6) and a luminosity of $\mathcal{L}_{\text{inst.}} = 1.3 \cdot 10^{32} \text{ cm}^{-2}\text{s}^{-1}$. The beam then will store 31.2 MJ of energy. By the beginning of August 2010 the delivered integrated luminosity reached $\mathcal{L}_{\text{int.}} = 1 \text{ pb}^{-1}$ with a peak instantaneous luminosity of $\mathcal{L}_{\text{inst.}} = 3.0 \cdot 10^{30} \text{ cm}^{-2}\text{s}^{-1}$. By the end 2011 the $\sqrt{s} = 7$ TeV phase will be completed and a one year shutdown with possible upgrades of the detectors will follow. In 2012 it is foreseen to reach the design beam energies and design luminosity.

3.2. The ATLAS Detector

The ATLAS detector [161, 162, 163] follows the typical design of a high-energy physics multi-purpose detector. The general layout of the ATLAS detector is shown in Figure 3.2. The coordinate system used here to describe the detector geometry can be found in Appendix B.

The detector cylindrically surrounds the interaction point and the collision fragments⁶ are detected, measured and identified in different layers of detector elements. The design features of the LHC accelerator require detector elements to have a fast response for the design bunch crossing rate of 40 MHz. Depending on the position of the detector element, it has to sustain a large dose of radiation without degrading its detection performance nor the read-out electronics. The huge particle density due to high multiplicity events and overlapping events requires a high detector granularity.

⁴A Large Ion Collider Experiment

⁵Large Hadron Collider beauty experiment

⁶The largest part of the fragments, i.e. the remnant of the proton goes undetected into the beam pipe.

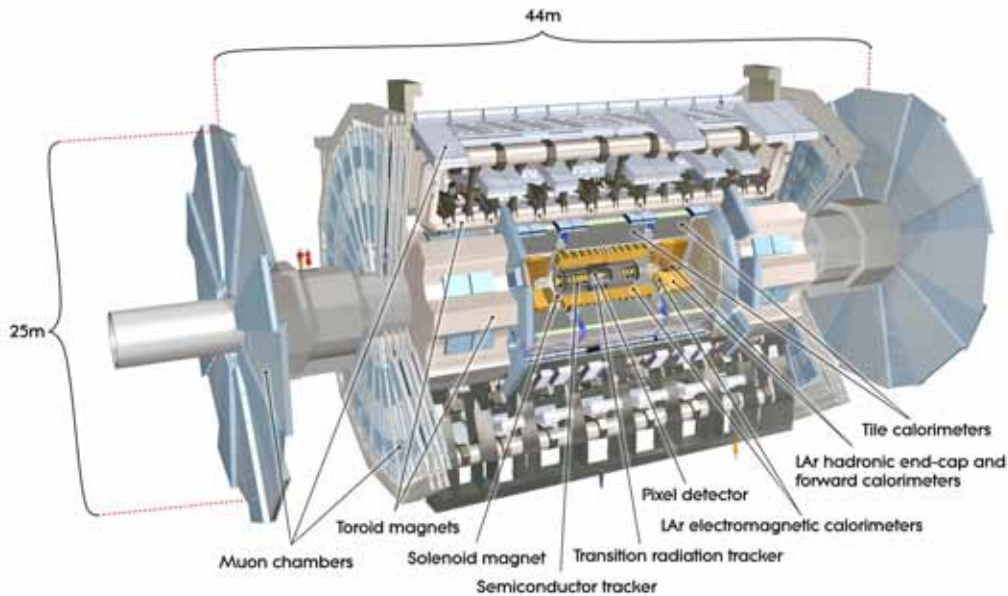


Figure 3.2.: A cut-out view of the ATLAS detector with the innermost tracking detectors, followed by the calorimeters and enclosed by the largest system, the muon system [163]. The magnet toroid structures in the barrel can be seen between the muon chambers.

The detector layout closely follows the requirements set by the physics goals. The physics requirements and the matching detector components are presented in the next section. Afterwards a short description of each detector component is given.

3.2.1. Physics Requirements

The acceptance of the detector has to cover a large pseudorapidity and almost full azimuthal range to provide a good hermeticity. A good detection efficiency and a precise inner tracking position determination for charged particles is required. The requirements are even higher for tracking detectors close to the interaction point that resolve the tracks from a primary collision or secondary vertex. At the same time the detector material of the inner tracker should be minimal in order not to degrade the position resolution and not to influence the following energy measurement of the particles. The inner tracking detector consists of a high-resolution semiconductor pixel detector, a strip detector, the *Semiconductor Tracker* (SCT), and a straw-tube *Transition Radiation Tracker* (TRT) and it covers $|\eta| < 2.5$.

The electromagnetic calorimeter has to have a good electron/photon separation and a good measurement of the electron and photon energy. This is provided by a *Liquid Argon* (LAR) *Electromagnetic Calorimeter* (EM) that measures the energy of charged and neutral electromagnetic interacting particles by showering sampling.

3. Experimental Environment

It is a high-granularity liquid-argon sampling calorimeter with a pseudorapidity coverage of $|\eta| < 3.2$.

The requirements on the hadronic calorimeter are also a good energy measurement of hadronic jets and a good hermeticity, so that the \cancel{E}_T can be determined accurately and the leak-through of charge particles into the muon system is minimised at the same time. In the range of $|\eta| < 1.7$ a three-segment, one barrel and two extended-barrels, scintillator tile-calorimeter is used. Hadronic calorimetry in the end-caps ($1.5 < |\eta| < 3.2$) is also provided by a liquid-argon detector.

For the forward region the precision requirements are looser, since the expected particle flux is higher and the detector performance has to be optimised towards radiation hardness. The liquid-argon forward calorimeter measures both electromagnetic and hadronic energy depositions and its coverage extends to $|\eta| < 4.9$.

For the muon spectrometer similar requirements on the detection efficiency and the precision as for the inner detector trackers have to be met. Especially the alignment of such a large system is a challenge. Muon tracks are measured by three layers of high precision drift tube chambers. In addition to the tracking chambers, trigger muon-chambers with a good timing resolution in the order of ns are installed to support the trigger system.

The magnet systems (see Figure 3.3) have to be designed such that the deflection of particles with a momentum at the upper end of the typical momentum range can be measured within the precision of the muon chambers and a reliable charge measurement can be achieved. The outer toroid magnets [167] consist of two end-cap and one barrel configuration and deliver a maximum magnetic field of ~ 2 T (barrel) to 4 T (in the end-cap) for the muon system. Eight Al/NbTi/Cu superconducting toroid air-coils, each contained in a vacuum vessel, form the barrel magnet. They are arranged in an eight-fold azimuthal symmetry around the centre of the detector. The end-cap toroids generate the bending power for muons in the end-cap region. It is a single cold mass build from eight flat, square coils and eight Al-alloy keystone wedges. The winding technology is same in the barrel and the end-caps. The magnetic field is monitored and mapped with Hall probes in the muon chambers.

A smaller solenoid magnet [168] is placed in the inner barrel with a ~ 2 T magnetic field. It shares a common vacuum vessel with the LAR calorimeter to spare an additional insulation wall. The single layer coil is wound with a high-strength Al-stabilised NbTi conductor. The flux is returned by the steel in hadron calorimeter and its girder structure. An in-situ mapping was done after the installation of all the magnet components, but before the installation of the inner detector. Permanently installed NMR⁷ probes measure the long-term variations to an accuracy of ~ 0.01 mT.

The requirements on the momentum/energy resolution of each detector system are summarised in Table 3.2.

⁷Nuclear Magnetic Resonance

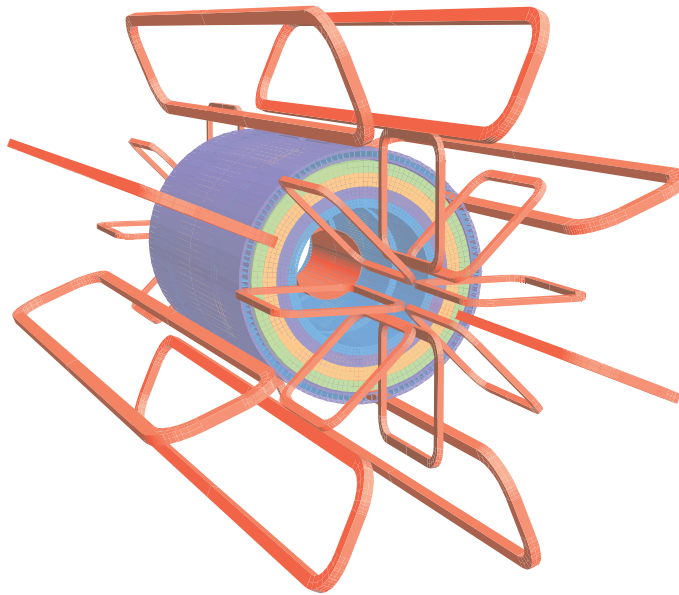


Figure 3.3.: The ATLAS magnet windings layout without the housing compartments and mechanical structures [163]. All other detector components are hidden except for the steel in the calorimeters that is used as the return yoke for the solenoid magnet.

Especially for colliders with such a high collision rate, it is important to trigger on events that contain interesting signatures. The interactions at the design luminosity of $\mathcal{L}_{\text{inst.}}=10^{34} \text{ cm}^{-2}\text{s}^{-1}$ are expected to happen at a rate of 1 GHz, but only a fraction of the events are interesting and can be recorded. This reduction is achieved by triggering on events in a three stage trigger system. Special trigger detectors have been designed for the ATLAS detector that primarily detect particles with a high rate and efficiency. They only roughly measure the energy/momentum of particles, which is enough to identify interesting signatures and reject other signatures within a few bunch crossings. The final rate of recorded events is 200 Hz. Since the rejection of unwanted events depends on the varying detector and accelerator condition, a configurable trigger system is required.

3.2.2. Inner Tracking Detectors

The challenge for the tracking system are the high interaction rate and the particle density with approximately 1000 particles every 25 ns within $|\eta| < 2.5$. Fast and high granularity tracking detectors are required to cope with this environment and the physics requirement.

The inner tracking detectors are contained in a cylindrical volume of 7 m in length and radius of 115 cm. The 2 T solenoid coil is directly attached to the outer enve-

Table 3.2.: Momentum/energy resolution requirements for the ATLAS detector parts, their $|\eta|$ coverage for momentum/energy measurement and trigger capabilities [163].

Detector system	Resolution	η coverage	
		measurement	trigger
Tracking	$\sigma_{p_T}/p_T = 0.05\%p_T \oplus 1\%$	± 2.5	
EM calorimeter	$\sigma_E/E = 10\%/\sqrt{E} \oplus 0.7\%$	± 3.2	± 2.5
HAD calorimeter			
barrel and end-cap	$\sigma_E/E = 50\%/\sqrt{E} \oplus 3\%$	± 3.2	
forward	$\sigma_E/E = 100\%/\sqrt{E} \oplus 10\%$	$3.1 < \eta < 4.9$	
Muon spectrometer	$\sigma_{p_T}/p_T = 10\%p_T$ at $p_T = 1$ TeV	± 2.7	± 2.4

lope of the inner detector systems. Figures 3.4 and 3.5 show the inner detector layout [163].

Tracks with transverse momentum larger than ~ 0.5 GeV and $|\eta| < 2.5$ can be measured in the inner tracker and electron identification is possible from 0.5 GeV up to 150 GeV. Table 3.3 summarises the features of the inner detectors.

Both silicon detectors deliver 3D space points of charged particles. The particles release electron-hole pairs along their track in the sensor material, which are separated by the electric field generated by the bias voltage between the two sensor sides.

The pixel detector

The high occupancy close to the interaction point demands a high granularity, so that a pixelated sensor and readout technology is used. The intrinsic resolution is given by the size of the pixel elements, which is limited by the size of the corresponding readout cell. In addition, material in front of the sensor can deteriorate the total resolution by multiple scattering.

The pixel detector [169] is build from 1744 identical pixel modules, which are arranged in three layers of staves in the barrel and three disks in each end-cap (both are so-called vertexing layers). A hybrid module is composed of a 250 μm thick, highly-oxygenated silicon sensor bump-bonded to standard CMOS⁸ read-out front-end chips. The modules in the barrel are placed with the longer side parallel to the z -axis and are tilted by 20° with respect to the tangent vector at the given radius. The modules on the end-cap disks are placed radially around the beam pipe and are perpendicular to the z -axis. Each module has 46080 active read-out pixel cells. To improve the spatial resolution, the pixel chips can perform a coarse charge

⁸Complementary Metal Oxide Semiconductor

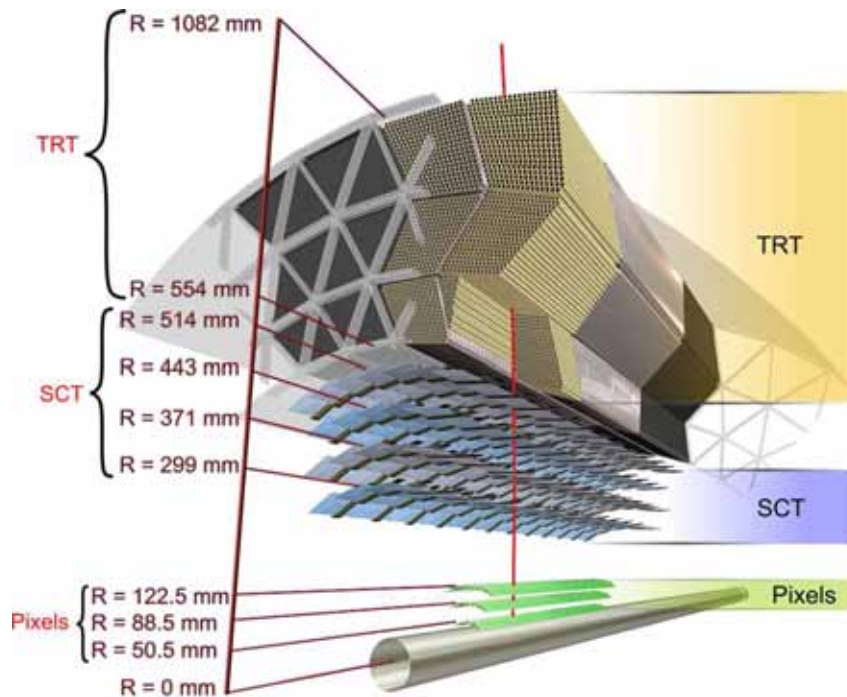


Figure 3.4.: Sector cut-out of the barrel inner detector [163] showing the beam pipe, the three pixel detector layers, the SCT layers and the TRT modules.

measurement, so that the hits can be weighted by the charge amount when two neighbouring pixels are hit. In total the pixel detector has roughly 80 Mio. read-out channels, which are 50% of all the read-out channels of ATLAS.

Semiconductor tracker

The lower occupancy allows for a simpler method to obtain the 3D space point information, thus strips are chosen and the readout electronics can be placed at the edge of the sensor. The coordinate along the strips is inferred from hits in two planes, which are glued back to back and rotated by a stereo-shift angle, γ . The resolution $\sigma_{r,\phi}$ perpendicular to the strips is given by the strip pitch. The resolution, σ_z , along the strips is determined by $\sigma_z = \sigma_{r,\phi} / \sin \gamma$.

The SCT [170] is built from 15912 sensors and AC⁹-coupled readout strips with a thickness of $\sim 285 \mu\text{m}$ [171, 172]. In the barrel region the sensors have a total of 768 active strips per sensor. Two sensors are daisy chained to a set, two sets are glued back-to-back on a substrate with a stereo angle to form a module and the read-out electronics are arranged at one edge of a module. In total there are ~ 6000 modules. The modules as well as the strips are oriented parallel to the z -axis, tilted by $\sim 11^\circ$

⁹Alternating Current

Table 3.3.: Overview of the inner detector features describing the technology used, the smallest sensor element size, the single-point resolution in the barrel in $R - \phi$ and z direction and the number of space points recorded by each subsystem [163].

	Pixel detector	SCT detector	TRT detector
Technology			
	Si n ⁺ -in-n pixel	Si p-in-n strips	Al cathode and W anode wire drift tube
Sensor element size			
	400 × 50 μm	80 μm strip pitch with 20 mrad stereo angle	4 mm diameter tube
Single point resolution (barrel)			
$R - \phi$	10 μm	17 μm	130 μm
z	115 μm	580 μm	only sign
Number of space points and layers (except for the TRT)			
barrel	3	4	22–36
end-cap	3	up to 9	

relative to the local tangent vector and are arranged in four layers. The end-cap sensors are perpendicular to the beam-axis and arranged in nine layers. They have a trapezoidal shape with on average 80 μm pitched radial strips with a stereo angle of 20 mrad.

Transition radiation tracker

The TRT [173, 174] can record hits from charged particles and allows for pion/electron separation by absorbing and measuring the transition-radiation photons. The position of a hit is determined by gas-filled polyimide drift straw tubes [175]. Charged particles traversing the gas create electron-ion pairs. The electrons are then collected on the anode wire in the middle of the tube. The position is determined from the drift time of the generated charges in the gas mixture. The charge collection time is ~ 48 ns.

The voids between the tubes are filled with polypropylene foils (end-cap) or fibres (barrel) with a different dielectric constant, so that the particles emit transition radiation. Electrons tend to radiate more transition radiation than the heavier pions. The average transition-radiation photon energy of electrons is 8 – 10 keV while the passing of other charged particles only leaves ~ 2 keV. Thus the read-out electronics has implemented two thresholds in order to perform this separation. Typically seven to ten high-threshold hits are found for electrons.

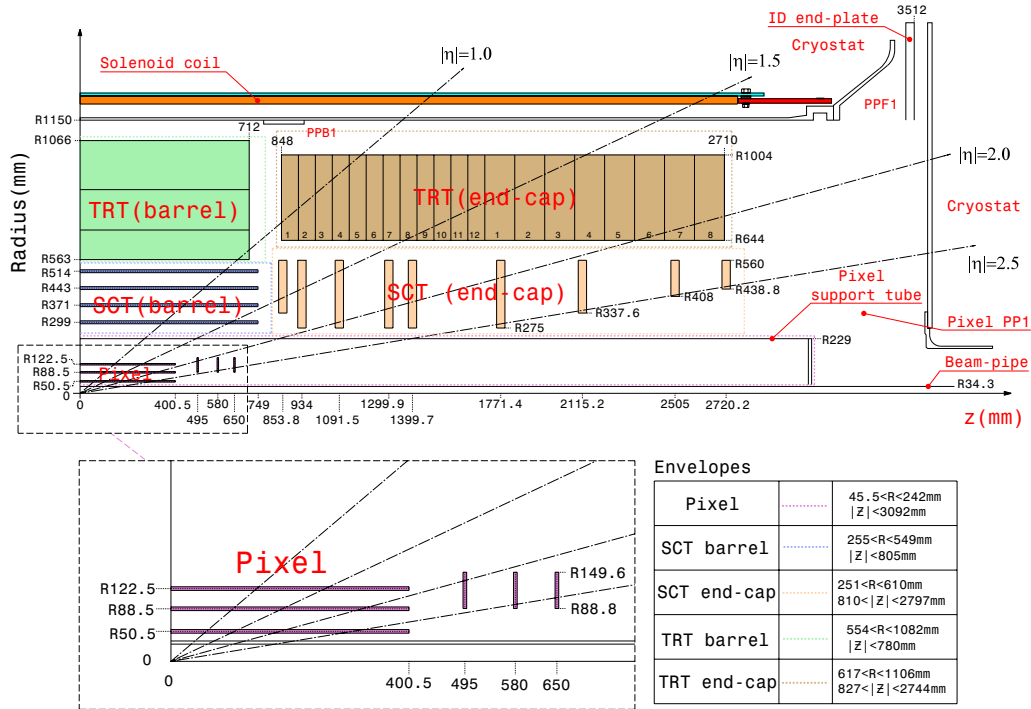


Figure 3.5.: Technical layout of one quarter of the inner detector system [163] with the positions of the detector elements and the support and solenoid structures.

For the barrel layers the straw anode wire is mechanically and electrically separated by a support plastic in the middle, so that the barrel is separated into two halves.

In total a charged particle with $p_T > 0.5 \text{ GeV}$ and $|\eta| < 2.0$ will cross at least 36 straws, in the barrel-end-cap transition region still 22 straws are crossed. The orientation of the straws in the barrel is along the z -axis. The 37 cm long straws in the end-cap region are oriented radially.

3.2.3. Calorimeters

ATLAS detector calorimeters [176, 177] are sampling calorimeters. Tables 3.4 and 3.5 give a short overview of the ATLAS calorimeters and Figure 3.6 shows an overview of the calorimeter system. Except for the hadronic tile-calorimeter they are placed in one barrel and two end-cap cryostats that are filled with an active medium, liquid argon. The response of liquid argon is linear and stable over time, furthermore it is intrinsically radiation hard. The electromagnetic calorimeter measures the energy of electrons (positrons) and photons very precisely in one barrel (EMB) and two end-cap (EMEC) arrangements. Hadronically interacting particles are stopped in the *Hadronic Calorimeter* (HCAL) in one barrel and two extended barrel ar-

3. Experimental Environment

rangements. The two electromagnetic end-cap calorimeters share the cryostats with the *Hadronic End Cap* (HEC) and the *Forward Calorimeter* (FCAL). The forward calorimeter provides electromagnetic and hadronic calorimetry up to $|\eta| < 4.9$.

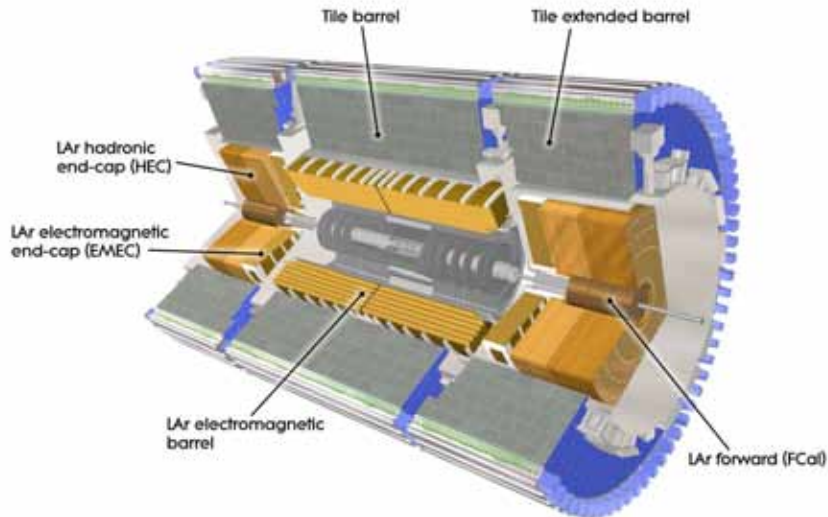


Figure 3.6.: Overview of the ATLAS calorimeter systems [163].

Presampler detectors are used in the region $|\eta| < 1.8$ and between the barrel and end-cap in the region $1.5 < |\eta| < 1.8$. They are singly instrumented argon layers and located within the cryostat, but before the active electromagnetic calorimeter. They provide a first shower sample, so that the losses in the cryostat walls can be partially recovered.

The resolution σ_E/E of a sampling calorimeter is typically a function of $a/\sqrt{E} \oplus c$, where a is the stochastic term, since the energy is measured by counting the number of secondary charges that is released from the incoming particle and c is a constant that absorbs e.g. calibration uncertainties.

Electromagnetic calorimeter

Electromagnetically interacting particles are mostly electrons, positrons and photons. Incoming electrons/positrons radiate off bremsstrahlung photons and in turn photons produce electron-positron pairs. Thus a cascade of electrons/photons is generated from both types of particles. The cascade is measured then by interleaved active material. The cascade electrons/positrons travel to and ionise the active material. Finally, the amount of ionisation is measured by collecting the charges on

Table 3.4.: Overview of the ATLAS electromagnetic calorimeter systems [163].

Electrom.	EM barrel	EM end-cap	FCAL1
η coverage	$ \eta < 1.475^*$	$1.375 < \eta < 3.2^*$	$3.10 < \eta < 4.83$
structure	two half-barrels in z	two co-axial wheels on each side	end-cap wheel
absorber	lead	lead	copper matrix and rods
active medium	liquid argon	liquid argon	liquid argon
granul. max	0.075×0.025	0.1×0.1	$3.0 \times 2.6^+$
$\Delta\eta \times \Delta\phi$ min	$0.025/8 \times 0.1$	$0.025/8 \times 0.1$	$\sim 4 \times \text{finer}^\#$
depth	2–3 layers	2–3 layers	no segmentation
thickness	$22 - 33 \times X_0$	$24 - 38 \times X_0$	$27.6 \times X_0$
σ_E/E^\dagger	$10\%/\sqrt{E} \oplus 0.7\%$	same as barrel	$100\%/\sqrt{E} \oplus 10\%$

*Without presamplers.

†Expected resolution.

electrodes. A shower traverses several layers of the absorber/active material sandwich¹⁰. Typically 95% of the shower is contained in $2 \times R_m$ and in $14 - 16 \times X_0$ [178].

The readout electrodes are placed in the middle between the absorbers. The segmentation along the depth and the η direction for the barrel is done by etching separation paths into the readout layers. The segmentation in the η direction follows the lines of equal η coordinates. A ϕ segmentation for the barrel layers is done by stacking the absorber and readout layers. Along the radial direction the absorber/readout structure is folded into an accordion shape¹¹. This provides a full ϕ coverage without any cracks. The segmentation is different in the different layers in depth. The finest granularity has the innermost layer, the outermost layer has the coarsest granularity. The reduced granularity is of advantage when the layer is used for the building of trigger objects.

The barrel is made of two half barrels. Each cover the positive and negative z -hemisphere. The length of a half barrel is 3.2 m and the diameter ranges from $d = 2.8 - 4$ m. One half-barrel contains 1024 accordion-shaped absorbers. The drift time for the signal charges is 450 ns. Figure 3.7 shows the layout of three layers of one barrel module.

¹⁰A crucial number is the thickness of the sampling calorimeter in the longitudinal direction in units of the radiation length X_0 . The lateral width is given by the Molière radius R_m and depends mainly on the multiple scattering.

¹¹i.e. the waves run radially. The folding angle varies to keep the spacing between the layers constant.

Table 3.5.: Overview of the ATLAS hadronic calorimeter systems [163].

Hadronic	barrel	hadronic end-cap	FCAL2-3
η coverage	$ \eta < 1.7^*$	$1.5 < \eta < 3.2^*$	$3.1 < \eta < 4.9^*$
structure	one barrel and two extended barrels	two wheels on each side	two end-cap wheels
absorber	steel	copper	tungsten matrix and rods
active medium	polystyrene	liquid argon	liquid argon
granul. max	0.2×0.1	0.2×0.2	$5.4 \times 4.7^+$
$\Delta\eta \times \Delta\phi$ min	0.1×0.1	0.1×0.1	$\sim 4 \times$ finer [#]
in depth	3	4	two elements
thickness	$7.4 \times \lambda_I$	$\sim 10 \times \lambda_I$	$(3.68 + 3.60) \times \lambda_I$
σ_E/E^\dagger	$50\%/\sqrt{E} \oplus 3\%$	same as barrel	$100\%/\sqrt{E} \oplus 10\%$

*Without presamplers.

+This is $\Delta x \times \Delta y$ in cm.

#This refers to the maximum granularity of the FCAL.

†Expected resolution.

fluctuations in the number of produced neutral pions, which increase the already dominating stochastic term in the energy resolution formula.

The ATLAS hadronic calorimeter [180] is located in the region of $|\eta| < 1.7$ behind the electromagnetic calorimeter. It consists of a central barrel and two extended barrels at both ends. Each barrel is made of 64 modules with a size in $\Delta\phi$ of 0.1.

The scintillator and the steel absorber form a periodic structure with alternating (in both η and r directions) absorber and active material layers with a volume ratio of 1 : 4.7. The tiles are radially oriented and normal to the beam line. The scintillator is polystyrene in which ionising particles produce ultraviolet scintillation light, which is converted into visible light by 1 mm diameter wavelength shifters. Figure 3.8 shows a sketch of a tile-calorimeter module.

The scintillator light is grouped almost projectively in η and guided by the wavelength shifters to the back side of the tile module. The signal is readout by photomultipliers. The girder structure, which holds the barrel modules, acts at the same time as the return yoke for the solenoid field. In the gap region between the barrel and the extended barrel special modules or even thinner scintillation counters are used in order to accommodate the limited space availability in the crack region and to correct for the losses in the inactive material.

The hadronic end-cap calorimeter

The HEC is made of two wheels (HEC1 and HEC2) in each end-cap cryostat with 32 identical wedge-shaped modules. A sketch of the HEC is shown in Figure 3.9. The absorber plates are normal to the z -direction. Three read-out electrodes are located in the gaps, which are held in position by honeycomb spacers. The drift time for electrons in the drift zone is 430 ns. The middle electrode layer is also segmented, which defines the readout granularity of the calorimeter. The etched pattern in the readout layers and the grouping of the readout cells is approximately projective in the η direction.

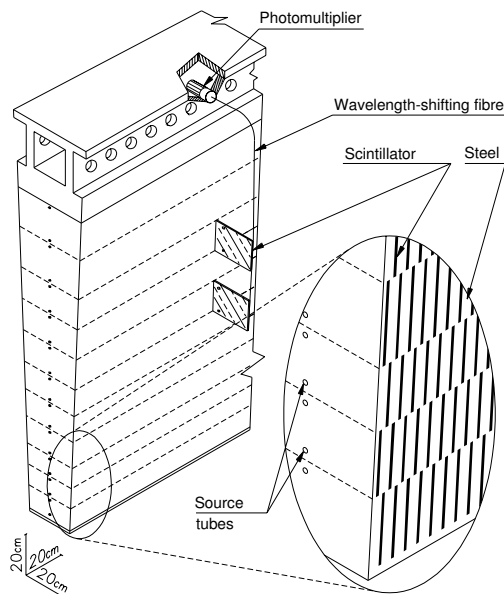


Figure 3.8.: A sketch of the tile-calorimeter module [163].

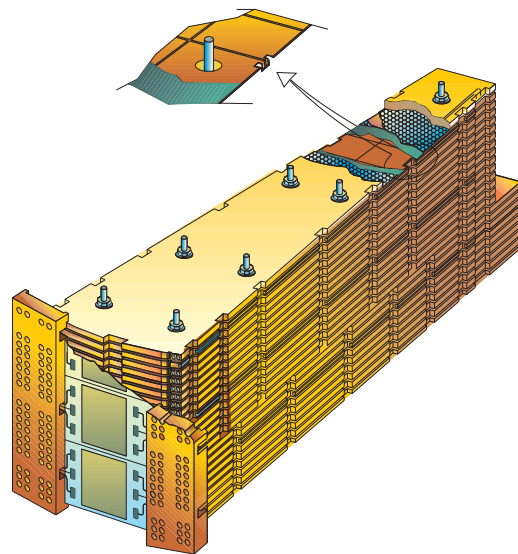


Figure 3.9.: An artistic view of a hadronic end-cap module [163].

The forward calorimeters

The forward calorimeters [181] are heavily exposed to a high energy particle flux that is 30 times higher than the dose in the hadronic end-caps. The high particle flux requires a small drift distance for fast readout at the cost of the signal height and a low ion build-up, so that the design of the FCAL is different from the other calorimeters. The electrodes are rods parallel to the beam, embedded into the absorber matrix of the same material, so that a high density is achieved. The electrodes are copper tubes, which are held in position by radiation hard fibres around the rod. The drift time in the first layer (FCAL1) is 60 ns. Copper as an optimal absorber for the FCAL1 has a good heat conduction, but still maintains a good resolution. For the FCAL2 and FCAL3 tungsten was chosen as the absorber

and readout-rod material, which keeps the lateral size of the shower small. Finally, behind the last layer of the forward calorimeter an absorber made of copper alloy is placed to shield the muon system from the remaining shower particles. Figure 3.10 shows schematically the layout of the FCAL.

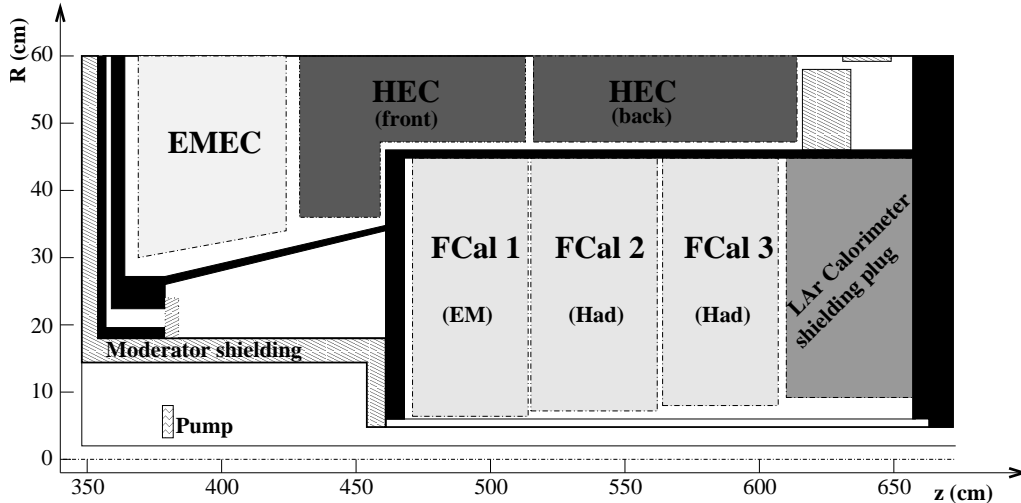


Figure 3.10.: The layout of the forward calorimeters [163] FCAL1-3 and their position relative to the electromagnetic and hadronic end-caps.

3.2.4. The Muon System

The muon system [182] is made of two main sub-systems, the precision chambers that measure the track positions accurately in $R - \phi$ and z for a muon momentum precision of 10% for 1 TeV muons, and the trigger chambers that identify muon tracks within the time to the next bunch crossing with a high efficiency. There are several acceptance holes in the muon spectrometer at $|\eta| \sim 0$ that contain service lines for the calorimeters, the cryostat and the inner detector. In addition there are two inactive areas where the ATLAS feet supports are positioned. The layout of the muon system is shown in Figure 3.11 for one quadrant in the $R - z$ view, in Figure 3.12 a front view and in Figure 3.13 a zoom into one sector in the $R - \phi$ view is shown.

The precision chambers are made of *Monitored Drift Tubes* (MDTs) and of *Cathode Strip Chambers* (CSCs). The trigger is provided by *Resistive Plate Chambers* (RPCs) and *Thin Gap Chambers* (TGCs). Table 3.6 gives an overview of the muon chambers.

The muon spectrometer is the largest detector system and extends up to a radius of ~ 10 m and z -position of 21.5 m. These huge dimensions present a big challenge for the alignment of the detector modules. The precision chamber alignment must

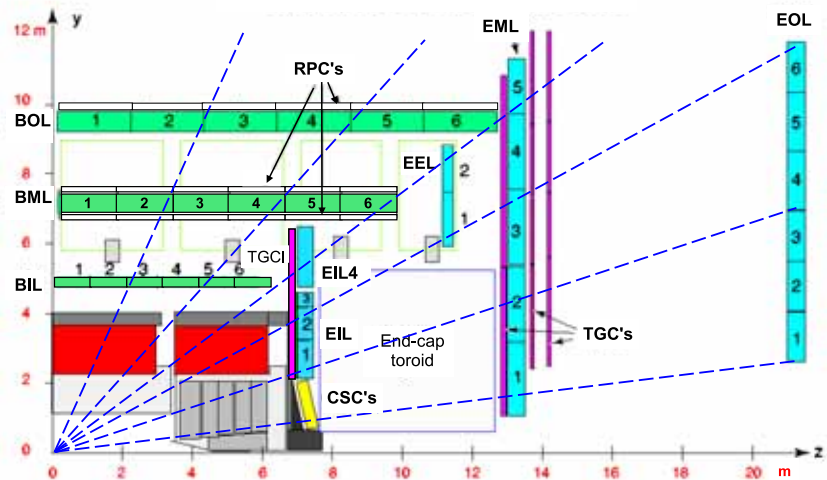


Figure 3.11.: $R - z$ view of the muon system with infinite momentum tracks as dotted lines [163]. The abbreviations are BOL, BML and BIL for barrel outer/middle/inner and EIL, EML and EOL for end-cap MDT layers (EEL are extra layers), RPCs are the resistive plate chambers, TGCs the thin gap chambers and CSC are the cathode strip chambers.

be known to $< 30 \mu\text{m}$ precision. This can only be achieved by a combination of intra- and inter-chamber alignment techniques for the relative alignment as well as the alignment with straight tracks [183, 184] for the absolute alignment.

The trigger chambers provide the trigger system with the information about the multiplicity and transverse momentum of muons. It also complements the precision chambers with additional information about the track position in the non-bending plane, which is the ϕ coordinate. The granularity has to be finer than for the precision chambers, since the bending power is almost zero in some areas of the detector, esp. the chambers outside of the magnetic field or in some areas where the magnetic field has a complex field geometry due to the overlap between the barrel and end-cap toroid field.

Precision chambers: Monitored drift tubes

The precision chambers use monitored drift tubes [185] to measure the track position. Similar to the drift tubes in the TRT detector a precision chamber consist of a number of pressurised gas-filled tubes¹⁴. The expected resolution per tube is $80 \mu\text{m}$ ¹⁵.

¹⁴Although this drift time is longer than in usual gas mixtures and the gas shows a non-linear behaviour, it has good ageing properties.

¹⁵The exact space drift-time relation depends on the environment conditions such as temperature, pressure and magnetic field.

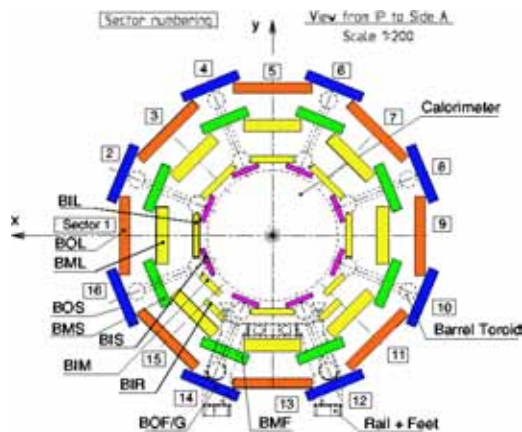


Figure 3.12.: $R-\phi$ view of the muon sectors showing the eight-fold symmetry and the interleaved MDT layers [163]. These are denoted by three letter abbreviations, e.g. the first letter B stands for barrel, the second letter I, M, O for inner, middle and outer layer and the last letter S, M, L stands for small, medium, large chambers while G, F are modified chamber sizes.

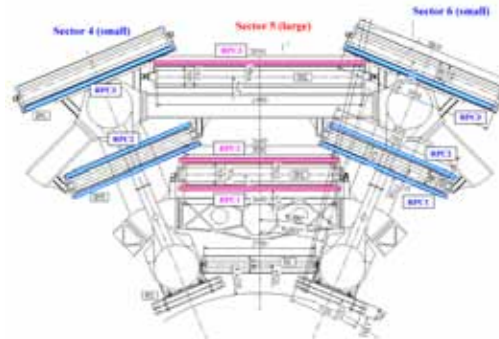


Figure 3.13.: $R-\phi$ view of the muon chamber sector, specially marking the positions of the RPC chambers [163], which are attached to the MDTs.

The drift tubes are arranged perpendicular to the beam line, since the toroid magnet bends the tracks in the $R-z$ plane. A regular MDT chamber consists of two multi-layers separated by a rigid mechanical frame. The multi-layers are made of 3–4 layers of drift tubes in the innermost and outer chambers, respectively.

The arrangement of the precision chambers follow the eight-fold symmetry of the toroid magnets. The barrel chambers are mounted either on the toroid coils or between the coils. In the end-cap the chambers are arranged in four layers, one layer in front of, two layers behind and the last layer is positioned around the end-cap toroid. There are special chambers around the ATLAS feet, so that the inefficiency can be minimised.

Precision chambers: Cathode-strip chambers

The cathode-strip chambers [186] are installed in the end-cap regions for $|\eta| > 2$ since the rates, which are expected for this η -region in the first layer, exceed the maximum rate of 150 Hz/cm^2 for the MDTs. The disk arrangement consists of two rings with eight large and eight small chambers and each chamber has four detector planes.

Table 3.6.: Overview of the muon chambers divided into the precision tracking and trigger chambers [163].

	MDT	CSC	RPC	TGC
Function	tracking	tracking	trigger	trigger
Resolution				
z/R	$z : 35 \mu\text{m}$	$R : 40 \mu\text{m}$	$z : 10 \text{mm}$	$R : 2 - 6 \text{mm}$
ϕ	-	5 mm	10 mm	3 - 7 mm
Timing resolution	-	7 ns	1.5 ns	4 ns
Measurements/track				
barrel	20	-	6	-
end-cap	20	4	-	9
η coverage	$ \eta < 2.0$	$2.0 < \eta < 2.7$	$ \eta < 1.05$	$1.05 < \eta < 2.4$
Number of chambers	1150	32	544	3588
Number of channels	354k	30.7k	373k	318k

A cathode-strip chamber is a multi-wire proportional chamber with a $30 \mu\text{m}$ diameter gold-plated tungsten wires, which serve as the anodes and the two cathode planes, which are segmented in parallel and perpendicular direction to the anode wires. The spacing between the anode wires and the cathode strips is equal. Only the signal from the cathode strips is used and a hit position is inferred from the relative charged induced into several plates. The rates up to which the CSCs can operate is $1000 \text{Hz}/\text{m}^2$. The chambers are tilted such that straight tracks from the interaction point are normal to the chambers and the effect of the spreading of the charge deposition is minimised. The spatial resolution in the sagitta direction per layer is $60 \mu\text{m}$. The measurement of the pulse height allows also a simple pairing of hits from different tracks.

Trigger chambers: Resistive plate chambers

A RPC [187] is a gaseous parallel electrode-plate detector. The plates are made of phenolic-melamnic plastic and have a distance of 2 mm. A track generates a signal with a width of 5 ns. The local rate capability is $\sim 1 \text{kHz}/\text{cm}^2$.

The RPCs are the trigger chambers in the barrel with three layers. Each chamber consists of two detector sub-layers that each measure η and ϕ independently¹⁶. The lever arm between the RPC chambers allow triggering of muons in the p_T -range of 9 - 35 GeV for high- p_T muons and of 6 - 9 GeV for low p_T -muons.

¹⁶The three layers measure 6 η and 6 ϕ coordinates.

Trigger chambers: Thin gap chambers

Thin gap chambers [188] are multi-wire proportional chambers with a wire diameter of 50 μm , a distance between the wires of 1.8 mm and a distance between the wire and the cathode of 1.4 mm. The cathodes are made of 1.6 mm thick plates with graphite coated on the side facing the wires and a copper plane on the other side.

The bending coordinate is measured by the wires and the azimuthal coordinate is measured by the strips. Each layer of a TGC has 2–3 wire layers and 4–6 strip layers. The three layers each consist of two concentric rings of detector modules.

3.2.5. The Trigger System

The ATLAS trigger [189] is a three stage trigger system. The goal is to reduce the number of events to be recorded to a rate of 200 Hz.

The three levels of the trigger system are called *Level-1* (L1), *Level-2* (L2) and *Event Filter* (EF). The L1 triggers only use special trigger-detector components that have a coarse granularity. The decision is made with electronics that was custom-made for this purpose. The L2 and EF filter form the *High Level Trigger* (HLT) [190], which have access to the full granularity and full precision of the event data. The information is processed on large cluster farms. The EF mostly uses offline algorithms to fully reconstruct objects for the trigger decision.

The L1 trigger can search for signatures of muons with the muon trigger chambers, for signatures of electrons/photons, tau and jets in the energy depositions of the electromagnetic and hadronic trigger towers, as well as for signatures of \cancel{E}_T and the transverse energy sum. The decision in the *Central Trigger Processor* (CTP) must be taken within the trigger latency of 2.0 μs . The trigger decision algorithms are programmable and consist of hit multiplicities for up to 16 p_T -thresholds for each object type. For some object types isolation from neighbouring energy depositions can be required. In total 256 trigger conditions can be processed and form 256 trigger items, which have a separate priority and a separate prescale factor. The event rate is reduced to 75 kHz (with an upgrade option to 100 kHz) by the L1 trigger.

If the logical OR of all L1 trigger items is positive, the event is passed on to the L2. The L1 provides the L2 with the information about the *Regions of Interests* (ROIs). The use of ROI reduces the amount of data to 1 – 2% of the full event data. The decision making process is designed such that an event can be rejected very early to minimise the amount of requested data. As soon as one trigger decision fails the processing and further data requests are stopped. The processing time of each node is < 40 ms. The L2 algorithms only request and process the necessary data from the detector sub-systems. Upon acceptance the event building is started that assembles all the event information into a single data structure that is then passed on to the EF trigger. The rate is reduced now to 3.5 kHz.

3. *Experimental Environment*

The event filter trigger is again a processing farm. In contrast to the L2 trigger the EF uses the full detector information and also uses standard offline reconstruction and analysis algorithms. In addition the events are classified into one or more data streams. Further, there are two special streams for detector calibration and monitoring purposes, the calibration and express stream. The event filter output nodes finally interface the data acquisition system with the CERN central data-recording facility and transfers the event data that have passed all trigger selection stages.

The details of the trigger algorithms that are executed in the several trigger stages will be described in more detail in Section 5.5.

4. Monte Carlo Simulation and Samples

The precision of the absolute number of events and the shape of the distributions that are modelled within the *Monte Carlo* (MC) generators have a considerable impact on the cross-section measurement. The shape influences the acceptance prediction and the total normalisation of a given sample influences the number of events that are expected. For some physics processes there are no methods available to obtain the shape and normalisation from data, so that the prediction fully relies on the MC simulation.

The following description outlines the general steps of the MC generation. Not all steps are valid for all generators nor are all steps handled in the same way.

The MC generation and simulation is separated into individual steps and for each step specialised programs are responsible. Two main features are simulated, the machine, such as the LHC in which a certain configuration of particles, a so-called event, is produced from the collision and interaction of two protons¹. The other feature is the interaction of the particles with detector while traversing the detector material. The first task is handled by many different process-specialised programs, the second step generically takes the outcome of the first step and simulates the interaction according to a model of the detector. The outcome of the second step has the same format as the real detector output data, but the original information from which particle the interaction started is still available. This is the so-called truth information about the true particles. The same algorithms that are applied to data can be applied to the MC simulated data and the efficiency and purity of certain procedures can be checked on the simulated data.

Also explained here is the signal signature for dileptonic top-quark pair events as it is simulated with a Monte Carlo generator. Background events that have a similar signature are also presented here. These must be taken into account in the study of dileptonic top-quark pair events and also simulated in order to study their properties and eventually to find strategies to remove them from the selection. Finally, the samples that were used for this study are listed here.

¹The “simulation” of the interaction is usually dubbed “generation”, so that it is distinguished from the detector simulation.

4.1. Monte Carlo Generators

The event generation follows a chain of individual steps [191] that are also shown in Figure 4.1. In general, each step can be done by separate programs. In some cases the whole chain is implemented in one program only. Each implementation has certain simplifications and limitations, so that there is no unique generation scheme and the individual programs have to be continuously checked and tuned with real data. There are numerous MC generators available, here only those are described that are used for the cross section study. Among these are the HERWIG [192] and PYTHIA [193] generators that use leading order calculations. Both programs can be used for parton showering, which is the hadronisation of single quarks and gluons and can also handle multiple interactions (HERWIG by the interface to JIMMY [194]). Multi-jet final states are available with ALPGEN [195]. Another leading-order generator is ACERMC [196]. For next-to-leading order calculations there is MC@NLO [34].

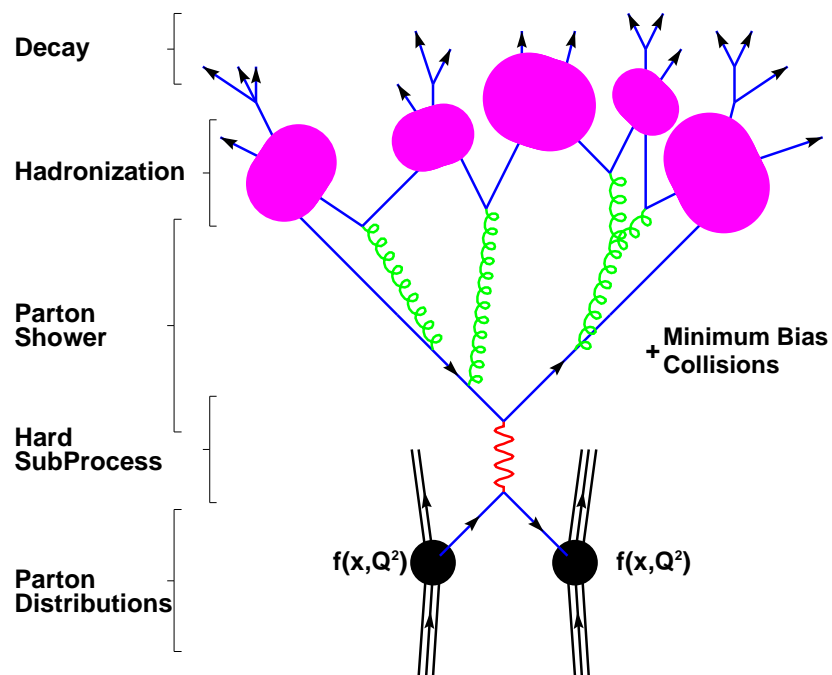


Figure 4.1.: Graphical representation of the steps in the MC generation [197].

Hard interaction

The generation starts with the two incoming protons with a given momentum and direction. The hard interaction takes place between the partons within the protons.

For this the *Parton Distribution Functions* (PDFs) are needed as an input, so that from these distributions randomly an initial state (i.e. the two initial partons) is chosen. The PDFs are derived from fits to low-energy collision-data, e.g. [27, 28, 29, 30]. The interaction between the two initial partons can be described by the Lagrangian of a theory. With the Feynman rules in the theory the matrix element and the available phase space the cross section of a process can be calculated. The cross section for the hard interaction takes the form described already in Section 2.2.1:

$$\sigma^{ab \rightarrow X}(s, x) = \sum_{i,j=q,\bar{q},g} \int dx_i dx_j f_i^a(x_i, \mu^2) f_j^b(x_j, \mu^2) \sigma^{ij \rightarrow X}(\hat{s}, x, \alpha_s(\mu^2), \mu^2), \quad (4.1)$$

where the cross section of a single process is $\sigma^{ij \rightarrow X}(\hat{s}, x, \alpha_s(\mu^2), \mu^2)$, depending on some input parameters² x , the centre-of-mass energy of the partons \hat{s} , the coupling constant $\alpha_s(\mu^2)$ at the factorisation and renormalisation scale μ .

The matrix element, which describes the dynamics in the transition from the initial state into a possible final state, can be calculated to a certain order of the perturbation theory. The lowest order implies only $2 \rightarrow 2$ tree processes, i.e. two incoming and two outgoing particles, but with the inclusion of higher order loop diagrams $2 \rightarrow 3$ processes can occur. On the one hand such processes are divergent if one of the partons has small energies ($E \rightarrow 0$) or if two partons become collinear ($\angle(\vec{p}_1, \vec{p}_2) \rightarrow 0$). On the other hand the interference between the loop diagrams (also called virtual corrections) and the tree diagrams are negatively divergent and thus the two divergences can cancel each other out, leaving finite terms. These NLO calculations have improved accuracy, but have to deal with these delicate cancellations between divergences.

Ideally, if a short-lived particle is produced in the process, the decay of the same particle should be included in the calculation, so that properties such as spin correlations can be transferred to the decay system. Some generators neglect this for certain processes, so that angular distributions cannot be described correctly, but the total cross section is not affected. E.g. the spin correlations for single top-quark events is only preserved in the latest version of MC@NLO [34].

Initial and final state radiation

The collision of partons implies colour charges to be accelerated and, as in the case of electromagnetic charges, Bremsstrahlung can occur. Emissions are called *initial state radiation* (ISR) if they are associated with incoming particles and emissions associated with outgoing particles are called *final state radiation* (FSR).

The emission in the final state can be described by higher order matrix element calculations, but the handling of the divergences can be cumbersome and therefore

²e.g. masses of particles etc.

approximate approaches are used. Parton showers form iteratively a multi-particle final state and the introduction of so-called Sudakov form factors gives a handle on the cancellation of tree and loop divergences. The iterative procedure breaks $2 \rightarrow n$ processes in a $2 \rightarrow 2$ process and absorbs the higher order in the parton shower. This works only if the $2 \rightarrow 2$ process is the one with the highest Q^2 . The probability that a (massless) quark splits into an almost collinear qg or $q\bar{q}$ pair is described by DGLAP³ [198, 199, 200] type equations. This procedure is only useful if the Q^2 of each splitting is strictly ordered such that $Q_1^2 > Q_2^2 \dots$ (e.g. PYTHIA). The shower evolution is cut off at around $Q^2 = 1 \text{ GeV}$. However, the choice of the evolution in Q^2 is not unique and different parton shower generators use different ordering schemes. It is also possible to order the evolution in terms of p_T^2 or $E^2\theta^2$ (e.g. HERWIG). The (non-) splitting probability is expressed in the so-called Sudakov form factors. They are a consequence of the conservation of probability and evaluate the probability of a splitting in terms of the $1/Q^2$ scale. The colour connection between the different out-going particles is not always treated properly and sometimes forced upon (e.g. in PYTHIA).

The initial state radiation can be treated in principle similarly to the final state radiation, it can be seen as the FSR of the initial partons. One of the radiated particles will eventually interact with the “FSR” of the other parton. This is, however, very inefficient if one wants to generate a specific process with defined initial particles, since the probability of the two “FSR” particles being the desired particles for the process of interest can be small. The most common way to simplify the procedure is to use a “backwards evolution” Ansatz and formulate a conditional probability of an ISR radiation with a higher Q^2 for a given hard process. Initial state radiation that is collinear is already absorbed by the DGLAP equations into the PDFs.

Although the parton shower seems to simplify higher order corrections, only the matrix element calculation with real emissions can correctly describe radiation that is not soft and collinear and will eventually produce a separate jet. Thus combining matrix element and parton showers is beneficial, but care needs to be taken that the full phase space is covered and overlap is removed. Either a hard cut-off is introduced to have whole phase-space coverage or weights are used to weight the parton shower events such that they agree with events from higher-order matrix element calculation including only real emissions. A common merging schemes is the MLM⁴ matching in ALPGEN in conjunction with HERWIG or PYTHIA.

Finally, in the NLO approach such as in MC@NLO the matrix element to NLO accuracy with all virtual corrections is calculated. The overlap between the matrix element at NLO and the parton shower is removed by calculating events with a LO MC generator with the first real emission. These events are added or subtracted

³Dokshitzer-Gribov-Lipatov-Altarelli-Parisi equations

⁴MLM parton shower matching algorithm named after M.L. Mangano

such that the soft limit distribution for the extra particle agrees. Currently this LO MC generator is similar to HERWIG and the parton showering after the NLO calculation can only be done with HERWIG.

Multiple interactions/underlying event

The next step is not only considering one parton pair collision, but also the possibility of further, multiple collisions, known as multiple interactions or summarised as underlying event. In the simplest model in PYTHIA the average number of interactions is calculated from a Poissonian distribution and from the ratio of the total cross section of $2 \rightarrow 2$ processes to the non-diffractive cross section. The divergence of the total cross section is damped by a colour-screening effect, so that the total cross section is not divergent. In JIMMY the number of interactions depends on an assumed hadron structure, so that it depends on the impact parameter and the overlap of the two incoming hadrons.

Each of the multiple collisions are also subject to ISR/FSR. A large fraction of the partons do not interact and carry their fraction of the beam energy away as beam remnant into the forward direction. Generally the quarks in the multiple interaction and in the ISR/FSR carry colour charge that must compensate the colour charge flow of the hard interaction. This feature is also not properly treated in all MC generators and extensive tunings on data events are usually performed.

Hadronisation

After the hard collision and after being subject to ISR/FSR, quarks and gluons, will no longer be treated as asymptotically free particles. The quarks hadronise and the process can only be described by models with certain assumptions. One common model is to have a confinement field between quarks with matching colour and anticolour that is stretched as the quarks move apart⁵. If the tension reaches a certain value, the break-up of the field produces new quark-antiquark pairs. Eventually quarks can recombine with adjacent quarks and matching colours to form hadrons. Some of the newly formed hadrons have a short lifetime, so that their decay is also included in the simulation. This is the regime where the particle simulation overlaps partially with the detector simulation.

The event generation can be part of the ATLAS detector simulation [201] framework *ATLAS software framework* (ATHENA) that is the same framework used for the offline analysis. E.g. the MC generators HERWIG and PYTHIA are already inside the framework whereas the result of the event generation of the other generators need to be imported into it. There are several interfaces inside ATHENA that allow this.

⁵This is the so-called string fragmentation model.

Figures 4.2, 4.3, 4.4, and 4.5 show some kinematic distributions of the MC generation of top quark events with different generators. Shown are the top quark, the lepton and the two highest- p_T jets distributions in p_T and η , as well as the jet multiplicity. The true top quark and true lepton distributions are directly from the generator, whereas the jets are formed by a cone algorithm (see Section 5.3) on the true particles with a cone radius of 0.4 in $\Delta\mathcal{R}$.

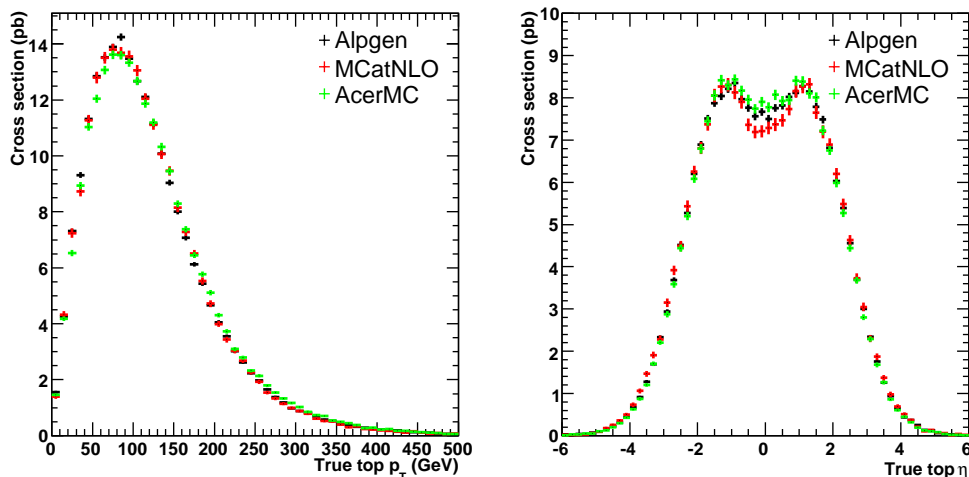


Figure 4.2.: True top quark p_T (left) and η distribution (right) for different MC generators [202].

4.2. Monte Carlo Simulation

After the event generation step follows the simulation step. This is done by G4ATLAS, which is based on the simulation toolkit GEANT4 [203]. The toolkit simulates the passage of the generated particles through the detector described as a collection of volume elements. This includes electromagnetic and hadronic interactions, the transport of particles in a magnetic field, the decay of particles and optical transport of optical photons. The transport of photons with a wavelength larger than the typical atomic spacing is important for simulation of Čerenkov or transition radiation. A large range of electromagnetic processes are included such as Compton scattering, photon-conversion, photo-electric effect, Bremsstrahlung, ionisation, δ -ray production, positron annihilation, synchrotron radiation and multiple scattering. The hadronic processes are based on data-driven models for e.g. neutron transport, parametrised models for e.g. hadron showers and theory based models for e.g. the extrapolation of other models. The decay of particles in GEANT4 mostly concerns secondary hadrons such as π , K -mesons, etc. and is simulated with

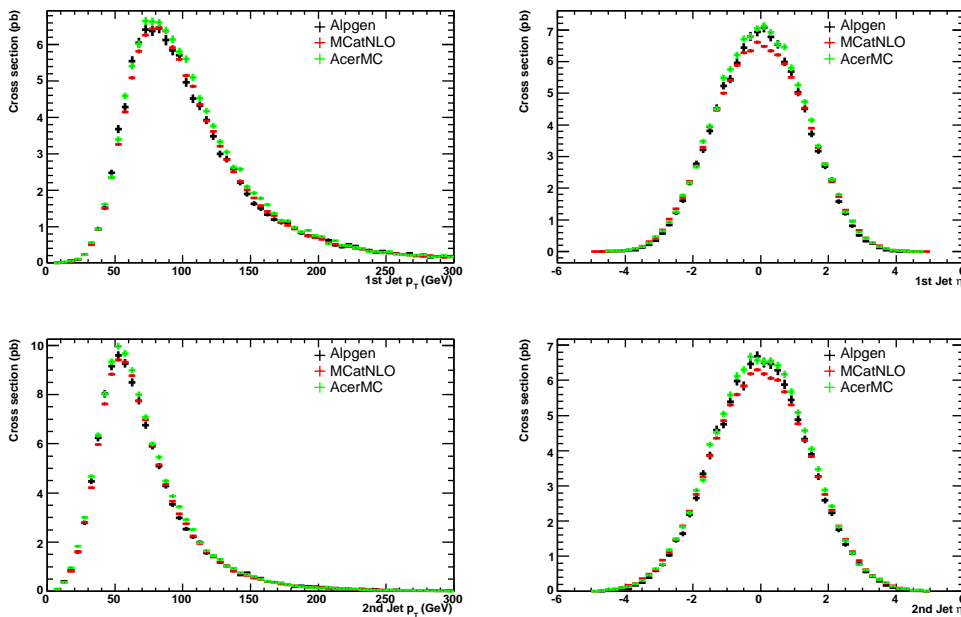


Figure 4.3.: p_T (left) and η distributions (right) for the highest (top row) and second highest p_T jet (bottom row) in $t\bar{t}$ events [202]. The jets are formed by a cone algorithm with a cone radius of 0.4 in $\Delta\mathcal{R}$ on true particles.

the help of a large database of lifetimes and branching ratios from the particle data group [7]. The detector geometry is built from a framework-independent description the so-called GEOMODEL. It is optimised for large numbers of volumes and includes alignment constants, which can be determined later in the running experiment.

From the detector responses in the sensitive elements, the so-called hits, the detector response, the digitisation is produced. This represents the raw data in the same format as produced by the real detector. From this point the simulation data and the real data are processed with the same software. The reconstruction algorithms convert the raw data into analysis objects such as calorimeter clusters, tracks and higher level objects such as electrons, muons and jets. The data is prepared in two formats the *Event Summary Data* (ESD) and the *Analysis Object Data* (AOD). With the ESDs the reconstruction can be re-run again while the AODs are specialised on the final offline analysis and omit memory consuming objects such as uncalibrated calorimeter clusters.

4.3. Experimental Signature and Background Events

With the generated and simulated MC samples it is possible to describe the signal signature and also check the background samples and how they mimic the signal.

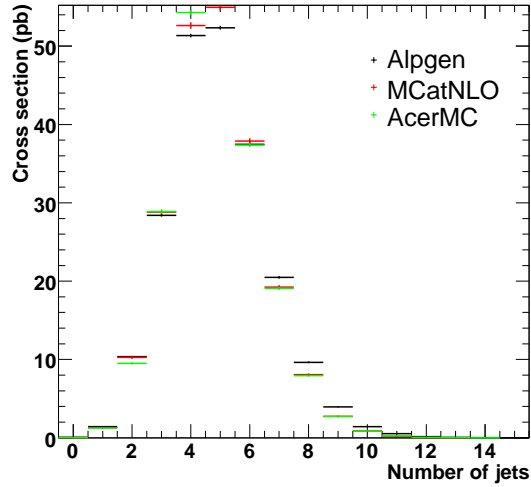


Figure 4.4.: Number of jets that are found by a cone algorithm with a cone radius of 0.4 in $\Delta\mathcal{R}$ on true particles in samples from different generators in $t\bar{t}$ events [202].

From this, strategies can be developed to suppress the background processes and to obtain a pure signal selection.

Experimental signature

The experimental signature derives from the decay of the top quark. In the SM it decays to almost 100% of the cases into a b -quark and a W -boson. For the dilepton channel a W -boson is required to decay into a lepton and a neutrino. The top quark with charge $+2/3 \cdot e$ decays into a b -quark with $-1/3 \cdot e$ and a W^+ -boson. The W^+ -boson decays into a positive lepton with an average branching fraction of

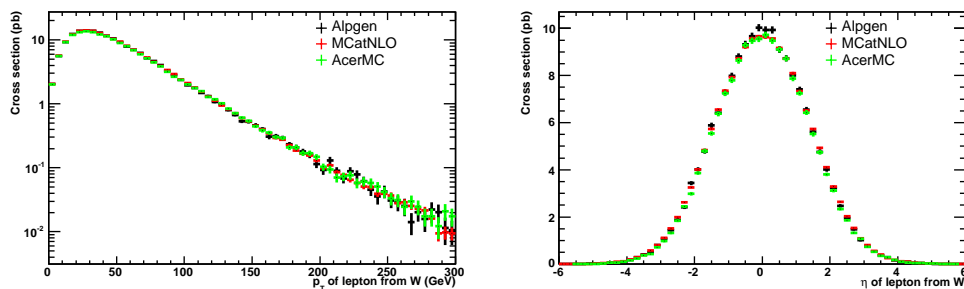


Figure 4.5.: p_T and η distributions for true leptons from leptonically decaying W -boson in top-quark samples from different generators in $t\bar{t}$ events [202].

(10.80 ± 0.09)% [7] and a neutrino. Since the $t\bar{t}$ pair is created from a neutral state, either a gluon or a $q\bar{q}$ pair, the charge signs for the antitop-quark decay particles is reversed. The expected experimental signature is two isolated, opposite-charged leptons, two jets originating from secondary vertices due to the hadronisation of the b -quarks and the long lifetime of B -hadrons⁶. These jets can be identified as b -quark jets if a tagging algorithm is used. Additional jets are due to QCD emissions and are expected to be of low transverse momentum. The two neutrinos escape the detector undetected and will create an imbalance of the calorimeter depositions in the transverse plane that is reconstructed as \cancel{E}_T . In summary the signature consists of two oppositely signed isolated leptons, two jets and \cancel{E}_T .

Background processes

There are several processes that can mimic the $t\bar{t}$ -dilepton signature in the detector. These processes can be divided into three classes. There are reducible background processes that have the same signature, but there are additional properties that can remove such backgrounds from the selection and there are irreducible background processes that cannot be simply removed. The distinction is often not obvious, but mostly a cut on kinematic variables is meant by a simple selection. Finally, there are instrumental background processes that create signatures by detector effects or mis-identifications of objects. Again, the definition is not useful, since arbitrary number of effects can create any signature. Often, only if in a process the most distinct signature is falsely created by detector effects, this process is called instrumental background. Eventually, the cross section and branching ratio of a process into the final state signature determines the importance of a process as a background process.

$Z \rightarrow e^+e^-$ and $Z \rightarrow \mu^+\mu^-$ processes (Drell-Yan) are reducible background for the dilepton ee and $\mu\mu$ sub-channels. There are two oppositely signed and isolated leptons. The jets can appear from ISR radiation of the initial partons and a small amount of \cancel{E}_T is created from detector resolution effects. These events can be removed by exploiting the fact that the invariant mass of the leptons is compatible with the Z -boson mass. For the $e\mu$ sub-channel the $Z \rightarrow \tau\tau$ is an irreducible background since the events can have an electron and a muon from the leptonic decay of the tau leptons. Also the tau-lepton decay creates neutrinos that contribute to \cancel{E}_T . A simple cut on the invariant mass of the leptons is not effective since the invariant mass distribution will not peak at the Z -boson region. $Z \rightarrow e^+e^-$ and $Z \rightarrow \mu^+\mu^-$ events represent also instrumental backgrounds for the $e\mu$ channel if one of the leptons is misidentified as the other lepton type. This is more likely the case for the mis-identification of muons as electrons. The energy depositions of muons in the calorimeter can be confused as electron energy depositions, but electrons are almost entirely stopped in the EM calorimeters and rarely reach the muon chambers.

⁶The average lifetime is 1.568 ± 0.009 ps [7].

Other background processes considered here are single top-quark events in the two most important channels. The Wt single top-quark channel contains mostly irreducible background events when the real W -boson decays leptonically as well as the single top-quark. The single top-quark t -channel contains instrumental background events, since the single top-quark is only accompanied by light quarks. W -boson events represent instrumental background, as well as semi-leptonic $t\bar{t}$ events. Mostly reducible background events are present in diboson events.

4.4. Samples

The MC simulation samples that were used are not from a single MC generator. Table 4.1 lists the sample, the sample size and the sample cross sections that are used for the cross-section analysis. A full list of all the samples can be found in the Appendix A.

Table 4.1.: List of samples with k factors, cross section and sample size for the cross-section analysis. The order refers to the order of the cross section after the k -factor has been applied. In the cross section the k factor is already applied.

Process	k -factor	calculation order	Ref.	sample cross section [pb]	sample size [pb ⁻¹]
$t\bar{t}$ MC@NLO	1.07	approx. NNLO	[204]	217.06	1639
Wt -channel	0.99	NLO	[205]	14.27	701
t -channel	1.05	NLO	[71]	43.18	585
$Z \rightarrow e^+e^- + np$	1.22	NNLO	[206]	1471.39	420
$Z \rightarrow \mu^+\mu^- + np$	1.22	NNLO	[206]	1469.10	408
$Z \rightarrow \tau\tau + np$	1.22	NNLO	[206]	1477.36	423
$W \rightarrow e\nu + np$	1.22	NNLO	[206]	16163.90	152
$W \rightarrow \mu\nu + np$	1.22	NNLO	[206]	16149.51	147
$W \rightarrow \tau\nu + np$	1.22	NNLO	[206]	16144.26	144
$W \rightarrow bb + np$	1.22	NNLO	[206]	17.86	2512
WW	1.69	NLO	[34]	26.40	938
ZZ	1.42	NLO	[34]	1.93	5193
WZ	1.81	NLO	[34]	8.82	1134

Several considerations among which is the experience at the Fermilab Tevatron Collider are taken into account when a certain generator was chosen. In order to scale the cross section from LO simulations to higher orders k -factors are used. These factors were derived from the cross sections that were calculated during the MC generation and the theoretically calculated cross sections in the given references.

For the simulation the same version of the ATHENA software was used and for the reconstruction versions with minor bug fixes were used.

The signal $t\bar{t}$ sample was generated with MC@NLO at NLO precision, the decay and parton shower was generated with HERWIG. The sample was filtered on truth level for at least one lepton. For the analysis in the dilepton channel the sample was split into a semileptonic and dileptonic sample.

The common parameters for the MC simulations are the following:

$$m_{\text{top}} = 172.5 \text{ GeV} , \quad (4.2)$$

$$M_Z = (91.1876 \pm 2.4952) \text{ GeV} , M_W = (80.403 \pm 2.141) \text{ GeV} . \quad (4.3)$$

Single top-quark samples were produced with ACERMC, but spin correlations were not taken into account. The Z/W -boson samples were generated with ALPGEN with separate parton multiplicities in the final state. The Z -boson sample also takes the interference between Z/γ into account, but a phase space cut on the invariant dilepton mass of $m_{ll} > 40 \text{ GeV}$ enhances the pure Z -boson production. For the diboson samples HERWIG was used.

5. Object Identification, Reconstruction and Object Selection for the Analysis at $\sqrt{s} = 10 \text{ TeV}$

In this chapter the algorithms are described that are used to identify and reconstruct the analysis objects. For the cross-section measurement electrons, muons, jets and the \cancel{E}_T need to be identified and reconstructed with the highest efficiency and purity. These are important performance figures for the algorithms. For each object also the calibration schemes are listed as well as data-driven in-situ calibration schemes. The algorithms work individually, so that there is some overlap between the objects. This overlap must be removed prior to the object selection. While most of the algorithms and their performance presented here were done on samples at $\sqrt{s} = 14 \text{ TeV}$, the algorithm steps are still valid. The object selection cuts, however, are specifically chosen for this cross section study at $\sqrt{s} = 10 \text{ TeV}$. The cuts remove instrumental background objects efficiently and the purity of the found objects is high. In addition the trigger algorithms are shortly described as well as methods to determine the luminosity.

5.1. Electrons

Electrons and photons are both stopped inside the electromagnetic calorimeter and produce similar shaped depositions. Their identification steps are very similar and mainly deviate after the matching of the electromagnetic cluster to a track. However, Bremsstrahlung photons can cause electrons to be identified as photons or photon conversion in the inner detector material can cause the reverse effect.

Electron identification and reconstruction

The electron finding algorithm uses a sliding window technique [207] to find and reconstruct electromagnetic clusters. The first step is the tower building with cells of the electromagnetic calorimeter. Over a grid of $N_\eta \times N_\phi = 200 \times 256$ elements of $\Delta\eta \times \Delta\phi = 0.025 \times 0.025$ size all cells with $|\eta| < 2.5$ in all layers in this window

are summed up to a tower¹. A window of 5×7 is moved around and the sum of the cell energies should be a local maximum and above a threshold. The position of this pre-cluster is the energy-weighted position of the cells in a smaller concentric 3×3 window. Duplicate pre-clusters are searched for within a window of 2×2 .

The energy is then summed up using the pre-cluster position as a seed for the cells in the cell-middle layers². Then successively the energy is summed up in the strips, pre-shower and back layers³. The total energy of the cluster is $E_{\text{reco}} = A(B + W_{\text{ps}}E_{\text{ps}} + E_1 + E_2 + W_3E_3)$, a linear, η dependent, weighted sum of the contributions from the presampler E_{ps} and the three calorimeter layers $E_{1\dots3}$. A is a scaling term and B corrects for energy losses before the calorimeter. All weights are determined by the minimisation of $(E_{\text{true}} - E_{\text{reco}})^2 / \sigma(E_{\text{true}})^2$ with the true energy E_{true} taken from single particle MC simulations.

The identification of an electron requires a matching track in $\Delta\eta \times \Delta\phi = 0.05 \times 0.10$ and a ratio of the track momentum and cluster energy of $E/p < 10$. The track is also compared to the tracks that were found to be converted photons and thus such electromagnetic clusters are identified as photons instead.

Electron energy reconstruction performance

The performance [208] of this method shows that the central value of the energy measurement is reconstructed with a high precision ($\sim 3 \cdot 10^{-4}$) whereas the distribution $E_{\text{reco}} - E_{\text{true}}$ is not a Gaussian and has a tail to the lower end. The distribution becomes wider with increasing $|\eta|$ and with increasing amount of material in front of the calorimeter. Figures 5.1 and 5.2 show the energy resolution $\sigma(E_{\text{reco}} - E_{\text{true}}) / E_{\text{true}}$ and energy linearity $(E_{\text{reco}} - E_{\text{true}}) / E_{\text{true}}$ for electrons (and photons). The parametrisation of the energy resolution $\sigma_E / E \propto a / \sqrt{E}$ yields $a = (10.17 \pm 0.33)\%$ for the barrel and $a = (14.5 \pm 1.0)\%$ for the end-cap region. The calorimeter performance in the region around the gap between $1.37 < |\eta| < 1.52$ is clearly degraded.

Electron in-situ calibration

It is planned [208, 209] to have an in-situ calibration procedure with real $Z \rightarrow e^+e^-$ events. This is done with a first-order parametrisation of the energy calibration $E_i^{\text{reco}} = E_i^{\text{true}} \cdot (1 + \alpha_i)$ in a certain region i . With a proper modelling of the Z -boson line shape with a Breit-Wigner and a parametrisation for the calorimeter resolution, the factors α_i can be extracted. The procedure enables the inter-calibration of the calorimeter regions to a level of 0.7% for the global constant term only with a small

¹Cells over several towers are split into appropriate fractions.

²In a window of $N_\eta \times N_\phi = 3 \times 5$ in the barrel and 5×5 in the end-cap

³Different window sizes and the bary-centre position of the previous layer is used as the seed position for the energy summing in a given layer.

bias of 0.2%. Additionally, the absolute electromagnetic scale can be determined to an accuracy of $\sim 0.1\%$.

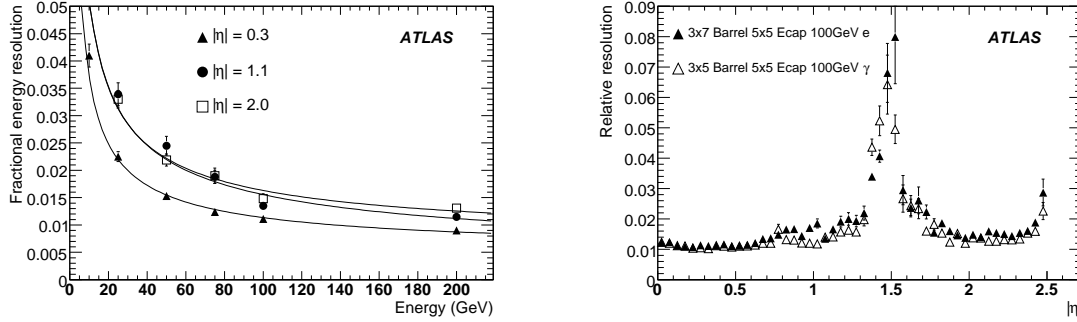


Figure 5.1.: Energy resolution $\sigma(E_{\text{reco}} - E_{\text{true}})/E_{\text{true}}$ for electrons as a function of p_T at different fixed $|\eta|$ positions (left) and of $|\eta|$ for 100 GeV electrons (right, filled triangles), for photons (open triangle) [208].

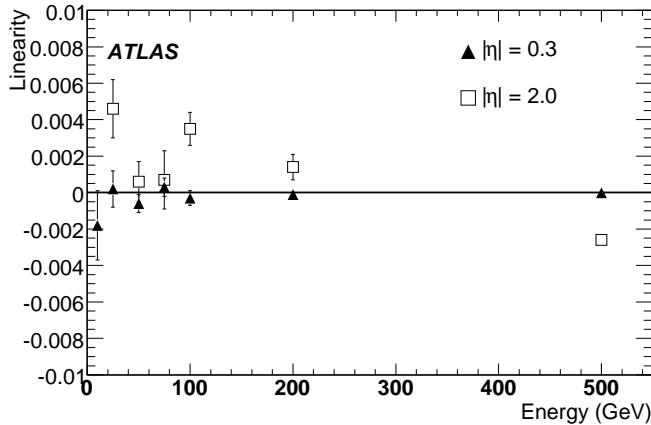


Figure 5.2.: The linearity $(E_{\text{reco}} - E_{\text{true}})/E_{\text{true}}$ for electrons versus p_T for two different $|\eta|$ regions [208].

There are also two additional electron identification methods for low- p_T electrons that use tracks as identification seeds [208]. The other algorithm is for forward electrons and it uses the information from the calorimeters only due to the lack of tracking coverage [208, 207].

Electron quality cuts

For high- p_T electrons cut-based quality criteria are used to classify electrons as loose, medium and tight electrons. The quality cuts are successive cuts, so that e.g. tight electrons are also medium and loose electrons.

The loose cuts provide an excellent identification efficiency, but have a low background rejection. It is based on the information from the calorimeter only⁴. The acceptance is restricted to $|\eta| < 2.47^5$, the hadronic leakage is calculated from the E_T -ratio in the first sampling calorimeter to the E_T in the electromagnetic cluster. Shower-shape variables use only middle-layer cells. A certain ratio of cell energies between a smaller and a larger window is required⁶.

The medium electron quality adds cuts on the strip layer of the electromagnetic calorimeter and some tracking variables. The strip-based cuts reject $\pi_0 \rightarrow \gamma\gamma$ decays by searching for two maxima in the strip-energy deposition. Also the ratio between the cluster energy and the energy of the second maxima is taken into account, as well as the shower width and structure. The tracking cuts are based on the number of hits in the pixel detector, the number in the pixel and the SCT detector and on the transverse impact parameter.

The tight cuts include the medium cuts and in addition cuts on the number of vertexing-layer hits, the number of hits in the TRT, the ratio of high-threshold hits to the total number of hits, the distance of the matching track to the cluster position in η and ϕ and the ratio E/p between the track momentum and the cluster energy. The tight cuts come in two variants, one with an additional calorimeter isolation cut (tight isol.) and one with a tighter cut on the TRT hits (tight TRT).

The efficiencies for electrons from different sources in a dijet sample are summarised in Table 5.1 for electrons with $E_T > 17$ GeV. It generally shows that with increasing quality cuts non-isolated electrons from heavy-flavour decays are rejected further while retaining a good efficiency for isolated electrons.

Table 5.1.: Efficiency of different electron quality cuts for different electron sources in a dijet sample and $E_T > 17$ GeV. Also the jet rejection is given, which is the inverse of the jet efficiency [208].

Quality Cut	$Z \rightarrow e^+e^-$ efficiency [%]	$b, c \rightarrow e$ efficiency [%]	Jet rejection
Loose	87.96 ± 0.07	50.8 ± 0.5	567 ± 1
Medium	77.29 ± 0.06	30.7 ± 0.5	2184 ± 13
Tight (TRT)	61.66 ± 0.07	22.5 ± 0.4	$(8.9 \pm 0.3) \cdot 10^4$
Tight (isol.)	64.22 ± 0.07	17.3 ± 0.4	$(9.8 \pm 0.4) \cdot 10^4$

⁴The track match is still required, but there are no further quality cuts on the track.

⁵Although the actual tracker and calorimeter coverage is up to $|\eta| < 2.5$, the range leaves out the last calorimeter element, avoids edge effects and maintains an uniform efficiency across the acceptance region.

⁶The small window has a size of $N_\eta \times N_\phi = 3 \times 7$ and 3×3 and the large window has a size of $N_\eta \times N_\phi = 7 \times 7$ and 3×7 for the barrel and end-cap region, respectively.

Finally, instead of a cut-based electron identification, also multivariate algorithms [208] are available for the electron identification.

Electron isolation

Isolation from energy deposits can be required in order to separate electrons that emerge from hard-processes, such as W/Z -boson or $t\bar{t}$ decays from electrons from heavy-flavour decay that are accompanied by further hadronic decay products. The isolation can also help to improve the quality and purity of the electron identification, since the isolated electron is usually contained in a less busy and unambiguous environment. The isolation of the electron can be calculated from the electromagnetic cell energies in a hollow cone of various radii $\Delta\mathcal{R} = 0.1$ to $\Delta\mathcal{R} = 0.4$. The inner cone corresponds to the energy deposited by the electron itself and has a size of $\Delta\eta \times \Delta\phi = 0.125 \times 0.175$. This isolation with an outer cone-radius of $\Delta\mathcal{R} = 0.2$ is used for the tight electron-quality cut.

5.2. Muons

The muon reconstruction and identification algorithms that are used at ATLAS find three categories of muons with a $p_T > 3$ GeV: Standalone muons are reconstructed from muon chamber hits only, combined muons are standalone muons combined with an inner detector track and tagged muons are formed by inner detector tracks combined with muons chamber hits from muons that did not cross the whole muon system. For each category two families of algorithms exist, the STACO [210] and the MUID [211] family. The following algorithms belong to the STACO family: MUONBOY and MUTAG. MOORE [212] and MUGIRL [213] belong to the MUID family.

Muon identification and reconstruction

The algorithms MUONBOY and MOORE reconstruct tracks from the muon stations only. MUONBOY uses seeds from the trigger chambers to identify regions of activity. The hits are combined into local track segments via pattern recognition algorithms and the local track segments are combined to a track candidate. MOORE uses the same seeds, but performs the track reconstruction with IPATREC, an inner detector tracking algorithm.

An extrapolation back to the interaction point must be performed. It must take the energy loss and the multiple scattering of the muon in the calorimeter into account. MUONBOY extrapolates the tracks based on the calorimeter material that the muon crossed. MOORE additionally exploits the energy measurements along the

extrapolated track⁷. The $|\eta|$ -coverage for standalone muons is slightly higher than for muons with an inner detector track, but it suffers from the holes in the muon system. The efficiency for low momentum muons is also reduced since they do not traverse all three muon layers. Still, non-prompt muons from π or K decays can only be found with the standalone algorithms.

Combined muons are composed of tracks from the inner detector and muon spectrometer tracks. The measure for this matching is the following χ^2 -quantity:

$$\chi_{\text{match}}^2 = (\mathbf{T}_{\text{MS}} - \mathbf{T}_{\text{ID}})^T (\mathbf{C}_{\text{ID}} + \mathbf{C}_{\text{MS}})^{-1} (\mathbf{T}_{\text{MS}} - \mathbf{T}_{\text{ID}}) \quad (5.1)$$

where \mathbf{T} denotes the vector of track parameters and \mathbf{C} its covariance matrix. The subscripts ID and MS denote tracks from the inner detector and the muon system, respectively. The tracks from the muon system have been extrapolated into the inner detector region considering energy loss and multiple scattering in the calorimeter material. The combined track \mathbf{T} is constructed by the STACO algorithms in a statistical combination:

$$\mathbf{T} = (\mathbf{C}_{\text{ID}}^{-1} + \mathbf{C}_{\text{MS}}^{-1})^{-1} (\mathbf{C}_{\text{ID}}^{-1} \mathbf{T}_{\text{ID}} + \mathbf{C}_{\text{MS}}^{-1} \mathbf{T}_{\text{MS}}) \quad (5.2)$$

The combined track that is formed by the MUID algorithms is a refit of the matching tracks. It starts from the inner detector track vector and covariance matrix and adds the information of the outer track. The track fit again takes the energy loss and multiple scattering in the calorimeter into account.

The tagging algorithms MUTAG and MUGIRL were developed to find low- p_T muons that do not cross the entire muon system. Tagged muons are made of tracks from the inner tracker and are extrapolated to the first muon layer where hits matching to the track are searched for. MUTAG uses a χ^2 measure to find the hits in the muon stations that are closest to the extrapolated track, whereas MUGIRL uses an artificial neural network to define a discriminant that separates different hit-to-extrapolated-track hypotheses. In both cases the track is tagged as a muon and the kinematics are taken from the track only⁸. MUTAG uses inner detector tracks that were not used in any other STACO algorithm whereas MUGIRL uses all tracks.

Overlap between different muons are only removed within one family. In general standalone muons are not recorded again if the muon is also part of a combined muon. If there is more than one combined muon with the same outer muon track, one of them is marked as “best match”. The overlap between MUGIRL and other MUID muons are removed only if they have the same inner detector track.

⁷If the energy deposits are higher than the expected energy loss and if the muon is isolated.

⁸There are developments ongoing that expand the matching to hits in more than one layer and a track refit is performed afterwards.

Muon reconstruction performance

The performance is presented here only for combined muons, since these will be used in the following study⁹. The performance was evaluated with different samples representing different environments for the muon algorithms. The first is a $t\bar{t}$ sample with the distinction between muons that arise from a W -boson decay ($t\bar{t}$ direct sample) and that arise from heavy-flavour decay ($t\bar{t}$ indirect). Further, the $t\bar{t}$ -sample was overlaid with a background sample to simulate the expected effects of pile-up and cavern background at a luminosity of $\mathcal{L}_{\text{inst.}}=10^{33} \text{ cm}^{-2}\text{s}^{-1}$. Also a sample with Z' with a mass of 2 TeV was used that has been filtered for a dimuon invariant mass of $m_{\mu\mu} > 500 \text{ GeV}$. Another sample contains low- p_T muons from J/ψ decays. To match the reconstructed muons to true muons two quantities were defined. These are the reference distance

$$D_{\text{ref}} = \sqrt{(\Delta\phi/0.005)^2 + (\Delta\eta/0.005)^2 + ((\Delta p_T/p_{T,\text{reco}})/0.03)^2} \quad (5.3)$$

and the evaluation distance

$$D_{\text{eva}} = \sqrt{(\mathbf{T}_{\text{reco}} - \mathbf{T}_{\text{true}})^T \mathbf{C}_{\text{reco}}^{-1} (\mathbf{T}_{\text{reco}} - \mathbf{T}_{\text{true}})} \quad (5.4)$$

where the momentum $p_{T,\text{true/reco}}$ is a signed value. The matching requires $D_{\text{eva}} < 1000$ and $D_{\text{ref}} < 100$, which corresponds to $|\Delta\eta| < 0.5$, $|\Delta\phi| < 0.5$ and, for same sign matches, $p_{T,\text{reco}} > 0.25 \cdot p_{T,\text{true}}$ or for opposite sign matches $p_{T,\text{reco}} > 0.5 \cdot p_{T,\text{true}}$. For each true muon only the reconstructed muon with the smallest D_{ref} is kept. A tighter matching criteria is also used (good) if $D_{\text{eva}} < 4.5$. A fake muon is a reconstructed muon that has no true muon match within the tracking coverage.

Table 5.2 summarises the combined muon performance. For the fake probability a cut on the muons of $p_T > 20 \text{ GeV}$ was required in addition. The performance between the STACO and the MUID algorithms is quite similar. While the STACO algorithm has a higher efficiency, the fake rate seems to be smaller for the MUID algorithm.

Figure 5.3 shows the muon efficiency for the $t\bar{t}$ -direct sample versus η and Figure 5.4 shows the muon p_T resolution in bins of p_T and η . The holes in the muon spectrometer coverage can be clearly seen as well as the transition region between barrel and end-cap. The charge misidentification rate is around 0.01%.

Muon in-situ calibration

The in-situ calibration methods [208] for muons include the determination of the energy loss of the muons in the calorimeter, the momentum scale and the momen-

⁹For a full overview of the performance of all muon algorithms see [208].

Table 5.2.: Combined muon performance of the STACO and MUID algorithms for different physics samples [208]. “found” refers to a found match, “good” refers to a found match with tighter cuts and fake muons are muons without a truth match inside the tracking volume and a $p_T > 20$ GeV.

Sample	STACO			MUID		
	Efficiency		fake	Efficiency		
	found	good		found	good	fake
$t\bar{t}$ direct	0.943	0.875	0.34%	0.926	0.877	0.05%
$t\bar{t}$ indirect	0.933	0.767		0.888	0.748	
$t\bar{t}$ direct, high \mathcal{L}	0.941	0.871	0.43%	0.904	0.854	0.11%
Z'	0.910	0.824	0.52%	0.872	0.811	0.31%
J/ψ	0.943	0.873	0.01%	0.793	0.741	0.0%

tum resolution. Again, Z -boson events are used for this purpose. The energy loss correction can be found by a minimisation of

$$\chi^2 = \sum_{\text{dimuon pairs } k} \left(\frac{(p_{\text{corr},+,k} + p_{\text{corr},-,k})^2 - M_Z^2}{\sigma_k^2} \right) \quad (5.5)$$

where σ_k is the expected resolution for the Z -boson mass measurement and $p_{\text{corr},\pm,k}$ denotes the corrected momentum measurements that were corrected for tower dependent constants $E_{\text{rec,corr,tower}} = E_{\text{rec,tower}} + \delta E_{\text{corr,tower}}$. The $\delta E_{\text{corr,tower}}$ represent the correction for the energy loss of the muons. In a second step the momentum is corrected by $p_{T,\text{corr}} = \alpha \cdot (p_T - \delta p_T)$, where α represents the scale factor and δp_T accounts for the underestimation of the momentum resolution. The δp_T is drawn from a Gaussian distribution with a width equal to the momentum resolution $\sigma_{\text{res,reco}}$. Both values α and $\sigma_{\text{res,reco}}$ are determined from a line shape fit to the invariant mass distribution expected from the MC distribution.

Muon isolation

Similar calorimeter isolation variables are available for muons as they are for electrons. For muons two categories of isolation are available, track and calorimeter isolation. Calorimeter isolation is calculated from the energy depositions in the calorimeters in a cone with a defined $\Delta\mathcal{R}$ radius. To account for the energy depositions of the muon itself, the energy loss of the muon is subtracted from the calorimeter energy sum. The energy loss is calculated from a p_T and $|\eta|$ -dependent energy loss function [214] that treats the muon as a minimum ionising particle, including the relativistic rise and radiative effects. Track based isolation variables are

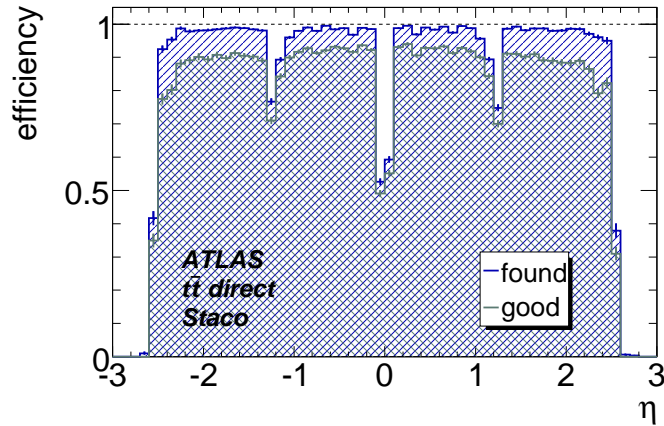


Figure 5.3.: Muon efficiency versus η for STACO muons and two different quality cuts (good quality muons have a lower efficiency) [208].

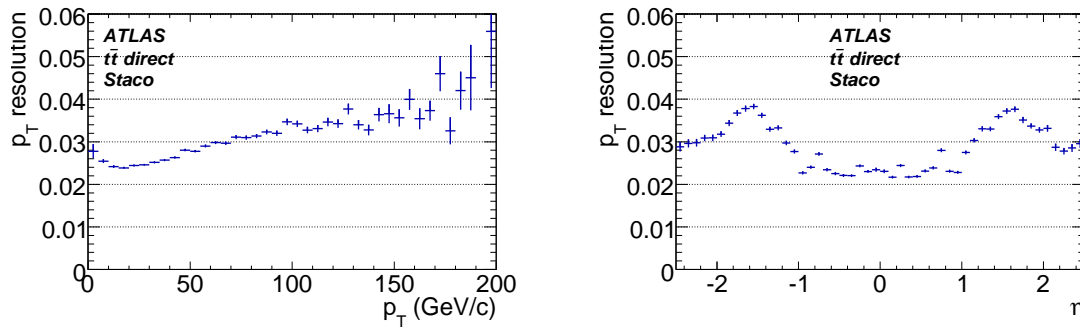


Figure 5.4.: Muon p_T resolution $|\Delta p_T|/p_T$ in bins of p_T (left) and η (right) [208].

the number of inner detector tracks in a cone around the muon and the p_T -sum of the tracks within a cone.

5.3. Jets

A jet is the collection of particles that emerges from the fragmentation and hadronisation of a parton. On reconstruction level a jet is an object that attempts to represent the parton by its visible final state products. There is no universal method that correctly and unambiguously assigns all particles of a quark or gluon to a single object. The assignment is also problematic from a theoretical point of view, if e.g. colour exchange between two quarks is taken into account, which can lead to the common radiation of gluons.

Jet algorithms at ATLAS

There are theoretical guidelines for a jet finding and building algorithms [215, 216], so that there is compatibility between the theoretical jet definition and the jet formed by reconstruction objects such as tracks or calorimeter cells.

A jet algorithm has to be infrared, collinear safe and order independent. Infrared safety means that any soft particle not originating from the fragmentation of a hard scattered parton does not influence the number of reconstructed jets¹⁰. Collinear safety means that a jet can be reconstructed if a large fraction of the transverse momentum is carried by a single particle or if the particle is split in two collinear particles. Order independence means that the same jet should be reconstructed on parton, particle and detector level.

The jet algorithms at ATLAS in general start with the building of proto-jets. As input objects either calorimeter clusters, tracks or generated true particles can be used, these are the so-called track jets and true particle jets, respectively. A quantity is defined that measures the “closeness” of objects that form a jet object. Then the proto-jets are merged or split according to some procedure in case that two proto-jets are too close together or a sub-structure was found within one proto-jet. The final step is the recombination of the objects to a jet, i.e. kinematics of the objects are combined to form the kinematics of a single jet. The recombination step for all ATLAS jet algorithms is the same, it adds the four-vectors of the objects to the final jet four-vector.

The widely used jet algorithm so far at ATLAS is the iterative seeded cone algorithm [216]. The seed is an object with the highest p_T and above the seed threshold. Starting from the seed all objects within the distance of $\Delta\mathcal{R} < R_{\text{cone}}$ are summed to the seed. The new position of this combination of objects is calculated and the objects are recollected according to their $\Delta\mathcal{R}$ distance. This procedure is continued until a stable proto-jet position is reached. Upon reconstruction of a stable jet, only the seed is removed from the list and the jet finding starts with the next available seed. Thus different jets can share constituent objects. In ATLAS a p_T -threshold of 1 GeV and cone sizes of $R_{\text{cone}} = 0.4$ and $R_{\text{cone}} = 0.7$ are used.

The merge and split procedure can partially recover the infra-red safety of the algorithm. If two jets share objects with a p_T fraction of more than 50% of the less energetic jet, they are merged. If the fraction is below 50% the shared objects are distributed among the two jets.

Another jet algorithm used at ATLAS is the k_T -jet algorithm [217, 218] that uses the relative transverse momentum as a distance measure between object i and j : $d_{ij} = \min(p_{T,i}^2, p_{T,j}^2) \cdot \Delta\mathcal{R}_{ij}^2 / R^2$. A second measure of distance is the transverse momentum of the object $d_i = p_{T,i}^2$. The only free parameter is the distance scaling R , at ATLAS $R = 0.4$ and $R = 0.7$ are commonly used. The procedure is then as

¹⁰E.g. the addition of soft particles between two jets should not cause the merging of the two originally separate jets.

follows: The minimum of all d_{ij} and d_i is calculated. If the minimum is from the list of d_i then this object is a jet and removed from the lists. If the minimum is from the list of d_{ij} , the two objects i and j are combined to a new object k . The objects i and j are removed from the lists and the object k is added to the lists. The recombination starts again until no objects are left. The advantage of this algorithm is that it is infra-red and collinear safe, the disadvantage is that the combination procedure is somewhat slower than the cone algorithm. There are also variants of this algorithm that introduce an additional cut-off parameter d_{cut} or use a different measure between two objects (such as the anti- k_T algorithm where $d_i = p_{T,i}^{-2}$).

Calorimeter objects as inputs for the jet algorithms

As inputs for the jets in real data two types of calorimetric objects are available [208]. Calorimeter towers are groups of electromagnetic and hadronic cells that are projected onto a grid¹¹ of $\Delta\eta \times \Delta\phi = 0.1 \times 0.1$ up to $|\eta| < 5$ such that the total number of towers is 6400. The threshold for the cluster energy is 15 GeV.

Topological clusters are groups of cells that start from a seed cell above a certain threshold in terms of energy-to-noise-ratio $E_{\text{cell}}/\sigma_{\text{noise}} > 4$. Directly neighbouring cells in all three dimensions are added to the seed and next-to-neighbouring cells are only added if they pass a lower threshold of $E_{\text{cell}}/\sigma_{\text{noise}} > 2$. Finally, a ring of guard cells with $E_{\text{cell}}/\sigma_{\text{noise}} > 0$ is added to the cluster¹². Afterwards a splitting algorithm is applied if more than one local maximum is found.

The four momentum that is assigned to a tower or to a cluster is calculated from the energy in the calorimeter and the position of the centre of the towers or the energy-weighted centre in case of topological cluster assuming a massless pseudo-particle.

Calibration and Performance of Jets

The calibration of the jets follows different strategies for the two types of calorimetric objects [208]. The calorimeter towers are only calibrated at the electromagnetic scale, i.e. there is only a correction of the electronic signal. A hadronic calibration is only applied after the jet building. This accounts for the effect that the ATLAS calorimeter is non-compensating and hadronic processes have a lower signal density than electromagnetic processes. Hence a reweighting of the signal is applied [219, 220], which depends on the signal density and location. The reweighted energy is $E = \sum_{i=\text{cells}} w_i(\rho_i, \vec{X}_i) \cdot E_i$ with a weight¹³ w_i depending on the cell energy density ρ_i

¹¹Cells that are not projective or do not fit into the grid contribute fractional to the energy of a tower.

¹²This is usually denoted as 4/2/0 scheme.

¹³To reduce the number of weights, the cells are divided into larger regions that partially exploit the longitudinal segmentation or the fact that the calorimeter cells are projective.

and the position \vec{X}_i . The weights are derived from a minimisation of the difference between the reconstructed jet energy and the closest true particle jet energy from QCD MC samples. The jets were reconstructed with the cone algorithm with a cone radius of 0.7 and a seed threshold of $E_T = 1$ GeV. The weights cannot account for non-linear effects such as energy loss due to particles being bent by the magnets out of the jet cone or energy losses in inactive regions of the calorimeter. This is done by additional corrections, which are E_T , η and jet algorithm dependent. Figures 5.5 show the E and $|\eta|$ dependence of the energy linearity of this calibration procedure for cone jets with a cone radius of 0.7. Linearity can be achieved over a large range of E and $|\eta|$. Only for low- p_T jets and in crack regions, deviations from the perfect calibration can be seen. Similar performance can be achieved for jets with a cone radius of 0.4 as it is used in physics analyses.

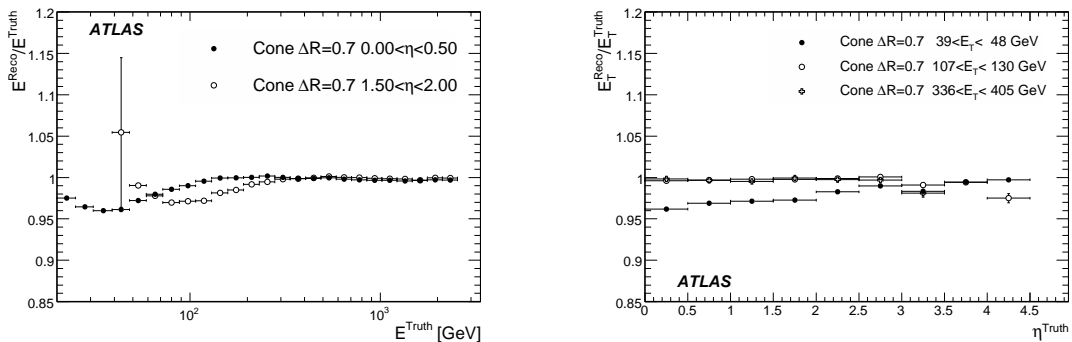


Figure 5.5.: Jet energy linearity versus E (left) and versus $|\eta|$ (right) for cone jets with a cone radius of $\Delta\mathcal{R} = 0.7$ and different $|\eta|$ regions or E_T ranges, respectively [208].

The jet energy resolution can be expressed as

$$\frac{\sigma_E}{E} = \frac{a}{\sqrt{E} [\text{GeV}]} \oplus b \oplus \frac{c}{E}, \quad (5.6)$$

where the sampling term a is due to statistical fluctuations in the energy deposits, the constant term b reflects the non-compensating nature of the calorimeter and c is the noise term. Table 5.3 shows the resolution contributions for cone and k_T -jets and Figures 5.6 [208] show the resolution dependence on p_T and $|\eta|$.

Finally, the jet is calibrated to the particle level, so that the jet resembles as much as possible the hard process quark from which the jet originated. This is done at the analysis stage and effects from the physics environment have to be applied depending on the specific analysis. Both steps can be achieved e.g. with a kinematically constrained system, so that the jet energy can be fit and the reconstructed jet energy can be calibrated against it.

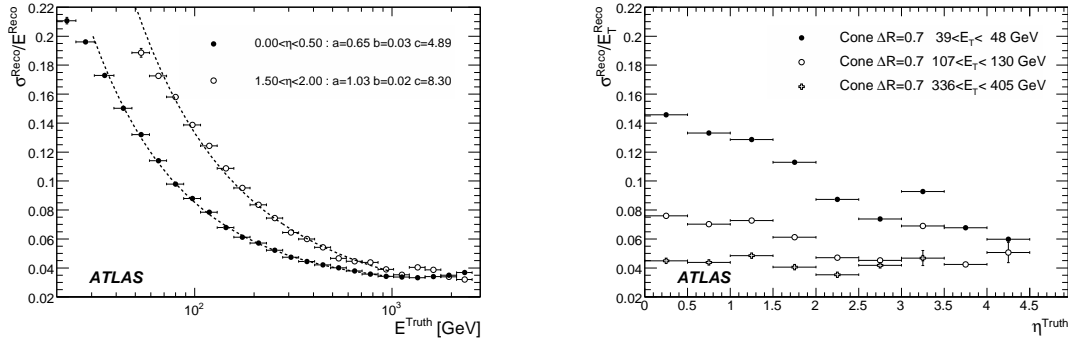


Figure 5.6.: Jet energy resolution for cone jets with a cone radius of $\Delta\mathcal{R} = 0.7$ versus E (left) and versus $|\eta|$ (right) [208].

Table 5.3.: Contribution to the jet energy resolution $\frac{\sigma_E}{E} = \frac{a}{\sqrt{E [\text{GeV}]}} \oplus b \oplus \frac{c}{E}$ [208].

Algorithm	$0 < \eta < 0.5$			$1.50 < \eta < 2.00$		
	a [%]	b [%]	c [GeV]	a [%]	b [%]	c [GeV]
Cone $R = 0.7$	64 ± 4	2.6 ± 0.1	4.9 ± 0.5	103 ± 10	2.6 ± 0.8	8 ± 1
k_T $R = 0.6$	68 ± 5	2.5 ± 0.2	6.3 ± 0.5	110 ± 1	1 ± 1	12.2 ± 2.5

The topological cluster jets are calibrated with an alternative procedure already at the jet building stage. The local hadron calibration [221] starts with a classification of the cluster into an electromagnetic, hadronic or noise cluster based on its location and shape. This classification works for 90% of the energy of charged/neutral pions being classified as hadronic/electromagnetic shower, respectively. Then according to the classification and signal density, weights are assigned to the clusters and corrections for losses in inactive areas of the detector and out-of-cone corrections are applied in bins of $|\eta|$, cluster energy and cell energy density. All the corrections are based on MC simulated detector response of single pions.

Another alternative calibration method restores the jet energy on a statistical basis. It can be applied after all the previously described calibration schemes. They are based on the response of a true jet with p_T^{true} in the detector, which is expressed as a conditional probability density function, $P(p_T^{\text{reco}}|p_T^{\text{true}})$, which is the probability of obtaining a jet with reconstructed p_T^{reco} given the true jet p_T^{true} . The reverse conditional probability in the Bayesian formalism is given as:

$$P(p_T^{\text{true}}|p_T^{\text{reco}}) = \frac{P(p_T^{\text{reco}}|p_T^{\text{true}})P(p_T^{\text{true}})}{\int P(p_T^{\text{reco}}|p_T^{\text{true}})P(p_T^{\text{true}})}. \quad (5.7)$$

The numerical inversion [222] describes how to obtain the response function and the true $P(p_T^{\text{true}})$ distribution in an iterative way, since the probability functions are not necessarily known from the beginning. It models the calibrated p_T as $p_T^{\text{reco,calib}} = R_{\text{reco} \rightarrow \text{true}}^{\text{est}}(p_T^{\text{reco}}) \cdot p_T^{\text{reco}}$ with a response function $R_{\text{reco} \rightarrow \text{true}}^{\text{est}}$ and a given p_T^{true} .

Jet in-situ calibration

In-situ calibration strategies using γ/Z +jet events were also developed. Events with leptonically decaying Z -bosons can be easily and almost background free selected in the $Z \rightarrow e^+e^-$ and $Z \rightarrow \mu^+\mu^-$ decay channels. Events with single photons suffer more from QCD background, but with proper selection cuts a clean and bias-free sample can be selected. In both cases it is expected that the calibration of the electromagnetic energy scale for the leptons and photons is in a good shape. The calibration exploits the p_T -balance between the probe object and the leading jet. The presence of additional jets is one difficulty of the calibration and requires either the inclusion of the additional jets in the p_T balance or it requires additional constraints such as the jet to be back-to-back with the probing object within a small tolerance. The former has the difficulty of assigning the correction to a particular jet, the latter lowers the statistics. The choice of the jet algorithm introduces systematic effects, e.g. the cone algorithms suffer more from out-of-cone losses than k_T algorithms.

The jets can also be calibrated with QCD events [208]. This is beneficial for the relative calibration of the jet response and when high statistics is needed. The uniformity of the events in ϕ can be checked by looking at the jet rate as a function of ϕ . Deviations from the uniformity point to dead cells and deviations from the expected statistical spread hint at the mis-calibration of a certain region. The uniform response in the $|\eta|$ direction can be checked with the p_T -balance between two jets. Multiple jets have to be taken into account in the balancing method for high- p_T jets, so that the highest- p_T jet is calibrated against the other low- p_T jets.

5.4. Missing Transverse Energy

The *missing transverse energy* (\cancel{E}_T) is the only way to recover information about non-interacting particles. Although the collision energy is known, the actual energy in the hard-scattering process cannot be predicted, so that the total momentum in the beam direction of the hard scattering is not known. Thus the only conserved quantity is the transverse momentum that should add to zero. Any deviation from zero is attributed to invisible particles. In the ideal case this is only one particle, such as a neutrino, but in practice also neutral hadrons or mesons in the hadronisation of jets contribute to the missing transverse energy. Finally, also effects such as underlying events, pile-up, electronics noise or leaks in the calorimeter coverage by dead cells, fake additional missing transverse energy.

Cell-based missing transverse energy reconstruction

The cell-based missing transverse energy is the sum of the following terms:

$$\cancel{E}_T = E_T^{\text{calo cells}} + E_T^{\text{muons}} + E_T^{\text{cryo}} \quad (5.8)$$

$$\cancel{E}_T = E^{\text{unassigned cells}} + E_T^{\text{Ref.}} + E_T^{\text{muons}} + E_T^{\text{cryo}} \quad (5.9)$$

The algorithm [208] starts with calorimeter cells that survive a noise suppression procedure. Topological clusters with the default scheme¹⁴ are already optimised to suppress noise. With this already a \cancel{E}_T scale uncertainty of 30% can be achieved. The next contribution E_T^{muons} that has to be taken into account are reconstructed muons. Good quality muons without any p_T cut are taken. In the region covered by tracking ($|\eta| < 2.5$) also a track match is required. The final contribution is the cryostat term that accounts for the energy loss in the cryostat between the LAR electromagnetic barrel calorimeter and the hadronic tile-barrel calorimeter. The cryostat term is $E_T^{\text{cryo}} = \sum_{\text{all jets}} E_{\text{jet}}^{\text{Cryo}} = \sum_{\text{all jets}} w^{\text{Cryo}} \sqrt{E_{\text{EM3}} \cdot E_{\text{HAD}}}$. Here w^{cryo} is the calibration weight, which is obtained in the course of the jet calibration, and E_{EM3} and E_{HAD} are the energy measurements of each jet in the third EM calorimeter layer and the first tile-barrel layer, respectively. The cryostat term is important for high- p_T jets and it contributes $\sim 5\%$ per jet for jets above 500 GeV.

The final step in the \cancel{E}_T measurement is the refinement with reconstructed objects that can be associated to calorimeter cells. The order of the objects are electrons, photons, muons, hadronically decaying tau leptons, b -quark jets and light quark jets. The energy measurement of a cell that is associated with an object is then replaced with the energy measurement of the object. If a cell is already associated to another kind of object the association of this object with a lower order is dropped. If a cell is shared by another object of the same kind, the cell energy is calculated from a weighted sum of the energies of the sharing objects. Corrections on the object energies such as out-of-cone corrections or corrections that are already accounted for in the \cancel{E}_T measurement are removed before using the object energy measurement. The calibration of these objects is known to a better precision than the global calibration of the calorimeter cells, so that this improves the \cancel{E}_T measurement.

An alternative method to calculate \cancel{E}_T is the object based reconstruction of \cancel{E}_T that starts from reconstructed objects and remove all the cells that are associated with them [208].

Missing transverse energy performance

The performance of the calorimeter-based and the object-based \cancel{E}_T is very similar [208], so that the evaluation of the performance did not distinguish between the two methods. The linearity of \cancel{E}_T improves with each correction that is applied.

¹⁴4/2/0 scheme

Starting with a systematic bias of 30% for the use of uncalibrated cells, the linearity using calibrated cells and the muon term is around 5%. The linearity was checked to be 1% if the cryostat term is included, except for $W \rightarrow e\nu$. Only with the refinement the \cancel{E}_T linearity can reach 1% also for $W \rightarrow e\nu$. The resolution is best after the last step.

Figures 5.7 show the linearity of the reconstructed \cancel{E}_T for various processes at different average \cancel{E}_T values and for the simulated Higgs boson $A \rightarrow \tau\tau$ over a large range of \cancel{E}_T . Figures 5.8 show the \cancel{E}_T resolution for low $\sum E_T$ and high $\sum E_T$ for various processes. The fit function is roughly $\sigma_{\cancel{E}_T} = a \cdot \sqrt{\sum E_T}$, where a varies between 0.53 and 0.57. For low $\sum E_T$ noise dominates the resolution whereas the constant term in the calorimeter resolution dominates at high $\sum E_T$.

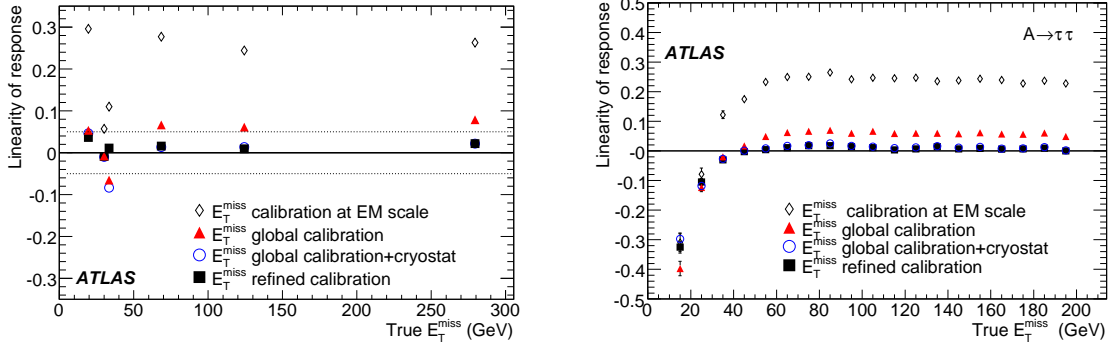


Figure 5.7.: Linearity $(\cancel{E}_T^{\text{True}} - \cancel{E}_T) / \cancel{E}_T^{\text{True}}$ of \cancel{E}_T [208] for the different \cancel{E}_T calibrations various processes that have different average \cancel{E}_T (left) and $A \rightarrow \tau\tau$ processes.

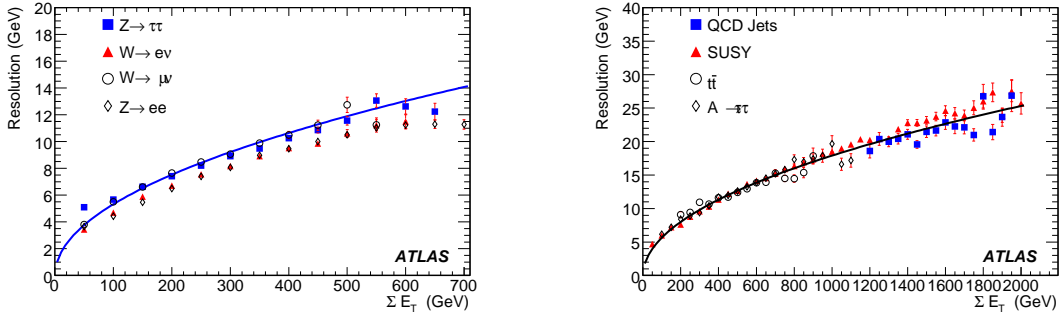


Figure 5.8.: Resolution of \cancel{E}_T [208] for different processes. The resolution is determined from the spread of the $(\cancel{E}_T^{\text{True}} - \cancel{E}_T)$ distribution. In the low- $\sum E_T$ region the resolution $\sigma_{\cancel{E}_T}$ is $0.53/\sqrt{\sum E_T}$ and in the high- $\sum E_T$ it is $0.57/\sqrt{\sum E_T}$.

Fake \cancel{E}_T is another issue for the precise \cancel{E}_T measurement. The sources for fake \cancel{E}_T are various, mainly caused by inefficiencies of the calorimeter. Mis-measurements of

calorimeter objects such as jets, taus, electrons or photons can cause fake \cancel{E}_T . It can be shown that there is a correlation between events with fake \cancel{E}_T and jets pointing to crack regions of the calorimeter. Leakage in the calorimeter can be checked by monitoring certain layers in the calorimeter (e.g. outermost layers of the *Hadronic Tile Calorimeter* (TILECAL) and the HEC) and setting thresholds for energy deposition ratios, so that events with large leakage can be rejected. Instrumental effects such as dead cell regions can also be found by monitoring the fraction of energy deposited in the electromagnetic calorimeter by a jet. Another check is the comparison of reconstructed calorimeter jets with track jets. Fake \cancel{E}_T from muons is caused by falsely identified muons from calorimeter punch-through or it is caused by muon reconstruction inefficiencies.

Missing transverse energy performance in data

The early data performance of \cancel{E}_T can be checked with processes with known size of \cancel{E}_T . High statistics can be obtained from minimum bias events. The mean \cancel{E}_T is 4.3 GeV whereas the true \cancel{E}_T from K/π decays in-flight and decay from charm and bottom hadrons has an average \cancel{E}_T of 0.06 GeV. The higher mean value is the result of the calorimeter resolution and acceptance losses. $Z \rightarrow \tau\tau$ events can be used to further check the \cancel{E}_T performance with an average \cancel{E}_T of 20 GeV and an average $\sum E_T$ of 200 GeV. From the reconstruction of the Z -boson mass peak from the hadronic and leptonic tau the \cancel{E}_T scale can be determined. In events with $Z \rightarrow e^+e^-$ and $Z \rightarrow \mu^+\mu^-$, where no real \cancel{E}_T is expected, it is possible to calculate projections of \cancel{E}_T on the axis that is formed by the sum of the lepton direction vectors. The distribution of the projection along this axis is related to the calibration of \cancel{E}_T whereas the projection orthogonal to this direction is related to the angular resolution. Finally, in complex decay topologies such as the semi-leptonic $t\bar{t}$ events, the true \cancel{E}_T scale can be fit. The system with three jets, one lepton, two constraints on the W -boson mass (for both top-quarks), two constraints on the top-quark mass and \cancel{E}_T can be fit under these constraints and the resulting \cancel{E}_T can be compared to the measured values.

5.5. Trigger Algorithms

Different trigger stages use different strategies for the identification of objects. The L1 uses hardware programmable thresholds to find L1 trigger objects while L2 uses dedicated software algorithms that are optimised for speed and robustness. EF algorithms use almost the same algorithms as the offline analysis. The only difference is the limited use of the detector information and the lower diversity of algorithms that are used.

The naming of the trigger chains are as follows: The trigger names denote the trigger level (L1, L2 and EF), the trigger type (**e** for electromagnetic and **mu** for muon trigger object) and the trigger threshold in GeV. Requirements such as **medium** can be added to the name. Denoted by **I** (for L1 trigger) and **i** (for HLT triggers) is the isolation requirement. For this analysis only the trigger algorithms for electrons and muons are shortly described. The description of the other trigger algorithms can be found in [208].

L1 Trigger algorithms

The calorimeter L1 trigger [223] uses groups of calorimeter cells and towers such that the trigger cells have a granularity of $\Delta\eta \times \Delta\phi \geq 0.1 \times 0.1$ and the number of cells is reduced to ~ 7000 . The data is sent after each bunch crossing to the CTP. The cluster processor makes the decision for electrons/photons and taus in a η -region of $|\eta| < 2.5$. Electron/photons are found by searching all 2×2 cluster cells [224] where at least one of the four possible two-cell sums of nearest-neighbour cells exceeds a certain threshold. If isolation is required, it is determined by the energy deposition in the surrounding 12 electromagnetic and surrounding 12 hadronic cells, as well as by the energy deposition in the 2×2 hadronic cells behind the electromagnetic core cells. To avoid multiple counting, the sum of the electromagnetic and hadronic core cells are required to be a local maximum when compared to the eight overlapping 2×2 neighbours (i.e. all 2×2 cells within a 4×4 region). In total eight thresholds for electron/photon triggers and further eight thresholds for either electron/photon or tau triggers can be programmed.

The muon L1 trigger decision requires at least one hit in the so-called pivot plane that is the second trigger plane in the barrel and the fourth plane in the end-cap. A sagitta measurement is performed with coincident hit patterns in the nearby plane for low- p_T and in the next-nearest plane for high- p_T muons. The distance from the hit and the extrapolated reference-track hit in the non-pivot plane is a measure for the p_T . Figure 5.9 shows some examples of muon hits in the trigger chambers. For each low- p_T and high- p_T muon three thresholds can be defined.

For the jet/energy module in total eight combinations of E_T and window sizes, four total E_T and eight \cancel{E}_T thresholds can be set.

L2 trigger algorithms

After the global OR of all L1 trigger accepts, the information is passed to the L2 algorithms in form of ROIs. The L2 trigger algorithms are optimised for speed and their ability to process only information from the ROIs. Starting with the L2 algorithms also tracking information can be used. The tracking is done in three steps. First the data from the detector is prepared, so that clusters are formed in the pixel and SCT detector that are then converted into space points. Two algorithms,

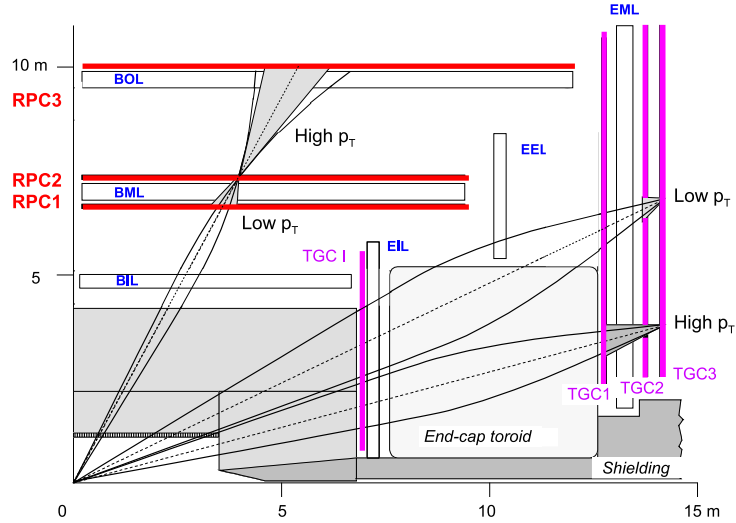


Figure 5.9.: Layout of the muon trigger chambers and an example of muon trigger hits [163]. Low p_T muons are found by hits in the pivot plane and extrapolated into the closest neighbouring layer, high p_T muons are extrapolated into the farthest layer.

IDSCAN and SiTRACK use pattern recognition in the ROIs to form track seeds that are then fit to a track by a Kalman filter [225].

For the electron/photon selection the L2 algorithm selects only cells in a window of $\Delta\eta \times \Delta\phi = 0.4 \times 0.4$ around the electron/photon ROI that was found by the L1 stage. Then the cell with the highest E_T in the second layer of the EM calorimeter is found and a cluster of $\Delta\eta \times \Delta\phi = 0.075 \times 0.175$ is formed around this cell. Several criteria are used to reject EM clusters from jets: the transverse energy of the EM cluster is usually high and the transverse energy in the first hadronic layer is usually small for electromagnetic showers. The ratio of the deposited energies in 3×7 cells and 7×7 cells is typically larger than 80% and there is no substructure in the shower that might come from a π^0 or η decay. Isolated electrons/photons have the energy contained almost in the first maximum while photons from π^0 decays share the energy over the two maxima.

The L2 muon algorithms consist of the MUFast algorithm for track finding and reconstruction with MDT hits and p_T determination with look-up tables, the MUCOMB for fast combination with inner detector tracks and the MUIso algorithm for the discrimination of isolated muons from non-isolated muons. The algorithms run on the full detector granularity, but are restricted to the ROIs. There are also algorithms that try to find tagged muons at L2 to increase the acceptance of muons.

EF trigger algorithms

After the event has passed the L2 trigger stage the results are passed to the EF stage in which mostly offline algorithms are used for the trigger decision.

The track reconstruction at the EF stage uses the new tracking software [226], which is also part of the offline tracking algorithms. It is only limited to the ROI regions and an inside-out approach of the track finding is used. The EF track reconstruction is used for many signatures such as electron, muons, taus and b -quark jets.

For the electrons the offline algorithms are used as much as possible. Also available are requirements on the electron quality and similar cuts as the offline electron selection such as `medium` are possible. For muons adapted offline algorithms are used. This algorithms starts from spectrometer tracks that were found during the L2 stage. Similarly to the offline algorithms the track is extrapolated into the inner detector and then combined with an inner detector track. For electron- and muon-trigger objects isolation can be required in addition.

5.6. Luminosity Determination

The instantaneous luminosity $\mathcal{L}_{\text{inst.}}$ can be defined through the event rate, R , and the corresponding cross section, σ , for the event:

$$\mathcal{L}_{\text{inst.}} = \frac{R}{\sigma}. \quad (5.10)$$

It is the number of incoming particles per area and time. The integrated luminosity $\mathcal{L}_{\text{int.}}$ is the integrated luminosity over time.

The LHC beam parameters can be used to obtain the luminosity:

$$\mathcal{L}_{\text{inst.}} = F \cdot \frac{f \sum_i^{k_b} N_1^i N_2^i}{4\pi \sigma_x^* \sigma_y^*} = F \cdot \frac{f N^2 k_b \gamma}{4\pi \epsilon_N \beta^*}, \quad (5.11)$$

with $F = 0.9$ for the non-zero crossing angle, f the revolution frequency of the beam, $N_{1,2}^i = N$ the number of protons per bunch (for each beam) and the transverse bunch widths $\sigma_{x,y}^*$ at the interaction point. The luminosity can be expressed through the normalised emittance $\epsilon_N = \sigma_x^* \sigma_y^* \gamma / \beta^*$, the Lorentz factor γ and the beam function, β^* , at the interaction point. k_b is the number of bunches. The horizontal and vertical beam sizes have to be determined by sweeping the beams through one another at the interaction point, the so-called Van-der-Meer scans [227]. During the scan the collision rates are measured by the ATLAS luminosity detectors. The shape of the rate function versus the beam displacement can be used to determine the beam sizes. The latest measurement [228, 229] indicates an uncertainty of 11%.

The luminosity for ATLAS can be determined additionally in various ways. One can distinguish between measurements with the ATLAS detector, external measurements with very forward detectors that are not part of the ATLAS detector and luminosity determination with known physics processes. Some of the luminosity determinations are only relative and have to be calibrated with absolute methods. Figure 5.10 shows the different external luminosity monitors and their respective positions.

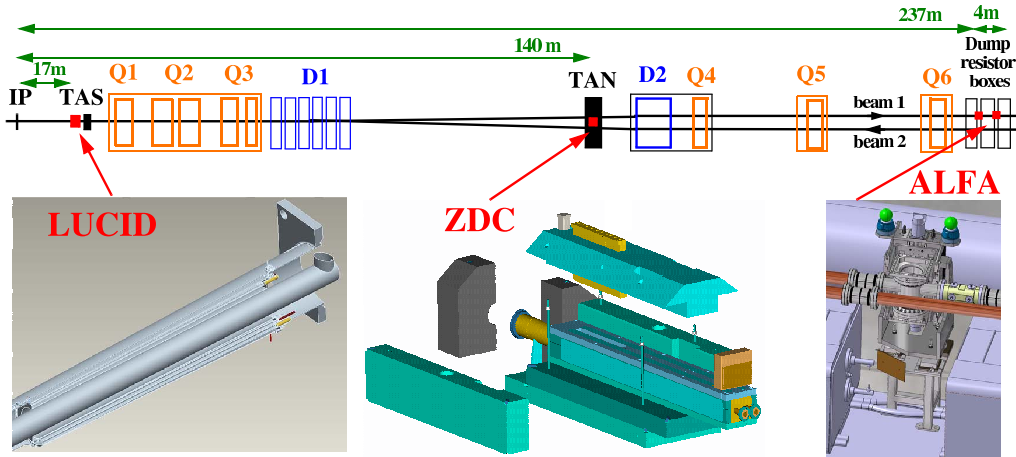


Figure 5.10.: External luminosity monitors for ATLAS [163].

A relative measurement of the luminosity can be made directly with the ATLAS forward detectors, the forward tile-calorimeter and forward LAR. The integrated anode current of photo-multiplier tube and high voltage current, respectively, is a measure of the particle flux and this can be related to the luminosity.

The *Beam Conditions Monitor* (BCM) [230] can also be exploited for the luminosity measurement. It consists of four $1 \times 1 \text{ cm}^2$, $500 \mu\text{m}$ thick diamond sensors, 1.8 m away from the interaction point and 5 cm away from beam axis. The $|\eta|$ -coverage is $3.9 < |\eta| < 4.1$. It has a good timing resolution that is able to resolve single bunch crossings. The amplitude is related to the number of events in the interaction point and this relates to the luminosity. It is well suited for a relative luminosity measurement.

The LUCID¹⁵ detector [231] was built explicitly for luminosity measurement. It is a Čerenkov detector 17 m away from the interaction point, which corresponds to $5.5 < |\eta| < 6.1$. It consists of 1.5 m long and 15 mm diameter Al tubes surrounding the beam pipe at a radial distance of 10 cm with pressurised gas (C_4F_{10}) at $1.2 - 1.4 \text{ bar}$. The time resolution enables the detector to resolve individual bunch crossings. The measurement uses inelastic events and counts the incoming particles from the interaction point to measure a relative luminosity. The pulse height is used

¹⁵Luminosity measurement using a Čerenkov Integrating Detector

as a measure of the number of particles. To reduce background events, the tubes are slightly tilted with respect to the axis parallel to the beam axis such that they point to the interaction region.

The *Absolute Luminosity For ATLAS* (ALFA) detectors [231] are designed to measure the absolute luminosity and to calibrate other luminosity detectors. The detectors are housed in stations at 240 m distance called Roman Pots. It uses elastic proton scattering in the Coulomb-Nuclear interference region¹⁶ to measure the absolute luminosity. The cross section is related to the luminosity by the optical theorem. A special run is needed to reach this region, the so-called high- β^* run, at low luminosity and at a low event rate of 30 Hz. The detectors consist of scintillating fibres that can track particles in a 2D-plane perpendicular to the beam. The fibres are arranged in a stereo $u - v$ geometry and 10 measurement layers are stacked together. The square fibres are 0.5 mm in width and have an active area of $32 \times 32 \text{ mm}^2$. The fibres will be positioned as close as 1 mm to the beam for a measurement with $\Delta\mathcal{L}/\mathcal{L} \sim 2 - 3\%$.

Among the physics processes that are used for relative luminosity are W/Z -boson production by rate counting. The uncertainty can reach $\Delta\mathcal{L}/\mathcal{L} \sim 5 - 10\%$ absolute and $\Delta\mathcal{L}/\mathcal{L} \sim 1 - 5\%$ relative for a range of $\mathcal{L}_{\text{inst.}} > 10^{33} \text{ cm}^{-2}\text{s}^{-1}$. Systematic effects that need to be controlled are the knowledge about the parton distribution functions, acceptance and detector efficiencies for the signal process. At an instantaneous luminosity $\mathcal{L}_{\text{inst.}} = 10^{33} \text{ cm}^{-2}\text{s}^{-1}$ one can reach statistical precision after 10 min only. $ee/\mu\mu$ counting is an alternative relative and absolute method with $\Delta\mathcal{L}/\mathcal{L} \sim 2\%$, but one needs to understand the background processes in addition to the systematic uncertainties that are important for the W/Z -boson rate counting.

The luminosity information is usually stored in blocks, i.e. luminosity is measured over a time interval, usually minutes. This is long enough, so that statistical uncertainty is smaller than systematic uncertainties, but also short enough to assume a constant instantaneous luminosity over time interval. This is given by the interval that is much smaller than the beam luminosity lifetime (up to 14 h). A short luminosity block is also beneficial for the minimisation of data-loss in case of detector problems and data-taking interruptions.

5.7. Object Selection for the analysis at $\sqrt{s} = 10 \text{ TeV}$

This section describes the object selection requirements that are used for this analysis at a centre-of-mass energy of $\sqrt{s} = 10 \text{ TeV}$ and targeted luminosity of $\mathcal{L}_{\text{int.}} = 200 \text{ pb}^{-1}$. From the reconstruction described earlier in this chapter the objects are required to fulfil quality cuts that are optimised for small amounts of data and that are not difficult to calibrate. The object selection was used throughout the analysis if not specified otherwise.

¹⁶Region between the Coulomb-scattering and the strong nuclear scattering region

When comparing the triggered and reconstructed leptons with true leptons from the MC simulation, it is always required that the leptons originate from a W -boson decay or from a tau lepton that originated from a W -boson decay.

5.7.1. Trigger

The trigger algorithms that are used for the trigger decision are described in Section 5.5. This analysis uses the trigger algorithms that allow the identification of electrons and muons. The choice of the exact trigger depends strongly on the luminosity conditions of the LHC. If the trigger rate exceeds a given data budget, the trigger must be prescaled, i.e. only every n th (prescale factor) trigger decision is accepted. This lowers the statistics of the triggered sample.

For the lepton triggers that are foreseen for this analysis a single electron or muon trigger is used. For instantaneous luminosities such as $\mathcal{L}_{\text{inst.}}=10^{32}$ cm⁻²s⁻¹ considered here, the threshold is 15 GeV. Since the trigger requirement is an implicit requirement on the lepton p_T , the threshold is desired to be lower than the offline requirement on the leptons. The offline cut on the p_T should be in a p_T -region in which the trigger efficiency is almost constant. The correction of the event-selection efficiency by the trigger efficiency in this case is simpler and not affected by fluctuations in the efficiency turn-on curve. Also, the use of a single lepton trigger eases the determination of the trigger efficiency from data.

For this study with an instantaneous luminosity of $\mathcal{L}_{\text{inst.}}=10^{32}$ cm⁻²s⁻¹ and for the data amount of integrated luminosity $\mathcal{L}_{\text{int.}}=200$ pb⁻¹ the triggers used have a threshold of 15 GeV. For the channels involving electrons the trigger chain “e15_medium” is used that is triggered by the triggers L1_EM13, L2_e15_medium and EF_e15_medium. For channels with muons the trigger chain “mu15” is used that is based on the triggers L1_mu11, L2_mu15 and EF_mu15. For the $e\mu$ channel an OR combination of both triggers is required.

The efficiencies of the triggers for the $t\bar{t}$ sample are shown in Figure 5.11 for the “e15_medium”. The efficiency is calculated with respect to the electrons selected offline with the selection cuts defined in the following sections. Also, the electrons have to match to a true electron originating from a W -boson (or from a tau lepton that originated from a W -boson decay) within a distance in $\Delta\mathcal{R}$ of 0.05 and to an EF electron trigger object within a $\Delta\mathcal{R}$ of 0.1.

In data the trigger efficiencies for single-lepton triggers will be measured with Z -boson events and the tag-and-probe method. The method can measure the efficiency with a statistical uncertainty of less than 1% during the early running period [208].

The trigger efficiency for this analysis is taken from the trigger simulation in the MC. The uncertainty in the efficiency when applying the efficiency measured in data will be taken into account as a systematic uncertainty in Section 7.2.

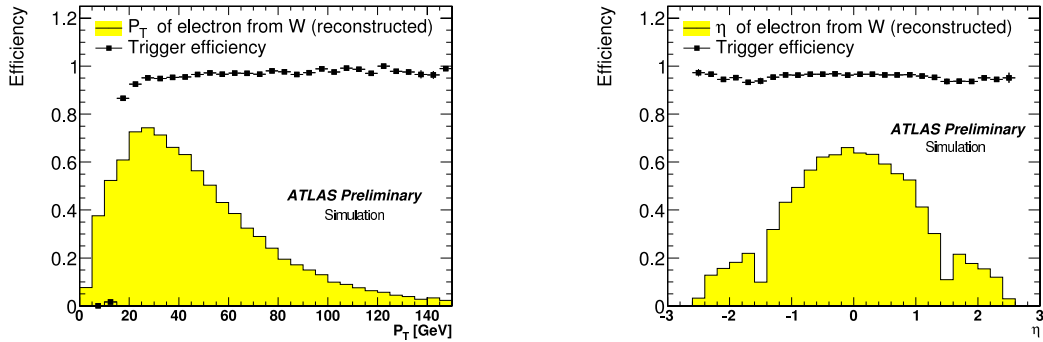


Figure 5.11.: Trigger efficiency for a $t\bar{t}$ sample for the “e15_medium” trigger compared to the reconstructed electron spectrum in bins of p_T (left) and η (right) [232].

5.7.2. Electrons

Electrons are identified and reconstructed according to the algorithms described in Section 5.1. It is ensured that only electrons with calorimeter seeds in the central detector region are selected. Since we expect the decay products of the $t\bar{t}$ pair to be central and because the region is also covered by the inner trackers, the selected electron should have a position of $|\eta| < 2.47$. The quality of the electron should be “medium”, which corresponds to the flag `isEM:medium`. The crack/transition region in $1.37 < |\eta| < 1.52$ between the barrel calorimeter and the end-cap is also removed from the acceptance. The region contains dead material and is not well instrumented. This avoids uncertainties from the performance of the electron finding and identification in this crack region. Absolute isolation of the electron in a cone of $\Delta\mathcal{R} = 0.2$ is also required to avoid falsely identified electrons from e.g. jets or electrons that arise from semileptonic decays of B -hadrons. Also a good rejection against background is a p_T cut on the electrons of 20 GeV. Table 5.4 summarises the electron selection criteria.

Figure 5.12 shows the reconstruction efficiency of the selected electrons originating from a W -boson decay (or tau lepton that originated from a W -boson decay) as a function of p_T and η in a $t\bar{t}$ sample.

5.7.3. Jets

Jets are found by the ATLAS cone algorithm as described in Section 5.3. The cone size is 0.4 and it is based on calorimeter towers that are calibrated accordingly. To match the inner detector coverage and also the requirements on the leptons, only jets within $|\eta| < 2.5$ are selected. This also maintains a good energy scale and resolution for the jets. The transverse momentum requirement is $p_T > 20$ GeV.

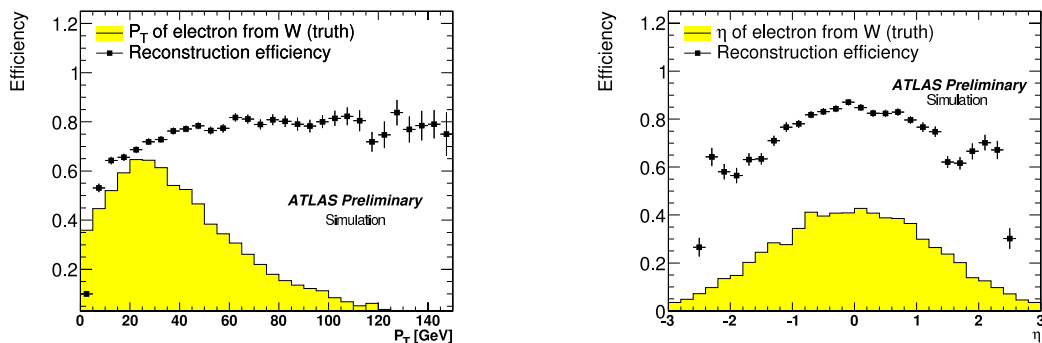


Figure 5.12.: Reconstruction efficiency for electrons in bins of p_T (left) and η (right) compared to the spectrum of true electrons originating from a W -boson in the $t\bar{t}$ sample [232].

Table 5.4.: Electron identification cuts

Variable	Cut
p_T	> 20 GeV
isEM	ElectronMedium
Fiducial cuts	$0 < \eta < 1.37$ or $1.52 < \eta < 2.47$
Absolute CAL Iso, cone=0.2	< 6 GeV

It is expected that the high- p_T jets in the dilepton event are mostly from the decay of B -hadrons, so that b -tagging would be useful in this channel. However, b -tagging systematic uncertainties might not be understood right from the beginning of data taking and more data might be needed for a good understanding than for a good cross-section measurement without it. An earlier study in [208] and this study show that it is not necessary for an initial cross-section measurement.

Since the jet and electron finder work independently on the calorimeter cells, electrons can be reconstructed as jets. To remove this overlap, jets are rejected if they overlap with a selected electron within $\Delta\mathcal{R} < 0.2$.

5.7.4. Muons

This analysis uses muons found by the STACO algorithm. The muons are restricted to muons from high- p_T algorithms only, i.e. tagged muons are excluded. In accordance with the inner detector tracking coverage the requirement on the $|\eta|$ position is again $|\eta| < 2.5$, so that the muon with the best matched inner detector track can be selected. The transverse momentum must be at least 20 GeV and isolation

in a cone of $\Delta\mathcal{R} = 0.2$ of 6 GeV is also required. Table 5.5 summarises the muon selection criteria.

Table 5.5.: Muon identification cuts used in this analysis.

Variable	Cut
Author	6 (STACO muons)
P_T	> 20 GeV
Fiducial cuts	$ \eta < 2.5$
Absolute CAL Iso, cone=0.2	< 6 GeV
IsCombinedMuon	1

Figure 5.13 shows the reconstruction efficiency of the selected muons. The efficiency is again shown with respect to muons originating from a W -boson decay (or from a tau lepton originated from a W -boson decay) as a function of p_T and η in a $t\bar{t}$ sample.

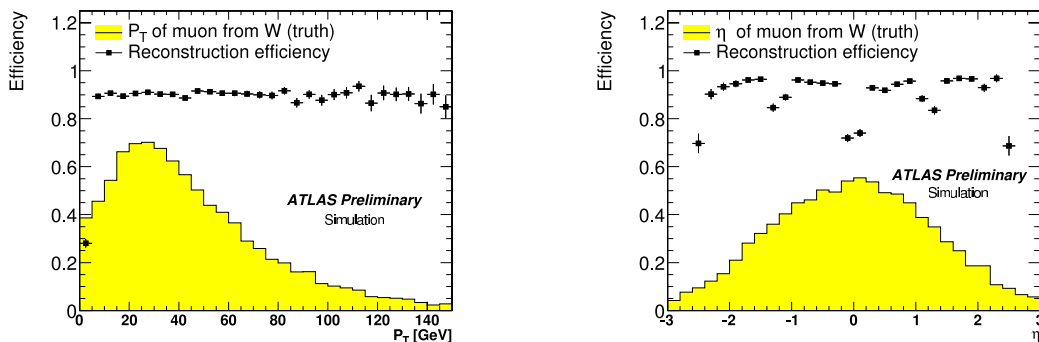


Figure 5.13.: Reconstruction efficiency for muons in bins of p_T (left) and η (right) compared to the spectrum of true muons originating from a W -boson in the $t\bar{t}$ sample [232].

Although the cuts have been chosen for similar reasons as for electrons, there is a class of undesired muons that are not rejected by the previous cuts. Muons are reconstructed very efficiently, so that even in the presence of a jet e.g. a semi-leptonically decaying B -hadron the muons are still found since they can escape the calorimeter. Even the mild isolation requirement does not reject those muons.

A muon is not counted for the event selection if it is close to a jet within a $\Delta\mathcal{R} < 0.3$ distance. The jets are filtered previously by the jet-electron overlap. Figure 5.14 shows the isolation variable “etcone20”, which is the energy in a hollow cone (to avoid the counting of the muon energy deposition) around the muon with

a cone radius of $\Delta\mathcal{R} < 0.2$ against the closest distance to a jet for muons that are close to a true b -quark. Although the distance is small for muons in the upper left corner, the isolation energy for some muons is also small. Only a combined cut on the isolation variable and the distance to jets can efficiently reject such muons.

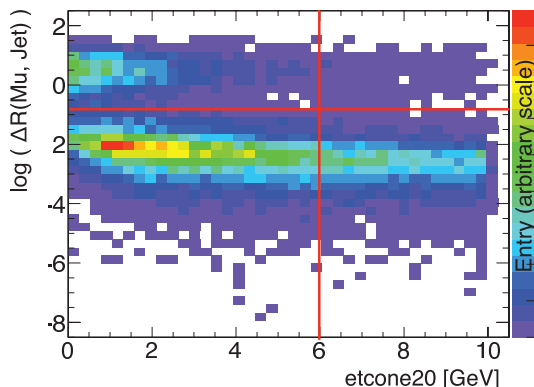


Figure 5.14.: $\Delta\mathcal{R}$ between a muon originating from a heavy flavour decay and the nearest jet against isolation E_T in an outer cone of $\Delta\mathcal{R} < 0.2$ [232]. The line indicates a typical muon rejection cut of $\Delta\mathcal{R} < 0.3$ and isolation $E_T = 6$ GeV. Although a fraction of muons have a small distance to a true b -quark, their isolation energy is below 2 GeV.

5.7.5. missing transverse energy

The \cancel{E}_T is calculated according to the description in Section 5.4. The best available \cancel{E}_T description “MET_RefFinal” is used which is the refined missing transverse energy that is refined by the measurement of reconstructed objects such as electrons, jets and muons. Still, the way \cancel{E}_T is corrected for muons and refined with objects can produce large tails in the distribution. This is best seen in the different \cancel{E}_T distributions for $Z \rightarrow e^+e^-$ and $Z \rightarrow \mu^+\mu^-$ events. In both cases \cancel{E}_T is due to detector resolution effects, but $Z \rightarrow \mu^+\mu^-$ events still have large \cancel{E}_T values (see \cancel{E}_T distribution in Figures 6.5 and 6.6 for Z -boson events). This is caused by muons that are falsely identified or that are missed in the reconstruction by the \cancel{E}_T algorithm.

\cancel{E}_T is a global and complex variable, since it depends on the calibration of many objects starting from the calibration of the calorimeter cells to the calibration of higher-level objects. Two additional detector effects have already been included in the simulated MC samples. The simulation corresponded to the detector status at the beginning of 2009 and one HEC quadrant was disabled. This hole in the calorimeter gives a small intrinsic imbalance of the calorimeter response. In addition the vertex was displaced from its nominal position at (0,0,0) mm to (1.5, 2.5, -9.0) mm. This leads to a small ϕ modulation of the \cancel{E}_T measurement.

5. Object Identification, Reconstruction and Selection

For the latter a fix that is derived from Z -boson events can be applied, which results in a slight overcorrection. However, both effects contribute less than 1% and 0.1%, respectively, to the event selection. Thus the latter fix was not applied in this analysis.

The effect of the first problem is shown in Figure 5.15 for a large range of \cancel{E}_T . Figure 5.16 shows the ϕ modulation with the HEC disabled in the simulation. Also the correction for the disabled HEC quadrant that can be applied is shown.

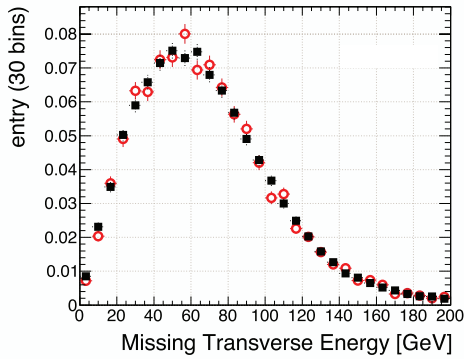


Figure 5.15.: Distribution of missing transverse energy for the dilepton $t\bar{t}$ events with hadronic end-cap calorimeter on (square, dotted) and off (open circles) [232].

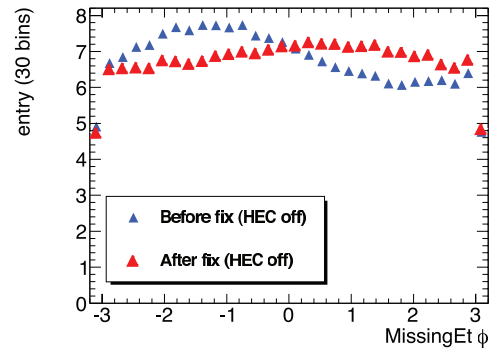


Figure 5.16.: \cancel{E}_T ϕ distribution modulated due to displaced beam spot and the effect of correction [232].

6. Cut-and-count Analysis at $\sqrt{s} = 10 \text{ TeV}$

The cut-and-count analysis [232, 233] follows a simple formula to extract the cross section:

$$\sigma = \frac{N_{\text{obs}} - N_{\text{bkg}}}{A \times \varepsilon \times \mathcal{L}_{\text{int}}}, \quad (6.1)$$

with N_{obs} being the number of observed events, N_{bkg} the number of expected background events, A the geometrical acceptance of the selection, ε the selection efficiency for signal events and \mathcal{L}_{int} the integrated luminosity.

The number of observed events is obtained from the selection on the data. The number of expected background events is either calculated from MC simulations or estimated with data-driven methods in order to reduce the dependence on the simulation or on theoretical uncertainties of the background cross sections. The geometrical acceptance is mostly taken from MC simulations of the detector and supported by measurements of the detector acceptance with homogeneous events (e.g. minimum bias events, dijet events). The efficiency ε contains the selection efficiency of signal events, which includes trigger and lepton reconstruction efficiencies. Finally, the luminosity, i.e. the total rate of events unfolds the signal cross section from the number of selected signal events.

6.1. Event Selection

The general selection of $t\bar{t}$ dilepton (ee , $\mu\mu$ and $e\mu$) candidate events requires a positive decision of a single high- p_T lepton trigger. Following the experimental signature, the events are required to have two oppositely-charged leptons (electron e or muon μ) candidates with a high transverse momentum of $p_T > 20 \text{ GeV}$. From the neutrinos it is expected that the $t\bar{t}$ dilepton events have large missing transverse energy, whereas one of the largest backgrounds for same-flavour channels, Drell-Yan events, should have small \cancel{E}_T coming only from resolution effects. Additionally, events in which the dilepton invariant mass is within $\pm 5 \text{ GeV}$ of the nominal Z -boson mass are vetoed.

The b -quarks are expected to form high- p_T jets and additional jets are only expected from QCD-Bremsstrahlung, which is mostly soft. So at least two jets with

$p_T > 20$ GeV are required for the event selection. As it was stated before, no b -tagging is applied.

In an earlier study in [208] the \cancel{E}_T cut was optimised for the best significance $S/\sqrt{S+B}$ as shown in Figure 6.1. The highest significance is reached at 20 GeV for the $e\mu$ channel and at 35 GeV for the ee and $\mu\mu$ channel. Although the study was for a collision energy of 14 TeV, the kinematic distributions of the decay products did not change significantly and the optimisation still holds. In the following the sub-channel specific event cuts are motivated. Table 6.1 summarises the event cuts. It is worth noting that the event cuts are exclusive, so that there is no overlap between the sub-channels.

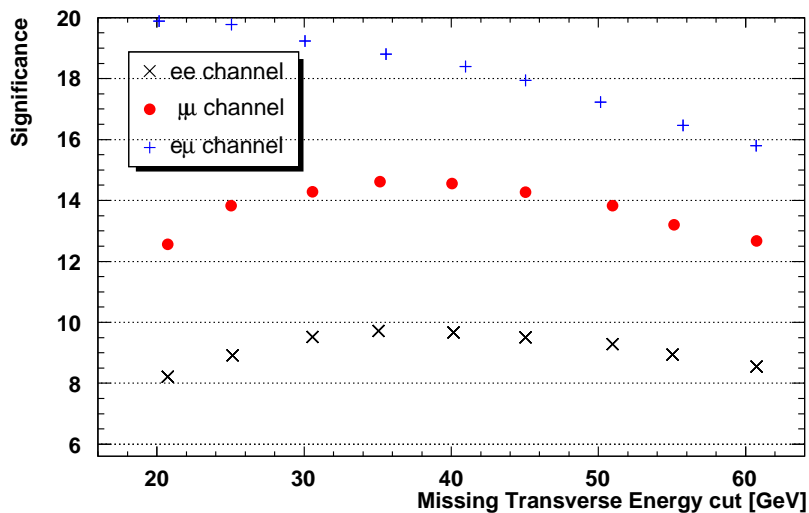


Figure 6.1.: Significance $S/\sqrt{S+B}$ versus the cut on \cancel{E}_T for the different sub-channels. The cut on the jet and lepton p_T is fixed at 20 GeV and the Z -boson mass window cut is fixed at ± 5 GeV. The significance does not include the single top-quark samples nor the W +jets events.

ee -channel

In addition to the common requirements, additional cuts are applied to suppress the Drell-Yan background. A veto on events with an invariant dilepton mass within a 10 GeV mass window centred around the Z -boson mass of 91 GeV is applied. Furthermore, these background events tend to have small \cancel{E}_T . The optimisation for the best significance determined a cut of $\cancel{E}_T > 35$ GeV that rejects a large fraction of $Z \rightarrow e^+e^-$ events. Figures 6.2 show the number of leptons without any cuts and the invariant dilepton mass after the two lepton requirement in each sample. Each distribution of the individual samples is normalised to unity and finally all

Table 6.1.: List of event cuts, optimised for significance. The jet and the lepton requirement are the same for all the sub-channels. The cuts for the same-flavour channels are almost the same, except for the trigger requirement. The cut on the invariant dilepton mass m_{ll} is only applied to same lepton events.

Cut	ee and $\mu\mu$	$e\mu$
trigger	EF_e15_medium, EF_mu15	EF_e15_medium or EF_mu15
lepton	two oppositely charged leptons, $p_T > 20$ GeV	
\cancel{E}_T	$\cancel{E}_T > 35$ GeV	$\cancel{E}_T > 20$ GeV
jets	No. of jets ≥ 2 jets of $p_T > 20$ GeV	
m_{ll}	$m_{ll} < 86$ GeV or $m_{ll} > 96$ GeV	

distributions are stacked. It can be seen that requiring exactly two leptons suppresses already most of the background events except for $Z \rightarrow \ell^+\ell^-$ events. The invariant dilepton mass of the $t\bar{t}$ sample is almost constant in the range of the Z -mass peak. Therefore a small cut window on the invariant mass is used.

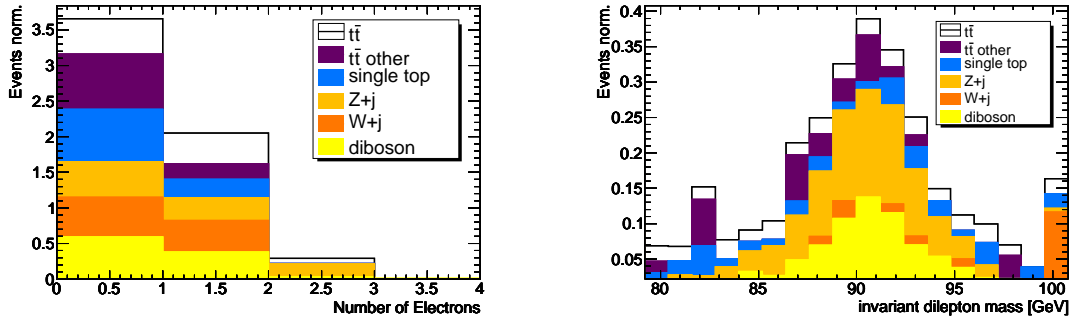


Figure 6.2.: Number of electrons for signal and background samples (left) without any cut and the invariant dilepton mass after requiring exactly two electrons (right). The distributions are normalised for each sample to unity and all distributions are stacked. The label “ $t\bar{t}$ ” other denotes $t\bar{t}$ processes other than dilepton processes.

$\mu\mu$ -channel

Similar considerations as taken for the ee -channel result in the same cuts on the invariant dilepton mass (veto on events with $86 \text{ GeV} < m_{ll} < 96 \text{ GeV}$) and on $\cancel{E}_T > 35 \text{ GeV}$, although the \cancel{E}_T distribution tends to have higher values for $Z \rightarrow \mu^+\mu^-$ events, the optimisation yields the same cut. From Figures 6.3 one can draw similar conclusion as for the ee channel.

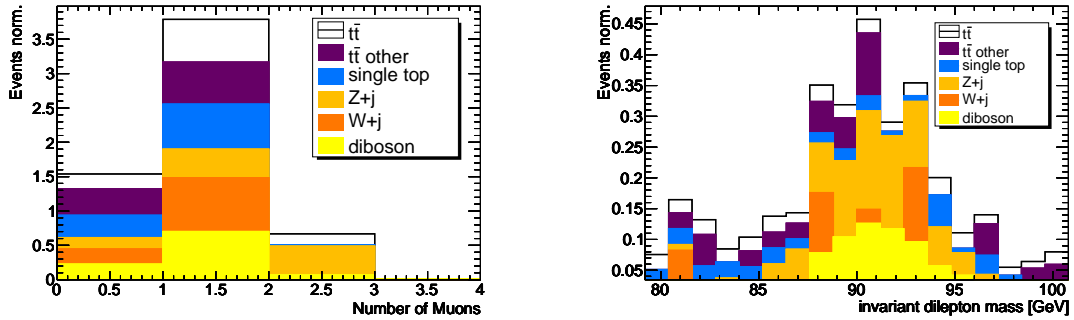


Figure 6.3.: Number of muons for signal and background samples (left) without any cut and the invariant dilepton mass after requiring exactly two muons (right). The distributions are normalised for each sample to unity and all distributions are stacked. The label “ $t\bar{t}$ ” other denotes $t\bar{t}$ processes other than dilepton processes.

$e\mu$ -channel

This channel is expected to have the best signal-to-background ratio, since it does not suffer from Drell-Yan background. Only in rare cases $Z \rightarrow e^+e^-$ or $Z \rightarrow \mu^+\mu^-$ events can have falsely identified leptons that contribute to the background. Therefore a tight cut on \cancel{E}_T is not required. More likely $Z \rightarrow \tau\tau$ events with real \cancel{E}_T are selected when both taus decay leptonically, but the branching ratio is relatively small ($\sim 2 \times (17\%)^2$). The \cancel{E}_T cut was optimised to be $\cancel{E}_T > 20 \text{ GeV}$. For the two lepton requirement the conclusion from Figures 6.4 is similar to the ee channel. The invariant mass distribution, however, shows that Z -boson events selected as $e\mu$ events do not show a peak at around 90 GeV. A small enhancement at around 60 GeV can be seen. These are mainly $Z \rightarrow \tau\tau$ events, but there is not special cut foreseen to remove these events.

MC event yields

Table 6.2 shows the absolute number of events expected for $t\bar{t}$ dilepton events and the corresponding relative efficiencies. It is important to notice that the trigger selection is very efficient and over 97% of the events are expected to pass the trigger. The trigger selection hardly biases the event selection.

6.2. Expected Number of Events from MC

For a first estimation of the expected number of events, the event selection is applied to the MC samples listed in Section 4.4 that contain $t\bar{t}$, single top-quark, W/Z +jets

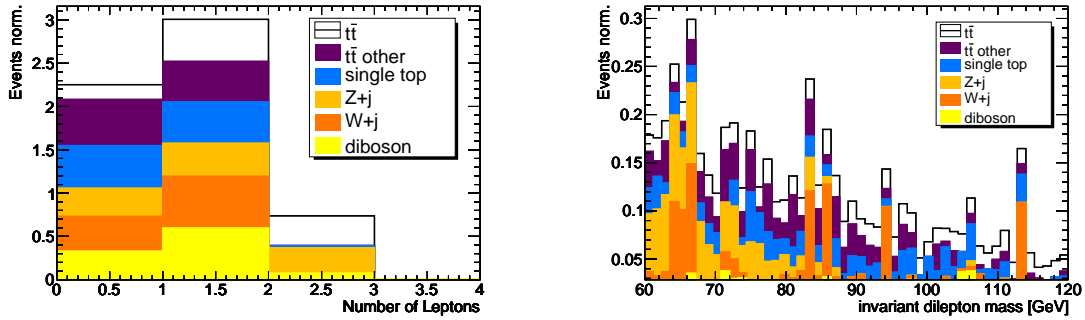


Figure 6.4.: Number of leptons for signal and background samples (left) without any cut and the invariant dilepton mass after requiring exactly two leptons (right). The distributions are normalised for each sample to unity and all distributions are stacked. The label “ $t\bar{t}$ ” other denotes $t\bar{t}$ processes other than dilepton processes.

Table 6.2.: Cutflow table for the ee , $\mu\mu$ and $e\mu$ channel selection for $t\bar{t}$ MC (numbers are for an integrated luminosity of $\mathcal{L}_{\text{int.}}=200 \text{ pb}^{-1}$). Relative ε is a ratio of the number of events passing a cut to the number of events before the cut.

	Lepton selection	Inv. mass cut	\cancel{E}_T cut	Jet cut	Trigger
Events ee	351	322	261	220	214
Relative ε	26.5%	91.7%	81.0%	84.2%	97.3%
Events $\mu\mu$	530	490	400	343	332
Relative ε	39.8%	92.4%	81.6%	85.8%	97.0%
Events $e\mu$	908	908	845	715	698
Relative ε	33.7%	100.0%	93.1%	84.6%	97.5%

and diboson events. The expected \cancel{E}_T and jet multiplicity distributions for Monte-Carlo signal and background after this selection are shown in Figures 6.5, 6.6 and 6.7. Generally, the signal events dominate in regions with a jet multiplicity larger than one and high \cancel{E}_T . Notable is the different \cancel{E}_T distribution for $Z \rightarrow \mu^+\mu^-$ events compared to $Z \rightarrow e^+e^-$ events in the ee channel.

The order of the cuts is first the requirement on two oppositely signed leptons, the veto on the invariant dilepton mass, the \cancel{E}_T cut, the cut on the number of jets and finally the trigger requirement. In real data the trigger requirement would be applied first, since the events are selected from streams that are sorted by the trigger that selected the particular event.

In the MC simulation there is overlap with the data-driven methods discussed in Section 6.3. The misidentification of leptons is already implemented into the

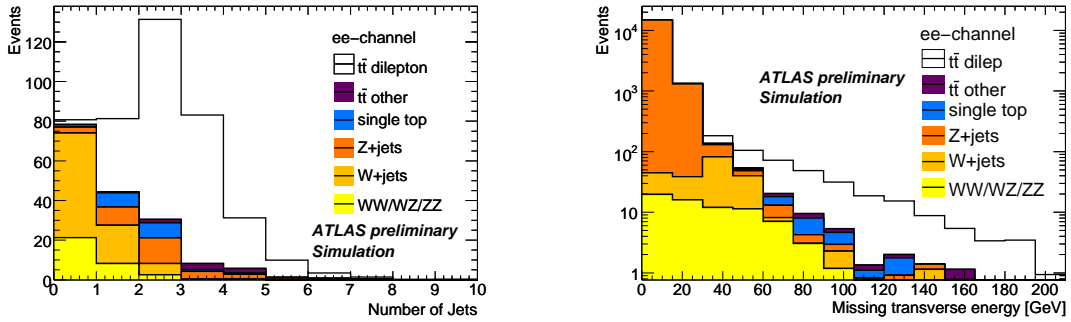


Figure 6.5.: Expected jet multiplicity (left) and E_T distribution (right) for ee events. For the distributions all cuts were applied except on the variable shown. The distributions are normalised for an integrated luminosity of $\mathcal{L}_{\text{int.}}=200\text{pb}^{-1}$ and cross sections at a centre-of-mass energy of $\sqrt{s} = 10$ TeV.

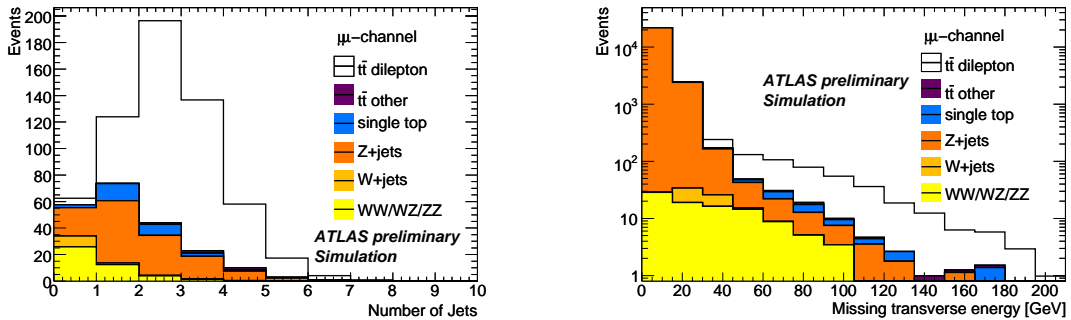


Figure 6.6.: Expected jet multiplicity (left) and E_T distribution (right) for $\mu\mu$ events. For the distributions all cuts were applied except on the variable shown. The distributions are normalised for an integrated luminosity of $\mathcal{L}_{\text{int.}}=200\text{pb}^{-1}$ and cross sections at a centre-of-mass energy of $\sqrt{s} = 10$ TeV.

simulation and these events with one or two misidentified leptons would be double counted. This can be avoided by imposing an additional cut on the reconstructed leptons. Figure 6.8 shows the distance in $\Delta\mathcal{R}$ of the first and the second lepton to true leptons originating from a W -boson decay or from a tau lepton decay if it originated from a W -boson. Most of the matching leptons have a distance to the true particle of $\Delta\mathcal{R} < 0.05$. This cut removes the overlap between the MC misidentified leptons and the estimation from data-driven methods. For the signal-to-background (S/B) estimation these events are considered as additional (instrumental) background events.

Tables 6.3, 6.4 and 6.5 show the cut flow for the ee , $\mu\mu$ and $e\mu$ sub-channel selection scaled to an integrated luminosity of $\mathcal{L}_{\text{int.}}=200\text{pb}^{-1}$. The last column shows the number of events that failed the truth-matching cut. It is notable that

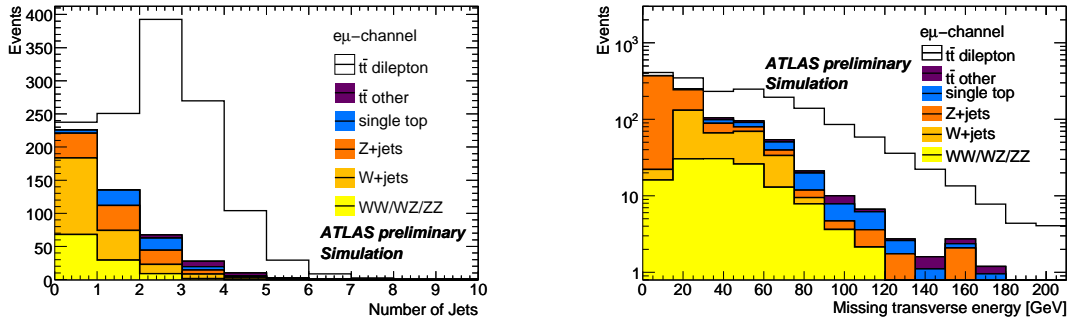


Figure 6.7.: Expected jet multiplicity (left) and \cancel{E}_T distribution (right) for $e\mu$ events. For the distributions all cuts were applied except on the variable shown. The distributions are normalised for an integrated luminosity of $\mathcal{L}_{\text{int.}}=200\text{pb}^{-1}$ and cross sections at a centre-of-mass energy of $\sqrt{s}=10\text{TeV}$. The fraction of $Z \rightarrow \ell^+\ell^-$ events is small and only visible in the low- \cancel{E}_T region.

around 2–4% of the dilepton-signal events do not pass the final cut and are classified as background. This is the case if one lepton originating from a W -boson is not identified or out of the acceptance and instead a non-isolated lepton from e.g. a semi-leptonically decaying B -hadron or a jet is misidentified as a lepton. Events containing misidentified leptons are already estimated with data-driven methods.

The estimation from the MC samples shows that in all three sub-channels the leptonically decaying Z -boson events are the largest background, followed by single top-quark events. Most of the Z -boson events are not removed by the invariant mass cut, but are reduced by over 90% (relative cut efficiency) by the cut on \cancel{E}_T . This cut is more effective for the ee channel than for the $\mu\mu$ channel. The reason is the different \cancel{E}_T distributions for the two $Z \rightarrow \ell^+\ell^-$ backgrounds. The \cancel{E}_T calculation for Z -boson events with muons is, despite the muon correction term, still not as good as for $Z \rightarrow e^+e^-$ events. The problem is that the correction does not deal with missed or fake muons and this can create large fluctuations for the refined \cancel{E}_T distribution. For $Z \rightarrow \mu^+\mu^-$ this can be seen from the \cancel{E}_T distribution, which has a larger tail towards higher \cancel{E}_T values, as it can be seen in Figure 6.6. Increasing the \cancel{E}_T cut would reduce the signal events more than it can reduce the background events, thus the same cut is kept for both same-lepton channels. A signal-to-background ratio between 3.8 and 5.6 can be reached and the significance is between 12.9 and 24.1, the cleanest channel is the $e\mu$ selection. The final acceptance for the signal events is summarised in Table 6.6.

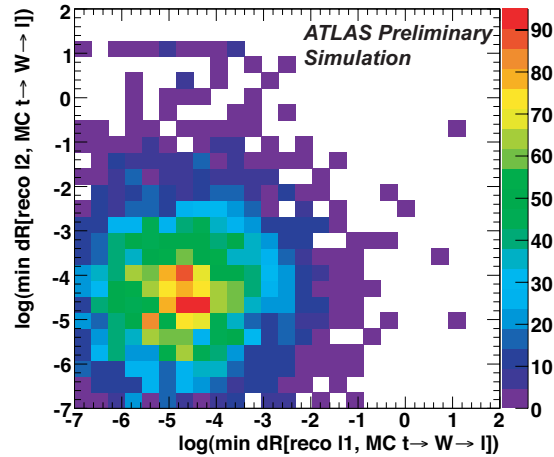


Figure 6.8.: Distance of reconstructed and true leptons for the first (x -axis) and the second (y -axis) lepton [232].

Estimation of the statistical uncertainty and significance for different luminosities

From the MC prediction a first estimate of the statistical uncertainty and the significance for different luminosities can be done. Table 6.7 shows the statistical uncertainties assuming Poissonian uncertainties for the number of selected events and taking the MC statistical uncertainty as the uncertainty on the number of background events. This first estimate shows that for the target integrated luminosity the top quark can be easily seen. It is even possible with an integrated luminosity of $\mathcal{L} = 50 \text{ pb}^{-1}$. The statistical uncertainty ranges between 15.9% – 4.6%.

6.3. Data-Driven Methods

The prediction on the number of expected signal and background events can be supported by a number of data-driven methods. For the most important background process $Z \rightarrow \ell^+ \ell^-$ and for the number of events with misidentified leptons, methods have been developed to estimate the number of events that are selected by the chosen cuts.

In the following section, the performance of the methods is evaluated with MC simulated samples, which are used as “data”.

Table 6.3.: Expected number of selected events for the ee channel selection for an integrated luminosity of $\mathcal{L}_{\text{int.}}=200 \text{ pb}^{-1}$ and a centre-of-mass energy of $\sqrt{s}=10 \text{ TeV}$ from MC only. The column labelled “true” represents the effect of applying truth-matching cuts, the column “fake” shows the number of events that failed the truth-matching cuts. The number of fake events are included into the S/B and $S/\sqrt{S+B}$ calculation.

	Lepton sel.	Mass cut	\cancel{E}_T cut	Jet cut	Trigger	True	Fake
$t\bar{t}$ dilepton	351	322	261	220	214 ± 6	209 ± 6	4
$t\bar{t}$ other	15	13	10	9	8 ± 1	$0_{-0}^{+0.1}$	8
single top	27	25	18	9	9 ± 2	7 ± 1	2
$Z \rightarrow e^+e^-$	68231	16283	24	14	13_{-1}^{+2}	11_{-1}^{+2}	2
$Z \rightarrow \tau\tau$	156	154	10	7	7_{-1}^{+2}	6_{-1}^{+2}	1
$W \rightarrow e\nu$	126	118	56	7	7_{-2}^{+4}	0_{-0}^{+4}	7
$W \rightarrow \tau\nu$	7	7	7	1	1_{-1}^{+4}	0_{-0}^{+4}	1
diboson	145	73	33	3	3 ± 1	2 ± 1	1
Sum bkg	68707	16673	157	51	49_{-3}^{+8}	54_{-3}^{+11*}	
S/B	0.0	0.0	1.7	4.3	$4.3_{-0.3}^{+0.7}$	$3.9_{-0.3}^{+0.8}$	
$S/\sqrt{S+B}$	1.3	2.5	12.5	13.4	13.2	12.9	

* Including all fakes.

6.3.1. Estimation of $Z \rightarrow \ell^+\ell^-$ /Drell-Yan Events from Side Bands

The two most effective cut variables for $Z \rightarrow \ell^+\ell^-$ events¹ are the \cancel{E}_T cut and the cut on the dilepton invariant mass. Still, a number of events pass the cuts, as can be seen from the MC prediction in Section 6.2. The prediction assumes a certain cross section and efficiency that is implemented in the simulation. With a dedicated analysis the number of background events in the signal selection region can be predicted from data measurements.

This data-driven technique divides the data events into bins of \cancel{E}_T and bins of the dilepton invariant mass. The division of the events can be seen in Figure 6.9. The bins A and C are dominated by $t\bar{t}$ events and the admixture of $Z \rightarrow \ell^+\ell^-$ events needs to be estimated. This is done by scaling the appropriate bins of the MC simulation to the number of events in real data in this bin. The bins G , I , B and H are measured in data, since they are dominated by $Z \rightarrow \ell^+\ell^-$ events and this

¹ l being electrons and muons

Table 6.4.: Expected number of selected events for the $\mu\mu$ channel selection for an integrated luminosity of $\mathcal{L}_{\text{int.}}=200\text{ pb}^{-1}$ and a centre-of-mass energy of $\sqrt{s}=10$ TeV from MC only. The column labelled "true" represents the effect of applying truth-matching cuts. The column labelled "fake" shows the number of events that failed the truth-matching cuts. The number of fake events are included into the S/B and $S/\sqrt{S+B}$ calculation.

	Lepton sel.	Mass cut	\cancel{E}_T cut	Jet cut	Trigger	Truth	Fake
$t\bar{t}$ dilepton	530	490	400	343	332 ± 8	327 ± 7	6
$t\bar{t}$ other	9	8	6	6	5 ± 1	$0_{-0}^{+0.1}$	5
single top	38	35	27	12	12 ± 2	11 ± 2	1
$Z \rightarrow \mu^+\mu^-$	109331	24716	113	49	47_{-2}^{+3}	44_{-2}^{+3}	4
$Z \rightarrow \tau\tau$	263	262	19	11	10_{-1}^{+2}	10_{-1}^{+2}	0
$W \rightarrow \mu\nu$	14	14	7	0	0_{-0}^{+4}	0_{-0}^{+4}	
$W \rightarrow \tau\nu$	1	1	0	0	0_{-0}^{+4}	0_{-0}^{+4}	
Wbb	1	1	1	0	$0.4_{-0.1}^{+0.2}$	$0_{-0}^{+0.2}$	
diboson	211	100	45	5	5 ± 1	5 ± 1	1
Sum bkg	109868	25137	218	84	81_{-3}^{+8}	87_{-3}^{+11*}	
S/B	0.0	0.0	1.8	4.1	$4.1_{-0.2}^{+0.4}$	$3.8_{-0.2}^{+0.5}$	
$S/\sqrt{S+B}$	1.6	3.1	16.1	16.6	16.4	16.1	

* Including all fakes.

gives the smallest bias. From the following scaling formulas the number of Z -boson events are estimated:

$$A_{\text{Est}} = G_{\text{Data}} \left(\frac{A_{\text{MC}}}{G_{\text{MC}}} \right) \left(\frac{H_{\text{MC}}}{B_{\text{MC}}} \right) \left(\frac{B_{\text{Data}}}{H_{\text{Data}}} \right), \quad (6.2)$$

$$C_{\text{Est}} = I_{\text{Data}} \left(\frac{C_{\text{MC}}}{I_{\text{MC}}} \right) \left(\frac{H_{\text{MC}}}{B_{\text{MC}}} \right) \left(\frac{B_{\text{Data}}}{H_{\text{Data}}} \right), \quad (6.3)$$

where $A-I$ denote the number of events in the corresponding bin of Figure 6.9 and the subscript MC or Data denote the number of events in MC and data, respectively.

The method was applied to a sample of simulated events that contained SM processes for an integrated luminosity of $\mathcal{L}_{\text{int.}}=134.8\text{ pb}^{-1}$. The prediction of this method was that 13.7 ± 0.9 events in the ee channel and 33.0 ± 4.1 events in the $\mu\mu$ channel should be coming from $Z \rightarrow \ell^+\ell^-$ events. Scaling the number of events in the MC prediction down to the luminosity of the test sample results in (7 ± 1) $Z \rightarrow e^+e^-$ events and (30_{-1}^{+2}) $Z \rightarrow \mu^+\mu^-$ events. Clearly this method overestimates the contribution in the ee channel, but the prediction for the $\mu\mu$ channel is within the statistical uncertainty.

Table 6.5.: Expected number of selected events for the $e\mu$ channel selection for an integrated luminosity of $\mathcal{L}_{\text{int.}}=200\text{pb}^{-1}$ and a centre-of-mass energy of $\sqrt{s}=10\text{TeV}$ from MC only. The column labelled “true” represents the effect of applying truth-matching cuts, the column “fake” shows the number of events that failed the truth-matching cuts. The number of fake events are included into the S/B and $S/\sqrt{S+B}$ calculation.

	Lepton sel.	\cancel{E}_T cut	Jet cut	Trigger	Truth	Fake
$t\bar{t}$ dilepton	908	845	715	698 ± 11	683 ± 11	15
$t\bar{t}$ other	24	21	21	20 ± 2	$0_{-0}^{+0.1}$	20
single top	59	55	26	25 ± 3	23 ± 3	2
$Z \rightarrow \mu^+\mu^-$	110	15	4	4_{-0}^{+1}	0_{-0}^{+1}	4
$Z \rightarrow \tau\tau$	421	97	28	27_{-2}^{+3}	25_{-2}^{+3}	2
$W \rightarrow e\nu$	14	11	2	2_{-1}^{+4}	0_{-0}^{+4}	2
$W \rightarrow \mu\nu$	165	144	20	17_{-4}^{+6}	0_{-0}^{+4}	17
$W \rightarrow \tau\nu$	11	9	2	2_{-1}^{+4}	0_{-0}^{+4}	2
Wbb	1	1	0	$0.4_{-0.1}^{+0.3}$	$0_{-0}^{+0.2}$	
diboson	135	111	11	10 ± 1	10 ± 1	0.2
Sum bkg	939	464	113	108_{-6}^{+10}	123_{-6}^{+12*}	
S/B	1.0	1.8	6.3	$6.5_{-0.3}^{+0.6}$	$5.6_{-0.3}^{+0.6}$	
$S/\sqrt{S+B}$	21.1	23.4	24.9	24.6	24.1	

* Including all fakes.

6.3.2. Fake Rate Estimation using the Matrix Method

The estimation of the rate of falsely identified leptons or fake rate from the data is important, since the number of events in the current MC samples is not sufficient to obtain a good estimation. The number of selected events with falsely identified leptons is small and the large statistical uncertainties together with the large cross section of e.g. W +jets or QCD result in a bad prediction. Furthermore, the rate is subject to instrumental effects that can be different from the simulation and it can vary with time. The following data-driven method tries to estimate the number of events that contain one falsely identified lepton. It is assumed that the rate of two falsely identified leptons, which are mainly from QCD multijet events, is low. The events also have low \cancel{E}_T , so that they are rejected already by the \cancel{E}_T cut.

The rate of fake events is derived from the fake rate, f , for single leptons and the efficiency, ε , to select real leptons. The fake rate is measured in fake lepton dominated events, the so-called control region, with a looser lepton selection. The efficiency is measured in $Z \rightarrow \ell^+\ell^-$ events with dominating real leptons and the default lepton selection.

Table 6.6.: Top-quark pair dilepton acceptances and top-quark pair branching ratios estimated from MC@NLO Monte Carlo simulation for the different sub-channels.

	ee [%]	$\mu\mu$ [%]	$e\mu$ [%]
A	16.5 ± 0.4	26.1 ± 0.4	26.5 ± 0.3
$\text{BR}(t\bar{t} \rightarrow l\bar{l})/\text{BR}(\text{all})$	1.67 ± 0.05	1.64 ± 0.05	3.40 ± 0.10

Table 6.7.: Statistical uncertainty on the cross section σ and significance for the different sub-channels from MC based signal and backgrounds. The uncertainty on the number of observed events is Poissonian and the uncertainty on the background estimation is taken from the statistical uncertainty of the MC sample.

statistical uncertainty $\Delta\sigma/\sigma$ [%]	ee	$\mu\mu$	$e\mu$
$\mathcal{L} = 10 \text{ pb}^{-1}$	34.3	27.6	18.3
50 pb^{-1}	15.9	12.7	8.4
100 pb^{-1}	11.7	9.3	6.1
200 pb^{-1}	7.8	6.2	4.4
significance $S/\sqrt{S+B}$	ee	$\mu\mu$	$e\mu$
$\mathcal{L} = 10 \text{ pb}^{-1}$	2.9	3.6	5.4
50 pb^{-1}	6.5	8.0	12.0
100 pb^{-1}	9.1	11.4	17.0
200 pb^{-1}	12.9	16.1	24.1

The loose lepton selection is chosen such that it is kinematically similar to the actual lepton selection, but some cuts are relaxed, so that the probability for a fake lepton is high to avoid large statistical uncertainties. For muons this is achieved by not requiring isolation. For electrons the `isEM:medium` requirement and the isolation cut is reversed. The tight selection is the same as the default object selection.

The definition of the efficiency ε and the fake rate f is

$$\varepsilon = \frac{N_{\text{tight,real}}}{N_{\text{tight,real}} + N_{\text{loose,real}}}, \quad (6.4)$$

$$f = \frac{N_{\text{tight,fake}}}{N_{\text{tight,fake}} + N_{\text{loose,fake}}}. \quad (6.5)$$

The efficiency is measured in $Z \rightarrow \ell^+\ell^-$ events that require two oppositely signed, same flavoured leptons with an invariant mass within ± 5 GeV of the Z -boson mass

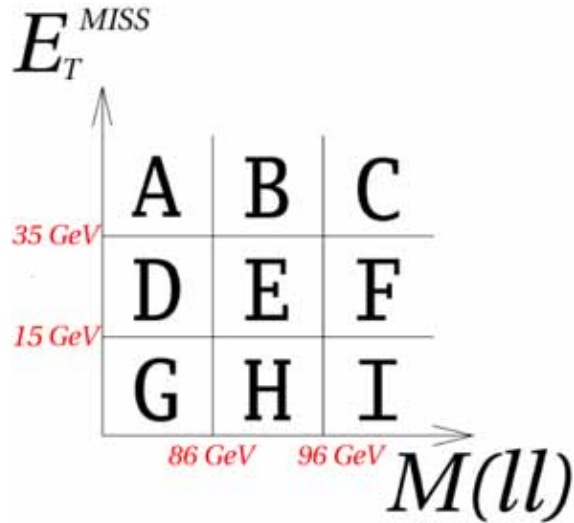


Figure 6.9.: E_T and dilepton invariant mass space with the labelled areas used for the data-driven background estimation of the $Z \rightarrow \ell^+\ell^-$ background [232].

and $E_T < 15$ GeV. The number of tight leptons and loose leptons are counted and the equation above is applied.

While the selection of real lepton events is very clear, the selection for event dominated by loose leptons is tested in two regions. In addition special care has to be taken of events with W -bosons. The two regions are also useful to estimate the systematic uncertainty of this method and thus are chosen to be orthogonal. Both regions require one loose or one tight lepton, the first region requires also $E_T < 15$ GeV while the other requires $E_T > 15$ GeV and $\Delta\phi(\text{lepton}, \cancel{E}_T) < 1$ rad. The requirement of low E_T rejects 98% of W -boson events while the angular cut only rejects between 75 – 80% of the events. The number of remaining events with real leptons is estimated from W -boson and single-lepton $t\bar{t}$ MC events employing the control region selection cuts and an additional cut on the transverse mass² of $m_T > 60$ GeV. This estimation is subtracted from the number of tight leptons in the control region that is used in the calculation of the fake rate f .

The single lepton efficiency and fake rate is correlated to the event fake rate as follows: The sources for events with two tight (TT), one tight and one loose lepton (TL, ordered by p_T) and one loose and one tight lepton (LT) are events with two real leptons (RR), one real and one fake lepton (RF) or one fake and one real lepton (FR). E.g. the number of events with two tight leptons (N_{TT}) is related to the number of real/fake lepton events (N_{RR} , N_{RF} , N_{FR}) such as $N_{TT} =$

²The transverse mass is defined from the transverse lepton and the \cancel{E}_T vector.

$\varepsilon_1\varepsilon_2N_{\text{RR}} + \varepsilon_1f_2N_{\text{RF}} + f_1\varepsilon_2N_{\text{FR}}$, where the subscripts denote the first and second highest p_T lepton. All cases can be summarised into a vector equation:

$$\begin{bmatrix} N_{\text{TT}} \\ N_{\text{TL}} \\ N_{\text{LT}} \end{bmatrix} = \begin{bmatrix} \varepsilon_1\varepsilon_2 & \varepsilon_1f_2 & f_1\varepsilon_2 \\ \varepsilon_1(1-\varepsilon_2) & \varepsilon_1(1-f_2) & f_1(1-\varepsilon_2) \\ (1-\varepsilon_1)\varepsilon_2 & (1-\varepsilon_1)f_2 & (1-f_1)\varepsilon_2 \end{bmatrix} \begin{bmatrix} N_{\text{RR}} \\ N_{\text{RF}} \\ N_{\text{FR}} \end{bmatrix} \quad (6.6)$$

The number of fake events is obtained by inverting this relation and adding the number of events with one fake lepton:

$$N_{\text{RF}} + N_{\text{FR}} = N_{\text{Fake}} = \left[\frac{f_2(\varepsilon_2 - 1)}{\varepsilon_2 - f_2} + \frac{f_1(\varepsilon_1 - 1)}{\varepsilon_1 - f_1} \right] \quad (6.7)$$

The efficiencies and fake rates can also be expressed as functions of kinematic variables, so that the event fake rate is also a function of these variables. For example in Figures 6.10 the fake rate f is shown for electrons and muons as a function of p_T and η . The fake event estimate is given as a function of the jet multiplicity in Figures 6.11 for the different sub-channels. From the figures it can be seen that the assumption made earlier that the fake rate estimation should be independent of the method is not very well fulfilled. Only in a small phase space of the fake event estimation do the two control regions result in the same prediction. This difference could be an effect of the different fake sources that were not distinguished, e.g. heavy-flavour decay or real instrumental effects. Until the effects of these two sources are not separated, the difference in the two control regions can be taken as a systematic uncertainty of this method.

6.3.3. Background Normalisation in Control Regions

A simple way to check the background normalisation is to choose a set of cuts that provide a clean selection of the background events. The background normalisation for Z +jets and W +jets events can be easily compared when the following cuts are employed: For Z -boson events a selection of the leptons as described before and an invariant cut on the dilepton invariant mass within a window of 10 GeV can be applied. This yields a background fraction of 0.28% and 0.25% for $Z \rightarrow e^+e^-$ and $Z \rightarrow \mu^+\mu^-$, respectively. This can be seen in Figure 6.12, which shows the invariant dilepton mass distribution for the $Z \rightarrow e^+e^-$ selection. If from this selection the normalisation of the Z +jets is derived, this will lead to a statistical uncertainty of 0.46% ($Z \rightarrow e^+e^-$) and 0.57% ($Z \rightarrow \mu^+\mu^-$) on the normalisation, respectively. The systematic uncertainty depends on the background fraction of this selection. In a pessimistic scenario the actual number of background events in data could be twice as high as the selection in MC. In this case the systematic uncertainty would be 0.45% ($Z \rightarrow e^+e^-$) and 0.56% ($Z \rightarrow \mu^+\mu^-$).

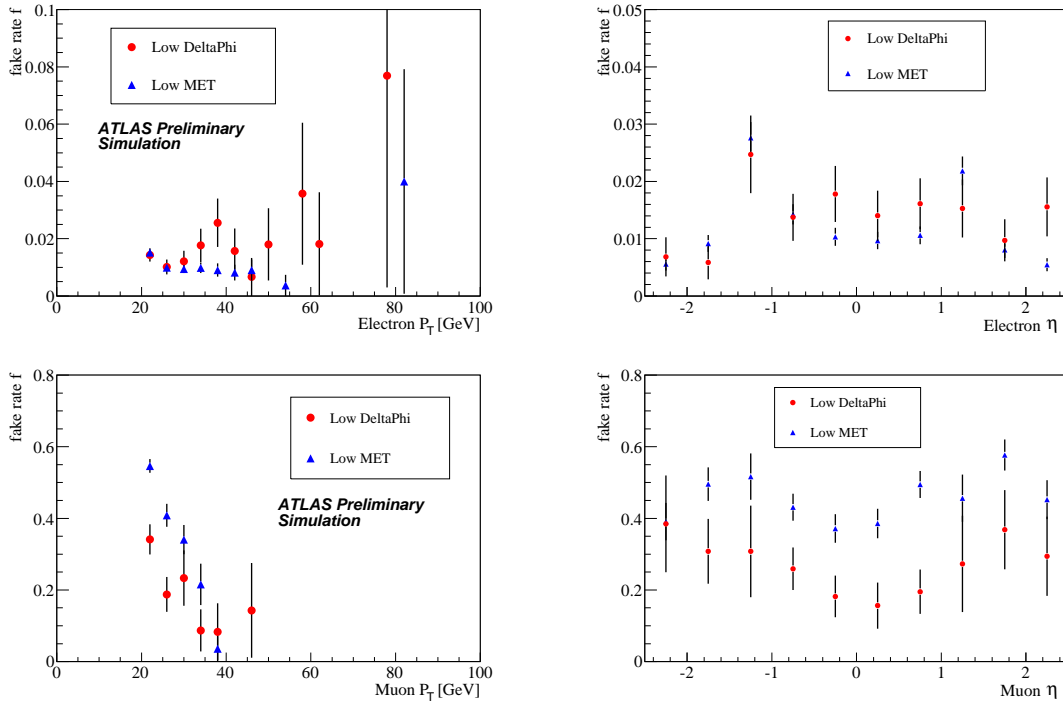


Figure 6.10.: Fake rate f for electrons (upper row) and muons (bottom row) as a function of p_T (left) and η (right) in the two control regions [232].

For the W +jets events the selection of one isolated lepton, as defined in Section 5.7, is required. A cut of $\cancel{E}_T > 35$ GeV is required to reject QCD events with sufficient efficiency. Furthermore, only events with 0 or 1 jets are considered. With these cuts a background fraction of 1.48% and 5.16% can be achieved. Figure 6.13 shows the jet multiplicity distribution for the $W \rightarrow \mu\nu$ selection. The statistical uncertainty of the normalisation is only 0.20% whereas the systematic uncertainties taking into account twice the background rate is 3.0% and 5.6% for $W \rightarrow e\nu_e$ and $W \rightarrow \mu\nu_\mu$, respectively.

Other background sources such as single top-quark, diboson etc. are difficult to select as clean as W/Z -boson events, so that their normalisation is taken from the theoretical cross-section calculation and the efficiency in MC.

6. Cut-and-count Analysis at $\sqrt{s} = 10 \text{ TeV}$

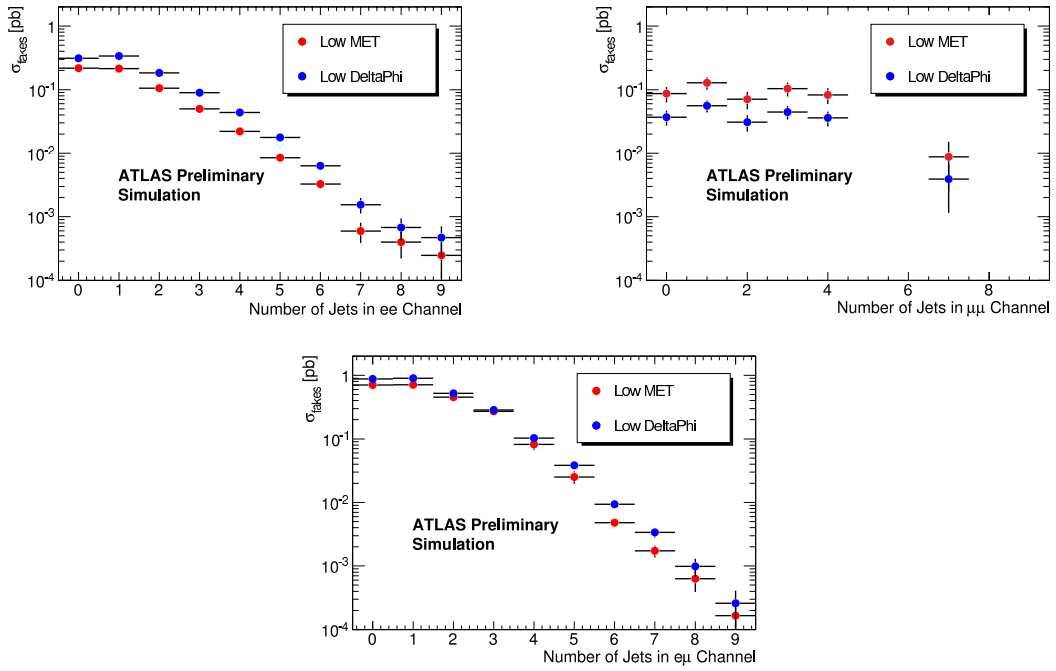


Figure 6.11.: Fake event rate estimation as a function of the jet multiplicity in the ee (top left), $\mu\mu$ (top right) and $e\mu$ (bottom) channel [232].

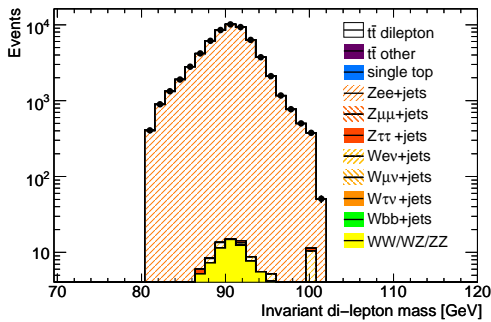


Figure 6.12.: Invariant dilepton mass distribution for the Z -boson control region. Here only the $Z \rightarrow e^+e^-$ selection is shown.

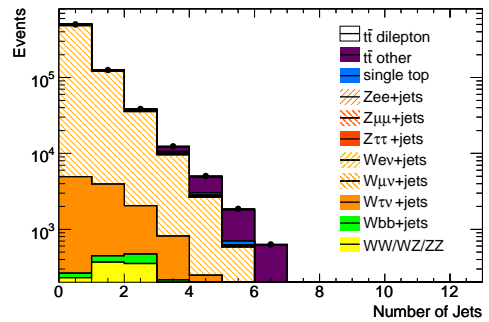


Figure 6.13.: Jet multiplicity distribution for the $W \rightarrow \mu\nu$ control region.

7. Systematic Uncertainties for the Cut-and-Count Analysis

The cross-section measurement is affected by a number of uncertainties that will bias the measurement. Not all effects can be taken into account in the full chain of the MC simulation and thus have to be estimated with approximate methods. In the following an extensive list of systematic uncertainties are investigated. The effect on the cross section is found by redoing the analysis with a systematic change and comparing it with the default analysis. The procedure uses the total number of expected events as N_{obs} in Formula 6.1, but uses the number of signal and background events from the varied analysis. The geometrical acceptance A and the luminosity $\mathcal{L}_{\text{int.}}$ are assumed to be constant and the difference between the so calculated cross section and the nominal cross section is taken as the systematic variation. Some systematic effects concerning directly the quantities in the cross-section calculation Formula 6.1 can be evaluated by simply using the relative uncertainty.

7.1. Luminosity

The luminosity determines the total rate of collisions and all counting studies relate the cross section to the total number of events. An uncertainty on the luminosity affects the normalisation of the signal cross-section. The luminosity precision can reach a level of a few percent as it is shown in Section 5.6, depending on the detector and method used for the determination. It is expected that this precision will not be reached right at the beginning, so that a pessimistic scenario with an uncertainty of 20% is assumed for this study. The influence on the cross-section measurement is factorisable, so that it is quoted separately from the remaining systematic uncertainties.

7.2. Trigger and Lepton Identification Efficiencies

The trigger and lepton efficiencies are simulated in the MC and this influences the number of selected events. The efficiencies are determined in data and efficiency corrections for the MC selection are obtained. These corrections can be measured with the tag-and-probe method [208]. The precision of this method is assumed to be

1% in a conservative assumption for each trigger and lepton identification efficiency and for each lepton type. The total effect is 4% for each channel if the effects are assumed to be fully correlated. This effect was studied by simply increasing/reducing the number of selected events by 4% uniformly over all p_T and η regions for signal and background, but calculating the cross section assuming the nominal sum of expected signal and background events, N_{obs} . Table 7.1 shows the effect on the cross section applying only this systematic variation.

Table 7.1.: Cross section uncertainty due to a trigger efficiency and lepton identification efficiency variation of 4%.

Efficiency variation electrons	ee	$\mu\mu$	$e\mu$
+4%	5.7%	-	2.4%
-4%	-4.7%	-	-2.3%
Efficiency variation muons	ee	$\mu\mu$	$e\mu$
+4%	-	5.2%	2.4%
-4%	-	-4.8%	-2.3%

7.3. Missing Transverse Energy

The selection of the events requires a cut on the \cancel{E}_T value of the event and the signal acceptance is changed when varying the \cancel{E}_T scale. As seen in the Section 6.2 this suppresses Z -boson events substantially and an uncertainty on the scale would also affect this background contribution much. It is assumed that the largest contribution of this scale uncertainty comes from the uncertainty of the calorimeter-cell energy calibration. This uncertainty in turn would be reflected in the lepton and jet energy scale uncertainty. The simple approach is to use a full correlation between the \cancel{E}_T and the energy scale uncertainties. If the lepton/jet energies are varied, \cancel{E}_T is changed to preserve the total transverse momentum:

$$\text{If for all jets/leptons } i \quad [v_E, v_{px}, v_{py}, v_{pz}]'_i = [v_E, v_{px}, v_{py}, v_{pz}]_i \cdot (1 + ES) \quad (7.1)$$

$$\text{then } [\cancel{E}_{Tx}, \cancel{E}_{Ty}]' = [\cancel{E}_{Tx}, \cancel{E}_{Ty}] - \sum_{\text{all jets/leptons } i} [v_{px}, v_{py}]_i \cdot ES, \quad (7.2)$$

where v is the four-vector of the lepton/jets with their respective E , p_x , p_y , p_z components, the two missing transverse energy components $\cancel{E}_{Tx/y}$ and the energy scale factor ES .

Still, the uncertainty is related to several effects and the exact correlation is difficult to evaluate. The amount of missing transverse energy from instrumental effects (fake \cancel{E}_T , pile-up) and from the fraction of neutral particles in an event has an influence on the correlation between the uncertainty and the jet/lepton energy-scale uncertainty. Also the calibration of the cells that is used for the \cancel{E}_T calculation is lacking the jet-level calibration and finally cells unassigned to jets/leptons are not included in this procedure.

7.4. Lepton Energy Scale

As a cut on the lepton p_T is required in the event selection, an uncertainty in the lepton energy scale has an influence on the final result. The uncertainty is assumed to be $\pm 1\%$, since the lepton energy-scales can be determined very precisely with Z -boson events (see [208] and Sections 5.1 and 5.2). The lepton four-vectors are scaled after the reconstruction rather than scaling the calorimeter cluster energies and redoing the reconstruction. The scaling is applied before the object selection, so that leptons that were not selected before the scaling can pass the object-selection p_T -requirement. The \cancel{E}_T was scaled according to the scheme presented in previous Section 7.3. Table 7.2 shows the effect of this scaling on the signal efficiency, the number of background events and the cross section.

Table 7.2.: Change of the selection efficiency ε for signal, the number of background events N_{bkg} and the cross-section measurement due to the lepton energy scale (LES) uncertainty.

$LES + 1\%$	ee	$\mu\mu$	$e\mu$
$\Delta\varepsilon_{sig} [\%]$	0.1	0.1	0.1
ΔN_{bkg}	1.1	3.3	1.2
$\Delta\sigma/\sigma [\%]$	2.0	1.8	1.0
$LES - 1\%$	ee	$\mu\mu$	$e\mu$
$\Delta\varepsilon_{sig} [\%]$	0.0	-0.1	-0.1
ΔN_{bkg}	0.5	-0.1	-1.5
$\Delta\sigma/\sigma [\%]$	-0.9	-1.3	-0.9

7.5. Jet Energy Scale

Again, the cut on the jet p_T produces a dependence of the selection efficiency for signal and background events on the jet energy scale uncertainty. As for the leptons the jet four-vectors are only rescaled after the reconstruction and before object selection. Effects on the cluster threshold requirement during the jet reconstruction cannot be studied with this scheme. The scaling factor was doubled for jets that have $|\eta| > 3.2$, because it is assumed that the jet energy scale in the forward region is more difficult to determine. Jets that overlap with selected electrons within a $\Delta\mathcal{R} < 0.2$ are not subject to the rescaling. This follows the construction of the “MET_RefFinal” quantity. The energy measurement from cells that are identified as cells from reconstructed objects is replaced by the energy measurement of the object. In case jets and electrons share the same cells, the cell energies for the \cancel{E}_T calculation are replaced by the energy of the electron. The electron energy-uncertainty is neglected here, so that these “jets” do not modify \cancel{E}_T .

Figure 7.1 shows the average jet p_T for all jets before the selection as a function of η before and after the jet energy scale variation. The jet energy scale uncertainty is investigated here in two scenarios, a pessimistic one with an uncertainty of $\pm 10\%$ and an optimistic scenario with $\pm 5\%$.

\cancel{E}_T was scaled according to the scheme presented in Section 7.3. The effect on \cancel{E}_T can be seen in Figure 7.2 for the $t\bar{t}$ sample. The change of the jet energy scale has in combination with the \cancel{E}_T scaling the biggest effect on $Z \rightarrow e^+e^-$ and $Z \rightarrow \mu^+\mu^-$ events. Although both event types have similar number of jets and the jet- p_T spectrum is comparable, the \cancel{E}_T distribution in $Z \rightarrow \mu^+\mu^-$ have larger tails. This can be seen in Figure 7.3 that compares the \cancel{E}_T distribution for Z -boson and $t\bar{t}$ events after selecting events with two leptons and it persists even after the full event selection (see \cancel{E}_T distribution in Figures 6.5 and 6.6). This can cause the scale variation to have the opposite effect on the selection for the ee and $\mu\mu$ channel for a certain variation. This can be seen from Table 7.3.

7.6. PDF Uncertainties

The PDF uncertainty arises from the different PDF fits on global QCD fits to deep inelastic scattering and from the uncertainties of the fits themselves. The effect on the analysis is investigated by reweighting the events according to the best fit PDFs of each PDF dataset. Some examples are the PDFs from the CTEQ [27] or MRST [29, 30] collaborations. When the uncertainty of a specific PDF fit is investigated, the reweighting is done with a PDF error set. This represents a set of PDFs in which each diagonalised fit parameter is varied by $\pm 1\sigma$, so that for n

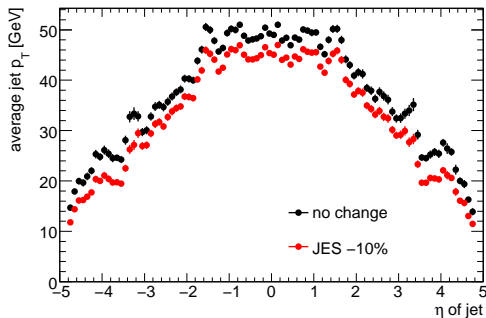


Figure 7.1.: Average jet p_T in bins of η for all jets before the selection between a nominal $t\bar{t}$ sample (black points) and a -10% jet energy scale varied sample (lighter points).

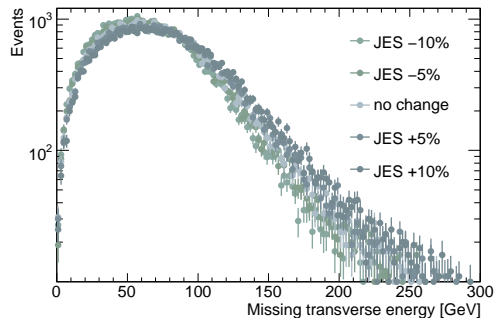


Figure 7.2.: \cancel{E}_T distribution for samples with different jet energy scale variations for a $t\bar{t}$ sample. The different jet energy scales are coloured from light colours to darker colours for -10% variation to $+10\%$ variation.

parameters $2 \cdot n$ error PDFs are available. The uncertainty due to this error set for a quantity ε is evaluated with the Hessian approach [27]:

$$\Delta\varepsilon = \frac{1}{2} \sqrt{\sum_i (\varepsilon_i^+ - \varepsilon_i^-)^2}. \quad (7.3)$$

The subscript i denotes the PDF where the i^{th} parameter is varied by 1σ and the superscripts $+$, $-$ denote the sign of the variation. As the final PDF uncertainty conservatively the largest value from either the uncertainty within an error PDF set or among the best fit PDFs is chosen.

Reweighting is required since the generation of events with a new PDF would require a re-running of the entire simulation chain which is not feasible given the large number of PDFs and error PDFs are evaluated. The reweighting method has known theoretical limits. The Sudakov form factors that are used for the calculation of the parton shower do not depend linearly on the PDF.

For the calculation of the weight the flavour i and j of the initial partons, the momentum fraction x_i and x_j and the momentum transfer Q^2 must be known. The original PDF is $f_{0,i}$ and the target PDF is $f_{N,i}$ for the initial parton flavour i . Each event is assigned to a weight w that is the following ratio:

$$w = \frac{f_{N,i}(x_i, Q^2) \cdot f_{N,j}(x_j, Q^2)}{f_{0,i}(x_i, Q^2) \cdot f_{0,j}(x_j, Q^2)}, \quad (7.4)$$

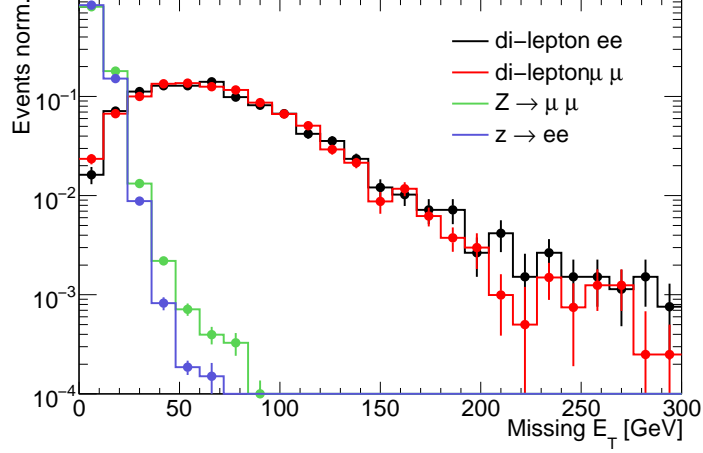


Figure 7.3.: Comparison of the \cancel{E}_T distribution for Z -boson and $t\bar{t}$ events after selecting events with two leptons. While the distributions for $t\bar{t}$ events are very similar, the $Z \rightarrow \mu^+\mu^-$ sample has a larger \cancel{E}_T tail compared to $Z \rightarrow e^+e^-$ events [232].

which is the ratio of the probabilities that a certain parton pair i and j with their corresponding momentum fractions $x_{i/j}$ and the momentum transfer Q^2 exists in the proton under the PDF f_0 and f_N .

This information is extracted from the truth information. With a centre-of-mass energy of $\sqrt{s} = 10$ TeV the fractions are calculated from the z -momentum p_z : $x_{i/j} = \frac{p_{z,i/j}}{5 \text{ TeV}}$. The momentum transfer is not obviously the energy transfer in the hard process, but it is defined by the MC generators such that it gives a smaller scale uncertainty in the calculation of the cross section. In the case of the $t\bar{t}$ processes generated with MC@NLO this is

$$Q^2 = \frac{p_T^2(\text{top}_1) + p_T^2(\text{top}_1)}{2} + m_{\text{top}}^2. \quad (7.5)$$

Due to the lack of information about the initial partons or the Q^2 calculation in the background samples, the reweighting is only applied to signal events. The MC@NLO $t\bar{t}$ sample was generated with the CTEQ6m PDF. The uncertainty is evaluated with the CTEQ6mE (20 parameters), MRST2001E (15 parameters), CTEQ6.6 (22 parameters) and MRST2006nnlo (15 parameters) PDFs. Since the CTEQ6.6 and MRST2006nnlo PDFs are updated versions of the other PDFs and they are at least calculated at NLO, only these versions of the PDFs are considered for the final uncertainty. Table 7.4 shows the uncertainty on the signal efficiency for the PDF sets and their corresponding error PDF sets and in Figures 7.4 the effect on the selection efficiency can be seen. As it is the largest uncertainty, the PDF

Table 7.3.: Change of the selection efficiency ε for signal, the number of background events N_{bkg} and the cross-section measurement due to the jet energy scale (JES) systematic uncertainty. Two scenarios are considered with 5% and 10% effect.

$JES + 5\%$	ee	$\mu\mu$	$e\mu$	$JES + 10\%$	ee	$\mu\mu$	$e\mu$
$\Delta\varepsilon_{sig} [\%]$	0.1	0.1	0.2		0.2	0.2	0.4
ΔN_{bkg}	5.6	-2.3	3.5		17.8	11.0	7.0
$\Delta\sigma/\sigma [\%]$	5.4	1.5	2.3		13.4	6.7	4.2
$JES - 5\%$	ee	$\mu\mu$	$e\mu$	$JES - 10\%$	ee	$\mu\mu$	$e\mu$
$\Delta\varepsilon_{sig} [\%]$	-0.1	-0.2	-0.2		-0.3	-0.4	-0.5
ΔN_{bkg}	-0.6	9.2	-2.9		0.9	29.6	-8.9
$\Delta\sigma/\sigma [\%]$	-3.0	-0.3	-2.2		-6.7	3.3	-5.5

uncertainty of the CTEQ PDF set is taken as the final result. Although there is a mismatch between the order of CTEQ6.6 (NLO) and the MRST'06nnlo, the difference between MRST'06nnlo and MRST'06nlo is smaller than the difference between the PDFs. This fact does not change the final result.

Table 7.4.: PDF systematic uncertainties on the selection efficiency ε for the different sub-channels. For comparison the Monte-Carlo statistical uncertainty on the efficiency is also given.

$\Delta\varepsilon/\varepsilon (= \Delta\sigma/\sigma) [\%]$	ee	$\mu\mu$	$e\mu$
statistical $\Delta\varepsilon$	2.0	1.6	1.1
CTEQ6.6	2.2	1.5	1.7
MRST2006nnlo*	0.6	0.3	0.4
(CTEQ6mE)	3.0	2.0	2.4
(MRST2001E)	1.1	0.7	0.8
difference between PDFs			
MRST2006nnlo to CTEQ6.6	-0.5	-0.3	-0.5
(MRST2001E to CTEQ6mE)	2.0	1.3	1.5
(CTEQ6.6 to CTEQ6mE)	-0.3	-0.3	-0.2

*About the order mismatch, see text.

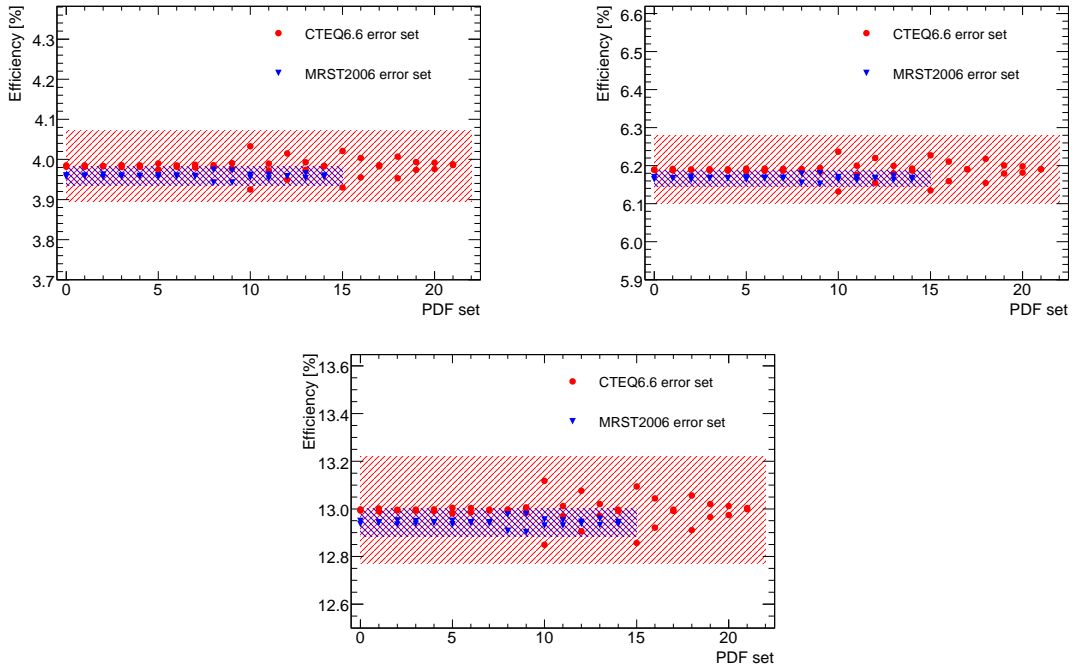


Figure 7.4.: PDF uncertainty in the different sub-channels (ee top left, $\mu\mu$ top right, $e\mu$ bottom) with the CTEQ6.6 and MRST2006nnlo error set. The x -axis denotes the number of the PDF parameter that was changed in the error PDF. Each point corresponds to a change of the parameter by $\pm 1\sigma$, there are 22 parameters for CTEQ6.6 and 15 parameters for MRST2006nnlo. The bands reflect the PDF uncertainty for the selection efficiency calculated with the Hessian approach.

7.7. Initial and Final State Radiation

As seen from Section 4.1 the theoretical description of ISR and FSR is only approximate and requires the introduction of a certain evolution ordering and cut-off scales. The ISR and FSR has an effect on the jet multiplicities in the signal and in the background samples. To cover the uncertainty of these scales, two samples with increased ISR and at the same time decreased FSR and vice versa have been produced. Originally, the samples were chosen such that the top-quark mass in the semi-leptonic channel reconstructed from three true quarks (b -quark and two quarks from the hadronically decaying W -boson) is shifted maximally up- and downwards as it can be seen in Figure 7.5. Only the change in jet multiplicities is the main effect for the uncertainty in the cross-section measurement. The distribution of the different samples can be seen in Figure 7.6. The parameters that steer the amount of radiation is the Λ_{QCD} scale at which the transition between matrix element and parton shower happens and the p_T cut-off for the shower evolution. Table 7.5 shows

the result for the different sub-channels that quotes the largest difference of the two ISR/FSR samples to the nominal sample.

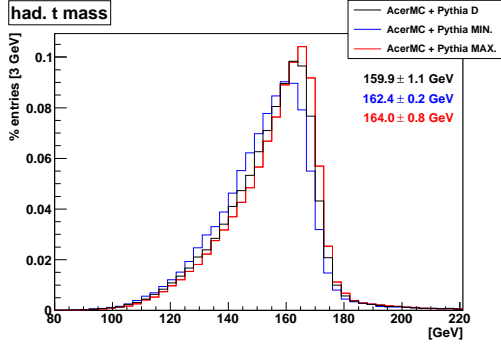


Figure 7.5.: Top-quark mass distribution, reconstructed from three true quarks (b -quark and two quarks from the hadronically decaying W -boson), for the ISR/FSR varied samples [202].

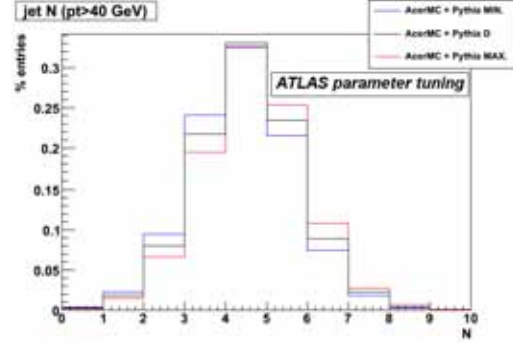


Figure 7.6.: Jet multiplicity distribution for ISR/FSR varied samples [202].

Table 7.5.: Initial and final state systematic uncertainties on the selection efficiency ε for the different sub-channels [232].

$\Delta\varepsilon/\varepsilon$ ($=\Delta\sigma/\sigma$) [%]	ee	$\mu\mu$	$e\mu$
ISR/FSR	5.2	4.0	2.2

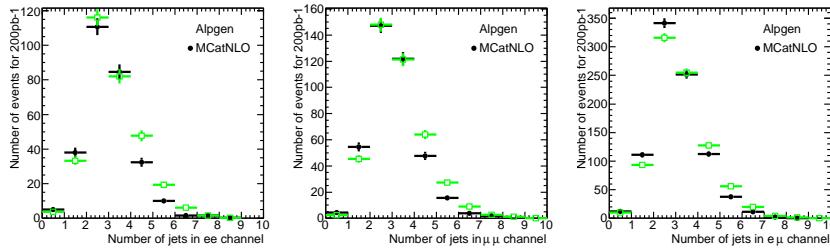
7.8. Monte-Carlo-Model

Although from a theoretical point of view the Monte-Carlo calculations at NLO are believed to be the most precise calculation in existence, there is no direct comparison of the predicted shapes with the shapes from data, yet. A conservative estimation of the uncertainties is done by comparing different generators for the $t\bar{t}$ -signal process and the largest difference is taken as the systematic uncertainty. For this study only two LO generators are available, ACERMC and ALPGEN, that can be compared to the main NLO generator MC@NLO. Table 7.6 shows the relative differences between the number of selected events after each cut in the different sub-channels comparing the two LO generators with MC@NLO.

While the ACERMC sample agrees with the nominal sample within 3%, the ALPGEN sample differs by over 10%. Figure 7.7 shows that the largest difference arises from the jet multiplicity distribution.

Table 7.6.: Relative difference of the number of selected events between a MC@NLO and ACERMC or ALPGEN $t\bar{t}$ sample [232].

relative difference	lepton selection	inv. mass cut	\cancel{E}_T cut	jet cut
ACERMC				
ee	-2.1%	-2.3%	-4.7%	-2.7%
$\mu\mu$	2.7%	2.8%	2.3%	1.9%
$e\mu$	1.5%	1.6%	1.7%	2.0%
ALPGEN				
ee	5.1%	6.4%	6.0%	10.8%
$\mu\mu$	4.0%	4.4%	5.6%	9.6%
$e\mu$	0.1%	0.5%	3.0%	5.4%


Figure 7.7.: Differences in the jet multiplicity distribution for all these sub-channels (from left to right: ee , $\mu\mu$ and $e\mu$) between the generators MC@NLO and ALPGEN [232].

7.9. Theoretical Cross Section

Uncertainties in the normalisation of the Monte-Carlo simulations are investigated by changing the theoretical cross section within their uncertainties. Especially for the background processes, this is the only feasible method to study MC model uncertainties due to the lack of samples from different MC generators. For the Drell-Yan background the normalisation is taken from the data-driven methods. For the other backgrounds an uncertainty of 5% is assumed, this is supported by e.g. [234], which estimates for the diboson events an uncertainty of 3% from scale uncertainties and of 4% from PDF uncertainties. Only for the single top-quark Wt background a larger uncertainty of 8% is assumed, according to [205].

7.10. Drell-Yan Background Estimation

The systematic uncertainties for the data-driven background estimation of the Drell-Yan background is obtained by varying the cut values of the grid in the \cancel{E}_T and m_{ll} space. \cancel{E}_T is lowered to 10 GeV and the Z -boson window is widened by 1 GeV to cover the range of $85 \text{ GeV} < m_{ll} < 97 \text{ GeV}$. The total systematic uncertainties from this window shift is 15% for the ee and $\mu\mu$ channel for an integrated luminosity of $\mathcal{L}_{\text{int.}}=200 \text{ pb}^{-1}$.

7.11. Jets Misidentified as Leptons

The systematic uncertainties for the fake event rate can currently be derived only from the difference between the two control regions. The limited statistics of the QCD sample that is available for this study does not allow an accurate extrapolation to the signal region. From the experience for early data analyses at the Fermilab Tevatron Collider with an uncertainty of the order of 50 – 100%, the uncertainty here is taken as 100% for electrons and 50% for muons.

7.12. Summary of Statistical and Systematic Uncertainties for the Analysis at $\sqrt{s}=10 \text{ TeV}$ and $\mathcal{L}_{\text{int.}}=200 \text{ pb}^{-1}$

The values for the systematic uncertainties are summarised in Table 7.7 together with the statistical uncertainty for $\mathcal{L}_{\text{int.}} = 200 \text{ pb}^{-1}$. The last column simply uses the sum of all events in all channels and the systematic uncertainty is investigated with these events.

The largest uncertainties come from the jet energy scale and the chosen MC model. For events with electrons the uncertainty on the fake event rate becomes the largest uncertainty.

7.13. Pile-up Effects

Although the effects from pile-up are not considered in the list of systematic uncertainties, this effect has to be studied. There are two types of pile-up effects that can influence the dilepton selection. The first is the multiple proton-proton interactions that will cause an overlap of two hard interactions. The second effect is detector pile-up that is caused by slow detector components that have not reached their initial state before the next collision happens. This will cause overlap effects that partially look like two hard-interactions, but are the remnant of the previous

Table 7.7.: Summary of the systematic uncertainties considered for the analysis at $\sqrt{s} = 10$ TeV and for $\mathcal{L}_{\text{int.}} = 200 \text{ pb}^{-1}$. The last column with the combination is the systematic effect for the sum of all events in the three sub-channels. For comparison also the statistical uncertainty is shown.

Uncertainty [%]	ee	$\mu\mu$	$e\mu$	Combination
Statistical	7.8	6.2	4.4	3.1
Luminosity	20	20	20	20
e eff.	-4.7 / 5.7	-	-2.3 / 2.2	-2.6 / 1.8
μ eff.	-	-4.8 / 5.2	-2.3 / 2.4	-2.6 / 2.7
JES	-3.0 / 5.4	-0.3 / 1.5	-2.2 / 2.3	-1.8 / 2.6
LES	-0.9 / 2.0	-1.3 / 1.8	-0.9 / 1.0	-1.0 / 1.4
PDF	2.2	1.5	1.7	1.7
ISR/FSR	5.2	4.0	2.2	3.1
MC model	-9.5 / 11.6	-9.2 / 11.3	-9.4 / 11.4	9.3 / 11.4
Theo. cross.	0.7	0.5	0.7	0.7
D-Y background	0.9	2.1	0.1	0.8
Lepton fakes	11.4	2.6	8.1	7.2

collision. Until now the MC samples do not include any multiple interactions nor detector pile-up.

Pile-up effects will strongly depend on the beam conditions for the first data. For this study an instantaneous luminosity of $\mathcal{L}_{\text{inst.}} = 10^{32} \text{ cm}^{-2} \text{ s}^{-1}$ and a bunch spacing of 450 ns is assumed. This will result in an average number of proton-proton interactions of four per bunch crossing. Included in the MC samples are also cavern background effects like back-scattered neutrons. The samples are limited to the $t\bar{t}$ samples, $Z \rightarrow e^+e^-$ and $Z \rightarrow \mu^+\mu^-$ and only the main effects are discussed here. The conclusions do not enter the final systematic uncertainty result and should be seen as an outlook on further studies with pile-up simulation samples.

For the $t\bar{t}$ sample the general tendency is that the total jet multiplicity increases, so that the acceptance due to the jet multiplicity requirement increases. This can be seen in Figures 7.8. The acceptance for channels with muons decreases due to effects from the cavern background on the muon spectrometer. The lepton isolation energy increases, so that the acceptance for leptons decreases. This effect can be seen in Figure 7.9 for electrons. In the electron selection this effect is compensated by the increased fake rate due to the increased jet multiplicity. The total acceptance is almost unchanged due to all effects.

Background events such as $Z \rightarrow \ell^+\ell^-$ are partially suppressed by the requirement on the jet multiplicity, so that the increase of the average jet multiplicity will have an impact on the S/B ratio. The effect has a strong jet- p_T dependence, so that a

higher jet- p_T cut can reduce the difference between the selection with and without pile-up.

The conclusion is that the effect of pile-up seems to have compensating effects on the signal acceptance and the increased acceptance by the higher jet multiplicity can be recovered. Still, not all background processes have been studied and a more detailed optimisation with a more precise pile-up description has to be performed.

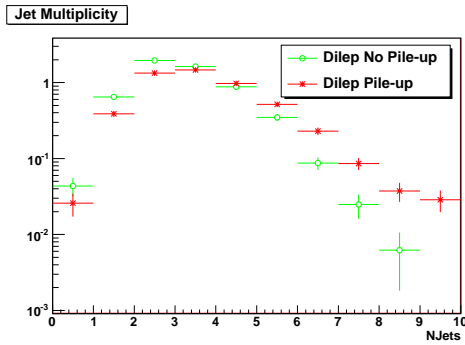


Figure 7.8.: Jet multiplicity distribution for selected dilepton events in samples with (crosses) and without (open circles) pile-up [232].

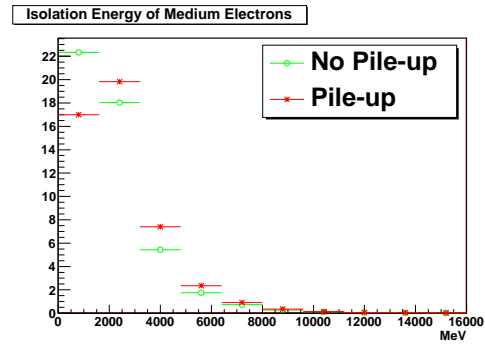


Figure 7.9.: Distribution of the isolation energy for electrons with pile-up (crosses) and without (open circles) pile-up [232].

8. Expected Precision of ATLAS for the $t\bar{t}$ Cross-Section Measurement

The expected sensitivity of the study for an integrated luminosity of $\mathcal{L}_{\text{int.}}=200 \text{ pb}^{-1}$ and a centre-of-mass energy of $\sqrt{s}=10 \text{ TeV}$ is summarised here. A likelihood is constructed and it uses the results from the Chapters 6 and 7 to correlate the systematic effects in each sub-channel and in a combination of all channels. Implicitly a total correlation between the systematic effects in all sub-channels is assumed. The outcome is comparable to the approach when the systematic effects are evaluated separately and are treated as being uncorrelated. The result quotes the statistical, systematic and luminosity uncertainties.

In the end a possibility is shown, how one can define a top-mass like distribution such that it can be used to cross-check the $t\bar{t}$ dilepton signal. This can help to identify possible pollution of the event selection by dilepton-like events from e.g. new physics.

8.1. Combination of Uncertainties

The statistical and systematic uncertainties are calculated using a special pseudo dataset. The so-called Asimov dataset [235] consists of distributions for every observable, which are derived from the MC models and are scaled to the desired integrated luminosity. This scaling does not introduce any statistical fluctuations.

The 68% and 95% (1 and 2 σ) confidence levels are derived from a likelihood function. The number of observed events N_{obs} follows a Poissonian distribution around an expected number of events $N_{\text{exp}}^{\text{tot}}$ from all signal and background contributions k :

$$L(\sigma_{\text{sig}}) = \text{Poiss}(N_{\text{obs}}|N_{\text{exp}}^{\text{tot}}) = \text{Poiss}(N_{\text{obs}}|\sum_k N_{\text{exp}}^{(k)}). \quad (8.1)$$

The expected number of events, if not derived directly from data-driven methods, is generally a product of the cross section, $\sigma^{(k)}$, for a sample k and the product of several efficiencies, $\varepsilon^{(j)}$, (the integrated luminosity is abbreviated as \mathcal{L}):

$$N_{\text{exp}}^{(k)} = \mathcal{L}\sigma^{(k)} \prod_j \varepsilon^{(j,k)}. \quad (8.2)$$

The uncertainty on the luminosity can be added to the likelihood by multiplying a Gaussian distribution of the luminosity around the nominal estimate, $\tilde{\mathcal{L}}$, with its uncertainty, $\Delta_{\mathcal{L}}$, given the true luminosity \mathcal{L} :

$$L(\sigma_{\text{sig}}, \mathcal{L}) = \text{Poiss}(N_{\text{obs}}|N_{\text{exp}}^{\text{tot}}) \times \text{Gauss}(\tilde{\mathcal{L}}|\mathcal{L}, \Delta_{\mathcal{L}}). \quad (8.3)$$

Similarly the uncertainties for the efficiencies, $\Delta_{\varepsilon^{(j,k)}}$, are introduced. It is convenient to consider the ratio of the nominal estimate, $\tilde{\varepsilon}^{(j,k)}$, and the true efficiency, $\varepsilon^{(j,k)}$, and express the number of expected events in terms of the nominal estimate for the expected number of events, $\tilde{N}_{\text{exp}}^{(k)}$:

$$N_{\text{exp}}^{(k)} = \mathcal{L}\sigma^{(k)} \prod_j \tilde{\varepsilon}^{(j,k)} \frac{\varepsilon^{(j,k)}}{\tilde{\varepsilon}^{(j,k)}} = \tilde{N}_{\text{exp}}^{(k)} \prod_j \frac{\varepsilon^{(j,k)}}{\tilde{\varepsilon}^{(j,k)}}, \quad (8.4)$$

$$L(\sigma_{\text{sig}}, \mathcal{L}, \varepsilon^{(j,k)}) = \text{Poiss}(N_{\text{obs}}|N_{\text{exp}}^{\text{tot}}) \times \text{Gauss}(\tilde{\mathcal{L}}|\mathcal{L}, \Delta_{\mathcal{L}}) \times \prod_j \text{Gauss}(\tilde{\varepsilon}^{(j,k)}|\varepsilon^{(j,k)}, \Delta_{\varepsilon^{(j,k)}}). \quad (8.5)$$

The uncertainties for the efficiencies are usually only available at $\pm 1\sigma$ variations $\varepsilon^{(j,k)}(\pm 1\sigma)$. In order to have a linear interpolation and a correlated variation among all channels k a new variable $\alpha^{(j)}$ is introduced:

$$\varepsilon^{(j,k)}(\alpha^{(j)}) = \begin{cases} \varepsilon^{(j,k)} + \alpha^{(j)}(\varepsilon^{(j,k)}(+1\sigma) - \varepsilon^{(j,k)}) & \text{if } \alpha^{(j)} > 0 \\ \varepsilon^{(j,k)} & \text{if } \alpha^{(j)} = 0 \\ \varepsilon^{(j,k)} + \alpha^{(j)}(\varepsilon^{(j,k)}(-1\sigma) - \varepsilon^{(j,k)}) & \text{if } \alpha^{(j)} < 0 \end{cases}, \quad (8.6)$$

$$N_{\text{exp}}^{(k)} = \mathcal{L}\sigma^{(k)} \prod_j \tilde{\varepsilon}^{(j,k)} \frac{\varepsilon^{(j,k)}(\alpha^{(j)})}{\tilde{\varepsilon}^{(j,k)}} = \tilde{N}_{\text{exp}}^{(k)} \prod_j \frac{\varepsilon^{(j,k)}(\alpha^{(j)})}{\tilde{\varepsilon}^{(j,k)}}, \quad (8.7)$$

$$L(\sigma_{\text{sig}}, \mathcal{L}, \alpha^{(j)}) = \text{Poiss}(N_{\text{obs}}|N_{\text{exp}}^{\text{tot}}) \times \text{Gauss}(\tilde{\mathcal{L}}|\mathcal{L}, \Delta_{\mathcal{L}}) \times \prod_j \text{Gauss}(\tilde{\alpha}^{(j)}|\alpha^{(j)}, \Delta_{\alpha^{(j)}} = 1). \quad (8.8)$$

This likelihood can be extended to combine the sub-channels ee , $\mu\mu$ and $e\mu$, indexed with i :

$$L(\sigma_{\text{sig}}, \mathcal{L}, \alpha^{(j)}) = \prod_{i \in \{ee, \mu\mu, e\mu\}} \left[\text{Pois}(N_{\text{obs}}^{(i)} | N_{\text{exp}}^{\text{tot}, i}) \times \text{Gauss}(\tilde{\mathcal{L}} | \mathcal{L}, \Delta_{\mathcal{L}}) \times \prod_j \text{Gauss}(\tilde{\alpha}^{(j)} | \alpha^{(j)}, \Delta_{\alpha^{(j)}} = 1) \right]. \quad (8.9)$$

With this likelihood the statistical and systematic uncertainties can be evaluated on the Asimov dataset. The maximum of the function gives the best estimates $\hat{\sigma}_{\text{sig}}$, $\hat{\mathcal{L}}$ and $\hat{\alpha}^{(j)}$. The likelihood ratio r at this point is defined as

$$r(\sigma_{\text{sig}}) = \frac{L(\sigma_{\text{sig}}, \hat{\mathcal{L}}, \hat{\alpha}^{(j)})}{L(\hat{\sigma}_{\text{sig}}, \hat{\mathcal{L}}, \hat{\alpha}^{(j)})}, \quad (8.10)$$

and the profile likelihood λ is defined with the conditional best estimates $\hat{\mathcal{L}}$ and $\hat{\alpha}^{(j)}$ with the condition that σ_{sig} is fixed:

$$\lambda(\sigma_{\text{sig}}) = \frac{L(\sigma_{\text{sig}}, \hat{\mathcal{L}}, \hat{\alpha}^{(j)})}{L(\hat{\sigma}_{\text{sig}}, \hat{\mathcal{L}}, \hat{\alpha}^{(j)})}. \quad (8.11)$$

The range of σ_{sig} for which $-2 \log r(\sigma_{\text{sig}}) < 1$ will cover the 68% probability range. The difference between the ranges of the profile likelihood and the likelihood ratio can be attributed to the systematic effects.

Figures 8.1 and 8.2 show the likelihood ratio and profile likelihoods for the different sub-channels and the combination of all channels. The values of the likelihood for the $1 - 3\sigma$ ranges are indicated in the figures.

Table 8.1 lists the statistical uncertainties and the breakdown of the systematic uncertainties for each sub-channel and the combination. The luminosity uncertainty is treated separately, so that this uncertainty can be changed with an updated estimate. This table is comparable with the uncertainties listed separately in Table 7.7. The correlations decrease some of the systematic uncertainties and the uncertainties become asymmetric, because some of the background samples have low statistics. Table 8.2 shows the breakdown of the correlation between the systematic effects. Strong correlations between e.g. luminosity and the cross section are as expected.

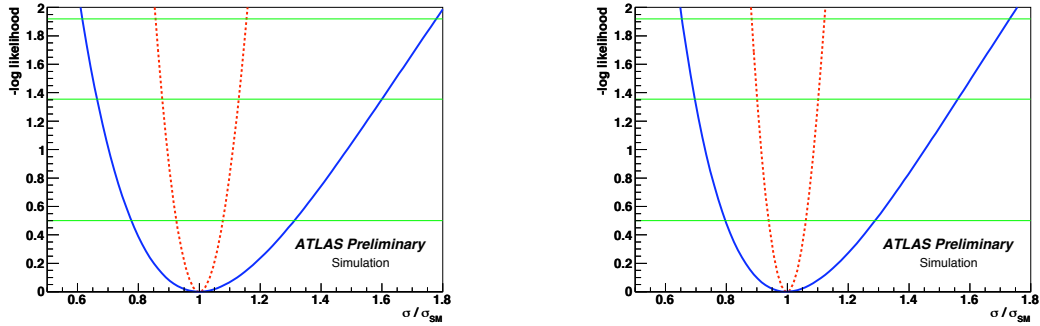


Figure 8.1.: Profile likelihood (full line) and likelihood ratio (dotted line) for the ee (left) and $\mu\mu$ channel (right). The dotted line represents the statistical likelihood function, whereas the full line includes the systematic uncertainties. The horizontal lines indicate likelihood values for the $1 - 3\sigma$ ranges [232].

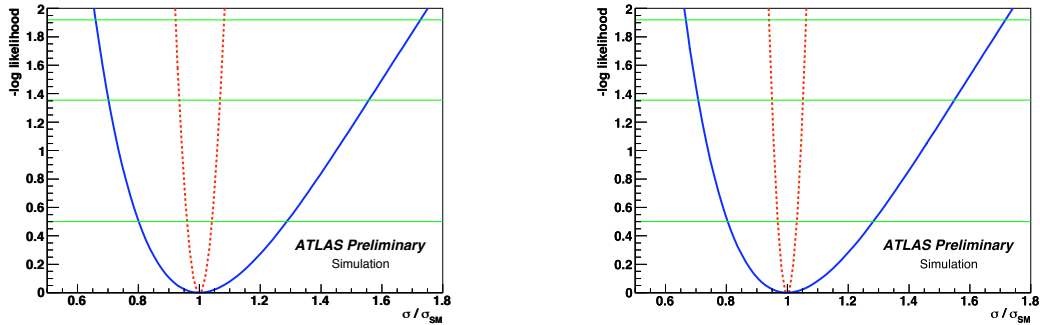


Figure 8.2.: Profile likelihood (full line) and likelihood ratio (dotted line) for the $e\mu$ channel (left) and the combination of all channels (right). The dotted line represents the statistical likelihood function, whereas the full line includes the systematic uncertainties. The horizontal lines indicate likelihood values for the $1 - 3\sigma$ ranges [232].

Table 8.1.: Individual contributions to the relative uncertainty on the cross section expected for an integrated luminosity of $\mathcal{L}_{\text{int.}}=200 \text{ pb}^{-1}$ and a centre-of-mass energy of $\sqrt{s}=10 \text{ TeV}$ for each of the channels individually and in combination [232]. The uncertainties are listed as “negative uncertainty / positive uncertainty”. They are asymmetric and define a 68% confidence interval.

$\Delta\sigma/\sigma$ (%)	ee	$\mu\mu$	$e\mu$	combination
Stat only	-7.5 / 7.8	-6.0 / 6.2	-4.0 / 4.1	-3.1 / 3.1
Luminosity	-17.3 / 26.3	-17.4 / 26.2	-17.4 / 26.2	-17.4 / 26.2
e efficiency	-4.5 / 5.0	/	-2.2 / 2.4	-1.9 / 1.9
μ efficiency	/	-4.6 / 5.2	-2.1 / 2.2	-2.2 / 2.3
Jet energy scale	-3.4 / 3.2	-3.0 / 4.5	-2.5 / 2.5	-2.8 / 3.0
Lepton energy scale	-0.3 / 1.6	-2.4 / 2.0	-0.5 / 0.5	-0.8 / 0.8
PDF uncertainty	-2.1 / 2.3	-1.4 / 1.6	-1.6 / 1.8	-1.7 / 1.8
ISR/FSR	-4.0 / 4.2	-3.6 / 3.7	-3.5 / 3.5	-3.6 / 3.7
MC model	-4.7 / 5.4	-4.6 / 5.4	-4.7 / 5.3	-4.7 / 5.3
Theo. cross section	-0.3 / 0.3	-0.3 / 0.3	-0.3 / 0.3	-0.3 / 0.3
D-Y background	-1.4 / 1.3	-2.2 / 2.2	-0.5 / 0.5	-0.8 / 0.9
Lepton fakes	-9.7 / 9.5	-1.1 / 1.1	-6.2 / 6.2	-4.0 / 4.0
All syst., but \mathcal{L}	-12.7 / 13.9	-8.9 / 10.2	-9.4 / 10.2	-8.7 / 9.6
All syst. uncert.	-21.0 / 30.3	-19.3 / 28.3	-19.5 / 28.5	-19.3 / 28.1
Stat. + Syst.	-22.3 / 31.3	-20.2 / 29.0	-19.9 / 28.8	-19.5 / 28.3

Table 8.2.: The correlation coefficients for the combined fit including all systematic uncertainties [232]. The diagonal elements are unity by definition. The non-zero off-diagonal elements indicate a correlated impact on the final observables.

\mathcal{L}	$\frac{\sigma_{\text{sig}}}{\sigma_{\text{SM}}}$	e efficiency	μ efficiency	Jet energy scale	Lepton energy scale e	Lepton energy scale μ	PDF uncertainty	ISR/FSR	MC model	Theoretical cross section	Data-driven Drell-Yan ee	Data-driven Drell-Yan $\mu\mu$	Fake leptons	
\mathcal{L}	1.00	-0.91												
$\frac{\sigma_{\text{sig}}}{\sigma_{\text{SM}}}$	-0.91	1.00	-0.06	-0.16	-0.14	-0.01	-0.04	-0.07	0.15	-0.22	-0.01	-0.02	-0.04	-0.21
e efficiency		-0.06	1.00	0.11	0.02		0.04	-0.02	0.01		-0.02	0.04	-0.23	
μ efficiency		-0.16	0.11	1.00	-0.04		-0.05	0.02	-0.01		0.02	-0.06	0.25	
Jet energy scale		-0.14	0.02	-0.04	1.00	0.01	-0.03		0.01		-0.01	-0.04	0.09	
Lepton energy scale e		-0.01			0.01	1.00	0.01					0.01	-0.01	
Lepton energy scale μ		-0.04	0.04	-0.05	-0.03	0.01	1.00					-0.03	0.11	
PDF uncertainty		-0.07	-0.02	0.02				1.00					-0.03	
ISR/FSR		0.15	0.01	-0.01	0.01				1.00				0.01	
MC model		-0.22								1.00				
Theoretical cross section		-0.01									1.00			
Data-driven Drell-Yan ee		-0.02	-0.02	0.02	-0.01							1.00	-0.03	
Data-driven Drell-Yan $\mu\mu$		-0.04	0.04	-0.06	-0.04	0.01	-0.03						1.00	0.12
Fake leptons		-0.21	-0.23	0.25	0.09	-0.01	0.11	-0.03	0.01		-0.03	0.12		1.00

The total sensitivity for the cross-section measurement of the dileptonic $t\bar{t}$ channel at a centre-of-mass energy of $\sqrt{s} = 10$ TeV and an anticipated, integrated luminosity of $\mathcal{L}_{\text{int.}} = 200 \text{ pb}^{-1}$ can be summarised as follows:

$$\frac{\Delta\sigma_{ee}}{\sigma_{ee}} [\%] = {}^{+7.8}_{-7.5}(\text{stat})^{+13.9}_{-12.7}(\text{syst})^{+26.3}_{-17.3}(\text{lumi}) \quad (8.12)$$

$$\frac{\Delta\sigma_{\mu\mu}}{\sigma_{\mu\mu}} [\%] = {}^{+6.2}_{-6.0}(\text{stat})^{+10.2}_{-8.9}(\text{syst})^{+26.2}_{-17.4}(\text{lumi}) \quad (8.13)$$

$$\frac{\Delta\sigma_{e\mu}}{\sigma_{e\mu}} [\%] = {}^{+4.1}_{-4.0}(\text{stat})^{+10.2}_{-9.4}(\text{syst})^{+26.2}_{-17.4}(\text{lumi}) \quad (8.14)$$

$$\frac{\Delta\sigma_{\text{combined}}}{\sigma_{\text{combined}}} [\%] = {}^{+3.1}_{-3.1}(\text{stat})^{+9.6}_{-8.7}(\text{syst})^{+26.2}_{-17.4}(\text{lumi}) \quad (8.15)$$

The dilepton cross-section measurement is clearly dominated by systematic effects. While the statistical uncertainty is between 4% in the $e\mu$ channel and 8% in the ee channel, the systematic uncertainty is around 9–14%, excluding luminosity. This is dominated by the jet energy scale, the MC model and, for channels with electrons, by the electron fake rate uncertainty. When the luminosity is included, this becomes the largest systematic uncertainty.

8.2. Cross-Check of Dilepton Top-Pair Events with the Stransverse Mass

The simple cut-and-count analysis that is used for the selection of dileptonic top-quark events exploits kinematic properties of the individual decay products only. Due to the two neutrinos, it is not simply possible to reconstruct all the kinematics in the system, especially the kinematics of the top quarks. The decay pattern in principle could also apply to numerous processes that are predicted in new physics models. Some of the patterns are shown in Figure 8.3: two identical particles decay into numerous visible particles and into a number of invisible particles. If the top-quark pair is not directly produced from e.g. gluon fusion, but via a pair of heavier mother particles, the kinematic selection would not necessarily be sensitive to this. A kinematic reconstruction of the decay can provide better insight into the mother particle.

The top quark in the semi-leptonic channel can be reconstructed simply by adding the four vectors of the visible b -quark jet and the light jets from a hadronically decaying W -boson. Large systematic effects arise from the assignment of the jets to the correct top quark. Still, Figure 8.4 shows the invariant three-jet mass distribution for the jets with the highest p_T and a broad peak around the top-quark mass can be seen. The combinatorial background can be reduced further by constraining any two jet combination to the invariant mass of the W -boson, as shown in Figure 8.5.

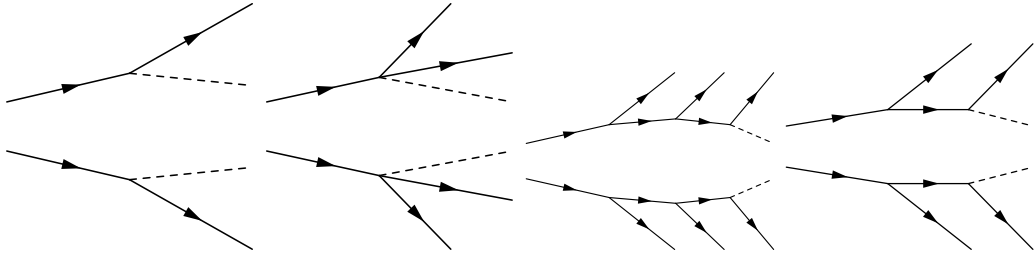


Figure 8.3.: Configuration of particle decays that can be used with the m_{T2} variable to determine the mass of the mother particle [236]. Both mother particles need to be identical. The dotted lines are particles that escape the direct detection and only the transverse energy component can be measured.

The peak is even more pronounced. With b -tagging of the jets this combinatorial effect could be even reduced further. The leptonic top quark can be reconstructed by solving kinematic equations and the solution has a two-fold ambiguity.

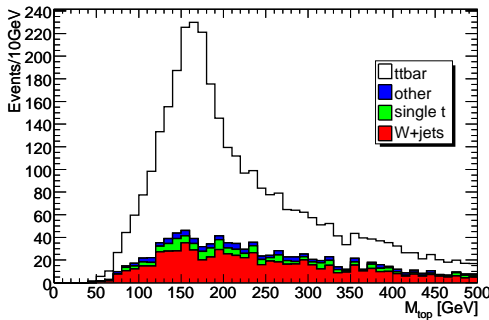


Figure 8.4.: Hadronic top-quark mass “peak” in the semi-leptonic channel [208].

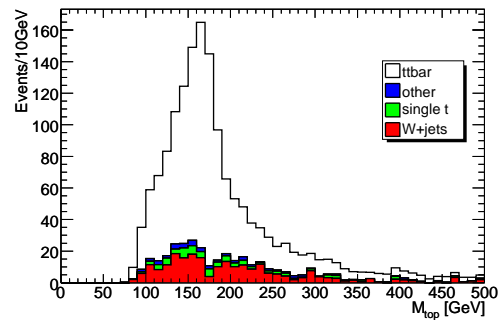


Figure 8.5.: Hadronic top-quark mass “peak” in the semi-leptonic channel with the W -boson mass constraint [208].

For the dileptonic top-quark decay there does not exist such a simple kinematic reconstruction, since the system of kinematic equations is underdetermined. The kinematics can be solved by a quadratic equation [237] with a four-fold ambiguity and additional inputs are needed such as the W -boson mass and the top-quark mass. In addition, the efficiency of solving the equation drops if the input variables are smeared by e.g. detector resolutions, so that in practice these equations are very unstable. An alternative method is the collinear approximation, which is used in $H \rightarrow \tau\bar{\tau} \rightarrow l\bar{\nu}l\nu\bar{\nu}\nu$ searches, where the direction of the neutrinos is approximated to be in the same direction as the leptons. In the case of top-quark events the approximation is not so good, since the leptons from a W -boson decay are not

boosted as much as in the case of the tau leptons and hence the direction of the neutrinos cannot be approximated by the direction of the leptons.

Stransverse mass m_{T2}

An ansatz, made when measuring the W -boson mass, is to use the transverse mass, $m_T = \sqrt{2p_T^{\text{lepton}} p_T^{\nu}(1 - \cos \Delta\phi)}$, with the transverse momentum of the lepton, p_T^{lepton} , the transverse momentum of the neutrino, p_T^{ν} , and the angle, $\Delta\phi$, between them in the transverse plane. In this case a mass peak is not expected, but a kinematic edge can be seen, as shown in Figure 8.6 for the W -boson transverse mass.

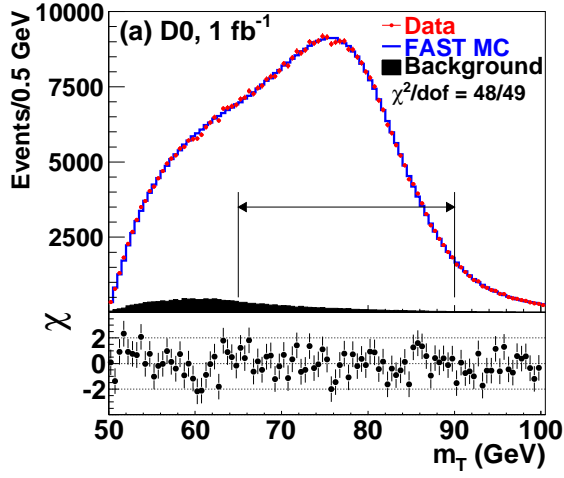


Figure 8.6.: Transverse W -boson mass distribution that is used to measure the W -boson mass at e.g. D0 [238]. The kinematic edge is smeared out by detector effects. A fit to the shape to simulations with different W -boson mass hypotheses is used to determine the mass.

In the case of the dileptonically decaying top quark, there are two neutrinos in the system, so that the procedure is more elaborate. A new variable is introduced which is named stransverse mass, m_{T2} [239].

$$m_{T2}^2 = \left[\max\{m_T^2(p_T^{lj(1)}, \not{p}_{(1)}), m_T^2(p_T^{lj(2)}, \not{p}_{(2)})\} \right] \rightarrow \text{minimise with } \not{p}_{(1)} + \not{p}_{(2)} = \cancel{E}_T, \quad (8.16)$$

where

$$m_T^2(p_T^{lj(i)}, \not{p}_{(i)}) = m_{lj(i)}^2 + m_{\not{p}_{(i)}}^2 + 2[E_T^{lj(i)} E_T^{\not{p}_{(i)}} - \vec{p}_T^{lj(i)} \cdot \vec{p}_T^{\not{p}_{(i)}}], \quad (8.17)$$

and

$$E_T = \sqrt{m^2 + p_T^2}, \quad (8.18)$$

with the transverse momentum of the composite object of one lepton and one jet, $\vec{p}_T^{lj(i)}$, of the trial neutrino, $\not{p}_{(i)}$, and their transverse energy, E_T , and masses, m . The minimisation of equation 8.16 uses trial momenta for the neutrinos, which only have to satisfy the measured \cancel{E}_T . The quantity that is minimised is the maximum of the transverse mass of each top that is formed by a pair lepton/jet and the “trial” neutrino. Ideally, the lepton and jet pairing should be the lepton and the b -quark jet from the same top quark. Since this is unknown in data, for the two possible combinations of the two highest p_T jets and leptons m_{T2} is calculated and the smallest value is chosen.

The distribution has a sensitivity on the mass scale of the dileptonically decaying mother particle. In the case of the $t\bar{t}$ -dilepton signal the distribution shows an end-point at the mass of the top-quark such that $m_{T2} \leq m_{\text{top}}$. For particles with a higher mass and a dilepton final state that is selected by the event selection, the transverse mass distribution would shift to higher values. The following discussion is not targeted at measuring the mass of new particles or the discovery thereof. It establishes something similar to the top-quark mass peak for the semi-leptonic channel. It motivates a distribution that depends on a characteristic feature, the top-quark mass, of events that are compatible with dilepton top-quark pair events.

m_{T2} distribution for true top-quark events

The application of the m_{T2} calculation on true top-quark events with kinematics at the generator level is shown in Figure 8.7. Here the b -quark from the top-quark decay is used as “jet”. MC@NLO $t\bar{t}$ events at a centre-of-mass energy of $\sqrt{s} = 7$ TeV are used¹ and the events are selected such that the two top quarks decay into a W -boson that decays leptonically. Also different methods of jet-to-lepton pairing are tested. The correct pairs of jets and leptons do not necessarily have the same order in p_T , are spatially close together or have the smallest invariant mass $m(lb)$. The best pairing can be achieved as described above, by choosing the combination that gives the smallest m_{T2} .

The dependence on the mass of the mother particle can be seen in Figure 8.8. Here the calculation of m_{T2} was done on samples with top-quark masses ranging from 160 to 190 GeV.

Two additional distributions have been made to test the reliability of this method. The first can be seen in Figure 8.9 where, instead of a vectorial p_T sum of the true neutrinos, the total missing transverse energy in the event was used. This includes all neutral particles from other decays or hadronisation processes in the event. This shifts \cancel{E}_T towards higher values. This represents a mis-measurement of \cancel{E}_T . From

¹The discussion about the difference of the distribution at $\sqrt{s} = 10$ TeV and at $\sqrt{s} = 7$ TeV centre-of-mass energy follows later.

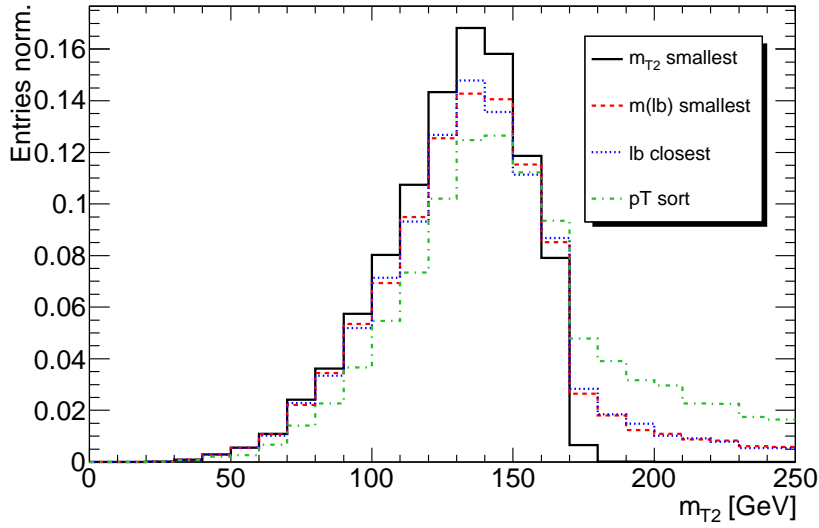


Figure 8.7.: m_{T2} distribution for true top-quark events with different methods to combine the lepton and the b -quark in the event. The method to calculate m_{T2} for both permutations and taking the smallest value gives the best kinematic edge. Other methods are the p_T sorting of the pairs, the smallest invariant lepton-jet mass and the pairing by spatial distance.

the figure it can be seen that this causes the edge to smooth out and that there are events with m_{T2} higher than the allowed edge.

The other test is to use only the leptons and ignoring the jets. This can be used to probe the W -boson mass. From Figure 8.10 the kinematic edge at 80 GeV can be seen. It does not depend on the mass of the top-quarks that decayed into the W -boson.

m_{T2} distribution for reconstructed events

The calculation is now tested on reconstructed events. To increase the acceptance, events are not selected by the full cut flow as described in Section 6.1. Instead, only two good leptons and two good jets are required. Again, samples with different top-quark masses are used to demonstrate the dependence of the edge on the mass of the mother particle. From Figure 8.11 it can be seen that still an edge is visible, but the distribution does not fall off to zero and has a non-negligible tail towards higher m_{T2} values. It is caused by the detector resolution that smears the measured input quantities. Also wrong pairing of the jets to the leptons dilute the kinematic edge.

The power of this variable to distinguish between a dileptonic top-quark pair decay and a heavier new particle can be tested with a SUSY benchmark scenario.

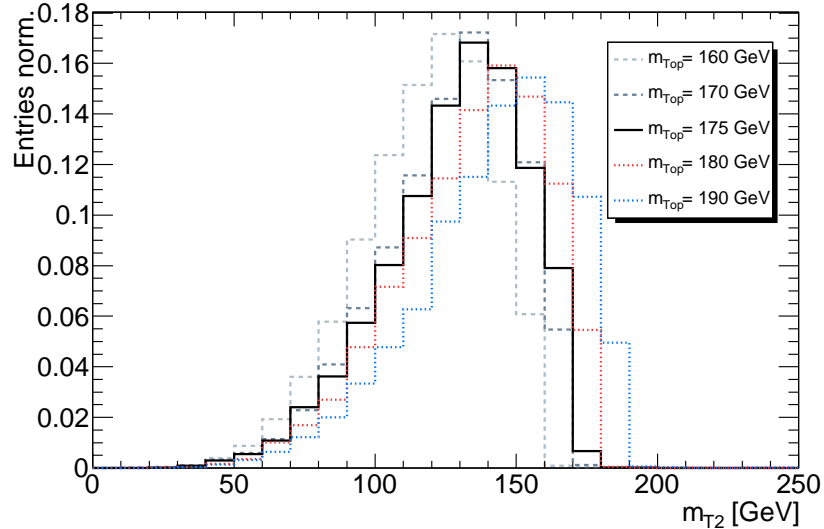


Figure 8.8.: m_{T2} distribution for true top-quark event samples with different top-quark masses. A dependence on the mass of the “mother” particle can be seen.

The benchmark point SUSY SU4 is described in [208] and in [240]. It is a low mass point mSUGRA² [241, 242] scenario and the particle spectrum is close to the current Fermilab Tevatron Collider limits for SUSY particles³. Important for this discussion is that the cross section is the largest of all SUSY scenarios that are considered in ATLAS. At $\sqrt{s} = 14$ TeV the cross section is 402.2 pb (50% of the $t\bar{t}$ cross section), at $\sqrt{s} = 7$ TeV the cross section is still 59.9 pb ($\sim 38\%$ of the $t\bar{t}$ cross section). The mass spectrum of strongly interacting particles is in the range of 410–420 GeV. Relevant particles are the supersymmetric top-quark partner $m_{\tilde{t}_2} = 236.04$ GeV and the neutralino $\tilde{\chi}_0 = 59.84$ GeV. In this scenario the following decay (as a pair) can mimic the top-quark dilepton signature:

$$\tilde{t}_2 \rightarrow \tilde{\chi}_0 t \rightarrow W b \tilde{\chi}_0 \rightarrow l b \nu \tilde{\chi}_0 \quad (8.19)$$

This is only one of the decay scenarios, but in general much higher values for the edge are expected than from $t\bar{t}$ events. The effect does not depend on the centre-of-mass energy.

Both features, the shift of the distribution towards higher m_{T2} masses and the independence from the centre-of-mass energy can be seen in Figure 8.12. The distributions are normalised to unit area, so that the effect is more visible.

²Minimal super-gravity model

³The parameters are as follows: Scalar masses $m_0 = 200$ GeV, gaugino mass $m_{1/2} = 160$ GeV, soft breaking trilepton coupling constant $A_0 = 400$ GeV, ratio of the vacuum expectation values $\tan \beta = 10$ and Higgsino mass parameter $\mu > 0$.

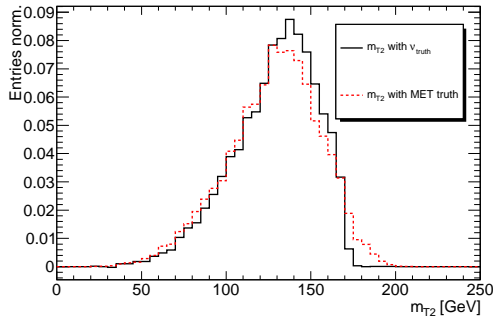


Figure 8.9.: m_{T2} distribution for true top-quark events using the transverse momentum of the neutrinos (solid line) and the true \cancel{E}_T (dashed line). The edge will smear out when in the missing transverse energy neutral particles other than the neutrinos are included.

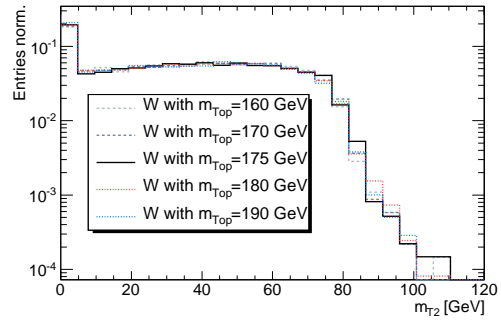


Figure 8.10.: Logarithmic m_{T2} distribution for true top-quark events using only the leptons. This probes the W -boson mass and the kinematic edge is at 80 GeV.

Finally, m_{T2} distributions are shown for $t\bar{t}$ signal and SM background processes in Figures 8.13 together with the SU4 sample for an integrated luminosity of $\mathcal{L}_{\text{int.}}=10 \text{ pb}^{-1}$ at $\sqrt{s}=7 \text{ TeV}$ centre-of-mass energy after all cuts⁴ for the three sub-channels. The number of events in the high mass tail from the SU4 sample is slightly higher than the SM background. With this selection and a proper amount of data any pollution of SU4 events in the $t\bar{t}$ dilepton selection can be found. A discrimination of the $t\bar{t}$ dilepton events against other dileptonic events can be made with the m_{T2} variable and the signature can be established convincingly.

⁴Although a sample at $\sqrt{s}=7 \text{ TeV}$ is used, the set of cuts are from the selection at $\sqrt{s}=10 \text{ TeV}$.

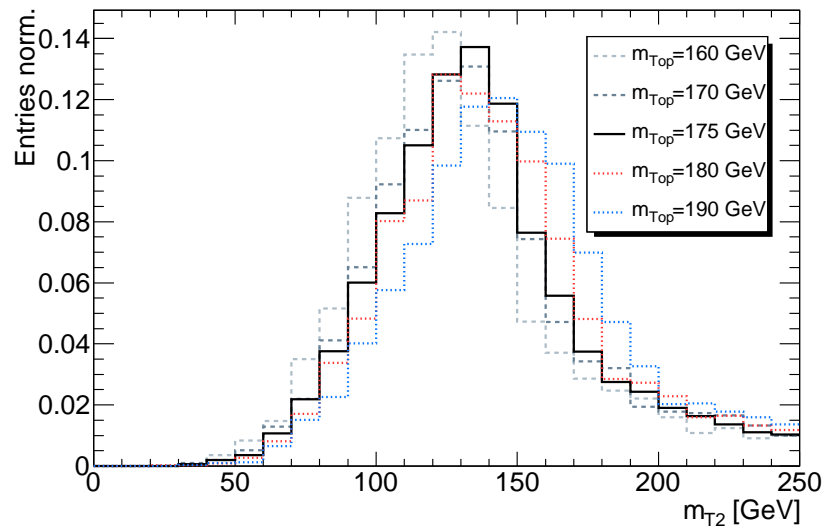


Figure 8.11.: m_{T2} distribution for reconstructed events of samples with different top-quark masses.

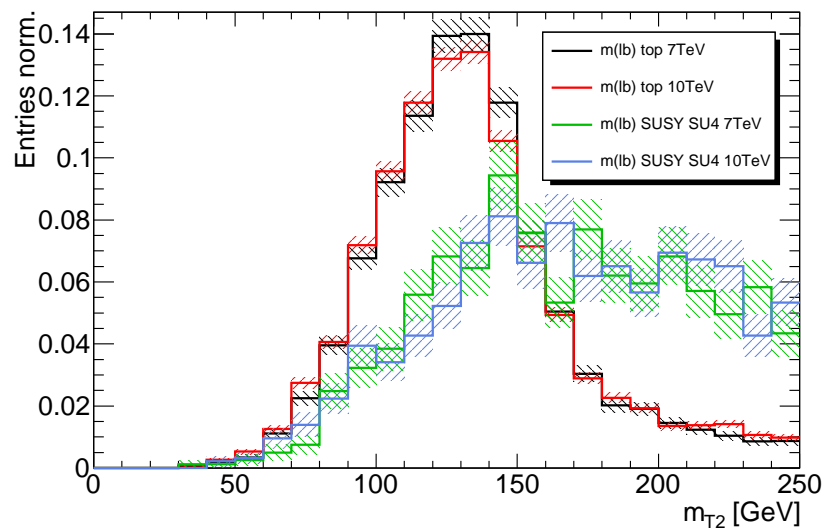


Figure 8.12.: m_{T2} distribution for reconstructed events of samples with different centre-of-mass energies (10 GeV and 7 GeV) and for a benchmark SUSY SU4 sample. The shaded areas represent the statistical uncertainty.

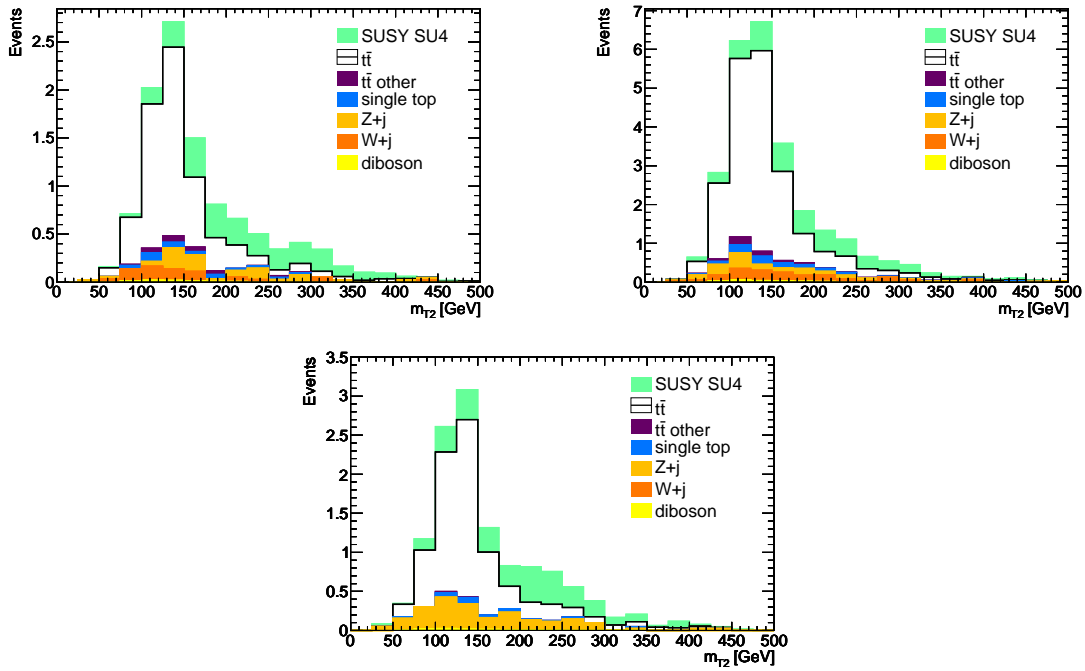


Figure 8.13.: m_{T2} distribution for signal and background processes together with the SUSY SU4 sample after the ee (top left), $\mu\mu$ (top right) and $e\mu$ (bottom) event selection for an integrated luminosity of $\mathcal{L}_{\text{int.}}=10 \text{ pb}^{-1}$ at $\sqrt{s}=7 \text{ TeV}$ centre-of-mass energy.

9. Analyses at Different Centre-of-Mass Energies

This analysis has also been performed at different centre-of-mass energies to adapt to the changed run conditions at the LHC. The basic analysis has not changed for the different centre-of-mass energies. The cuts have been slightly optimised to adapt to fact that the background cross section does not scale as the signal cross section. Also detector geometry description and reconstruction algorithms have been improved in later analyses. Improvements from the comparison of the performance in actual data have been included. The list of background samples and the systematic uncertainties that were investigated vary slightly, so that the results are not directly comparable. The comparison should give a prospect on the potential of this analysis for these higher energies as well as the latest estimate of this analysis for the current LHC 7 TeV run period.

9.1. Cross Section Analysis at $\sqrt{s} = 14$ TeV

The cross-section analysis [208] at $\sqrt{s} = 14$ TeV was targeted at an integrated luminosity of $\mathcal{L}_{\text{int.}} = 100 \text{ pb}^{-1}$ and an early low luminosity phase with an instantaneous luminosity of $\mathcal{L}_{\text{inst.}} = 10^{31} \text{ cm}^{-2} \text{ s}^{-1}$. It uses the same MC@NLO signal MC sample. As background processes Z +jets, W +jets, single top-quark and diboson events were considered. The sample cross-sections used for this study are listed in Table 9.1. The sample cross-sections for Z +jets and W +jets samples are not directly comparable, since here inclusive final states with two or one lepton were considered, respectively.

In general the cross section for the signal increases by over a factor of ~ 2.3 while the inclusive cross section for W/Z +jets events increases (at LO) only roughly by 1.6. The diboson cross-sections also increase by the same factor. The inclusive cross section for single top-quark s - and t -channel increases between 1.6 and 1.8 while the cross section for the Wt -channel increases at much as the $t\bar{t}$ signal¹. Still, the dominating background process cross-sections do not increase as much as the signal and hence a better signal-to-background ratio is expected.

¹The LO cross sections ratios quoted here were evaluated with MADGRAPH [247].

Table 9.1.: Sample cross sections for the cross-section analysis at $\sqrt{s}=14$ TeV.

Process	k -factor	calculation order	Ref.	sample cross section [pb]	sample size [pb ⁻¹]
$t\bar{t}$ MC@NLO ¹	1.00	approx. NNLO	[243]	450.0	964
Wt -channel	1.14	NLO	+	29.1	571
s -channel	1.50	NLO	[71]	3.5	2826
t -channel	0.98	NLO	*	79.7	271
$Z \rightarrow e^+e^- + np$	1.22	NLO	[206]	1727.2	279
$Z \rightarrow \mu^+\mu^- + np$	1.22	NLO	[206]	1808.5	103
$Z \rightarrow \tau\tau + np$	1.22	NLO	[206]	95.5	1851
$W \rightarrow e\nu + np$	1.22	NLO	[206]	10900	14
$W \rightarrow m\nu + np$	1.22	NLO	[206]	11946	28
WW	1.57	NLO	[244]	39.1	1280
ZZ	1.29	NLO	[244]	2.8	19577
WZ	1.89	NLO	[244]	13.9	3600

⁺References: [76, 75, 205]

*References: [71, 245, 246]

9.1.1. Differences Between the Analysis at $\sqrt{s}=14$ TeV and $\sqrt{s}=10$ TeV

The reconstruction algorithms are following the description in Chapter 5, but some object requirements are different:

- The jet-muon overlap cut used a $\Delta\mathcal{R} < 0.2$ cut to reject muons that overlap with a reconstructed jet.
- Muons with $\eta < 0.1$ and between $1.0 < |\eta| < 1.3$ were not used, since the muon chambers are inefficient in this regions.

The detector geometry that was used is an early description of the misaligned, as-built detector geometry. Additional material had been added in the inner detector and in front of the electromagnetic calorimeter.

The event cuts were unchanged compared to the event cuts used for the cross-section analysis at $\sqrt{s}=7$ TeV except for the following points:

- The trigger requirement was dropped for this study. A combination of single lepton and dilepton trigger is expected to have $> 98\%$ trigger efficiency.
- No data-driven methods were employed here and also no difference is made between background from real and fake leptons.

- The results of the single sub-channels were not combined with the likelihood method, but instead a combined selection that is flavour-blind (ll final state, with $l = e$ or $l = \mu$) was used with a lower \cancel{E}_T cut of $\cancel{E}_T > 30$ GeV.

9.1.2. Event Yields for the Event Selection at $\sqrt{s}=14$ TeV

Table 9.2 shows the number of expected events for each sub-channel and the combined selection and Table 9.3 summarises the expected uncertainty on the cross-section measurement and significance for different integrated luminosities. Figures 9.1 show the \cancel{E}_T distribution after the event selection for each sub-channel. The number of selected events is similar to the number of selected events for the analysis at $\sqrt{s}=10$ TeV. The acceptance is somewhat lower due to the older reconstruction algorithms and especially for the channels with muons, fiducial cuts were applied. Fake dilepton events were not properly studied here. Also the sample sizes used here were smaller, so that the uncertainty on the background numbers are larger.

The main tendency that $Z \rightarrow \ell^+\ell^-$ events are the dominating background is also true here. The second largest background are single top-quark events. The problem with the large tails in the \cancel{E}_T distribution for $Z \rightarrow \mu^+\mu^-$ events and thus a larger contribution from this background remains, although the relative fraction of events is small in the $\mu\mu$ selection. A signal-to-background ratio between 3.4 and 6.3 was achieved, the S/B in the muon channel is lower than in the ee channel, since fiducial cuts removed a large amount of the signal muons. The acceptances are between 14.7% and 20.2%.

9.1.3. Systematic Uncertainties for the Analysis at $\sqrt{s}=14$ TeV

Systematic uncertainties that were considered here are the following:

- The uncertainty of the luminosity was taken as 5%.
- The jet energy scale uncertainty was taken as $\pm 5\%$ and the correlation to \cancel{E}_T is 100% as described in Section 7.3. The overlap of jets with electrons was not used nor the doubling of the jet energy scale for forward jets.
- ISR/FSR systematic uncertainties were taken into account with the use of PYTHIA simulated samples. The parameters such as the Λ_{QCD} scale or the p_T cut-off for the shower evolution were changed such as the resulting sample has increased/decreased ISR/FSR individually. The uncertainty was quoted as the largest uncertainty in each positive and negative direction.
- PDF uncertainties were taken into account with CTEQ6.1 and MRST2001E PDF sets at NLO.

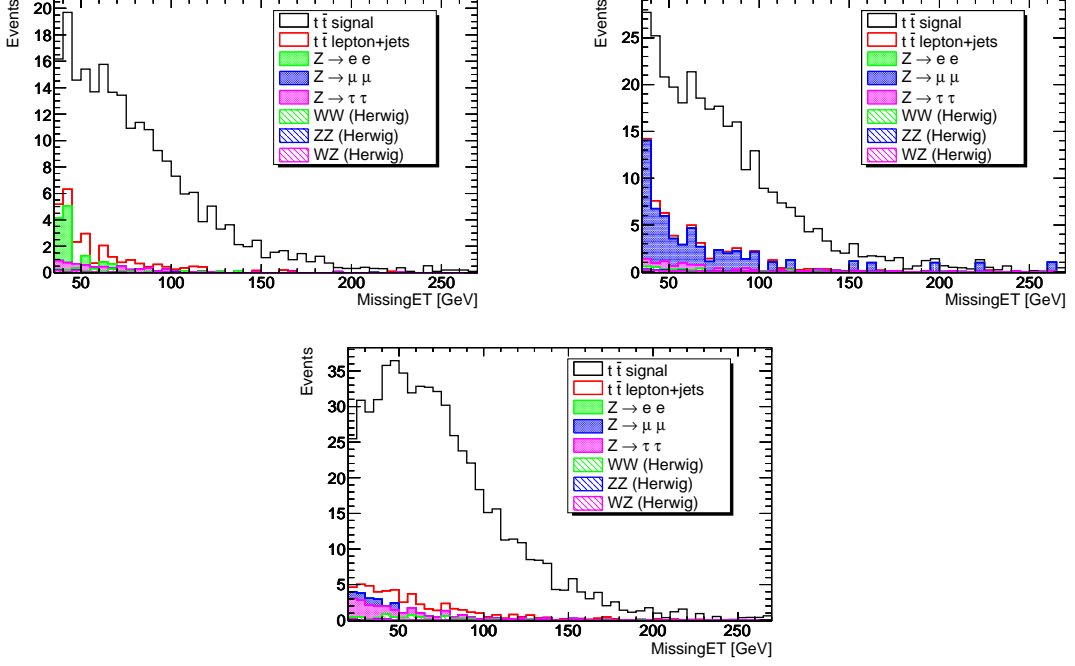


Figure 9.1.: \cancel{E}_T distribution for the different sub-channels (ee top left, $\mu\mu$ top right and $e\mu$ bottom) after the event selection at $\sqrt{s} = 14$ TeV.

Figures 9.2 show, as an example for a systematic uncertainty, the PDF uncertainties with the CTEQ6.1 and MRST2006 PDF sets at NLO that were used for Table 9.4.

The results from the systematic studies are summarised in Table 9.4. All the investigated systematic uncertainties have similar sizes.

9.1.4. Expected Sensitivity for the Analysis at $\sqrt{s} = 14$ TeV

The sensitivity of the cut-and-count analysis at a centre-of-mass energy of $\sqrt{s} = 14$ TeV and a target integrated luminosity of $\mathcal{L}_{\text{int.}} = 100 \text{ pb}^{-1}$ on the cross-section measurement is as follows:

$$\frac{\Delta\sigma_{ee}}{\sigma_{ee}} [\%] = 9.8(\text{stat})_{-3.1}^{+4.1}(\text{syst}) \pm 5.0(\text{lumi}) \quad (9.1)$$

$$\frac{\Delta\sigma_{\mu\mu}}{\sigma_{\mu\mu}} [\%] = 9.0(\text{stat})_{-2.9}^{+5.5}(\text{syst}) \pm 5.0(\text{lumi}) \quad (9.2)$$

$$\frac{\Delta\sigma_{e\mu}}{\sigma_{e\mu}} [\%] = 5.5(\text{stat})_{-3.7}^{+6.6}(\text{syst}) \pm 5.0(\text{lumi}) \quad (9.3)$$

$$\frac{\Delta\sigma_{\text{combined}}}{\sigma_{\text{combined}}} [\%] = 4.2(\text{stat})_{-2.0}^{+5.0}(\text{syst}) \pm 5.0(\text{lumi}) \quad (9.4)$$

Table 9.2.: Number of selected events by the event selection for the analysis at $\sqrt{s}=14$ TeV, scaled to an integrated luminosity of $\mathcal{L}_{\text{int.}}=100$ pb $^{-1}$.

	ee	$\mu\mu$	$e\mu$	comb.
$t\bar{t}$ dilepton	202 ± 5	253 ± 5	555 ± 7	987 ± 10
acceptance [%]	14.7	18.3	20.2	17.3
$t\bar{t}$ other	12 ± 1	4 ± 1	24 ± 2	39 ± 2
$Z \rightarrow e^+e^-$	9 ± 2	$0_{-0}^{+0.4}$	$0_{-0.5}^{+0.4}$	20 ± 3
$Z \rightarrow \mu^+\mu^-$	0_{-0}^{+1}	50 ± 7	5_{-2}^{+3}	79 ± 9
$Z \rightarrow \tau^+\tau^-$	4 ± 1	7 ± 1	17 ± 1	25 ± 1
$W \rightarrow e\nu_e$	7_{-5}^{+10}	0_{-0}^{+8}	7_{-5}^{+10}	14_{-8}^{+13}
$W \rightarrow \mu\nu_\mu$	0_{-0}^{+4}	7_{-4}^{+7}	25_{-9}^{+11}	33_{-10}^{+12}
diboson	2.7 ± 0.4	$3.5_{-0.4}^{+0.5}$	7 ± 1	14 ± 1
single top	$1.3_{-0.5}^{+0.8}$	$1.1_{-0.5}^{+0.8}$	3 ± 1	$5.4_{-1.2}^{+1.5}$
Total bkg.	36_{-6}^{+12}	73_{-8}^{+13}	88_{-10}^{+16}	228_{-16}^{+20}
S/B	$5.6_{-2.4}^{+2.2}$	$3.4_{-0.9}^{+0.7}$	$6.3_{-1.7}^{+1.4}$	$4.3_{-0.7}^{+0.5}$

The statistical uncertainties are quite similar to those of the analysis at $\sqrt{s}=10$ TeV. This is mainly because the target luminosity was chosen such that the number of selected events in both cases are similar. Despite the better signal-to-background ratio and the better significance at $\sqrt{s}=14$ TeV, the efficiency and purity of the event selection at $\sqrt{s}=10$ TeV is improved due to more optimised object selection cuts and improved reconstruction algorithms.

The systematic uncertainties cannot be compared directly, since much more systematic effects were investigated for the analysis at $\sqrt{s}=10$ TeV. When similar systematic effects, such as jet energy scale uncertainties, PDF uncertainties and ISR/FSR effects, are looked at, the effects are comparable.

9.2. Cross Section Analysis at $\sqrt{s}=7$ TeV

The analysis at $\sqrt{s}=7$ TeV [248, 249, 250, 251, 252, 253, 254, 255, 256, 257, 258] was revised in every aspect in order to adapt to the latest machine and detector conditions. The targeted integrated luminosity is $\mathcal{L}_{\text{int.}}=10$ pb $^{-1}$ and the foreseen instantaneous luminosity is planned to increase up to $\mathcal{L}_{\text{inst.}}=10^{31}$ cm $^{-2}$ s $^{-1}$ by the time this amount of data is collected. The Monte-Carlo samples used for this study have been updated with $Z \rightarrow bb$ +jets samples.

The cross sections are reduced by almost the same factors when going from $\sqrt{s}=14$ TeV to $\sqrt{s}=10$ TeV. This is a factor of ~ 2.6 for $t\bar{t}$, ~ 1.6 for W/Z +jets

Table 9.3.: Statistical uncertainty on the cross section σ and significance for the different sub-channels from MC based signal and backgrounds at $\sqrt{s}=14$ TeV. The uncertainty on the number of observed events is Poissonian and the uncertainty on the background estimation is taken from the statistical uncertainty of the MC sample.

statistical uncertainty $\Delta\sigma/\sigma$ [%]	ee	$\mu\mu$	$e\mu$	comb.
$\mathcal{L} = 10 \text{ pb}^{-1}$	24.9	23.2	14.8	11.4
50 pb^{-1}	12.4	11.5	7.2	5.5
100 pb^{-1}	9.8	9.0	5.5	4.2
200 pb^{-1}	8.2	7.4	4.5	3.4
significance $S/\sqrt{S+B}$	ee	$\mu\mu$	$e\mu$	comb.
$\mathcal{L} = 10 \text{ pb}^{-1}$	4.1	4.4	6.9	9.0
50 pb^{-1}	9.3	9.9	15.5	20.0
100 pb^{-1}	13.1	14.0	21.9	28.3
200 pb^{-1}	18.5	19.8	31.0	40.0

and dibosons. The decrease for single top-quark t - and s -channel is between 1.7 and 2.0 and the Wt -channel is decreased by the same factor as the $t\bar{t}$ signal². The sample cross sections are summarised in Table 9.5. In the end the decrease of the centre-of-mass energy disfavourers the signal process and the main backgrounds are enhanced.

9.2.1. Differences Between the Analysis at $\sqrt{s}=7$ TeV and $\sqrt{s}=10$ TeV

The main reconstruction algorithms have not been changed, but the selection was refined, to increase the purity and efficiency [248, 249, 250]:

- The electron cluster position is used for the fiducial cuts. The relative isolation requires the isolation energy in a cone of $\Delta\mathcal{R} < 0.3$ to be smaller than $4 \text{ GeV} + 0.023 \cdot p_T$. This relative cut maintains a constant efficiency across a large p_T range. A hit in the b-layer of the pixel detector is required, if there is an active and good b-layer module in this region. This reduces electrons from conversions. Electrons are rejected in regions where the power supply of the data front-end boards of the electromagnetic calorimeter is known to be off (dead OTX region).

²The LO cross section ratios quoted here were calculated with MADGRAPH [247].

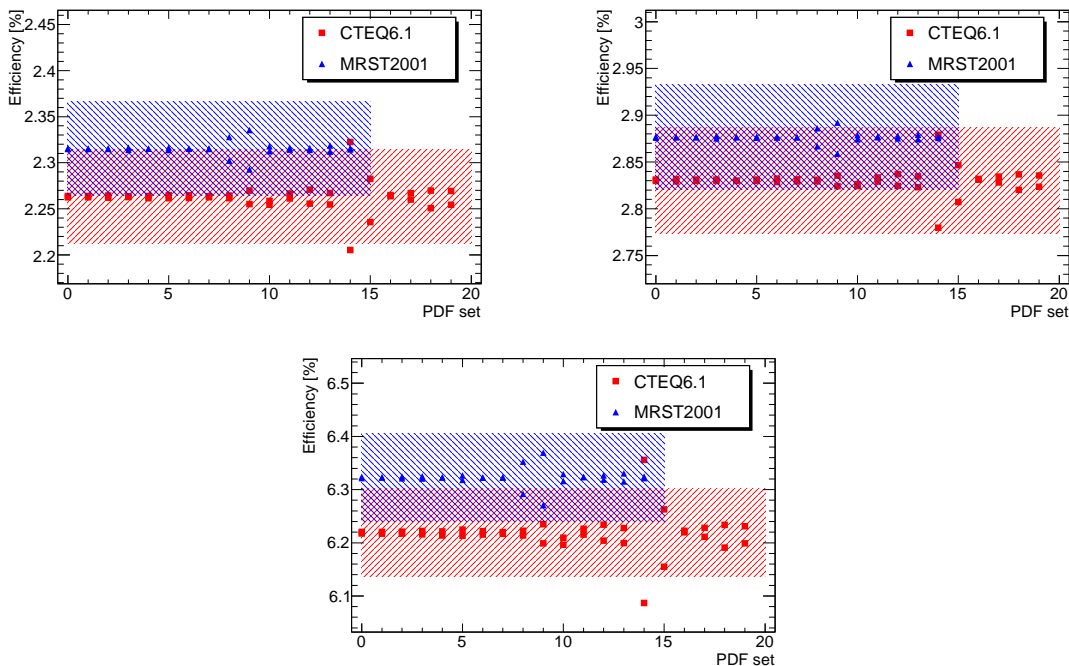


Figure 9.2.: PDF uncertainties on the selection efficiency with the CTEQ6M and MRST2001E PDF sets at NLO for the ee (top left), $\mu\mu$ (top right) and the $e\mu$ (bottom) channel at $\sqrt{s} = 14$ TeV. The x -axis denotes the number of the PDF parameter that was changed in the error PDF. Each point corresponds to a change of the parameter by $\pm 1\sigma$. There are 20 parameters for CTEQ6.1, 15 parameters for the MMRST2001E set. The bands correspond to the uncertainty within the respective PDF set calculated with the Hessian approach.

- Muons are selected from the MUID algorithms, since the rejection of fake muons seems to be better than with the STACO algorithms. There are also two isolation requirements, an absolute isolation from energy depositions of 4 GeV in the calorimeter in a cone of $\Delta\mathcal{R} < 0.2$ and an absolute isolation from tracks in a cone of $\Delta\mathcal{R} < 0.3$ with a total p_T -sum of 4 GeV. Moreover only combined muons are used.
- Jets are formed by the anti- k_T algorithm using topo clusters that is a variant of the k_T algorithm with a distance measure of $d_i = p_{T,i}^{-2}$ (see Section 5.3) and a $R = 0.4$, which forms jets with an approximate cone radius of $\Delta\mathcal{R} = 0.4$. The overlap of an anti- k_T jet with an electron is removed within a cone of $\Delta\mathcal{R} < 0.2$ (comparing the cluster position of the electron) and only the closest jet is removed.

Table 9.4.: Summary of the systematic uncertainties at $\sqrt{s}=14$ TeV and an integrated luminosity of $\mathcal{L}_{\text{int.}}=100$ pb $^{-1}$.

Uncertainty [%]	ee	$\mu\mu$	$e\mu$	comb.
statistical	9.8	9.0	5.5	4.2
Luminosity	5.0	5.0	5.0	5.0
JES -5%	-2.0	0.0	-3.1	-2.1
JES +5%	2.4	4.1	4.7	4.6
PDF CTEQ6.1	2.4	2.9	2.0	2.4
PDF MRST2001E	0.9	1.1	0.7	0.9
ISR	1.1	1.1	1.2	1.1
FSR	2.0	2.0	4.0	2.0

- \cancel{E}_T components that fail the comparison with data are not used, so that the $\cancel{E}_{T\text{cryo}}$ term is omitted and only the refined terms from electrons, jets, the muon terms from MUID muons and the remaining unassigned cells are used.
- Both \cancel{E}_T and the jets are calibrated with the same calibration scheme that is the electromagnetic scale (EM) plus the numerical inversion applied afterwards.

The event selection is supplemented by two additional cuts that are aimed at reducing events with low data quality [254, 258]. Also the \cancel{E}_T and Z -mass-window cut have been optimised:

- The first event-quality cut requires a primary vertex with at least 5 tracks. This ensures that a good primary vertex with sufficient precision is found.
- The second cut vetoes against jets in the event that are found to have a bad quality in terms of calorimeter timing and fraction of energy in the hadronic and electromagnetic calorimeter. This usually indicates that a jet was found as the result of a calorimeter response that was not in time with the beam by e.g. noise or pile-up effects. Another possibility is that the jet was found in a bad calorimeter region, where either the electromagnetic or the hadronic calorimeter has dead or noisy cells, which would deteriorate the energy fractions. Such events with at least one bad jet of $p_T > 20$ GeV at the EM scale are rejected, since these faulty cells are also taken into account in the \cancel{E}_T calculation and would affect the whole event selection.
- The \cancel{E}_T and Z -mass window cut has been optimised, since the width of the invariant Z -boson mass peak has changed with more and more updated geometry description. For the ee channel the requirement is now $\cancel{E}_T > 40$ GeV

Table 9.5.: Sample cross sections for the cross-section analysis at $\sqrt{s} = 7$ TeV.

Process	k -factor	calculation order	Ref.	sample cross section [pb]	sample size [pb ⁻¹]
$t\bar{t}$ MC@NLO ¹	1.09	approx. NNLO	[204]	87.4	8844
Wt -channel	1.00	NLO	[34]	14.27	911
s -channel	1.00	NLO	[34]	43.18	18007
t -channel	1.00	NLO	[34]	43.18	832
$Z \rightarrow e^+e^- + np$	1.22	NNLO	[195]	1471.39	381
$Z \rightarrow \mu^+\mu^- + np$	1.22	NNLO	[195]	1469.10	382
$Z \rightarrow \tau\tau + np$	1.22	NNLO	[195]	1477.36	382
$Z \rightarrow bb + np$	1.22	NNLO	[195]	17.86	7496
$W \rightarrow e\nu + np$	1.22	NNLO	[195]	16163.90	178
$W \rightarrow m\nu + np$	1.22	NNLO	[195]	16149.51	178
$W \rightarrow \tau\nu + np$	1.22	NNLO	[195]	16144.26	176
$W \rightarrow bb + np$	1.22	NNLO	[195]	17.86	1734
WW	1.69	NLO	[192]	26.40	21263
ZZ	1.42	NLO	[192]	1.93	255604
WZ	1.81	NLO	[192]	8.82	72986

and the Z -mass window is ± 5 GeV, for the $\mu\mu$ channel the requirement is $\cancel{E}_T > 30$ GeV and the Z -mass window is ± 10 GeV. For the $e\mu$ channel, instead of \cancel{E}_T , the scalar sum of the leptons and all jets (H_T) is considered and required to be $H_T > 150$ GeV. The significance $S/\sqrt{S+B+\delta_{\text{sys.}}}$ is optimised where $\delta_{\text{sys.}}$ is the systematic uncertainty when \cancel{E}_T is varied by 8%.

- For electrons a matching trigger object must be found to ensure that the event was triggered by the selected electron in the beginning. This matching is not applied to muons, since the muons trigger objects that are out of time are not stored in the AODs.
- In MC samples the leptons are also required to originate from a simulated true lepton.

The data-driven methods are also employed for the analysis. More methods for the fake-event rate estimation have been explored beside the methods described in Section 6.3.2 and an overview can be found in [252]. The estimation of the Z -boson background from the side-bands as described in Section 6.3.1 is also used. The other background contributions are again estimated by MC samples.

9.2.2. Event Yields for the Event Selection at $\sqrt{s} = 7$ TeV

Table 9.6 and 9.7 show the number of expected events for each sub-channel and the sum of all channels. For the sum of the events it is noted that the event selection in the sub-channels are mutually exclusive, so that there is no overlap between the sub-channels. Figures 9.3, 9.4 and 9.5 show the \cancel{E}_T/H_T and jet multiplicity distribution after the event selection for each sub-channel. The number of selected events is much smaller than the number for the analysis at $\sqrt{s} = 10$ TeV. The cross section is decreased by 50% and the target luminosity is only 5% of the target luminosity for the analysis at $\sqrt{s} = 10$ TeV. The acceptance increases to 17 – 26.8% due to the improvement in the reconstruction algorithm and moreover due to the optimisation of the object selection cuts. Fake dilepton events are included here as MC estimates. The samples sizes are increased, also due to the small target luminosity, so that the statistical uncertainty on the event yield is smaller than for the analysis at $\sqrt{s} = 10$ TeV.

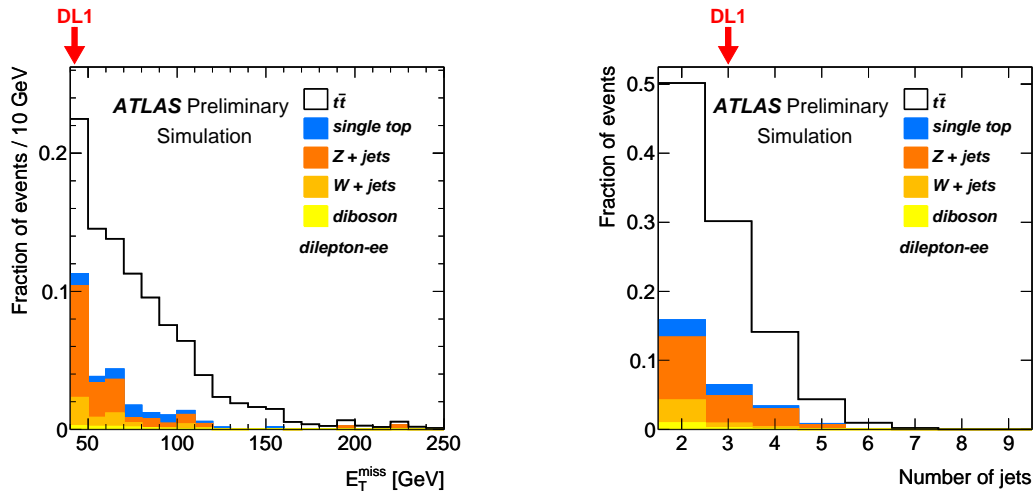


Figure 9.3.: \cancel{E}_T (left) and jet multiplicity distribution (right) for selected ee events in signal and background samples at 7 GeV. The distributions are normalised to unity. The arrows indicate the event candidates in the first 280 nb^{-1} of data.

The same order of importance for the background events can be found here. The largest background is $Z \rightarrow \ell^+\ell^-$ followed by single top-quark events. The problem with the larger \cancel{E}_T tail in $Z \rightarrow \mu^+\mu^-$ events persists, although the ratio between selected $Z \rightarrow e^+e^-$ events in the ee channel and $Z \rightarrow \mu^+\mu^-$ events in the $\mu\mu$ has decreased from 5/1 to 3/1. This is also partially attributed to the simpler \cancel{E}_T definition. The signal-to-background ratio is between 2.5 and 5.0. For an integrated luminosity of $\mathcal{L}_{\text{int.}} = 10 \text{ pb}^{-1}$ the significance lies in all channels below 5. Not even

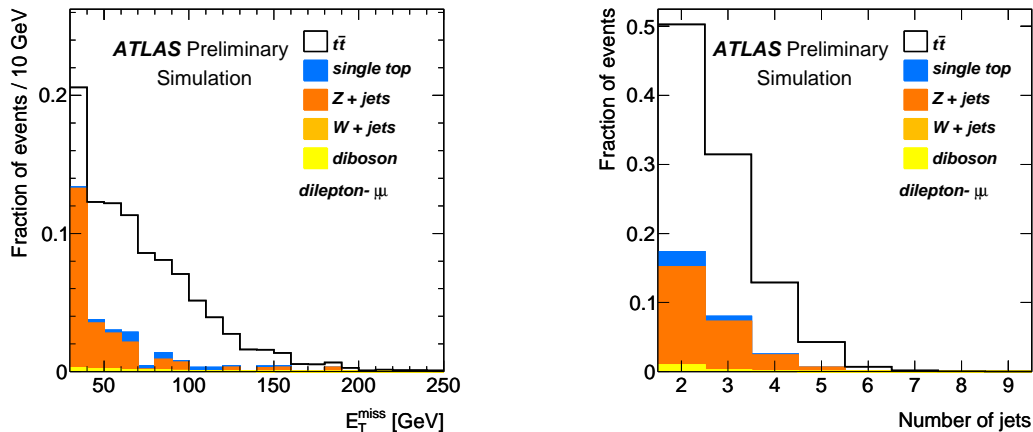


Figure 9.4.: \cancel{E}_T (left) and jet multiplicity distribution (right) for selected $\mu\mu$ events in signal and background samples at 7 GeV. The distributions are normalised to unity.

the clean $e\mu$ channel or the combination of all channels can reach the significance of 5 as can be seen from Table 9.8.

9.2.3. Systematic Uncertainties for the Analysis at $\sqrt{s} = 7$ TeV

As systematic uncertainties the following are considered, but not all of them are already investigated:

- The luminosity uncertainty is around 11% from the latest luminosity scans [228, 229].
- The uncertainty of the MC signal modelling is derived from the difference of the signal acceptance in MC@NLO, HERWIG and ALPGEN samples.
- Uncertainties from the data-driven methods are provided by the respective studies [252, 254].
- ISR/FSR variations are studied with PYTHIA samples with separate ISR/FSR variations.
- The jet energy scale uncertainty is found to be 8% for low- p_T jets and 6% for high- p_T jets ($p_T > 100$ GeV) [259], the lepton energy scale is assumed to have an uncertainty of 5%. The uncertainty on the jet/lepton energy can be propagated to the uncertainty of the \cancel{E}_T by calculating the weight each object

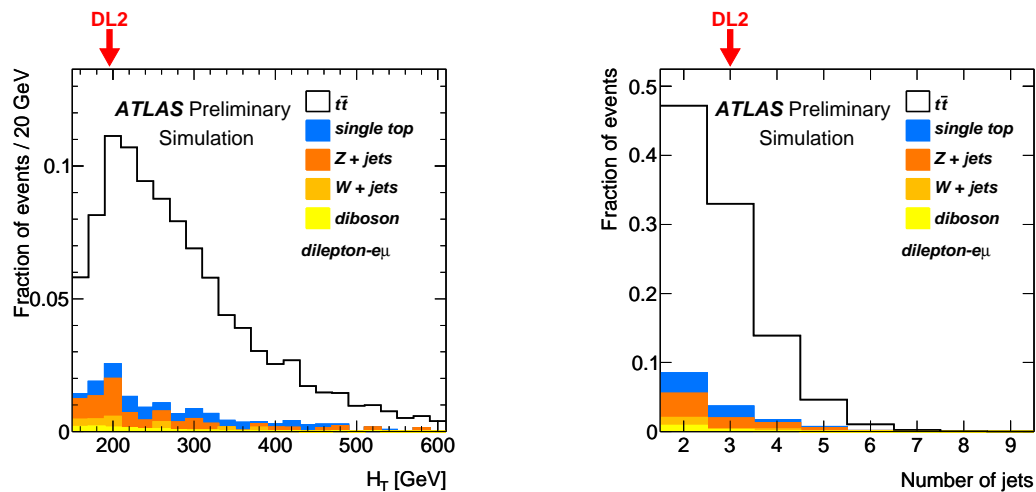


Figure 9.5.: H_T (scalar sum of all leptons and all jets) and jet multiplicity distribution for selected $e\mu$ events in signal and background samples at 7 GeV. The distributions are normalised to unity. The arrows indicate the event candidates in the first 280 nb^{-1} of data.

contributed to the final calculation. This can take the proper correlation into account.

- The uncertainty of the lepton trigger and reconstruction efficiency are provided by the optimisation of the lepton identification studies [248].
- The PDF uncertainties are investigated with the latest PDF fits, namely the CTEQ6.6, MSTW³2008nlo90CL and NNPDF20 PDF sets at NLO. Also variations in α_s are taken into account. The uncertainty bands are calculated with the Hessian approach, except for the NNPDF20 PDF set, where the *Root Mean Square* (RMS) represents the uncertainty from this PDF set. As the total systematic uncertainty the uncorrelated combination of all uncertainties is calculated, which is equal to the largest upward and downward deviation from the nominal cross section.
- Pile-up is taken fully into account with a MC simulated sample that has on average two proton-proton interactions per bunch crossing.

The systematic studies are not completed yet, so that the total sensitivity of the cross-section measurement cannot be determined, yet. Only three effects have been

³Martin-Stirling-Thorne-Watt

Table 9.6.: Number of selected events in signal and background samples by the event selection for the analysis at $\sqrt{s} = 7$ TeV, scaled to an integrated luminosity of $\mathcal{L}_{\text{int.}} = 10 \text{ pb}^{-1}$ for the ee and $e\mu$ channel. The number of fake events are given in brackets and they are also included as background.

	ee		$\mu\mu$	
$t\bar{t}$ dilepton acceptance [%]	4.6 \pm 0.1	(0.1)	6.7 \pm 0.1	(0.1)
$t\bar{t}$ other	0.10 \pm 0.01	(0.10)	0.02 \pm 0.01	(0.02)
$Z \rightarrow e^+e^-$	0.49 \pm 0.12	(0.00)	0.0 $^{+0.07}_{-0.00}$	(0.00)
$Z \rightarrow \mu^+\mu^-$	0.00 $^{+0.07}_{-0.00}$	(0.00)	1.6 \pm 0.2	(0.0)
$Z \rightarrow \tau^+\tau^-$	0.3 \pm 0.1	(0.1)	0.5 \pm 0.1	(0.0)
$Z \rightarrow bb + np$	0.06 \pm 0.01	(0.003)	0.14 \pm 0.1	(0.0)
$W \rightarrow e\nu_e$	0.29 $^{+0.14}_{-0.07}$	(0.29)	0.00 $^{+0.11}_{-0.00}$	(0.00)
$W \rightarrow \mu\nu_\mu$	0.00 $^{+0.11}_{-0.00}$	(0.00)	0.00 $^{+0.11}_{-0.00}$	(0.00)
$W \rightarrow \tau\nu_\mu$	0.00 $^{+0.12}_{-0.00}$	(0.00)	0.00 $^{+0.12}_{-0.00}$	(0.00)
$W \rightarrow bb + np$	0.01 $^{+0.01}_{-0.00}$	(0.01)	0.00 $^{+0.01}_{-0.00}$	(0.00)
diboson	0.08 \pm 0.01	(0.01)	0.11 \pm 0.01	(0.001)
single top	0.32 \pm 0.06	(0.02)	0.30 \pm 0.07	(0.00)
Total bkg.	1.6 $^{+0.3}_{-0.2}$		2.7 $^{+0.3}_{-0.2}$	
S/B	2.8 $^{+0.5}_{-0.3}$		5.0 $^{+0.6}_{-0.3}$	

studied so far: the PDF uncertainty, the jet and lepton energy scale and pile-up effects.

Figures 9.6 show the PDF uncertainties for the three PDF sets investigated for this analysis. The difference between the CTEQ6.6 PDF set and the other two sets is the largest while the other two sets have similar central values. Table 9.9 summarises the PDF uncertainty, which is taken as the envelope of all the PDF variations.

The second preliminary systematic result can be found in [250] and concerns the jet and lepton energy scale. It uses the quoted 6 – 8% for the jet energy scale and 5% for the lepton energy scale. The \cancel{E}_T is rescaled at the same time by the fraction in which the varied object contributes to the calculation. The result is that in the ee channel the total energy scale variation has an effect of 9 – 10% with roughly $\pm 5\%$ from each jet and lepton energy scale variation. For the $\mu\mu$ channel this is $\pm 8\%$ with $\pm 4\%$ from the jet and ± 4 – 5% from the lepton energy scale variation. Finally, for the $e\mu$ channel this is $\pm 8\%$ with $\pm 3\%$ from the jet and $\pm 4\%$ from the lepton energy scale variation.

Table 9.7.: Number of selected events in signal and background samples by the event selection for the analysis at $\sqrt{s}=7$ TeV, scaled to an integrated luminosity of $\mathcal{L}_{\text{int.}}=10\text{ pb}^{-1}$ for the $e\mu$ channel and the sum of all three sub-channels. The number of fake events are given in brackets and they are also included as background.

	$e\mu$		sum	
$t\bar{t}$ dilepton	14.6 \pm 0.1	(0.3)	25.7 \pm 0.2	(0.1)
acceptance [%]	26.8		23.8	
$t\bar{t}$ other	0.3 \pm 0.02	(0.3)	0.37 \pm 0.02	(0.37)
$Z \rightarrow e^+e^-$	0.02 $^{+0.07}_{-0.02}$	(0.02)	0.52 \pm 0.12	(0.02)
$Z \rightarrow \mu^+\mu^-$	0.4 \pm 0.1	(0.4)	2.1 \pm 0.2	(0.4)
$Z \rightarrow \tau^+\tau^-$	0.6 \pm 0.1	(0.1)	1.4 \pm 0.2	(0.1)
$Z \rightarrow bb + np$	0.07 \pm 0.01	(0.03)	0.27 \pm 0.01	(0.03)
$W \rightarrow e\nu_e$	0.09 $^{+0.13}_{-0.05}$	(0.02)	0.37 $^{+0.16}_{-0.09}$	(0.37)
$W \rightarrow \mu\nu_\mu$	0.24 $^{+0.14}_{-0.07}$	(0.24)	0.24 $^{+0.14}_{-0.07}$	(0.24)
$W \rightarrow \tau\nu_\mu$	0.04 $^{+0.13}_{-0.03}$	(0.04)	0.04 $^{+0.13}_{-0.03}$	(0.04)
$W \rightarrow bb + np$	0.00 $^{+0.01}_{-0.00}$	(0.00)	0.006 $^{+0.014}_{-0.004}$	(0.01)
diboson	0.20 \pm 0.01	(0.01)	0.38 \pm 0.01	(0.02)
single top	0.88 \pm 0.11	(0.05)	1.5 \pm 0.1	(0.1)
Total bkg.	2.8 $^{+0.3}_{-0.2}$		7.2 $^{+0.5}_{-0.3}$	
S/B	2.5 $^{+0.3}_{-0.2}$		3.5 \pm 0.2	

The last preliminary result is found in [258] and observes a negligible effect of pile-up effects for the $t\bar{t}$ selection. Again, the effect is that the lepton isolation is worse, but the jet multiplicity is higher. The effect compensates the object selection and event selection efficiency changes, so that the effect on the variation of the selection efficiency in the ee channel is $< 0.5\%$, $\sim 2\%$ for the $\mu\mu$ channel and $\sim 0.5\%$ for the $e\mu$ channel.

9.2.4. Expected Sensitivity of the Analysis at $\sqrt{s}=7$ TeV

Most of the studies have been done only on MC events and it shows a good acceptance for the selection. The statistical uncertainties are very large, due to the small event numbers for an integrated luminosity of $\mathcal{L}_{\text{int.}}=10\text{ pb}^{-1}$. The systematic uncertainties done so far show that the size of the effects are comparable to the effects seen in the other analyses. The data-driven methods might perform worse,

Table 9.8.: Statistical uncertainty on the cross section σ and significance for the different sub-channels from MC based signal and backgrounds at $\sqrt{s} = 7$ TeV. The uncertainty on the number of observed events is Poissonian and the uncertainty on the background estimation is taken from the statistical uncertainty of the MC sample.

statistical uncertainty $\Delta\sigma/\sigma$ [%]	ee	$\mu\mu$	$e\mu$	sum
$\mathcal{L} = 10 \text{ pb}^{-1}$	54.5	46.2	29.0	22.4
50 pb^{-1}	25.1	21.2	13.1	10.2
100 pb^{-1}	18.3	15.5	9.5	7.3
200 pb^{-1}	13.8	11.6	6.9	5.3
significance $S/\sqrt{S+B}$	ee	$\mu\mu$	$e\mu$	sum
$\mathcal{L} = 10 \text{ pb}^{-1}$	1.8	2.2	3.5	4.5
50 pb^{-1}	4.1	4.9	7.7	10.5
100 pb^{-1}	5.8	6.9	10.9	14.1
200 pb^{-1}	8.2	9.7	15.5	20.0

since their precision depends on the event yield in their respective control region. This is e.g. the case for the estimation of $Z \rightarrow \ell^+\ell^-$ events.

Once there will be enough data collected to announce an observation of top-quark dilepton events, the studies will be completed and a final result on cross-section measurement can be made.

Table 9.9.: PDF uncertainties for the different sub-channels and different PDFs. The first number is the deviation from the CTEQ6.6 central value and the “error” is the PDF uncertainty within the PDF set. The total uncertainty is the envelope of the PDF bands and the central value is in the middle of the envelope band.

no truth cut	ee	$\mu\mu$	$e\mu$
CTEQ6.6	$(0.0 \pm 1.64)\%$	$(0.0 \pm 1.28)\%$	$(0.0 \pm 1.60)\%$
MSTW2008nlo90CL	$(2.4^{+1.05}_{-1.14})\%$	$(2.0^{+0.75}_{-0.76})\%$	$(1.2^{+0.84}_{-0.92})\%$
NNPDF	$(3.5 \pm 0.82)\%$	$(3.5 \pm 0.63)\%$	$(1.7 \pm 0.62)\%$
envelope	$\pm 2.99\%$	$\pm 2.71\%$	$\pm 2.89\%$

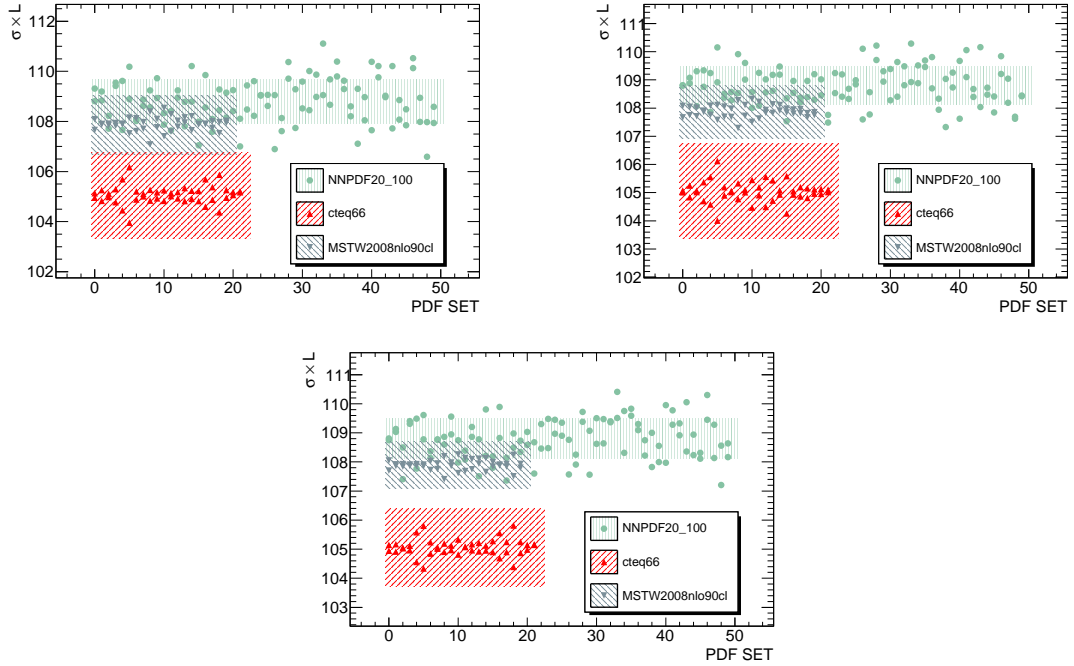


Figure 9.6.: Variation of the total cross section $\sigma_{tot} \times \mathcal{L}$ calculated from Formula 6.1 for the ee (top left), $\mu\mu$ (top right) and $e\mu$ (bottom) channel due to PDF variations. The x -axis denotes the number of the PDF parameter that was changed in the error PDF. Each point corresponds to a change of the parameter by $\pm 1\sigma$. There are 22 parameters for CTEQ6.6, 20 parameters for the MWST2008nlo90CL set and there are 100 variations of the NNPDF20 set. The bands correspond to the uncertainty within the respective PDF set. The PDFs with the α_s -variations are not shown here. The cross section was calculated using the predicted MC number before the truth matching cut.

10. Conclusion and Outlook

This study about the top-quark pair cross-section measurement in the dilepton channel has shown that the measurement at a centre-of-mass energy of $\sqrt{s} = 10$ TeV is feasible with a cut-and-count analysis. It is estimated that with this analysis the ATLAS experiment can achieve a measurement accuracy on the cross section in the dilepton $t\bar{t}$ channel of:

$$\frac{\Delta\sigma_{combined}}{\sigma_{combined}}[\%] = {}^{+3.1}_{-3.1}(\text{stat}){}^{+9.6}_{-8.7}(\text{syst}){}^{+26.2}_{-17.4}(\text{lumi})$$

This study originally considered the first months of the data taking period at a centre-of-mass energy of $\sqrt{s} = 10$ TeV and an integrated luminosity of $\mathcal{L}_{\text{int.}} = 200 \text{ pb}^{-1}$. The uncertainty on the luminosity (20%) was very pessimistic at that time and the latest estimate shows a smaller uncertainty of 11% [229].

The study includes two data-driven background-estimation methods that will reduce the dependence on the MC based estimation for the Drell-Yan background and on the simulated number of events with falsely identified leptons. An extensive list of systematic uncertainties was investigated and it was found that with increasing integrated luminosity the analysis is very soon no longer dominated by statistical uncertainties. The important significance of 5 can be reached already with a small amount of data, so that the observation of the top-quark in the dilepton channel is possible.

Compared to the golden channel, the semi-leptonic top-quark channel, a similar study for the same centre-of-mass energy and data amount [260, 261] showed a similar statistical uncertainty of 3 – 6% for each lepton channel, which is also comparable to the $e\mu$ channel uncertainty of ${}^{+4.1\%}_{-4.0\%}$. Furthermore, the clean selection that is possible with the dilepton selection showed a smaller systematic uncertainty for the cut-and-count analysis of $\sim 10\%$ compared to $\sim 20\%$ in the semi-leptonic channel.

The conclusion is that the statistical uncertainties at the LHC for the top-quark cross-section analysis are not the limiting uncertainties. The purer selection of the signal events is beneficial for a still dominant, but smaller systematic uncertainty.

The same analysis with even more refined object cuts is used to measure the cross section at a centre-of-mass energy of $\sqrt{s} = 7$ TeV. All the data-driven methods and methods to study the systematic uncertainties can be reused for the analysis on first data. Once there will be enough data collected to announce an observation

of top-quark dilepton events, a final result on the uncertainty of the cross-section measurement can be made and last, but not least a cross-section number can be published and compared with theoretical predictions. Hopefully this will contain some hint and shed some light on new physics beyond the Standard Model.

Dilepton top-pair event candidates for the first collisions at $\sqrt{s}=7$ TeV

Although insufficient data has been collected to make a proper cross-section analysis, single event candidates have been found in the first 280 nb^{-1} of data taken. The expectation for dileptonic top-quark events is one event every 100 nb^{-1} . The selection efficiency is around 20%, so that one expects a bit more than 0.5 signal events. Two candidate have been found which pass the selection cuts for the analysis at $\sqrt{s}=7$ TeV. Their properties are summarised in Table 10.1. Both candidate events have two oppositely signed, good leptons and three good jets. For the ee candidate the invariant lepton mass is $m_{ll} = 36.9 \text{ GeV}$ and the $\cancel{E}_T = 42.4 \text{ GeV} > 40 \text{ GeV}$. The $H_T = 196 \text{ GeV}$ for the $e\mu$ event is also well above the cut value of 150 GeV . In each case one jet has also been tagged as a b -quark jet. Here the vertex based SV0 tagger [262] at an efficiency of 50% is used. The distribution for the number of b -tagged events are shown in Figures 10.1.

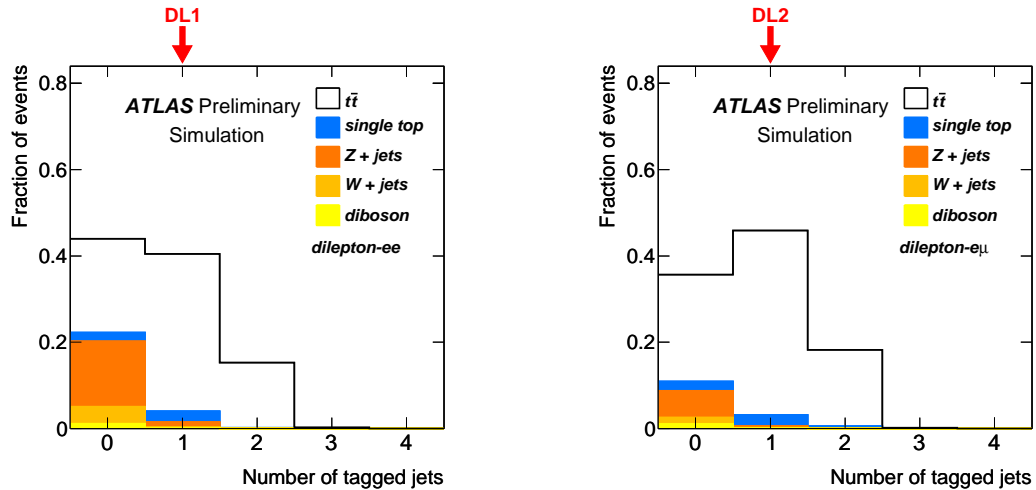


Figure 10.1.: b -tagged jet multiplicity distribution [263] for selected ee (left) and $e\mu$ (right) events at 7 GeV. The distributions are normalised to unity. The arrows indicate the event candidates in the first 280 nb^{-1} of data.

Figures 10.2 show the event display for the ee candidate and for the $e\mu$ candidate. The electrons of the first candidate are single tracks pointing to electromagnetic calorimeter clusters and they are close together. The jets appear as groups of 3 – 5

Table 10.1.: Dilepton event candidates in the first 280 nb^{-1} [263]. In brackets are given the number of b -tagged jets. Both candidates pass the event cuts for the analysis at a centre-of-mass energy of $\sqrt{s} = 7 \text{ TeV}$.

ID	Run number	Event number	Channel	p_T^{lep} [GeV]	\cancel{E}_T [GeV]	H_T [GeV]	# of jets
DL1	155678	13304729	ee	55.2/40.6	42.4	271	3 (1)
DL2	158582	27400066	$e\mu$	22.7/47.8	76.9	196	3 (1)

tracks, two of the three jets are in the lower hemisphere, the third jet points towards the hadronic end-cap.

The two leptons of the second candidate are easily identified on the one side by the track through the muon chambers and on the other side by the track pointing to an electromagnetic calorimeter cluster. In the lego plot both leptons have the largest energy entry.

With the two events in 280 nb^{-1} a peek into the kind of events that this analysis will measure has been given. The upward fluctuation of 2 events with an expectation of 0.5 is not enough to judge if the cross section will be different from the SM. Only the collection of a larger data amount can give a more significant result.

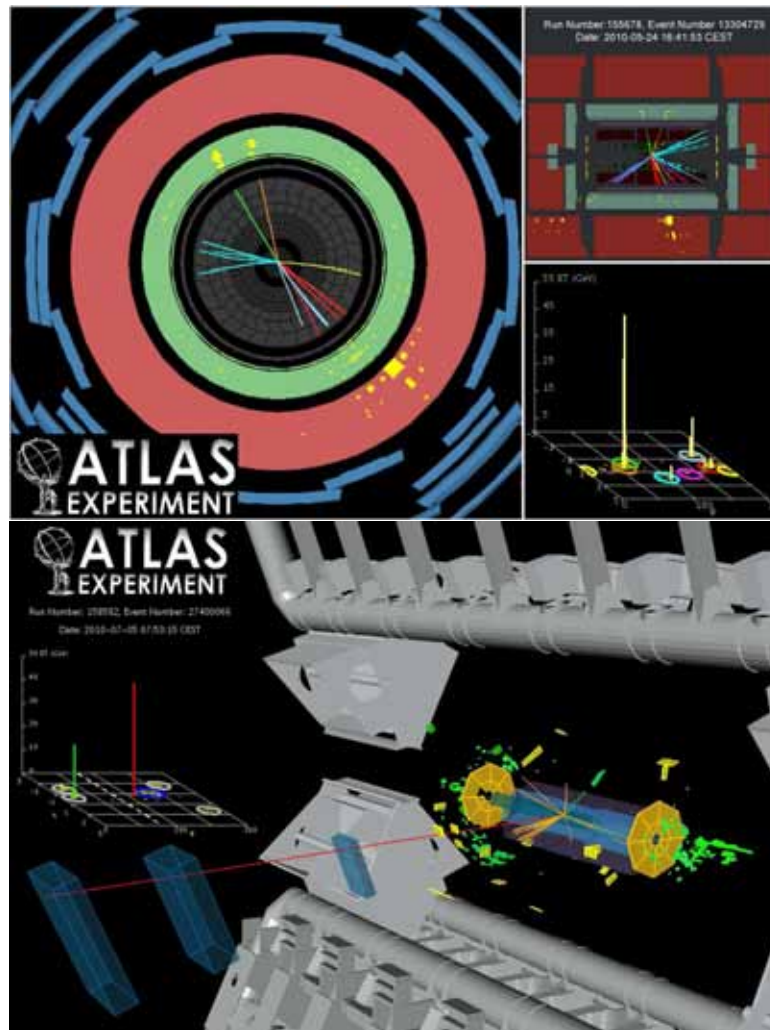


Figure 10.2.: Event display for the first dilepton ee candidate (top) and first dilepton $e\mu$ candidate [263] (bottom). The centre view of the top picture shows the transverse plane of the detector, the upper right show a $R - z$ view of the detector and the lower right lego plot shows the ϕ and η position of the energy entries in the calorimeters. The tracks are coloured according to the assigned object. The two electrons are located in the upper hemisphere and appear as single tracks with energy depositions in the electromagnetic calorimeter. The detector is displayed in the bottom picture as an exploded 3D model with the calorimeters, parts of the inner tracker and muon chambers removed. For the muon track the crossed muon chambers are highlighted and the energy depositions in the calorimeters are shown. The two leptons can be identified by the track through the muon chambers and by the track pointing to an electromagnetic calorimeter cluster. In the lego plot both leptons have the largest energy entry.

A. List of Samples Used for the Study at $\sqrt{s} = 10$ TeV

Listed here are the samples that were used for the main study at $\sqrt{s} = 10$ TeV. The lists contain the dataset names with the ATLAS production ids and tags. The cross sections and sample sizes are also listed for each sample with the k -factor already applied.

Table A.1.: Sample names and IDs.

Process	ID	dataset name ⁺	tag
$t\bar{t}$ MC@NLO	5200	T1_McAtNlo_Jimmy	e357_s462_r541
Wt -channel	5500	AcerMC_Wt	e352_s462_r541
t -channel	5502	AcerMC_tchan	e352_s462_r541
$Z \rightarrow e^+e^- + [0\dots 5]p$	765 <i>n</i>	AlpgenJimmyZeeNpn_pt20	e376_s462_r563
$Z \rightarrow \mu^+\mu^- + [0\dots 5]p$	766 <i>n</i>	AlpgenJimmyZmumuNpn_pt20	e376_s462_r563
$Z \rightarrow \tau\tau + [0\dots 5]p$	767 <i>n</i>	AlpgenJimmyZtautauNpn_pt20	e376_s462_r563
$W \rightarrow e\nu + [0\dots 5]p$	768 <i>n</i>	AlpgenJimmyWenuNpn_pt20	e376_s462_r563
$W \rightarrow \mu\nu + [0\dots 5]p$	769 <i>n</i>	AlpgenJimmyWmumuNpn_pt20	e376_s462_r563
$W \rightarrow \tau\nu + [0\dots 5]p$	770 <i>n</i>	AlpgenJimmyWtaunuNpn_pt20	e376_s462_r563
$W \rightarrow bb + [0\dots 5]p$	628 <i>n</i>	AlpgenJimmyWbbNpn_pt20	e376_s462_r563
WW	5985	WW_Herwig	e379_s462_r563
ZZ	5986	ZZ_Herwig	e379_s462_r563
WZ	5987	WZ_Herwig	e368_s462_r563

⁺The full dataset name is combined as mc08.10ID.dataset name.recon.AOD.tag/

A. List of Samples Used for the Study at $\sqrt{s}=10$ TeV

Table A.2.: Sample names and IDs.

Process	ID	dataset name ⁺	tag
$t\bar{t}$ MC@NLO r635	5200	T1_McAtNlo_Jimmy	e357_s462_r635
$t\bar{t}$ AcerMC	5206	AcerMCttbarHerwig	e393_s462_r635
$t\bar{t}$ AcerMC max m_t	6250	AcerMCttbar	e393_a84
$t\bar{t}$ AcerMC min m_t	6251	AcerMCttbar	e393_a84
$t\bar{t}$ fast sim	5200	T1_McAtNlo_Jimmy	e357_a68
$t\bar{t} \rightarrow l\nu l\nu + [0 \dots 5]p$	626 n	AlpgenJimmyttbarlnlnNpn	e355_a68
$t\bar{t} \rightarrow l\nu qq + [0 \dots 5]p$	626 n^*	AlpgenJimmyttbarlnqqNpn	e355_a68
QCD JF17	5802	JF17_pythia.jet_filter	e347_s462_r541

⁺The full dataset name is combined as mc08.10ID.dataset name.recon.AOD.tag/

*The dataset IDs start at 6264.

Table A.3.: Sample properties.

Process	Generator	Simulation	note
$t\bar{t}$ MC@NLO	MC@NLO	Full	no all-hadronic
Wt -channel	ACERMC	Full	
t -channel	ACERMC	Full	
$Z \rightarrow e^+e^- + [0 \dots 5]p$	ALPGEN	Full	
$Z \rightarrow \mu^+\mu^- + [0 \dots 5]p$	ALPGEN	Full	
$Z \rightarrow \tau\tau + [0 \dots 5]p$	ALPGEN	Full	
$W \rightarrow e\nu + [0 \dots 5]p$	ALPGEN	Full	
$W \rightarrow \mu\nu + [0 \dots 5]p$	ALPGEN	Full	
$W \rightarrow \tau\nu + [0 \dots 5]p$	ALPGEN	Full	
$W \rightarrow bb + [0 \dots 5]p$	ALPGEN	Full	
WW	HERWIG	Full	
ZZ	HERWIG	Full	
WZ	HERWIG	Full	
$t\bar{t}$ MC@NLO r635	MC@NLO	Full	no all-hadronic
$t\bar{t}$ AcerMC	ACERMC	Full	no all-hadronic
$t\bar{t}$ AcerMC max m_t	ACERMC	Fast	no all-hadronic, max. m_t
$t\bar{t}$ AcerMC min m_t	ACERMC	Fast	no all-hadronic, min. m_t
$t\bar{t}$ fast sim	MC@NLO	ATLFAST2	no all-hadronic
$t\bar{t} \rightarrow l\nu l\nu + [0 \dots 5]p$	ALPGEN	ATLFAST2	
$t\bar{t} \rightarrow l\nu qq + [0 \dots 5]p$	ALPGEN	ATLFAST2	

Table A.4.: Sample cross sections top-quark.

Process	k -factor	calculation order	Ref.	sample cross section [pb]	sample size [pb ⁻¹]
$t\bar{t}$ MC@NLO	1.07	approx. NNLO	[204]	217.06	1638.9
Wt -channel	0.99	NLO	[205]	14.27	700.9
t -channel	1.05	NLO	[71]	43.18	585.4

Table A.5.: Sample cross sections Z -boson, corrected to NNLO with k -factors [206].

Process	k -factor	sample cross section [pb]	sample size [pb ⁻¹]
$Z \rightarrow e^+e^- + 0p$	1.22	1095.78	238.2
$Z \rightarrow e^+e^- + 1p$	1.22	206.57	245.2
$Z \rightarrow e^+e^- + 2p$	1.22	88.45	2355.6
$Z \rightarrow e^+e^- + 3p$	1.22	25.72	2446.3
$Z \rightarrow e^+e^- + 4p$	1.22	7.32	2459.0
$Z \rightarrow e^+e^- + 5p$	1.22	2.11	2487.4
$Z \rightarrow \mu^+\mu^- + 0p$	1.22	1098.26	231.5
$Z \rightarrow \mu^+\mu^- + 1p$	1.22	250.36	243.5
$Z \rightarrow \mu^+\mu^- + 2p$	1.22	84.61	2341.9
$Z \rightarrow \mu^+\mu^- + 3p$	1.22	26.39	2376.8
$Z \rightarrow \mu^+\mu^- + 4p$	1.22	7.42	2489.6
$Z \rightarrow \mu^+\mu^- + 5p$	1.22	2.07	2623.9
$Z \rightarrow \tau\tau + 0p$	1.22	1101.31	241.4
$Z \rightarrow \tau\tau + 1p$	1.22	255.30	243.3
$Z \rightarrow \tau\tau + 2p$	1.22	85.60	2453.0
$Z \rightarrow \tau\tau + 3p$	1.22	25.71	2466.1
$Z \rightarrow \tau\tau + 4p$	1.22	7.37	2483.4
$Z \rightarrow \tau\tau + 5p$	1.22	2.09	2530.4

Table A.6.: Sample cross sections W -boson, corrected to NNLO with k -factors [206].

Process	k -factor	sample cross section [pb]	sample size [pb ⁻¹]
$W \rightarrow e\nu + 0p$	1.22	12425.33	106.2
$W \rightarrow e\nu + 1p$	1.22	2577.13	101.5
$W \rightarrow e\nu + 2p$	1.22	824.72	942.9
$W \rightarrow e\nu + 3p$	1.22	248.03	180.7
$W \rightarrow e\nu + 4p$	1.22	68.44	843.3
$W \rightarrow e\nu + 5p$	1.22	20.25	160.5
$W \rightarrow \mu\nu + 0p$	1.22	12353.35	106.7
$W \rightarrow \mu\nu + 1p$	1.22	2629.71	91.6
$W \rightarrow \mu\nu + 2p$	1.22	832.41	917.0
$W \rightarrow \mu\nu + 3p$	1.22	246.44	173.4
$W \rightarrow \mu\nu + 4p$	1.22	67.71	175.7
$W \rightarrow \mu\nu + 5p$	1.22	19.89	176.0
$W \rightarrow \tau\nu + 0p$	1.22	12417.53	102.1
$W \rightarrow \tau\nu + 1p$	1.22	2570.42	78.7
$W \rightarrow \tau\nu + 2p$	1.22	820.82	964.9
$W \rightarrow \tau\nu + 3p$	1.22	247.29	177.4
$W \rightarrow \tau\nu + 4p$	1.22	67.47	177.9
$W \rightarrow \tau\nu + 5p$	1.22	20.74	168.8
$W \rightarrow bb + 0p$	1.22	6.26	2476.6
$W \rightarrow bb + 1p$	1.22	6.11	2521.8
$W \rightarrow bb + 2p$	1.22	3.53	2539.3
$W \rightarrow bb + 3p$	1.22	1.96	2545.6

Table A.7.: Sample cross sections dibosons [34].

Process	k -factor	sample cross section [pb]	sample size [pb ⁻¹]
WW	1.69	26.40	937.6
ZZ	1.42	1.93	5193.4
WZ	1.81	8.82	1133.7

Table A.8.: Sample cross sections top-quark, all cross sections are scaled to approx. NNLO calculation [204].

Process	k -factor	sample cross section [pb]	sample size [pb ⁻¹]
$t\bar{t}$ MC@NLO r635	1.07	217.06	2598
$t\bar{t}$ AcerMC	2.01	217.06	569
$t\bar{t}$ AcerMC max m_t	2.01	217.06	252
$t\bar{t}$ AcerMC min m_t	2.01	217.06	571
$t\bar{t}$ fast sim	2.01	217.06	682
$t\bar{t} \rightarrow l\nu l\nu$ +0p	1.71	12.68	1064
$t\bar{t} \rightarrow l\nu l\nu$ +1p	1.71	13.72	1041
$t\bar{t} \rightarrow l\nu l\nu$ +2p	1.71	9.36	863
$t\bar{t} \rightarrow l\nu l\nu$ +3p	1.71	7.06	1301
$t\bar{t} \rightarrow l\nu qq$ +0p	1.71	51.80	929
$t\bar{t} \rightarrow l\nu qq$ +1p	1.71	57.11	841
$t\bar{t} \rightarrow l\nu qq$ +2p	1.71	38.30	785
$t\bar{t} \rightarrow l\nu qq$ +3p	1.71	27.63	688

B. Coordinate System

For orientation the coordinate system is shortly presented here. Also common definitions that describe the event topology are given. ATLAS uses a right-handed Cartesian coordinate system where the x -direction points towards the centre of the LHC ring and the z -direction is directed along the beam pipe. Thus the symmetry axis for the cylindrical structure is the z -axis and the $x-y$ plane spans the transverse plane containing the azimuthal angle ϕ . Quantities like the transverse momentum, p_T , transverse energy, E_T and the missing transverse energy, \cancel{E}_T , are also defined in this plane. The polar angle θ is measured with respect to the beam axis, but at hadron colliders the pseudorapidity η is more commonly used instead:

$$\eta = -\ln \tan\left(\frac{\theta}{2}\right). \quad (\text{B.1})$$

For a particle with a given four-vector the pseudorapidity, η , and the polar angle, ϕ , can be defined as

$$\eta = -\frac{1}{2} \ln\left(\frac{p + p_z}{p - p_z}\right), \quad (\text{B.2})$$

and

$$\phi = \text{atan2}(p_y/p_x). \quad (\text{B.3})$$

Furthermore, the rapidity y is defined as

$$y = -\frac{1}{2} \ln\left(\frac{E + p_z}{E - p_z}\right). \quad (\text{B.4})$$

The distance measure $\Delta\mathcal{R}$ is defined as the distance in the $\phi - \eta$ space:

$$(\Delta\mathcal{R})^2 = (\Delta\phi)^2 + (\Delta\eta)^2. \quad (\text{B.5})$$

Bibliography

- [1] S. Weinberg, “A model of leptons.” *Phys. Rev. Lett.*, vol. 19, pp. 1264–1266, 1967.
- [2] S. L. Glashow, “Partial symmetries of weak interactions.” *Nucl. Phys.*, vol. 22, pp. 579–588, 1961.
- [3] D. Griffiths, “Introduction to elementary particles.” Weinheim, USA: Wiley-VCH (2008) 454 p.
- [4] M. Herrero, “The Standard Model.”, 1998. Lectures presented at the NATO ASI 98 School, Techniques and Concepts of High Energy Physics, USA, June 18-29 1998, [arXiv:hep-ph/9812242](https://arxiv.org/abs/hep-ph/9812242).
- [5] P. W. Higgs, “Broken symmetries, massless particles and gauge fields.” *Phys. Lett.*, vol. 12, pp. 132–133, 1964.
- [6] P. W. Higgs, “Spontaneous symmetry breakdown without massless bosons.” *Phys. Rev.*, vol. 145, pp. 1156–1163, 1966.
- [7] C. Amsler *et al.* (Particle Data Group), “Review of particle physics.” *Phys. Lett.*, vol. B667, p. 1, 2008.
- [8] W. Bernreuther, “Top quark physics at the LHC.” *J. Phys.*, vol. G35, p. 083001, 2008. [arXiv:hep-ph/0805.1333](https://arxiv.org/abs/hep-ph/0805.1333).
- [9] J. R. Incandela, A. Quadt, W. Wagner, and D. Wicke, “Status and prospects of top-quark physics.” *Prog. Part. Nucl. Phys.*, vol. 63, pp. 239–292, 2009. [arXiv:hep-ex/0904.2499](https://arxiv.org/abs/hep-ex/0904.2499).
- [10] M. L. Perl *et al.*, “Evidence for anomalous lepton production in e^+e^- annihilation.” *Phys. Rev. Lett.*, vol. 35, pp. 1489–1492, 1975.
- [11] G. S. Abrams *et al.*, “Measurement of Z -decays into lepton pairs.” *Phys. Rev. Lett.*, vol. 63, p. 2780, 1989.
- [12] K. Kodama *et al.* (DONUT), “Observation of tau-neutrino interactions.” *Phys. Lett.*, vol. B504, pp. 218–224, 2001. [arXiv:hep-ex/0012035](https://arxiv.org/abs/hep-ex/0012035).

- [13] S. W. Herb *et al.*, “Observation of a dimuon resonance at 9.5 GeV in 400 GeV proton-nucleus collisions.” *Phys. Rev. Lett.*, vol. 39, pp. 252–255, 1977.
- [14] S. L. Glashow, J. Iliopoulos, and L. Maiani, “Weak interactions with lepton-hadron symmetry.” *Phys. Rev.*, vol. D2, pp. 1285–1292, 1970.
- [15] A. Bean *et al.* (CLEO), “Improved upper limit on flavor changing neutral current decays of the b -quark.” *Phys. Rev.*, vol. D35, p. 3533, 1987.
- [16] S. Pakvasa, D. P. Roy, and S. Uma Sankar, “Phenomenological analysis of a topless left-right model.” *Phys. Rev.*, vol. D42, pp. 3160–3168, 1990.
- [17] H. Albrecht *et al.* (ARGUS), “Observation of $B^0 - \bar{B}^0$ mixing.” *Phys. Lett.*, vol. B192, p. 245, 1987.
- [18] H. Albrecht *et al.* (ARGUS), “A study of $\bar{B}^0 \rightarrow D^{*+}$ lepton-anti-neutrino and $B^0 - \bar{B}^0$ mixing using partial D^{*+} reconstruction.” *Phys. Lett.*, vol. B324, pp. 249–254, 1994.
- [19] J. E. Bartelt *et al.* (CLEO), “Two measurements of $B^0 - \bar{B}^0$ mixing.” *Phys. Rev. Lett.*, vol. 71, pp. 1680–1684, 1993.
- [20] D. Schaile and P. M. Zerwas, “Measuring the weak isospin of b -quarks.” *Phys. Rev.*, vol. D45, pp. 3262–3265, 1992.
- [21] The ALEPH Collaboration, “Precision electroweak measurements on the Z -resonance.” *Phys. Rept.*, vol. 427, p. 257, 2006. [arXiv:hep-ex/0509008](https://arxiv.org/abs/hep-ex/0509008).
- [22] R. S. Moore, “An overview of Tevatron collider Run II at Fermilab.” (FERMILAB-CONF-02-320-E).
- [23] The Tevatron Collaboration, “Design report Tevatron 1 project.” (FERMILAB-DESIGN-1984-01).
- [24] F. Abe *et al.* (CDF), “Observation of top quark production in $p\bar{p}$ collisions.” *Phys. Rev. Lett.*, vol. 74, pp. 2626–2631, 1995. [arXiv:hep-ex/9503002](https://arxiv.org/abs/hep-ex/9503002).
- [25] S. Abachi *et al.* (D0), “Observation of the top quark.” *Phys. Rev. Lett.*, vol. 74, pp. 2632–2637, 1995. [arXiv:hep-ex/9503003](https://arxiv.org/abs/hep-ex/9503003).
- [26] J. C. Collins, D. E. Soper, and G. F. Sterman, “Factorization of hard processes in QCD.” *Adv. Ser. Direct. High Energy Phys.*, vol. 5, pp. 1–91, 1988. [arxiv:hep-ph/0409313](https://arxiv.org/abs/hep-ph/0409313).
- [27] J. Pumplin *et al.*, “New generation of parton distributions with uncertainties from global QCD analysis.” *JHEP*, vol. 07, p. 012, 2002. [arXiv:hep-ph/0201195](https://arxiv.org/abs/hep-ph/0201195).

-
- [28] P. M. Nadolsky *et al.*, “Implications of CTEQ global analysis for collider observables.” *Phys. Rev.*, vol. D78, p. 013004, 2008. [arXiv:hep-ph/0802.0007](#).
- [29] A. D. Martin, R. G. Roberts, W. J. Stirling, and R. S. Thorne, “Uncertainties of predictions from parton distributions. 1: Experimental errors.” *Eur. Phys. J.*, vol. C28, pp. 455–473, 2003. [arXiv:hep-ph/0211080](#).
- [30] A. D. Martin, W. J. Stirling, R. S. Thorne, and G. Watt, “Update of parton distributions at NNLO.” *Phys. Lett.*, vol. B652, pp. 292–299, 2007. [arXiv:hep-ph/0706.0459](#).
- [31] M. Cacciari, S. Frixione, M. L. Mangano, P. Nason, and G. Ridolfi, “Updated predictions for the total production cross sections of top and of heavier quark pairs at the Tevatron and at the LHC.” *JHEP*, vol. 09, p. 127, 2008. [arXiv:hep-ph/0804.2800](#).
- [32] S. Moch and P. Uwer, “Theoretical status and prospects for top-quark pair production at hadron colliders.” *Phys. Rev.*, vol. D78, p. 034003, 2008. [arXiv:hep-ph/0804.1476](#).
- [33] U. Langenfeld, S. Moch, and P. Uwer, “New results for $t\bar{t}$ production at hadron colliders.” (DESY-09-104, SFB/CPP-09-61, HU-EP-09/31), 2009. [arXiv:hep-ph/0907.2527](#).
- [34] S. Frixione and B. R. Webber, “Matching NLO QCD computations and parton shower simulations.” *JHEP*, vol. 06, p. 029, 2002. [arXiv:hep-ph/0204244](#).
- [35] W. Bernreuther, M. Fuecker, and Z.-G. Si, “Weak interaction corrections to hadronic top-quark pair production.” *Phys. Rev.*, vol. D74, p. 113005, 2006. [arXiv:hep-ph/0610334](#).
- [36] J. H. Kuhn, A. Scharf, and P. Uwer, “Electroweak effects in top-quark pair production at hadron colliders.” *Eur. Phys. J.*, vol. C51, pp. 37–53, 2007. [arXiv:hep-ph/0610335](#).
- [37] W. Hollik and M. Kollar, “NLO QED contributions to top-pair production at hadron collider.” *Phys. Rev.*, vol. D77, p. 014008, 2008. [arXiv:hep-ph/0708.1697](#).
- [38] S. Catani, “Aspects of QCD, from the Tevatron to the LHC.” (CERN-TH/2000-073), 2000. [arXiv:hep-ph/0005233](#).
- [39] J. H. Kuhn, “Theory of top quark production and decay.” (SLAC-R-494, CONF-9507258-UC-414, TTP96-18), 1996. [arXiv:hep-ph/9707321](#).

- [40] M. Jezabek and J. H. Kuhn, “QCD corrections to semileptonic decays of heavy quarks.” *Nucl. Phys.*, vol. B314, p. 1, 1989.
- [41] M. Jezabek and J. H. Kuhn, “Semileptonic decays of top quarks.” *Phys. Lett.*, vol. B207, p. 91, 1988.
- [42] A. Denner and T. Sack, “The top width.” *Nucl. Phys.*, vol. B358, pp. 46–58, 1991.
- [43] G. Eilam, R. R. Mendel, R. Migneron, and A. Soni, “Radiative corrections to top-quark decay.” *Phys. Rev. Lett.*, vol. 66, pp. 3105–3108, 1991.
- [44] M. Jezabek and J. H. Kuhn, “The top width: Theoretical update.” *Phys. Rev.*, vol. D48, pp. 1910–1913, 1993. [arXiv:hep-ph/9302295](#).
- [45] M.-A. Pleier, “Review of top quark properties measurements at the Tevatron.” *Int. J. Mod. Phys.*, vol. A24, pp. 2899–3037, 2009. [arXiv:hep-ex/0810.5226](#).
- [46] F. Abe *et al.* (CDF), “The CDF detector: An overview.” *Nucl. Instr. Meth.*, vol. A271, pp. 387–403, 1988.
- [47] R. Blair *et al.* (CDF-II), “The CDF-II detector: Technical design report.” (FERMILAB-PUB-96-390-E).
- [48] S. Abachi *et al.* (D0), “The D0 detector.” *Nucl. Instrum. Meth.*, vol. A338, pp. 185–253, 1994.
- [49] V. M. Abazov *et al.* (D0), “The upgraded D0 detector.” *Nucl. Instrum. Meth.*, vol. A565, pp. 463–537, 2006. [arXiv:physics/0507191](#).
- [50] T. Aaltonen *et al.* (CDF), “ $t\bar{t}$ -production cross section measurement in the all-hadronic channel (2.9 fb^{-1}).” (CDF Conf. Note 9841), 2009.
- [51] V. M. Abazov *et al.* (D0), “Measurement of the $p\bar{p} \rightarrow t\bar{t}$ production cross section at $\sqrt{s} = 1.96 \text{ TeV}$ in the fully hadronic decay channel.” *Phys. Rev.*, vol. D76, p. 072007, 2007. [arXiv:hep-ex/0612040](#).
- [52] T. Aaltonen *et al.* (CDF), “Measurement of the ratio of the top pair cross section with the Z -boson cross section in 4.3 fb^{-1} .” (CDF Conf. Note 9878), 2009.
- [53] T. Aaltonen *et al.* (CDF), “Measurement of the $t\bar{t}$ cross section in the lepton plus jets channel using neural networks in 4.6 fb^{-1} of CDF data.” (CDF Conf. Note 9950), 2009.

-
- [54] V. M. Abazov *et al.* (D0), “Measurement of the $t\bar{t}$ production cross section in $p\bar{p}$ collisions at $\sqrt{s} = 1.96$ TeV using kinematic characteristics of lepton+jets events.” *Phys. Rev.*, vol. D76, p. 092007, 2007. [arXiv:hep-ex/0705.2788](#).
- [55] V. M. Abazov *et al.* (D0), “Measurement of the $t\bar{t}$ production cross section in $p\bar{p}$ collisions at $\sqrt{s} = 1.96$ TeV.” *Phys. Rev. Lett.*, vol. 100, p. 192004, 2008. [arXiv:hep-ex/0803.2779](#).
- [56] D. E. Acosta *et al.* (CDF), “Measurement of the $t\bar{t}$ production cross section in $p\bar{p}$ collisions at $\sqrt{s} = 1.96$ TeV using dilepton events.” *Phys. Rev. Lett.*, vol. 93, p. 142001, 2004. [arXiv:hep-ex/0404036](#).
- [57] T. Aaltonen *et al.* (CDF), “A measurement of the $t\bar{t}$ cross section in $p\bar{p}$ collisions at $\sqrt{s} = 1.96$ TeV using dilepton events with a lepton plus track selection.” *Phys. Rev.*, vol. D79, p. 112007, 2009. [arXiv:hep-ex/0903.5263](#).
- [58] T. Aaltonen *et al.* (CDF), “Measurement of $t\bar{t}$ -production cross section in dilepton channel using 4.5 fb^{-1} of Run II data.” (CDF Conf. Note 9890), 2009.
- [59] V. M. Abazov *et al.* (D0), “Measurement of the $t\bar{t}$ production cross-section in $p\bar{p}$ collisions using dilepton events.” *Phys. Rev.*, vol. D76, p. 052006, 2007. [arXiv:hep-ex/0706.0458](#).
- [60] V. M. Abazov *et al.* (D0), “Measurement of the $t\bar{t}$ production cross section and top quark mass extraction using dilepton events in $p\bar{p}$ collisions.” *Phys. Lett.*, vol. B679, pp. 177–185, 2009. [arXiv:hep-ex/0901.2137](#).
- [61] T. Aaltonen *et al.* (CDF), “Combination of CDF top-quark pair production cross section measurements with up to 4.6 fb^{-1} .” (CDF Conf. Note 9913), 2009.
- [62] V. M. Abazov *et al.* (D0), “Combination of $t\bar{t}$ cross section measurements and constraints on the mass of the top quark and its decays into charged Higgs bosons.” *Phys. Rev.*, vol. D80, p. 071102, 2009. [arXiv:hep-ex/0903.5525](#).
- [63] T. Aaltonen *et al.* (CDF), “Top dilepton cross section in 5.1 fb^{-1} using the DIL selection.” (CDF Conf. Note 10163), 2010.
- [64] T. Arens and L. M. Sehgal, “Azimuthal correlation of charged leptons produced in $p\bar{p} \rightarrow t\bar{t} + \dots$ ” *Phys. Lett.*, vol. B302, pp. 501–506, 1993.
- [65] T. Aaltonen *et al.* (CDF), “Top production mechanism using azimuthal correlation of charged leptons.” (CDF Conf. Note 9432), 2008.

- [66] T. Aaltonen *et al.* (CDF), “Measurement of the fraction of $t\bar{t}$ production via gluon-gluon fusion in $p\bar{p}$ collisions at $\sqrt{s} = 1.96$ TeV.” *Phys. Rev.*, vol. D79, p. 031101, 2009. [arXiv:hep-ex/0807.4262](#).
- [67] The ALEPH Collaboration, “Precision electroweak measurements and constraints on the Standard Model.” (CERN-PH-EP/2008-020), 2008. [arXiv:hep-ex/0811.4682](#).
- [68] The ALEPH Collaboration, “Precision electroweak measurements and constraints on the Standard Model.” (CERN-PH-EP/2009-023), 2009. [arXiv:hep-ex/0911.2604](#).
- [69] The Tevatron Electroweak Working Group, CDF and D0 Collaboration, “Combination of CDF and D0 results on the mass of the top quark.” (FERMILAB-TM-2466-E, TEVEWWG-TOP-2010-07, CDF-NOTE-10210, D0-NOTE-6090), 2010. [arXiv:hep-ex/1007.3178](#).
- [70] B. W. Harris, E. Laenen, L. Phaf, Z. Sullivan, and S. Weinzierl, “The fully differential single top quark cross-section in next to leading order QCD.” *Phys. Rev.*, vol. D66, p. 054024, 2002. [arXiv:hep-ph/0207055](#).
- [71] Z. Sullivan, “Understanding single top-quark production and jets at hadron colliders.” *Phys. Rev.*, vol. D70, p. 114012, 2004. [arXiv:hep-ph/0408049](#).
- [72] J. M. Campbell, R. K. Ellis, and F. Tramontano, “Single top production and decay at next-to-leading order.” *Phys. Rev.*, vol. D70, p. 094012, 2004. [arXiv:hep-ph/0408158](#).
- [73] N. Kidonakis, “Single top production at the Tevatron: Threshold resummation and finite-order soft gluon corrections.” *Phys. Rev.*, vol. D74, p. 114012, 2006. [arXiv:hep-ph/0609287](#).
- [74] N. Kidonakis, “Higher-order soft gluon corrections in single top quark production at the LHC.” *Phys. Rev.*, vol. D75, p. 071501, 2007. [arXiv:hep-ph/0701080](#).
- [75] T. M. P. Tait, “The tW^- mode of single top production.” *Phys. Rev.*, vol. D61, p. 034001, 2000. [arXiv:hep-ph/9909352](#).
- [76] A. Belyaev and E. Boos, “Single top quark $tW + X$ production at the LHC: A closer look.” *Phys. Rev.*, vol. D63, p. 034012, 2001. [arXiv:hep-ph/0003260](#).
- [77] V. M. Abazov *et al.* (D0), “Evidence for production of single top quarks and first direct measurement of $|V_{tb}|$.” *Phys. Rev. Lett.*, vol. 98, p. 181802, 2007. [arXiv:hep-ex/0612052](#).

-
- [78] V. M. Abazov *et al.* (D0), “Evidence for production of single top quarks.” *Phys. Rev.*, vol. D78, p. 012005, 2008. [arXiv:hep-ex/0803.0739](#).
- [79] T. Aaltonen *et al.* (CDF), “Measurement of the single top quark production cross section at CDF.” *Phys. Rev. Lett.*, vol. 101, p. 252001, 2008. [arXiv:hep-ex/0809.2581](#).
- [80] T. Aaltonen *et al.* (CDF), “First observation of electroweak single top quark production.” *Phys. Rev. Lett.*, vol. 103, p. 092002, 2009. [arXiv:hep-ex/0903.0885](#).
- [81] V. M. Abazov *et al.* (D0), “Observation of single top-quark production.” *Phys. Rev. Lett.*, vol. 103, p. 092001, 2009. [arXiv:hep-ex/0903.0850](#).
- [82] D. Chang, W.-F. Chang, and E. Ma, “Alternative interpretation of the Tevatron top events.” *Phys. Rev.*, vol. D59, p. 091503, 1999. [arXiv:hep-ph/9810531](#).
- [83] V. M. Abazov *et al.* (D0), “Experimental discrimination between charge $\frac{2}{3}e$ top quark and charge $\frac{4}{3}e$ exotic quark production scenarios.” *Phys. Rev. Lett.*, vol. 98, p. 041801, 2007. [arXiv:hep-ex/0608044](#).
- [84] A. Beretvas *et al.* (CDF), “Finding the charge of the top quark in the dilepton channel.” (FERMILAB-CONF-06-251-E, Aug 2006), 2006. [arXiv:hep-ex/0707.1339](#).
- [85] W. Bernreuther, A. Brandenburg, and P. Uwer, “Transverse polarization of top quark pairs at the Tevatron and the Large Hadron Collider.” *Phys. Lett.*, vol. B368, pp. 153–162, 1996. [arXiv:hep-ph/9510300](#).
- [86] W. G. D. Dharmaratna and G. R. Goldstein, “Single quark polarization in quantum chromodynamics subprocesses.” *Phys. Rev.*, vol. D53, pp. 1073–1086, 1996.
- [87] V. D. Barger, J. Ohnemus, and R. J. N. Phillips, “Spin correlation effects in the hadroproduction and decay of very heavy top quark pairs.” *Int. J. Mod. Phys.*, vol. A4, p. 617, 1989.
- [88] A. Brandenburg, “Spin spin correlations of top quark pairs at hadron colliders.” *Phys. Lett.*, vol. B388, pp. 626–632, 1996. [arXiv:hep-ph/9603333](#).
- [89] D. Chang, S.-C. Lee, and A. Sumarokov, “On the observation of top spin correlation effect at Tevatron.” *Phys. Rev. Lett.*, vol. 77, pp. 1218–1221, 1996. [arXiv:hep-ph/9512417](#).

- [90] G. Mahlon and S. J. Parke, “Angular correlations in top quark pair production and decay at hadron colliders.” *Phys. Rev.*, vol. D53, pp. 4886–4896, 1996. [arXiv:hep-ph/9512264](#).
- [91] G. Mahlon and S. J. Parke, “Maximizing spin correlations in top quark pair production at the Tevatron.” *Phys. Lett.*, vol. B411, pp. 173–179, 1997. [arXiv:hep-ph/9706304](#).
- [92] W. Bernreuther, A. Brandenburg, Z. G. Si, and P. Uwer, “Top quark spin correlations at hadron colliders: Predictions at next-to-leading order QCD.” *Phys. Rev. Lett.*, vol. 87, p. 242002, 2001. [arXiv:hep-ph/0107086](#).
- [93] W. Bernreuther, A. Brandenburg, Z. G. Si, and P. Uwer, “Top quark pair production and decay at hadron colliders.” *Nucl. Phys.*, vol. B690, pp. 81–137, 2004. [arXiv:hep-ph/0403035](#).
- [94] P. Uwer, “Maximizing the spin correlation of top quark pairs produced at the LHC.” *Phys. Lett.*, vol. B609, pp. 271–276, 2005. [arXiv:hep-ph/0412097](#).
- [95] T. Aaltonen *et al.* (CDF), “First direct bound on the total width of the top quark in $p\bar{p}$ collisions at $\sqrt{s} = 1.96$ TeV.” *Phys. Rev. Lett.*, vol. 102, p. 042001, 2009. [arXiv:hep-ex/0808.2167](#).
- [96] T. Aaltonen *et al.* (CDF), “First direct limit on the top quark lifetime.” (CDF Conf. Note 8104), 2006.
- [97] W. M. Yao *et al.* (Particle Data Group), “Review of particle physics.” *J. Phys.*, vol. G33, pp. 1–1232, 2006.
- [98] D. E. Acosta *et al.* (CDF), “Measurement of $B(t \rightarrow Wb)/B(t \rightarrow Wq)$ at the Collider Detector at Fermilab.” *Phys. Rev. Lett.*, vol. 95, p. 102002, 2005. [arxiv:hep-ex/0505091](#).
- [99] V. M. Abazov *et al.* (D0), “Simultaneous measurement of the ratio $b(t \rightarrow wb)/b(t \rightarrow wq)$ and the top quark pair production cross section with the D0 detector at $\sqrt{s} = 1.96$ TeV.” *Phys. Rev. Lett.*, vol. 100, p. 192003, 2008. [arXiv:hep-ex/0801.1326](#).
- [100] J. A. Aguilar-Saavedra, “Top flavor-changing neutral interactions: Theoretical expectations and experimental detection.” *Acta Phys. Polon.*, vol. B35, pp. 2695–2710, 2004. [arXiv:hep-ph/0409342](#).
- [101] T. Aaltonen *et al.* (CDF), “Search for the flavor changing neutral current decay $t \rightarrow Zq$ in $p\bar{p}$ collisions at $\sqrt{s} = 1.96$ TeV.” *Phys. Rev. Lett.*, vol. 101, p. 192002, 2008. [arXiv:hep-ex/0805.2109](#).

-
- [102] F. Abe *et al.* (CDF), “Search for flavor-changing neutral current decays of the top quark in $p\bar{p}$ collisions at $\sqrt{s} = 1.8$ TeV.” *Phys. Rev. Lett.*, vol. 80, pp. 2525–2530, 1998.
- [103] T. Aaltonen *et al.* (CDF), “Search for top-quark production via flavor-changing neutral currents in $W+1$ -jet events at CDF.” *Phys. Rev. Lett.*, vol. 102, p. 151801, 2009. [arXiv:hep-ex/0812.3400](#).
- [104] J. J. Zhang *et al.*, “Next-to-leading order QCD corrections to the top quark decay via model-independent FCNC couplings.” *Phys. Rev. Lett.*, vol. 102, p. 072001, 2009. [arXiv:hep-ph/0810.3889](#).
- [105] V. M. Abazov (D0), “Search for production of single top quarks via $t\bar{c}g$ and $t\bar{u}g$ flavor-changing neutral current couplings.” *Phys. Rev. Lett.*, vol. 99, p. 191802, 2007. [arXiv:hep-ex/0801.2556](#).
- [106] W. Beenakker *et al.*, “Higgs radiation off top quarks at the Tevatron and the LHC.” *Phys. Rev. Lett.*, vol. 87, p. 201805, 2001. [arxiv:hep-ph/0107081](#).
- [107] W. Beenakker *et al.*, “NLO QCD corrections to $t\bar{t}h$ production in hadron collisions.” *Nucl. Phys.*, vol. B653, pp. 151–203, 2003. [arxiv:hep-ph/0211352](#).
- [108] S. Dawson, L. H. Orr, L. Reina, and D. Wackerth, “Associated top quark Higgs-boson production at the LHC.” *Phys. Rev.*, vol. D67, p. 071503, 2003. [arxiv:hep-ph/0211438](#).
- [109] S. Dawson, C. Jackson, L. H. Orr, L. Reina, and D. Wackerth, “Associated Higgs production with top quarks at the Large Hadron Collider: NLO QCD corrections.” *Phys. Rev.*, vol. D68, p. 034022, 2003. [arxiv:hep-ph/0305087](#).
- [110] U. Baur, A. Juste, L. H. Orr, and D. Rainwater, “Probing electroweak top quark couplings at hadron colliders.” *Phys. Rev.*, vol. D71, p. 054013, 2005. [arxiv:hep-ph/0412021](#).
- [111] U. Baur, A. Juste, D. Rainwater, and L. H. Orr, “Improved measurement of $t\bar{t}Z$ couplings at the CERN LHC.” *Phys. Rev.*, vol. D73, p. 034016, 2006. [arxiv:hep-ph/0512262](#).
- [112] V. Abazov *et al.* (D0), “Search for the Standard Model Higgs boson in the $t\bar{t}H \rightarrow t\bar{t}\bar{b}$.” (D0 Conf. Note 5739), 2008.
- [113] S. Dittmaier, P. Uwer, and S. Weinzierl, “NLO QCD corrections to $t\bar{t}$ +jet production at hadron colliders.” *Phys. Rev. Lett.*, vol. 98, p. 262002, 2007. [arXiv:hep-ph/0703120](#).

- [114] T. Aaltonen *et al.* (CDF), “Measurement of the forward-backward asymmetry in $t\bar{t}$ production in 3.2 fb^{-1} of $p\bar{p}$ collisions at $\sqrt{s} = 1.96\text{ TeV}$.” (CDF Conf. Note 9724), 2009.
- [115] T. Aaltonen *et al.* (CDF), “Forward-Backward asymmetry in top quark production in $p\bar{p}$ collisions at $\sqrt{s} = 1.96\text{ TeV}$.” *Phys. Rev. Lett.*, vol. 101, p. 202001, 2008. [arXiv:hep-ex/0806.2472](#).
- [116] V. M. Abazov *et al.* (D0), “First measurement of the forward-backward charge asymmetry in top quark pair production.” *Phys. Rev. Lett.*, vol. 100, p. 142002, 2008. [arXiv:hep-ex/0712.0851](#).
- [117] S. Y. Choi, C. S. Kim, and J. Lee, “ T odd gluon-top quark effective couplings at the CERN Large Hadron Collider.” *Phys. Lett.*, vol. B415, pp. 67–74, 1997. [arxiv:hep-ph/9706379](#).
- [118] T. G. Rizzo, “Constraints on anomalous top quark couplings at the LHC.” (SLAC-PUB-7294), 1996. [arXiv:hep-ph/9609311](#).
- [119] W. Bernreuther, O. Nachtmann, P. Overmann, and T. Schroder, “Angular correlations and distributions for searches of CP violation in top quark production and decay.” *Nucl. Phys.*, vol. B388, pp. 53–80, 1992.
- [120] J. P. Ma and A. Brandenburg, “CP violation and top quark decays.” *Z. Phys.*, vol. C56, pp. 97–102, 1992.
- [121] M. Jezabek and J. H. Kuhn, “V-A tests through leptons from polarized top quarks.” *Phys. Lett.*, vol. B329, pp. 317–324, 1994. [arxiv:hep-ph/9403366](#).
- [122] J.-j. Cao, R. J. Oakes, F. Wang, and J. M. Yang, “Supersymmetric effects in top quark decay into polarized W -boson.” *Phys. Rev.*, vol. D68, p. 054019, 2003. [arxiv:hep-ph/0306278](#).
- [123] H.-J. He, T. M. P. Tait, and C. P. Yuan, “New topflavor models with seesaw mechanism.” *Phys. Rev.*, vol. D62, p. 011702, 2000. [arXiv:hep-ph/9911266](#).
- [124] F. Hubaut, E. Monnier, P. Pralavorio, K. Smolek, and V. Simak, “ATLAS sensitivity to top quark and W -boson polarization in $t\bar{t}$ events.” *Eur. Phys. J.*, vol. C44S2, pp. 13–33, 2005. [arxiv:hep-ex/0508061](#).
- [125] J. A. Aguilar-Saavedra, J. Carvalho, N. F. Castro, A. Onofre, and F. Veloso, “ATLAS sensitivity to Wtb anomalous couplings in top quark decays.” *Eur. Phys. J.*, vol. C53, pp. 689–699, 2008. [arXiv:hep-ph/0705.3041](#).

-
- [126] C.-R. Chen, F. Larios, and C. P. Yuan, “General analysis of single top production and W -helicity in top decay.” *Phys. Lett.*, vol. B631, pp. 126–132, 2005. [arxiv:hep-ph/0503040](#).
- [127] M. Ciuchini, G. Degrossi, P. Gambino, and G. F. Giudice, “Next-to-leading QCD corrections to $B \rightarrow X/s\gamma$: Standard Model and two-Higgs doublet model.” *Nucl. Phys.*, vol. B527, pp. 21–43, 1998. [arXiv:hep-ph/9710335](#).
- [128] J. F. Gunion, H. E. Haber, G. L. Kane, and S. Dawson, “The Higgs hunter’s guide.” (SCIPP-89/13).
- [129] W. Hollik, W. M. Mosle, and D. Wackerth, “Top pair production at hadron colliders in nonminimal Standard Models.” *Nucl. Phys.*, vol. B516, pp. 29–54, 1998. [arxiv:hep-ph/9706218](#).
- [130] S. P. Martin, “A supersymmetry primer.” ([arXiv:hep-ph/9709356v5](#)), 1997. [arXiv:hep-ph/9709356](#).
- [131] S. Berge, W. Hollik, W. M. Mosle, and D. Wackerth, “SUSY QCD one-loop effects in (un) polarized top-pair production at hadron colliders.” *Phys. Rev.*, vol. D76, p. 034016, 2007. [arxiv:hep-ph/0703016](#).
- [132] J. J. Zhang, C. S. Li, Z. Li, and L. L. Yang, “Supersymmetric QCD corrections to single top quark production at hadron colliders.” *Phys. Rev.*, vol. D75, p. 014020, 2007. [arxiv:hep-ph/0610087](#).
- [133] M. Beccaria *et al.*, “A complete one-loop calculation of electroweak supersymmetric effects in t -channel single top production at LHC.” *Phys. Rev.*, vol. D77, p. 113018, 2008. [arXiv:hep-ph/0802.1994](#).
- [134] M. Beccaria *et al.*, “A complete one-loop description of associated tW production at LHC and a search for possible genuine supersymmetric effects.” *Eur. Phys. J.*, vol. C53, pp. 257–265, 2008. [arXiv:hep-ph/0705.3101](#).
- [135] C. T. Hill and E. H. Simmons, “Strong dynamics and electroweak symmetry breaking.” *Phys. Rept.*, vol. 381, pp. 235–402, 2003. [arXiv:hep-ph/0203079](#).
- [136] B. Lillie, L. Randall, and L.-T. Wang, “The bulk RS KK-gluon at the LHC.” *JHEP*, vol. 09, p. 074, 2007. [arXiv:hep-ph/0701166](#).
- [137] T. G. Rizzo, “Testing the nature of Kaluza-Klein excitations at future lepton colliders.” *Phys. Rev.*, vol. D61, p. 055005, 2000. [arXiv:hep-ph/9909232](#).
- [138] T. Aaltonen *et al.* (CDF), “Limits on the production of narrow $t\bar{t}$ resonances in $p\bar{p}$ collisions at $\sqrt{s} = 1.96$ TeV.” *Phys. Rev.*, vol. D77, p. 051102, 2008. [arXiv:hep-ex/0710.5335](#).

- [139] T. Aaltonen *et al.* (CDF), “Search for resonant $t\bar{t}$ production in $p\bar{p}$ collisions at $\sqrt{s} = 1.96$ TeV.” *Phys. Rev. Lett.*, vol. 100, p. 231801, 2008. [arXiv:hep-ex/0709.0705](#).
- [140] T. Aaltonen *et al.* (CDF), “A search for massive gluon decaying to top pair in lepton+jets channel.” (CDF Conf. Note 9164), 2008.
- [141] V. M. Abazov *et al.* (D0), “Search for $t\bar{t}$ resonances in the lepton plus jets final state in $p\bar{p}$ collisions at $\sqrt{s} = 1.96$ TeV.” *Phys. Lett.*, vol. B668, pp. 98–104, 2008. [arXiv:hep-ex/0804.3664](#).
- [142] V. Abazov *et al.* (D0), “Search for $t\bar{t}$ resonances in the lepton+jets final state in $p\bar{p}$ collisions at $\sqrt{s} = 1.96$ TeV.” (D0 Conf. Note 5600), 2008.
- [143] V. Abazov *et al.* (D0), “Search for $t\bar{t}$ resonances in the lepton+jets final state in $p\bar{p}$ collisions at $\sqrt{s} = 1.96$ TeV.” (D0 Conf. Note 5882), 2009.
- [144] J. C. Pati and A. Salam, “Lepton number as the fourth color.” *Phys. Rev.*, vol. D10, pp. 275–289, 1974.
- [145] R. N. Mohapatra and J. C. Pati, “Left-right gauge symmetry and an isoconjugate model of CP violation.” *Phys. Rev.*, vol. D11, pp. 566–571, 1975.
- [146] R. N. Mohapatra and J. C. Pati, “A natural left-right symmetry.” *Phys. Rev.*, vol. D11, p. 2558, 1975.
- [147] C. M. Magass, “Search for new heavy charged gauge bosons.” (FERMILAB-THESIS-2007-33).
- [148] A. Duperrin (CDF), “Searches for Higgs and BSM at the Tevatron.”, 2007. [arXiv:hep-ex/0710.4265](#).
- [149] T. Han, G. Valencia, and Y. Wang, “Hadron collider signatures for new interactions of top and bottom quarks.” *Phys. Rev.*, vol. D70, p. 034002, 2004. [arxiv:hep-ph/0405055](#).
- [150] C. Schwinn, “Unitarity constraints on top quark signatures of Higgsless models.” *Phys. Rev.*, vol. D71, p. 113005, 2005. [arxiv:hep-ph/0504240](#).
- [151] C. Valenzuela, “Spontaneous CP symmetry breaking at the electroweak scale.” *Phys. Rev.*, vol. D71, p. 095014, 2005. [arXiv:hep-ph/0503111](#).
- [152] V. M. Abazov *et al.* (D0), “Direct search for charged Higgs bosons in decays of top quarks.” *Phys. Rev. Lett.*, vol. 88, p. 151803, 2002. [arxiv:hep-ex/0102039](#).

-
- [153] A. Abulencia *et al.* (CDF), “Search for charged Higgs bosons from top quark decays in $p\bar{p}$ collisions at $\sqrt{s} = 1.96$ TeV.” *Phys. Rev. Lett.*, vol. 96, p. 042003, 2006. [arXiv:hep-ex/0510065](#).
- [154] G. Grenier, “Search for supersymmetric charged Higgs bosons at the Tevatron.”, 2007. [arXiv:hep-ex/0710.0853](#).
- [155] C. Boehm, A. Djouadi, and Y. Mambrini, “Decays of the lightest top squark.” *Phys. Rev.*, vol. D61, p. 095006, 2000. [arXiv:hep-ph/9907428](#).
- [156] A. A. Affolder *et al.* (CDF), “Search for the supersymmetric partner of the top quark in $p\bar{p}$ collisions at $\sqrt{s} = 1.8$ TeV.” *Phys. Rev.*, vol. D63, p. 091101, 2001. [arXiv:hep-ex/0011004](#).
- [157] O. S. Bruning, (Ed.) *et al.*, “LHC design report. Vol. I: The LHC main ring.” (CERN-2004-003-V-1).
- [158] O. Buning, (Ed.) *et al.*, “LHC design report. 2. The LHC infrastructure and general services.” (CERN-2004-003-V-2).
- [159] M. Benedikt, (Ed.), P. Collier, (Ed.), V. Mertens, (Ed.), J. Poole, (Ed.), and K. Schindl, (Ed.), “LHC design report. 3. The LHC injector chain.” (CERN-2004-003-V-3).
- [160] C. Lefevre, “The CERN accelerator complex, photo from the CERN Photo-Lab.” (CERN-DI-0812015), 2008.
- [161] The ATLAS Collaboration, “ATLAS: Detector and physics performance technical design report. Volume 1.” (CERN-LHCC-99-14).
- [162] The ATLAS Collaboration, “ATLAS detector and physics performance. Technical design report. Vol. 2.” (CERN-LHCC-99-15).
- [163] G. Aad *et al.* (ATLAS), “The ATLAS experiment at the CERN Large Hadron Collider.” *JINST*, vol. 3, p. S08003, 2008.
- [164] D. Acosta, M. Della Negra, L. Foa, A. Herve, and A. Petrilli, “CMS physics: Technical design report.” (CERN-LHCC-2006-001, CMS-TDR-008-1), 2006.
- [165] P. Giubellino (ALICE.), “The ALICE detector at LHC.” *Nucl. Instrum. Meth.*, vol. A344, pp. 27–38, 1994.
- [166] The LHCb Collaboration, “LHCb: Technical proposal.” (CERN-LHCC-98-004), 1998.
- [167] A. Dudarev *et al.*, “Construction of the ATLAS toroid magnet system.” To be submitted to JINST.

- [168] A. Yamamoto *et al.*, “The ATLAS central solenoid.” *Nucl. Instrum. Meth.*, vol. A584, pp. 53–74, 2008.
- [169] M. e. Gilchriese *et al.*, “Construction and performance of the ATLAS pixel detector.” To be submitted to JINST.
- [170] A. Ahmad *et al.*, “The silicon microstrip sensors of the ATLAS semiconductor tracker.” *Nucl. Instrum. Meth.*, vol. A578, pp. 98–118, 2007.
- [171] A. Abdesselam *et al.*, “The barrel modules of the ATLAS semiconductor tracker.” *Nucl. Instrum. Meth.*, vol. A568, pp. 642–671, 2006.
- [172] A. Abdesselam *et al.* (ATLAS), “The ATLAS semiconductor tracker end-cap module.” *Nucl. Instrum. Meth.*, vol. A575, pp. 353–389, 2007.
- [173] The ATLAS Collaboration, “ATLAS inner detector: Technical design report. Vol. 1.” (CERN-LHCC-97-16).
- [174] The ATLAS Collaboration, “ATLAS inner detector: Technical design report. Vol. 2.” (CERN-LHCC-97-17).
- [175] E. Abat *et al.* (ATLAS TRT), “The ATLAS transition radiation tracker (TRT) proportional drift tube: Design and performance.” *JINST*, vol. 3, p. P02013, 2008.
- [176] The ATLAS Collaboration, “ATLAS liquid argon calorimeter: Technical design report.” (CERN-LHCC-96-41).
- [177] The ATLAS Collaboration, “ATLAS tile calorimeter: Technical design report.” (CERN-LHCC-96-42).
- [178] C. Grupen and B. Schwartz, “Particle detectors.” Cambridge, UK: Cambridge Univ. Pr. (2008) 651 p.
- [179] M. Aleksa *et al.* (ATLAS), “Construction, assembly and tests of the ATLAS electromagnetic end-cap calorimeters.” *JINST*, vol. 3, p. P06002, 2008.
- [180] J. Abdallah *et al.* (ATLAS TileCal), “Design, construction and installation of the ATLAS hadronic barrel scintillator-tile calorimeter.” (ATL-TILECAL-PUB-2008-001). To be submitted to JINST.
- [181] A. Artamonov *et al.*, “The ATLAS forward calorimeters.” *JINST*, vol. 3, p. P02010, 2008.
- [182] S. Palestini, “The muon spectrometer of the ATLAS experiment.” *Nucl. Phys. Proc. Suppl.*, vol. 125, pp. 337–345, 2003.

-
- [183] F. Chevallier, “Alignment of the ATLAS barrel muon spectrometer.” (ATL-MUON-PROC-2008-001).
- [184] J. R. Bensinger, “ATLAS muon endcap alignment.” *Nucl. Phys. Proc. Suppl.*, vol. 150, pp. 136–139, 2006.
- [185] F. Bauer *et al.*, “Construction and test of MDT chambers for the ATLAS muon spectrometer.” *Nucl. Instrum. Meth.*, vol. A461, pp. 17–20, 2001.
- [186] V. Polychronakos *et al.*, “Construction of the ATLAS CSC chambers.” To be submitted to JINST.
- [187] G. Aielli *et al.*, “The RPC LVL1 trigger system of the muon spectrometer of the ATLAS experiment at LHC.” *IEEE Trans. Nucl. Sci.*, vol. 51, pp. 1581–1589, 2004.
- [188] O. Levison, L. Sasaki *et al.*, “The TGC trigger system.” To be submitted to JINST.
- [189] The ATLAS Collaboration, “ATLAS first-level trigger: Technical design report.” (CERN-LHCC-98-14).
- [190] The ATLAS Collaboration, “ATLAS high-level trigger, data acquisition and controls: Technical design report.” (CERN-LHCC-2003-022).
- [191] T. Sjostrand, “Monte Carlo generators.”, 2006. [arxiv:hep-ph/0611247](https://arxiv.org/abs/hep-ph/0611247).
- [192] G. Corcella *et al.*, “HERWIG 6.5: An event generator for hadron emission reactions with interfering gluons (including supersymmetric processes).” *JHEP*, vol. 01, p. 010, 2001. [arxiv:hep-ph/0011363](https://arxiv.org/abs/hep-ph/0011363).
- [193] T. Sjostrand, S. Mrenna, and P. Z. Skands, “PYTHIA 6.4: Physics and manual.” *JHEP*, vol. 05, p. 026, 2006. [arxiv:hep-ph/0603175](https://arxiv.org/abs/hep-ph/0603175).
- [194] J. M. Butterworth, J. R. Forshaw, and M. H. Seymour, “Multiparton interactions in photoproduction at HERA.” *Z. Phys.*, vol. C72, pp. 637–646, 1996. [arxiv:hep-ph/9601371](https://arxiv.org/abs/hep-ph/9601371).
- [195] M. L. Mangano, M. Moretti, F. Piccinini, R. Pittau, and A. D. Polosa, “ALPGEN, a generator for hard multiparton processes in hadronic collisions.” *JHEP*, vol. 07, p. 001, 2003. [arxiv:hep-ph/0206293](https://arxiv.org/abs/hep-ph/0206293).
- [196] B. P. Kersevan and E. Richter-Was, “The Monte Carlo event generator AcerMC version 2.0 with interfaces to PYTHIA 6.2 and HERWIG 6.5.”, 2004. [hep-ph/0405247](https://arxiv.org/abs/hep-ph/0405247).

- [197] M. Dobbs and J. B. Hansen, “The HepMC C++ Monte Carlo event record for high energy physics.” *Comput. Phys. Commun.*, vol. 134, pp. 41–46, 2001.
- [198] V. N. Gribov and L. N. Lipatov, “Deep inelastic electron scattering in perturbation theory.” *Phys. Lett.*, vol. B37, pp. 78–80, 1971.
- [199] G. Altarelli and G. Parisi, “Asymptotic freedom in parton language.” *Nucl. Phys.*, vol. B126, p. 298, 1977.
- [200] Y. L. Dokshitzer, “Calculation of the structure functions for deep inelastic scattering and e^+e^- annihilation by perturbation theory in quantum chromodynamics.” *Sov. Phys. JETP*, vol. 46, pp. 641–653, 1977.
- [201] A. Rimoldi (ATLAS), “The ATLAS detector simulation application.” *Nucl. Phys. Proc. Suppl.*, vol. 172, pp. 49–52, 2007.
- [202] A. Shibata, *et al.*. “Understanding monte carlo generators for top physics.” Int. note ATL-COM-PHYS-2009-334, CERN, Geneva, Jun 2009.
- [203] S. Agostinelli *et al.* (GEANT4), “GEANT4: A simulation toolkit.” *Nucl. Instrum. Meth.*, vol. A506, pp. 250–303, 2003.
- [204] S. Moch and P. Uwer, “Heavy-quark pair production at two loops in QCD.” *Nucl. Phys. Proc. Suppl.*, vol. 183, pp. 75–80, 2008. [arXiv:hep-ph/0807.2794](#).
- [205] J. M. Campbell and F. Tramontano, “Next-to-leading order corrections to Wt production and decay.” *Nucl. Phys.*, vol. B726, pp. 109–130, 2005. [arxiv:hep-ph/0506289](#).
- [206] K. Melnikov and F. Petriello, “The W -boson production cross section at the LHC through $O(\alpha_s^2)$.” *Phys. Rev. Lett.*, vol. 96, p. 231803, 2006. [arxiv:hep-ph/0603182](#).
- [207] W. Lampl, *et al.*, “Calorimeter clustering algorithms: Description and performance.” (ATL-LARG-PUB-2008-002, ATL-COM-LARG-2008-003), Apr 2008.
- [208] G. Aad *et al.* (ATLAS), “Expected performance of the ATLAS experiment-detector, trigger and physics.” (CERN-OPEN-2008-020), 2009. [arXiv:hep-ex/0901.0512](#).
- [209] F. Djama. “Using $Z^0 \rightarrow e^+e^-$ for electromagnetic calorimeter calibration.” Int. note ATL-LARG-2004-008, Aix-Marseille 2. Cent. Phys. Part., Marseille, Jun 2004.

-
- [210] S. Hassani *et al.*, “A muon identification and combined reconstruction procedure for the ATLAS detector at the LHC using the (MUONBOY, STACO, MuTag) reconstruction packages.” *Nucl. Instrum. Meth.*, vol. A572, pp. 77–79, 2007.
- [211] T. Lagouri *et al.*, “A muon identification and combined reconstruction procedure for the ATLAS detector at the LHC at CERN.” *IEEE Trans. Nucl. Sci.*, vol. 51, pp. 3030–3033, 2004.
- [212] D. Adams, *et al.*. “Track reconstruction in the ATLAS muon spectrometer with MOORE 007.” Int. note ATL-SOFT-2003-007, CERN, Geneva, May 2003.
- [213] Tarem, S. and Tarem, Z. and Panikashvili, N. and Belkind, O. “MuGirl – Muon identification in the ATLAS detector from the inside out.” In “Nuclear Science Symposium Conference Record, 2006. IEEE,” vol. 1, pp. 617–621, 29 2006-Nov. 1 2006. ISSN 1082-3654.
- [214] K. Nikolopoulos, D. Fassouliotis, C. Kourkoumelis, and A. Poppleton, “Muon energy loss upstream of the muon spectrometer.” (ATL-MUON-PUB-2007-002, ATL-COM-MUON-2006-019), Sep 2006.
- [215] C. Buttar *et al.*, “Standard Model handles and candles working group: Tools and jets summary report.”, 2008. [arXiv:hep-ph/0803.0678](https://arxiv.org/abs/hep-ph/0803.0678).
- [216] G. C. Blazey *et al.*, “Run II jet physics.”, 2000. [arxiv:hep-ex/0005012](https://arxiv.org/abs/hep-ex/0005012).
- [217] S. Catani, Y. L. Dokshitzer, and B. R. Webber, “The K^- perpendicular clustering algorithm for jets in deep inelastic scattering and hadron collisions.” *Phys. Lett.*, vol. B285, pp. 291–299, 1992.
- [218] S. D. Ellis and D. E. Soper, “Successive combination jet algorithm for hadron collisions.” *Phys. Rev.*, vol. D48, pp. 3160–3166, 1993. [arxiv:hep-ph/9305266](https://arxiv.org/abs/hep-ph/9305266).
- [219] J. P. Dishaw, “The production of neutrinos and neutrino like particles in proton-nucleus interactions.” (FERMILAB-THESIS-1979-08).
- [220] I. Abt *et al.* (H1), “The tracking, calorimeter and muon detectors of the H1 experiment at HERA.” *Nucl. Instrum. Meth.*, vol. A386, pp. 348–396, 1997.
- [221] T. Barillari, *et al.*, “Local hadronic calibration.” (ATL-LARG-PUB-2009-001, ATL-COM-LARG-2008-006), Jun 2008.

- [222] D. Lopez Mateos, E. W. Hughes, and A. Schwartzman. “A simple p_T - and η -dependent Monte Carlo-based jet calibration.” Int. note ATL-COM-PHYS-2009-076, CERN, Geneva, Feb 2009.
- [223] The ATLAS Collaboration, “The ATLAS level-1 calorimeter trigger.” To be submitted to JINST.
- [224] J. Garvey *et al.*, “Use of an FPGA to identify electromagnetic clusters and isolated hadrons in the ATLAS level-1 calorimeter trigger.” *Nucl. Instrum. Meth.*, vol. A512, pp. 506–516, 2003.
- [225] R. Fruhwirth, “Application of Kalman filtering to track and vertex fitting.” *Nucl. Instrum. Meth.*, vol. A262, pp. 444–450, 1987.
- [226] T. Cornelissen, *et al.*, “Concepts, design and implementation of the ATLAS new tracking (NEWT).” (ATL-SOFT-PUB-2007-007, ATL-COM-SOFT-2007-002), Mar 2007.
- [227] S. van der Meer, “Calibration of the effective beam height in the ISR.” (CERN-ISR-PO-68-31, ISR-PO-68-31), 1968.
- [228] A. Bertin, *et al.* (ATLAS). “Calibrating the ATLAS luminosity detectors using beam separation scans.” Int. note ATL-COM-LUM-2010-021, CERN, Geneva, Jun 2010.
- [229] The ATLAS Collaboration. “Luminosity determination using the ATLAS detector.” Conf. note ATLAS-CONF-2010-060, CERN, Geneva, Jul 2010.
- [230] V. Cindro, *et al.*, “The ATLAS beam conditions monitor.” *J. Instrum.*, vol. 3, p. P02004, 2008.
- [231] P. Jenni and M. Nessi, “ATLAS forward detectors for luminosity measurement and monitoring.” (CERN-LHCC-2004-010. LHCC-I-014), Mar 2004.
- [232] M. Cristinziani, *et al.*. “Sensitivity of the top dilepton cross-section measurement at $\sqrt{s} = 10$ TeV.” Int. note ATL-PHYS-INT-2009-066, CERN, Geneva, Jul 2009.
- [233] The ATLAS Collaboration, “Prospects for measuring top pair production in the dilepton channel with early ATLAS data at $\sqrt{s} = 10$ TeV.” (ATL-PHYS-PUB-2009-086), Aug 2009.
- [234] M. Grazzini, “Soft-gluon effects in WW production at hadron colliders.” *JHEP*, vol. 01, p. 095, 2006. [arxiv:hep-ph/0510337](https://arxiv.org/abs/hep-ph/0510337).

-
- [235] G. Cowan, K. Cranmer, E. Gross, and O. Vitells, “Using the Profile Likelihood in Searches for New Physics.”, Jul. 2010. [arXiv:physics.data-an/1007.1727](#).
- [236] A. J. Barr and C. G. Lester, “A review of the mass measurement techniques proposed for the large hadron collider.”, 2010. [arXiv:hep-ph/1004.2732](#).
- [237] L. Sonnenschein, “Analytical solution of $t\bar{t}$ dilepton equations.” *Phys. Rev.*, vol. D73, p. 054015, 2006. [arxiv:hep-ph/0603011](#).
- [238] V. M. Abazov *et al.* (D0), “Measurement of the W -boson mass.” *Phys. Rev. Lett.*, vol. 103, p. 141801, 2009. [arXiv:hep-ex/0908.0766](#).
- [239] C. G. Lester and D. J. Summers, “Measuring masses of semiinvisibly decaying particles pair produced at hadron colliders.” *Phys. Lett.*, vol. B463, pp. 99–103, 1999. [arxiv:hep-ph/9906349](#).
- [240] The ATLAS Collaboration. “Early supersymmetry searches in channels with jets and missing transverse momentum with the ATLAS detector.” Conf. note ATLAS-COM-CONF-2010-066, CERN, Geneva, Jun 2010. (Was originally ‘ATL-COM-PHYS-2010-411’).
- [241] R. Barbieri, S. Ferrara, and C. A. Savoy, “Gauge models with spontaneously broken local supersymmetry.” *Phys. Lett.*, vol. B119, p. 343, 1982.
- [242] L. J. Hall, J. D. Lykken, and S. Weinberg, “Supergravity as the messenger of supersymmetry breaking.” *Phys. Rev.*, vol. D27, pp. 2359–2378, 1983.
- [243] R. Bonciani, S. Catani, M. L. Mangano, and P. Nason, “NLL resummation of the heavy-quark hadroproduction cross-section.” *Nucl. Phys.*, vol. B529, pp. 424–450, 1998. [arxiv:hep-ph/9801375](#).
- [244] J. M. Campbell and R. K. Ellis, “An update on vector-boson pair production at hadron colliders.” *Phys. Rev.*, vol. D60, p. 113006, 1999. [arxiv:hep-ph/9905386](#).
- [245] Q.-H. Cao, R. Schwienhorst, and C. P. Yuan, “Next-to-leading order corrections to single top quark production and decay at Tevatron. 1. s -channel process.” *Phys. Rev.*, vol. D71, p. 054023, 2005. [arxiv:hep-ph/0409040](#).
- [246] Q.-H. Cao, R. Schwienhorst, J. A. Benitez, R. Brock, and C. P. Yuan, “Next-to-leading order corrections to single top quark production and decay at the Tevatron: 2. t -channel process.” *Phys. Rev.*, vol. D72, p. 094027, 2005. [arxiv:hep-ph/0504230](#).

- [247] J. Alwall *et al.*, “MadGraph/MadEvent v4: The New Web Generation.” *JHEP*, vol. 09, p. 028, 2007. [arXiv:hep-ph/0706.2334](#).
- [248] The ATLAS Collaboration. “Top physics analysis with first data, Note I: Lepton selection for top physics.” Int. note, CERN, Geneva, 2010. To be published.
- [249] The ATLAS Collaboration. “Top physics analysis with first data, Note II: Jet selection for top physics.” Int. note, CERN, Geneva, 2010. To be published.
- [250] The ATLAS Collaboration. “Top physics analysis with first data, Note III: Missing ET in top physics.” Int. note, CERN, Geneva, 2010. To be published.
- [251] The ATLAS Collaboration. “Top physics analysis with first data, Note IV: b -tagging for top physics.” Int. note, CERN, Geneva, 2010. To be published.
- [252] The ATLAS Collaboration. “Top physics analysis with first data, Note V: Data-driven determination of lepton fake rate and QCD background estimate.” Int. note, CERN, Geneva, 2010. To be published.
- [253] The ATLAS Collaboration. “Top physics analysis with first data, Note VI: Study of W +jets background for $t\bar{t} \rightarrow \text{lepton} + \text{jets}$ analysis.” Int. note, CERN, Geneva, 2010. To be published.
- [254] The ATLAS Collaboration. “Top physics analysis with first data, Note VII: Study of Z +jets background for $t\bar{t} \rightarrow \text{dilepton}$ analysis.” Int. note, CERN, Geneva, 2010. To be published.
- [255] The ATLAS Collaboration. “Top physics analysis with first data, Note VIII: Description of TopPhys caches used in production and definition of D2PD contents.” Int. note, CERN, Geneva, 2010. To be published.
- [256] The ATLAS Collaboration. “Top physics analysis with first data, Note IX: Monte carlo samples used for top physics.” Int. note, CERN, Geneva, 2010. To be published.
- [257] The ATLAS Collaboration. “Top physics analysis with first data, Note X: Search for $t\bar{t}$ production in the lepton + jets channel.” Int. note, CERN, Geneva, 2010. To be published.
- [258] The ATLAS Collaboration. “Top physics analysis with first data, Note XI: Search for $t\bar{t}$ production in the dilepton channel.” Int. note, CERN, Geneva, 2010. To be published.

-
- [259] M. Begel, *et al.* (ATLAS). “Jet energy scale and its systematic uncertainty in ATLAS for jets produced in proton-proton collisions at $\sqrt{s} = 7$ TeV.” Conf. note ATLAS-COM-CONF-2010-058, CERN, Geneva, Jun 2010. (Was originally ‘ATL-COM-PHYS-2010-404’).
- [260] The ATLAS Collaboration, “Prospects for the top pair production cross-section at $\sqrt{s} = 10$ TeV in the single lepton channel in ATLAS.” (ATL-PHYS-PUB-2009-087), Aug 2009.
- [261] B. Acharya, *et al.*. “Prospects for measuring the top quark pair production cross-section in the single lepton channel at ATLAS in 10 TeV p-p collisions.” Int. note ATL-PHYS-INT-2009-071, CERN, Geneva, Jul 2009.
- [262] The ATLAS Collaboration. “Performance of the ATLAS secondary vertex b -tagging algorithm in 7 TeV collision data.” Conf. note ATLAS-CONF-2010-042, CERN, Geneva, Jul 2010.
- [263] B. Abi, *et al.* (ATLAS). “Search for top pair candidate events in ATLAS at $\sqrt{s} = 7$ TeV.” Conf. note ATLAS-COM-CONF-2010-046, CERN, Geneva, Jul 2010.
- [264] D. B. Ta (ATLAS), “Top-antitop cross section measurement in the di-lepton decay channel with ATLAS.” *Nuovo Cim.*, vol. 123B, pp. 1331–1333, 2008. [arXiv:hep-ex/0808.1124](https://arxiv.org/abs/hep-ex/0808.1124).
- [265] D. B. Ta (ATLAS), “Top quark pair production at the LHC with the ATLAS detector.” *PoS*, vol. EPS-HEP2009, p. 426, 2009.
- [266] T. Stockmanns *et al.*, “Realization of serial powering of ATLAS pixel modules.” *IEEE Trans. Nucl. Sci.*, vol. 52, pp. 2721–2725, 2005.
- [267] D. B. Ta *et al.*, “Serial powering: Proof of principle demonstration of a scheme for the operation of a large pixel detector at the LHC.” *Nucl. Instrum. Meth.*, vol. A557, pp. 445–459, 2006.
- [268] D. B. Ta *et al.*, “Concept, realization and characterization of serially powered pixel modules (serial powering).” *Nucl. Instrum. Meth.*, vol. A565, pp. 113–118, 2006. [arXiv:physics/0604194](https://arxiv.org/abs/physics/0604194).
- [269] Proceedings to the 11th Workshop on Electronics for LHC and Future Experiments. CERN-2005-011. CERN, Geneva, 2005.

Curriculum Vitae

Personal Details

Name	Duc Bao, Ta (Family name)
Date and place of birth	20 th February 1979 Haiphong, Vietnam
Nationality	German

Last positions

- **September 2010**

Postdoctoral position at NIKHEF, Amsterdam, Netherlands

- **March 2005 – August 2010**

Graduate student, this thesis, Supervisor Norbert Wermes and Markus Cristinziani, University of Bonn, Germany

Thesis work contributed to ATLAS internal notes [232, 258] and public note [233]

Thesis work contributed to publication [208], subchapter “cross section measurement in the di-lepton channel“

Results were presented at the Top 2008 Workshop, Elba Italy [264] and were presented within a general overview talk about top pair cross section measurements at ATLAS at the Top Workshop ”From Tevatron to LHC“ (2007) and ”From Tevatron to ATLAS“ (2008), Grenoble, France

Results were also presented at European Physical Society HEP 2009, Krakow, Poland [265]

Mandatory graduate course: Physics from and with quarks, E. Hilger

Participant in the BIGS Programme (Bonn International Graduate School), in the Joint-CERN-Fermilab HCP Summer School 2006, in the German HEP Autumn School Maria Laach 2008

- **April 2008 – January 2009**

Research sojourn at CERN, finalising my analysis in collaboration with people from the top working group

- **Until 2007**

Installation and administration of the group computer cluster (Debian Linux, 30 workstations plus 20 server nodes)

- **Until 2006**

Pixel detector module and stave testing in Bonn, supervision of four students for stave testing

- **Throughout undergraduate studies, diploma thesis and PhD thesis**

Teaching of students as a tutor for various physics lectures and tutor for laboratory courses and one advanced laboratory course (bubble chamber)

Education

- **October 2002 – February 2005**

Diplom (diploma) in physics, overall grade 1.15 (sehr gut), thesis topic: Development and demonstration of “Serial Powering” with ATLAS pixel modules and module ladders (functionality and reliability test), Supervisor Norbert Wermes, University of Bonn, Germany

Thesis results were published as [266, 267] and presented at the Pixel 2005 workshop, Bonn [268] and at the 11th Workshop on Electronics for LHC and Future Experiments, Heidelberg [269].

Participant in the BIPP Bonn International Physics Programme

- **October 2001 – June 2002**

Third year physics courses at Trinity College Dublin, Ireland, overall grade 76% with additional courses in theoretical physics (quantum mechanics and numerical simulations)

Scholarship holder DAAD (German Academic Exchange Service)

- **October 1999 – September 2001**

Vordiplom (pre-diploma), subject: physics, overall grade 1.0 (sehr gut), University of Bonn, Germany semester 1–4

- **September 1998 – October 1999**

Civil service in a residence for elderly people, Sebastianusstift Huerth, Germany

- **September 1989 – June 1998**

Abitur (general qualification for university entrance) overall grade 1.2, High School Gymnasium Bonnstrasse Huerth, Germany